

**TR diss
2542**

**APPLICATION OF CHEMICAL VAPOUR DEPOSITION
IN CATALYST DESIGN**



**APPLICATION OF CHEMICAL VAPOUR DEPOSITION
IN CATALYST DESIGN**

Development of high surface area silicon carbide as catalyst support

PROEFSCHRIFT

ter verkrijging van de graad van doctor
aan de Technische Universiteit Delft,
op gezag van de Rector Magnificus, Prof. ir. K.F. Wakker,
in het openbaar te verdedigen ten overstaan van een commissie,
door het College van Dekanen aangewezen,

op dinsdag 18 april 1995 te 13.30 uur

door

Robert MOENE

scheikundig ingenieur
geboren te Leidschendam



Dit proefschrift is goedgekeurd door de promotoren:

Prof. dr. J.A. Moulijn

Prof. dr. J. Schoonman

Toegevoegd promotor: dr. ir. M. Makkee

Samenstelling promotiecommissie:

Rector Magnificus (of zijn vervanger)

Prof. dr. J.A. Moulijn

Prof. dr. J. Schoonman

Dr. ir. M. Makkee

Prof. dr. ir. H. van Bekkum

Prof. ir. J.W. Geus

P.W. Lednor, Ph.D.

Dr. F.T.B.J. van den Brink

The research described in this thesis has been carried out as a joint project of the section Industrial Catalysis of the Department of Chemical Process Technology and the section Applied Inorganic Chemistry of the Department of Inorganic Chemistry and Thermodynamics of the Faculty of Chemical Technology and Materials Science, Delft University of Technology, with financial support of the Innovation-oriented Research Programme on Catalysis of the Ministry of Economic Affairs, The Netherlands.

CIP-DATA KONINKLIJKE BIBLIOTHEEK, DEN HAAG

Moene, R.

Application of Chemical Vapour Deposition in catalyst design, Development of high surface area silicon carbide as catalyst support /

R. Moene. - Delft : Delft University Press. - Ill.

Thesis Delft University of Technology. - With ref. - With summary in Dutch.

ISBN 90-407-1109-7

NUGI: 841

Subject headings: Chemical Vapour Deposition (CVD) / Catalyst manufacture /

High surface area silicon carbide.

Copyright © 1995 by R. Moene

All rights reserved. No part of the material protected by this copyright notice may be reproduced or utilized in any form or by any means, electronic or mechanical, including photocopying, recording, or by any information storage and retrieval system, without permission from the publisher: Delft University Press, Stevinweg 1, 2628 CN Delft, The Netherlands.

CONTENTS

CHAPTER 1	
General introduction	1
CHAPTER 2	
Evaluation of Isothermal Chemical Vapour Infiltration with Langmuir-Hinshelwood type kinetics	15
CHAPTER 3	
Chemical Vapour Deposition as a novel technique for catalyst preparation; modelling of active phase profiles	41
CHAPTER 4	
Coating of activated carbon with silicon carbide by Chemical Vapour Deposition to improve the oxidation resistance and mechanical strength	59
CHAPTER 5	
Nickel-catalyzed conversion of activated carbon extrudates into high surface area silicon carbide by Reactive Chemical Vapour Deposition	87
CHAPTER 6	
Synthesis of high surface area silicon carbide by Fluidized Bed Chemical Vapour Deposition	115
CHAPTER 7	
High surface area silicon carbide as catalyst support; characterization and stability	131
CHAPTER 8	
Synthesis and thermal stability of nickel, copper, cobalt, and molybdenum catalysts based on high surface area silicon carbide	149
CHAPTER 9	
The stability of high surface area silicon carbide in a high temperature gas-phase reaction; carbon dioxide reforming of methane	171
CHAPTER 10	
General conclusions and summary	183
SAMENVATTING	193
NAWOORD	197
CURRICULUM VITAE	199
LIST OF PUBLICATIONS	201



Chapter 1

General introduction

1. GENERAL INTRODUCTION

Activated carbon holds several advantages over oxidic ceramic catalyst supports. The first one comprises the relative inertness of its surface, which prohibits solid-state reactions between the support and the catalytically active material in almost all cases. Secondly, undesirable side reactions, catalyzed by the support, are generally avoided to a larger extent on the carbon surface. Thirdly, the stability of activated carbon in strong acidic and alkaline environments has resulted in a widespread use in liquid-phase reactions at demanding pH-conditions for the production of fine-chemicals. Fourthly, and finally, the large heat conductivity limits the formation of hot spots in strong exothermic reactions. The use of activated carbon as catalyst support has been mainly restricted by its reactivity with oxygen and hydrogen at elevated temperatures. Additionally, attrition of the support in liquid-phase reactions, catalyzed by noble metals, is a major problem. This results in the loss of precious metals and difficulties in separation (filtration) of the catalyst and product due to the formation of fines. This last drawback of activated carbon can be minimized to a certain extent by optimization of its production method.

In general, activated carbon can be synthesized from an arbitrarily chosen carbonaceous material. In Europe, the production of activated carbon is based on wood (saw-dust), charcoal, peat, peat coke, certain types of hard and brown coal, and the semi-coke of brown coal as raw material. Activated carbon synthesized in the USA finds its origin primarily in brown carbon and petroleum products. Fig. 1 displays the world capacities for activated carbon production in 1974 and 1990 [1], showing an increase of 40% over 15 years. This increase is believed to be maintained over the next decade.

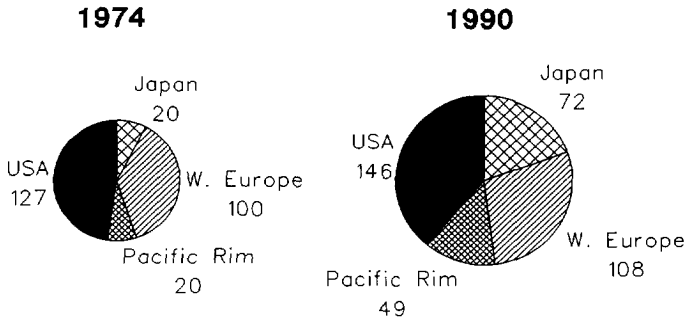


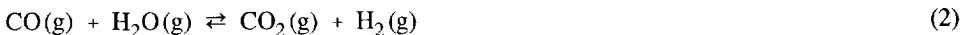
Fig. 1. World production of activated carbon in kilotons in 1974 and 1990

Based on the engineering requirements for various processes, activated carbons are manufactured in three forms: granular, powdered, and shaped products. Powdered activated carbons are mostly applied in liquid-phase operations as single-use commodities, whereas granular and shaped activated carbon are employed both in liquid and gas-phase applications.

Basically two types of manufacturing techniques can be distinguished. Wood based activated carbon is synthesized by mixing pieces of wood with a strong dehydrating agent (*e.g.* phosphoric acid or zinc chloride) and a subsequent treatment at 800 K. After removal of the chemicals, a porous carbonaceous material is obtained, which still embodies the internal structure of the original raw material. This type of activation is called chemical activation, although principally the porous structure is developed by dissolution of tar-like material formed during the activation. On the other hand, physical activation is applied for partly graphitized material. After carbonization in a nitrogen atmosphere at elevated temperatures (1000 K), activation is achieved by reacting the solid with steam at about 1300 K as depicted in reaction 1.



The water-gas shift reaction (eq. 2) is under these conditions in equilibrium. Nearly equal amounts of carbon dioxide and carbon monoxide are observed.



Reaction 3 displays the activation of carbon by carbon dioxide (reverse Boudouard reaction).



Introduction

The surface chemistry will be dealt with in the next paragraph. This production method provides the opportunity of designing the external morphology of the activated carbon. Prior to the carbonization, binders (usually tar-like material) are added, followed by extrusion of the mixture, carbonization and steam-activation. Thus, activated carbon extrudates can be manufactured, which additionally may exhibit a substantially improved mechanical strength, depending on the physico-chemical properties of the coal and binding agent. However, when utilized as catalyst support and subjected to high stirring speeds in a liquid, the rate of attrition is generally considered to be still too high.

1.1 Chemistry involved in steam activation of chars.

The following mechanism is generally accepted to describe the steam-activation process in detail; it comprises a cycle in which the formation of oxygen-containing sites at defects in the basal planes of the activated carbon and the subsequent desorption of these carbon and oxygen containing molecules results in the gasification of the carbon to form the desired porous structure [2,3].



where $\text{H}_2\text{O}-\text{C}_f$ and $\text{O}-\text{C}_f$ display the adsorption of H_2O and atomic oxygen, respectively, on a reactive carbon atom in the basal plane. Desorption of carbon monoxide (reaction 6) generates a new reactive carbon site (C_f').

Hydrogen may inhibit the gasification by blocking the active sites:



This mechanism is also useful in clarifying the relationship between active sites and the reactivity of activated carbon in oxygen containing environments and provides insight into the methods used to improve its resistance against oxidation at elevated temperatures (>1100 K). Several techniques are reported to inhibit oxidation. Most of them are based on the concept of deactivating the oxygen containing defects in the carbon structure [4-6]. However, coating of carbon components with a ceramic material, to act as a diffusion barrier for oxygen, has proven to be a more successful way of improving the oxygen resistance [7]. This coating can be applied by sol-gel methods (*e.g.* the deposition of borate and silicate

Chapter 1

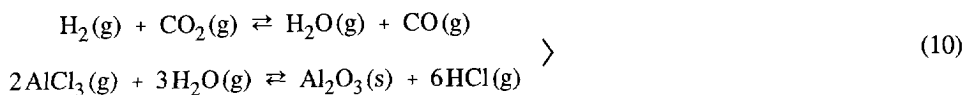
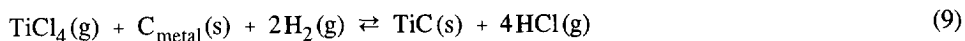
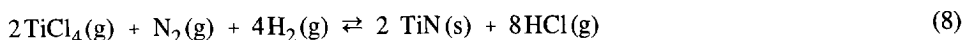
glasses), and by Chemical Vapour Deposition (CVD). In this thesis, research for modifying activated carbon is only directed towards utilization and evaluation of this last technique, which will be described in more detail.

2. CHEMICAL VAPOUR DEPOSITION

2.1 General.

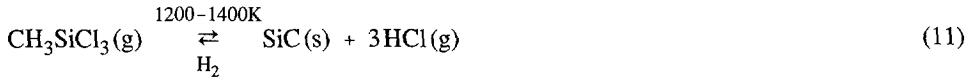
CVD is a well known technique for the deposition of solids from gaseous precursors in the production of solid-state devices, formation of protective coatings, and the structural design of ceramics. Examples of electronic materials produced by CVD are films of insulators, dielectrics, semiconductors, conductors, and magnetic materials. The combination of the synthesis of high purity films and the uniform deposition makes CVD very suitable for the production of Very Large Scale Integrated (VLSI) fine-line devices. Typical properties of these devices are windows and interconnections of sub-micron dimensions and thicknesses.

To improve the corrosion resistance, oxidation resistance, or wear resistance of a component, CVD can be utilized to deposit a thin ceramic film with the desired properties on the substrate. Various types of coating can be distinguished, classified according to their purpose or chemical composition. The cutting tool industry is a major market for CVD coatings. Titanium nitride deposition, often preceded by titanium carbide formation by reaction of TiCl_4 with the carbon present in the metal, and aluminium oxide deposition are primarily used. Generation of steam is carried out by utilizing the water-gas shift reaction during alumina deposition. The CVD-reactions are given below.



The improvement in oxidation resistance of carbon-carbon composites by silicon carbide coatings has led to a widespread use of these materials as aerospace heat shields and turbine components. In this field, methyltrichlorosilane is the primary precursor to deposit stoichiometric SiC.

Introduction



The high oxidation resistance of silicon carbide originates from the formation of a thin glass-like SiO_2 layer at oxygen pressures exceeding 30 Pa, which protects the underlying silicon carbide from additional oxidation [8]. For optimum performance at temperatures above 1600 K, however, it is advisable to use the multi-layer concept in order to improve the mechanical compatibility and oxidation resistance. Thus, carbon-carbon composites are subsequently coated with pyrolytic carbon (mechanical compatibility), silicon carbide (carbon diffusion barrier) and alumina (oxygen barrier). The operation temperature can thus be increased up to 2000 K.

Finally, CVD enables the production of fibre reinforced composites. The substrate consists of a porous body in which a homogeneous deposition has to be achieved. The CVD process for densifying porous preforms is referred to as Chemical Vapour Infiltration (CVI). An important property of ceramic materials is their sensitivity to crack formation. By using the CVI technique, composites can be fabricated which consist of a tough material (*e.g.* woven carbon fibres) which is densified with a ceramic material (*e.g.* SiC). Thus, ceramic parts can be fabricated in various dimensions and with improved physical properties. The major problem in producing composites by CVI is achieving a small density gradient. Due to the obvious mass transport difficulties and resulting premature pore closure, the deposition rate is limited by the rate of diffusion of the gaseous reactants. The production of thin (3 mm) CVI composites can, therefore, take up to several weeks, in which the deposition of the matrix is repeatedly interrupted for intermediate diamond machining operations to remove material from the surface and open passageways to the interior of the preform.

2.2 CVD as a tool in catalyst design.

Chemical Vapour Deposition has enormous potential in the field of catalyst design and manufacture. The presence of the liquid phase as a transport medium of the catalyst precursors can be avoided; deposition of a solid is achieved by the decomposition of gaseous components. Basically, four areas of application can be distinguished, *i.e.* modification of existing catalyst supports by introducing active material, modification of catalyst supports by support coating, conversion of the catalyst support, and total support synthesis *via* the gas phase. The first class of materials synthesized by CVD consists of materials which can be acquired by conventional synthesis routes, displaying new catalytic properties owing to the characteristic structures or compositions achieved by the CVD preparation technique. The second class contains completely new materials whose synthesis is made possible by applying CVD.

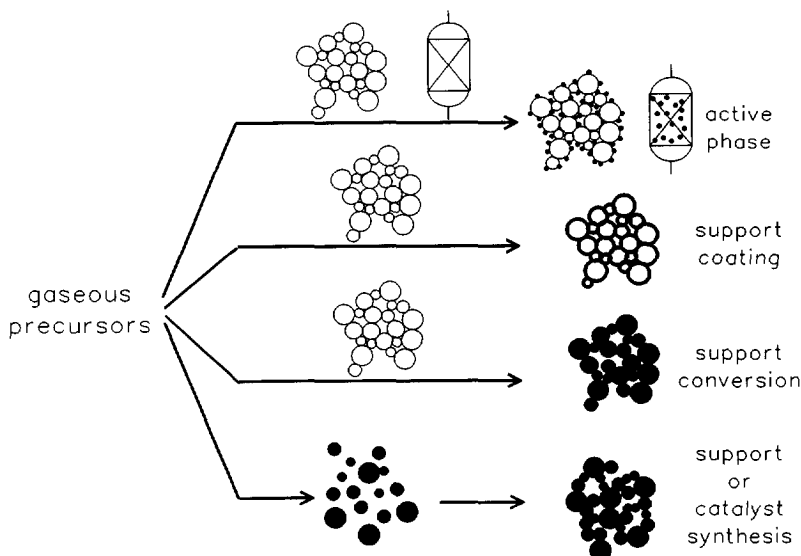


Fig. 2. Concepts in catalyst design utilizing CVD

Regeneration of deactivated catalysts or catalytic reactors is the third area of application. Catalytic activity can be restored by either re-dispersing the catalyst (*e.g.* chlorine treatment of a Pt-reforming catalyst), or depositing additional catalytic material in the reactor. Fig. 2 shows the prospects for catalyst design schematically; moving from the upper to the lower route, the innovative character of the synthesis process increases.

The methods used in this field are pure CVD gas-phase reactions and gas-solid reactions (Reactive Chemical Vapour Deposition). Several illustrations are given below, which by no means give a complete picture. However, the objective is only to depict some of the possibilities of CVD-techniques in catalyst design.

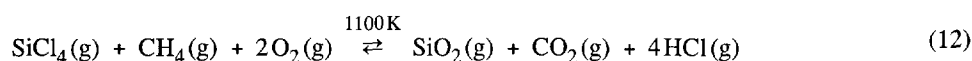
2.2.1 From conventional support via CVD to active catalyst. Modifying traditional catalyst supports *via* the gas phase provides the possibility of creating catalysts which are difficult or impossible to synthesize *via* conventional production routes. Examples are vapour decomposition of metal alkoxides or halides to modify the acidity of the support or adjust the pore size of zeolites. The deposition of B_2O_3 from $B(OC_2H_5)_3$ on silica resulted in a catalyst with higher activities and selectivities for the Beckmann rearrangement of cyclohexanone oxime than those prepared by impregnation [9]. This improvement has been ascribed to the

Introduction

formation of a larger amount of effective acid sites which display a more uniform acid strength, compared to those resulting from impregnation with H_3BO_3 . The structure of V_2O_5 on SiO_2 , prepared by impregnation, is reported to consist of micro-crystallites [10]. EXAFS and XANES analyses show that Chemical Vapour Deposition of V_2O_5 on SiO_2 from $\text{VO}(\text{OC}_2\text{H}_5)_3$ results, however, in highly disperse V_2O_5 [11]. Thin overlays of V_2O_5 on silica of $200 \text{ m}^2/\text{g}$ were found at loading levels up to 5 weight percent [12]. Several methods of modifying pore openings of zeolites have been reported. Examples are the deposition of GeO_2 from germanium methoxide on mordenite [13] and SiO_2 from silicon methoxide on mordenite [14] and on HZSM-5 [15].

Tailoring the interaction between the gas-phase precursor and surface chemistry of the support, a wide range of monometallic catalysts with varying dispersions can be designed. Furthermore, bimetallic catalysts can be synthesized, which consist of a thermodynamically meta-stable composition [16]. The versatility of CVD precursors opens possibilities in loading various supports displaying different thermo-stabilities. An example is application of Pt and Pd on zeolites by Organo-Metallic CVD [17]. Moreover, deposition of metals can be applied to structured catalytic reactors (*e.g.* monoliths). Thus, homogeneous and inhomogeneous activity profiles can be achieved which are prerequisites for attaining an optimal performance of catalytic reactors.

2.2.2 Design of novel catalysts and catalyst supports. A nice example of application of CVD technology in the field of support manufacture is the production of pyrogenic silica. Utilizing CVD techniques, very high purity silica ("Aerosil" or "Cabosil") is obtained by oxidizing a mixture of silicon tetrachloride and methane.



Development of non-oxidic ceramic catalyst (supports) discloses classes of materials which possibly exhibit novel catalytic properties. Application of CVD may be indispensable to achieve high surface area ceramics. Of course, some disadvantages have to be mentioned for catalyst manufacture by CVD. First of all, deposition of the desired metals on catalyst supports has to be carried out in fluidized bed reactors to ensure a homogeneous application of the active phase. Susceptibility for attrition of these catalyst supports will limit the range of applicability. Furthermore, in the course of the CVD process, part of the material will be deposited on the reactor wall unless appropriate measures are taken. In general, CVD reactions are carried out at elevated ($> 800 \text{ K}$) temperatures; these conditions are usually not acceptable in catalyst preparation owing to sintering of the support. However, these problems can be avoided by utilizing organo-metallic CVD precursors. These components decompose

increase of these precursors results in a general trend of CVD compared to well established preparation techniques, in that CVD methods are usually more expensive. As a consequence, it is advisable to apply CVD in those circumstances in which conventional synthesis methods do not result in the desired tailor-made catalysts.

Silicon carbide is one of the ceramic materials which shows promising prospects as catalyst support for processes operating at severe reaction conditions. Furthermore, CVD of silicon carbide can be useful in improving the chemical and mechanical properties of activated carbon. General aspects of silicon carbide production and application will be highlighted below.

3. SILICON CARBIDE

3.1 General.

In 1824 Berzelius [18] was the first to report the possible formation of "Kohlensilicium", Schützenberger [19] defined the stoichiometric formula "SiC" in 1892. In the previous year, Acheson had founded the firm Carborundum, and started producing SiC based on his own patents by the method on which current manufacture still relies on [20]. In this process the following reactions take place at 2300 K to produce "Acheson-SiC".



High purity quartz is used as silicon donor, carbon is usually supplied by cokes. To increase the rate of withdrawal of carbon monoxide, sawdust is usually added to this mixture.

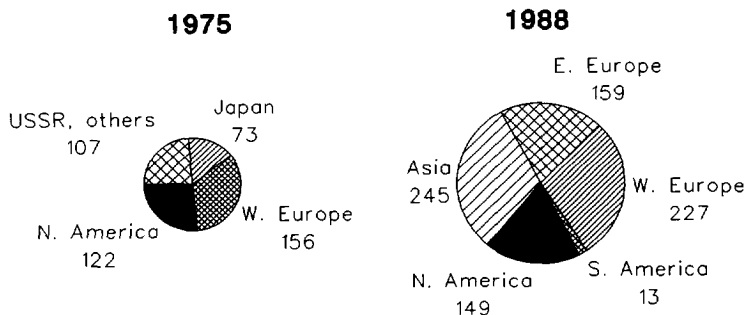


Fig. 3. World production of SiC in kilotons in 1975 and 1988

Introduction

Until 1918, the world production of SiC did not exceed 8.2 kton/year, in 1975 the annual production reached a total of 457 kton, growing to 790 kton in 1988 [21]. Fig. 3 displays the 1975 and 1988 production volumes. While the first application of silicon carbide was as an abrasive, additional markets in metallurgy and refractories have been developed. The variation in fields of application in the past decade is shown in Fig. 4. In ferrous metallurgy, SiC is added to molten iron, yielding a vigorous exothermic reaction, decomposing the silicon carbide, which results in a hotter melt. As a result, the metal is deoxidized and fluidity thereof is promoted.

3.2 Silicon carbide as catalyst and catalyst support.

Silicon carbide is well known for its high hardness, high resistance towards oxidation, high thermostability, thermal conductivity, thermal shock resistance, low reactivity with inorganic acids, and inert surface. However, utilization as catalyst support is mainly hampered by the difficulties in attaining a sufficiently high surface area. Commercial application of SiC is limited to processes in which the low surface area is no disadvantage. Furthermore, silicon carbide can be used in fundamental studies as catalytically inactive support (*e.g.* isotope exchange by tribochemical reaction [22]). Several authors report the use of Acheson SiC as catalyst or catalyst support. Vernon *et al.* [23] investigated the catalytic vapour-phase esterification of benzoic acid with ethyl alcohol over various oxides, supported on SiO₂, Al₂O₃, TiO₂, and Acheson SiC. They reported the highest yields for the system TiO₂/Al₂O₃. By extrapolating the catalyst activity to zero space velocities, the best catalyst was found to be MgO/SiC, of which the performance was attributed to the excellent adherence between the active material and the support.

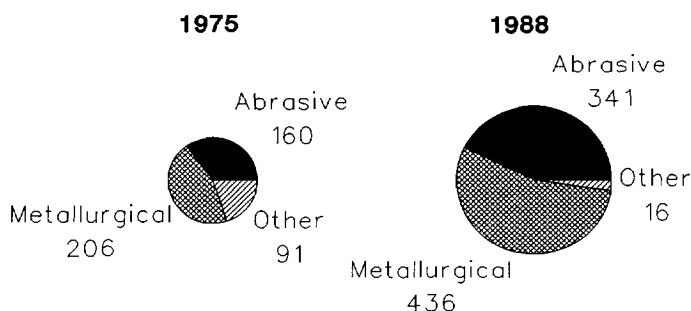


Fig. 4. The variation in fields of application of SiC in 1975 and 1988. The numbers are in kilotons

Chapter 1

Photo-catalytic reduction of carbon dioxide with metal loaded SiC powders has shown to be possible by Yamamura *et al.* [24]. In this case the semi-conducting properties of SiC allow this catalytic application. SiC supported Ag catalysts are used in the epoxidation of ethene [25] and the oxidative dehydrogenation of ethylene glycol into glyoxal [26]. The inertness of the SiC surface is a major advantage for these last two applications. Boutonnet Kizling investigated α -SiC powder as wash-coat on ceramic monoliths to obtain an improved thermostability [27]. A micro-emulsion technique was used to deposit metals on the monolith to overcome the presumed scarcity of reactive sites on the SiC surface, and the resulting problems in anchoring metal ions [28]. Furthermore, they studied the rate of oxidation of SiC in oxygen and oxygen-water mixtures and the catalytic effect of rhodium loading thereof [29].

Due to the low surface area of non-porous Acheson SiC, much effort has been devoted to the synthesis of high surface area SiC. Preparation of other high surface area non-oxidic ceramics (heavy-metal carbides and nitrides) has been the subject of intensive research as well. Vannice *et al.* [30] prepared porous SiC ($< 50 \text{ m}^2/\text{g}$) by decomposing organosilicon compounds ($\text{Si}(\text{CH}_3)_4$) at 1723 K, and tested Pt and Ni loaded SiC catalysts for the synthesis of substitute natural gas (SNG). Hayata and Kono used CVD on graphite to co-deposit SiC and C from SiCl_4 , CH_4 and H_2 at 1673 K and 6.6 kPa [31]. Subsequent removal of the carbon resulted in SiC with 60% porosity and an average pore radius of 3 μm . Fox *et al.* [32] pyrolyzed a silicon containing organic gel ($\text{RSiO}_{1.5}$)_n (R = alkyl, allyl, aryl) to arrive at high surface area SiC ($179 \text{ m}^2/\text{g}$). Lednor and de Ruiter [33] investigated the thermal and hydrothermal stability of this material.

Ledoux and co-workers investigated a modified version of the Acheson process [34-36]. Gaseous SiO was formed by a solid-state reaction between SiO_2 and Si at 1500 K, which was subsequently transferred to a second reaction chamber to let it react with activated carbon at 1375 K. Then, porous SiC is obtained, exhibiting a surface area of $197 \text{ m}^2/\text{g}$ before calcination and $59 \text{ m}^2/\text{g}$ after calcination. Pre-impregnation of the activated carbon with uranium or cerium in amounts of about 10 w% is reported to increase the total surface area (after calcination) to 131 and $141 \text{ m}^2/\text{g}$, respectively.

4. SCOPE OF THIS THESIS

The work described in this thesis deals with the modification of activated carbon by Chemical Vapour Deposition of silicon carbide. This modification has to expand the use of activated carbon as a catalyst support. Two concrete targets have been defined at the start of the project, *viz.*, achieving considerable improvements in both the mechanical strength and

Introduction

the resistance against oxidation. The technique to be used in achieving these goals is restricted to CVD. Initially, deposition of a thin, but gas-tight SiC layer onto the carbon surface was aimed for. The beneficial physical properties of SiC and the texture of the activated carbon can thus be combined. In this thesis the results of that research are reported. It comprises the development of a mathematical model for CVI, evaluation of several modification methods (within the scope of CVD) and characterization and testing of high surface area SiC developed by a new method.

Chapter 2 of this thesis describes the development of a mathematical model to evaluate the use of CVD in coating and densification of porous structures with ceramics (route 2 of Fig. 2). In Chapter 3 the deposition of active phases in catalyst supports and structured catalytic reactors by decomposing gaseous precursors is modelled and evaluated (route 1 of Fig. 2).

Experimental results of conventional Chemical Vapour Deposition of SiC on activated carbon are reported in Chapter 4. Improvements of mechanical strength and oxidation resistance are discussed in detail. The mathematical model described in Chapter 2 is evaluated by comparing the predicted amounts of mass deposited in various experiments.

A novel method to convert activated carbon into porous SiC has been developed, and the results of the fixed bed conversion of activated carbon extrudates are reported in Chapter 5. The chemical part of this conversion mechanism is clarified. Additionally, the influence of mass transfer is investigated.

Chapter 6 describes the use of Fluidized Bed CVD at ambient and reduced pressures for the conversion of activated carbon granulates. The influence of various reaction parameters on carbon conversion and textural properties is studied.

In Chapter 7 crucial physical properties of silicon carbide are reported. The stability at demanding pH in the liquid phase as well as the thermal and hydrothermal stability are investigated.

Chapter 8 elaborates on the synthesis and characterization of silicon carbide based catalysts. Much attention is devoted to the stability of the catalysts at elevated temperatures.

Finally, high-temperature test reactions are carried out to provide insight into the activity, selectivity, and stability of this support in the field of carbon dioxide reforming of methane. The results of these screening experiments are highlighted in Chapter 9.

Chapter 10 concludes this thesis and focuses on the possible application of SiC as catalyst support. Moreover, the potential of CVD in catalyst design is evaluated.

Chapter 1

REFERENCES

1. Kirk Othmer, Encyclopedia of Chemical Technology, 4th ed., Vol. 4, John Wiley & Sons, New York, 1992, p. 1022.
2. H. Jankowska, A. Swiatkowski, and J. Choma, "Active Carbon", Ellis Horwood Series in Physical Chemistry, New York, 1991, p. 40.
3. T. Wigmans in "Carbon and Coal Gasification", J.L. Figueiredo and J.A. Moulijn (eds.), NATO ASI Series, Serie E, Martinus Nijhoff Publishers, Dordrecht, 1986, p. 559.
4. D.W. McKee, *Carbon*, **10** (1972) 491.
5. R.C. Asher and T.B.A. Kirstein, *J. Nuclear Mat.*, **25** (1968) 344.
6. D.W. McKee and C. L. Spiro, *Carbon*, **23** (1985) 437.
7. S. Stegenga, M. van Waveren, F. Kapteijn, and J.A. Moulijn, *Carbon*, **30** (1992) 577.
8. Kirk Othmer, Encyclopedia of Chemical Technology, vol. 4, John Wiley & Sons, New York, 1992, p. 897.
9. Satoshi Sato, Kazuo Urabe, and Yusuke Izumi, *J. Catal.*, **102** (1986) 99.
10. F. Roozenboom, M.C. Mittelmeijer-Hazeleger, J.A. Moulijn, J. Medema, V.H. de Beer, and P.J. Gellings, *J. Phys. Chem.*, **84** (1980) 2783.
11. K. Inumaru, T. Okuhara, M. Misono, N. Matsubayashi, H. Shimada, and A. Nisijima, *J. Chem. Soc. Faraday Trans*, **87**, (1991) 1807.
12. K. Inumaru, T. Okuhara, M. Misono, N. Matsubayashi, H. Shimada, and A. Nisijima, *J. Chem. Soc. Faraday Trans*, **88**, (1992) 625.
13. M. Niwa, C.V. Hidalgo, T. Hattori, and Y. Murakami, in "New Developments in Zeolite Science and Technology", Proceedings of the 7th International Zeolite Conference, Tokyo, Y. Murakami, A. Iijima, and J.W. Wood (Editors), Kodansha Tokyo & Elsevier Amsterdam, 1986, p. 297.
14. T. Hibino, M. Niwa, A. Hattori, and Y. Murakami, *Appl. Catal.*, **44** (1988) 95.
15. T. Hibino, M. Niwa, and Y. Murakami, *J. Catal.*, **128** (1991) 551.
16. L. Guzzi and A. Beck, *Polyhedron*, **7** (1988) 2387.
17. C. Dossi, R. Psaro, A. Bartsch, E. Brivio, A. Galasco, and P. Losi, *Catal. Today*, **17** (1993) 527.
18. J.J. Berzelius, *Ann. Phys., Lpz.*, **1** (1824) 169.
19. P. Schützenberger, *C. r.*, **114** (1892) 1089.
20. Ullmanns Encyklopädie der Technische Chemie, Band 21, Verlag Chemie, Weinheim, 1982, p. 431.
21. Kirk Othmer Encyclopedia of Chemical Technology, vol. 4, John Wiley & Sons, New York, 1992, p. 891.

Introduction

22. T. Shirakawa, K. Shimizu, K. Toi, and T. Ito, *Chem. Lett.* (1975) 1097.
23. A.A. Vernon and B.M. Brown, *Ind. Eng. Chem.*, **33** (1941) 1289.
24. S. Yamamura, H. Kojima, J. Iyoda, and W. Kawai, *J. Electroanal. Chem.*, **247** (1988) 333.
25. Kirk Othmer, *Encyclopedia of Chemical Technology*, vol. 9, John Wiley & Sons, 1980, p. 448.
26. P. Gallezot, S. Tretjak, Y. Christidis, G. Mattioda, A. Schouteeten, Yip-Wah Chung, and T.S. Sriram, *Catal. Lett.*, **13** (1992) 305.
27. M. Boutonnet-Kizling, P. Stenius, S. Andersson, and A. Frestad, *Appl. Catal. B*, **1**, (1992) 149.
28. M. Boutonnet, J. Kizling, P. Stenius, and G. Maire, *Coll. Surf.*, **5** (1982) 209.
29. M. Boutonnet Kizling, J.P. Gallas, C. Binet, and J.C. Lavalley, *Mat. Chem. Phys.*, **30** (1992) 273.
30. M.A. Vannice, Yu-Lin Chao, and R.M. Friedman, *Appl. Catal.*, **20** (1986) 91.
31. Yoshiho Hayata and Takeshi Kono, *Jpn. Kokai, Tokkyo Koho JP 03 69,574* [91 69,574], (CA 115:97926k).
32. J.R. Fox, D.A. White, S.M. Oleff, R.D. Boyer, P.A. Budinger, *Mater. Res. Soc. Symp. Proc.*, **73** (1986) 395.
33. P.W. Lednor and R. de Ruiter, in "inorganic and Metal-Containing Polymeric Materials, J. Sheats ed., Plenum Press, New York, 1990, p. 187.
34. M.J. Ledoux, S. Hantzer, C. Pham Huu, J. Guille, and M-P. Desaneaux, *J. Catal.*, **114** (1988) 176.
35. M.J. Ledoux and C. Pham Huu, *Catal. Today*, **15** (1992) 263.
36. M.J. Ledoux, J. Guille, S. Hantzer, and D. Dubots, *Eur. Pat. Appl.*, EP 0 313 480 A1.

Evaluation of Isothermal Chemical Vapour Infiltration with Langmuir-Hinshelwood type kinetics*

ABSTRACT

A model has been developed for the mathematical description of Isothermal Chemical Vapour Infiltration (ICVI) processes. Three types of adsorption of the reactive species are incorporated into the kinetic equations: weak associative adsorption, strong associative adsorption, and dissociative adsorption. The kinetic models are based on Langmuir-Hinshelwood equations. Weak associative adsorption of the reactive species gives rise to an exponentially shaped final deposition profile, whereas strong associative and dissociative adsorption result in a sigmoidal shaped deposition profile in the pore. This originates from a shift in deposition mechanism from a layered growth (weak associative adsorption) to a moving front growth (strong associative and dissociative adsorption). For weakly adsorbing reactive species, the residual porosity of a preform can be decreased by lowering the process pressure. Assuming strong associative or dissociative adsorption the reverse effect can be found at the investigated process conditions. This is caused by the change in reaction rate dependence of the concentration inside the pore. Application of the concept of a generalized Thiele modulus shows that for all investigated kinetic models the residual porosity of densified preforms is smaller than one percent when the Thiele modulus is kept below 0.02. For weak associative adsorption, this region can be achieved by lowering the pressure. With strong associative and dissociative adsorption of the active species, it is realized by an increase in concentration and total pressure.

*R. Moene, J.P. Dekker, M. Makkee, J. Schoonman, and J.A. Moulijn, *J. Electrochem. Soc.*, **141** (1994) 282-290.

1. INTRODUCTION

Ceramic materials are well known for their refractory character and outstanding mechanical properties. Their use is mainly limited due to their sensitivity to crack propagation [1]. Improved toughness can be achieved by using fibres or whiskers in a ceramic matrix fabricated by *e.g.* extrusion, sintering, and hot pressing. However, the material properties of these fibre reinforced composites are worsened by fibre damaging and/or final porosity [2]. Composites can also be fabricated by Chemical Vapour Infiltration (CVI); the matrix material is then deposited in the porous preform which consists of 2 or 3 dimensional woven fibre structures. These preforms are subjected to much lower stresses and temperatures in comparison with the aforementioned densification methods. A homogeneous deposition, which results in complete pore filling of the substrate, requires a slow reaction rate with respect to the reactant diffusion in the preform. Due to this limitation in reaction rate, the overall densification rate becomes extremely low and the operation time for full densification can take up to 500 hours [3-5]. Another application of CVI comprises the coating of carbon based catalyst carriers with a thin layer of silicon carbide (SiC), to increase their oxidation resistance and mechanical strength. Forcing reactant gases through a preform will enhance the growth rate in the pores, and a temperature gradient opposite to the pressure gradient can be established to obtain a high and homogeneous densification. This forced flow CVI with a temperature gradient has been developed at Oak Ridge National Laboratory [6, 7]. The authors have reported considerably shorter process times with respect to Isothermal Chemical Vapour Infiltration (ICVI). However, it is expected to be of limited use for densification of irregularly shaped preforms due to difficulties in obtaining a well defined temperature and pressure gradient across the preform. Pulse CVI is another explored procedure which exists in a repetitive cycle of evacuation and instantaneous source-gas filling of the reactor [8]. It is reported that in this mode the problem of counter-current diffusion of the active species and gaseous products in the pore can be overcome. This will result in an improved densification of the preform and a decrease in processing time. Inductive heating of carbon preforms is also reported to exhibit a positive influence on the total densification and processing time with respect to ICVI [9], because this kind of heating can lead to temperature profiles which result in a densification from "the inside to the outside". By mathematical calculations, this principle has been proven to be promising.

To gain insight and to optimize the CVI conditions, several models are proposed to describe the densification of various substrates. The geometry of the pores changes during deposition, and as a result, the diffusion rate of the reactants in the pore is dependent of place and time. This implies a strong dependency of the pore radius and, hence, the axial place on the effective diffusivity. A mathematical model should describe these changes with

Evaluation of ICVI with Langmuir-Hinshelwood type kinetics

equations that are added to the mass balances. Most ICVI models assume that the preform can be described as a single pore in which reaction and diffusion take place simultaneously [10-12].

The implementation of correct kinetic equations is another important aspect of CVI modelling, especially because the densification should be performed in the regime in which the reaction kinetics are rate limiting. Middleman [13] and Sheldon and Besmann [14] have studied the influence of a possible gas-phase reaction preceding the heterogeneous reaction in the CVI process. They have discussed the kinetics as a function of process conditions at the beginning of the process. However, the evolution of densification with time will influence the gas-phase kinetics and transport properties, which can lead to discrepancies in the modelling results. The kinetic equations used to describe the reaction rate in CVI systems on the pore surface are usually assumed to be first order in the gas-phase concentrations. Lin *et al.* [15] developed a model which incorporates a n^{th} order dependence of the reactants on the reaction rate.

The kinetics of a Chemical Vapour Deposition (CVD) process can be easily compared with kinetic behaviour encountered in heterogeneous catalysis. The reactants chemisorb on a surface, react and desorb (catalysis) or form a solid product on the substrate surface (CVD). One physically sound way to describe adsorption (and desorption) is by using equations of Langmuir isotherms. The resulting equations are often referred to as Langmuir-Hinshelwood kinetic equations. It is shown that these equations provide a mathematical description of the kinetics of heterogeneously catalyzed reactions [16]. They have a theoretical basis and, in practice, can be applied to multi-component systems. Similar behaviour (kinetics based on adsorption isotherms) is found for CVD reactions *e.g.* for the deposition of Si [17-19], BP [20], BC [21], TiN [21-25], and Si_3N_4 [26,27]. Recently, kinetic equations have been derived for the deposition of silicon carbide in which homogeneous and heterogeneous reactions are included [28]. The practical advantage of these Langmuir-Hinshelwood equations is found in the rationalization of a changing reaction rate order behaviour of CVD systems by means of a physically meaningful kinetic equation. For a mathematical description of CVI, the necessity of applying these kinetics is obvious. Three possible kinetic equations are given below, which describe kinetic mechanisms that can be found in CVD systems. These will be implemented in the mathematical modelling of CVI. A detailed description of the modelling of surface kinetics is given by Yang and Hougen [29]. The derivations of the kinetic equations based on Langmuir adsorption isotherms [30] can be found in the appendix. Table 1 shows these three types of adsorption mechanisms and their corresponding kinetic equations.

Chapter 2

Table 1. Adsorption mechanisms and corresponding kinetic equations

Adsorption mechanism	Kinetic equation
weak associative adsorption (wa)	$R_A = kK_A C_A$
strong associative adsorption (sa)	$R_A = k \frac{K_A C_A}{1 + K_A C_A}$
strong dissociative adsorption (sd)	$R_{A-B} = k \frac{K_{A-B} C_{A-B}}{(1 + K_{A-B} C_{A-B})^2}$

Fig. 1 displays the normalized reaction rate (R/k), for the three kinetic models considered, as a function of the product of concentration and adsorption constant (KC).

In the present chapter, a model is presented for the one-dimensional simulation of densification by means of ICVI using a time variable pore geometry and Langmuir-Hinshelwood kinetics. The main objective of this work is to determine the influence of Langmuir-Hinshelwood kinetics on the deposition profile in the pore. The three types of adsorption mechanisms displayed in Table 1 are implemented as being indicative for this kinetic behaviour. Multi-component competitive adsorption is excluded.

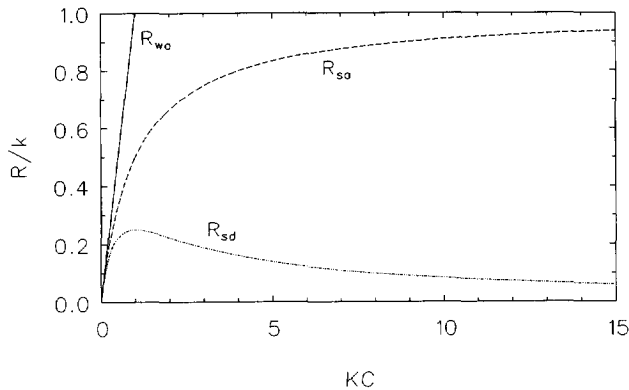


Fig. 1. The normalized reaction rate for the kinetic models plotted as a function of the product of partial pressure and adsorption constant

Evaluation of ICVI with Langmuir-Hinshelwood type kinetics

The first-order rate expression that results from the weak associative adsorption is used to evaluate the differences in deposition mechanisms and resulting deposition profiles arising from the three adsorption mechanisms. Applicability of the concept of the generalized Thiele modulus is tested and used to define general criteria for achieving optimal ICVI conditions. Validation of the model with experimental data will be published elsewhere [31].

2. MODEL DEVELOPMENT

Mathematical modelling of CVI processes is complicated by the difficulty to describe the initial pore geometry. To obtain a model describing simultaneous diffusion, chemisorption, and reaction, a one dimensional cylindrical pore is defined as a simplified structure of the preform (Fig. 2). A full evolution of the pore structure is beyond the scope of this article, because only the influence of surface kinetics in the ICVI process is evaluated. The gas mixture is modelled as an ideal gas with properties that depend on temperature, pressure and pore geometry. The general mass balance equation over a differential volume element $\delta x \delta y \delta z$ for component i reads,

$$\frac{\partial(VC_i)}{\partial t} + \nabla(VJ_i) = R_i S \quad (1)$$

where J_i is the three dimensional molar flux of component i , $(-R_i)$ is the consumption rate of component i in the gas-phase per unit surface area, V is the volume $\delta x \delta y \delta z$, S is the surface area of the pore, and t is the time.

The following additional assumptions are incorporated into the model: (a) the reactant adsorption takes place at an energetically homogeneous surface, and the adsorption characteristics of the deposited layer are equal to those of the original surface;

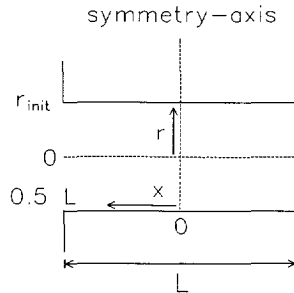


Fig. 2. Schematic drawing of a model pore

Chapter 2

(b) the reaction rate is proportional to the surface area; (c) the pore structure of the preform can be modelled as a one-dimensional cylindrical pore; (d) the vapour concentration gradient in the radial direction is negligible due to the large length over pore radius ratio; (e) reactant concentrations are small, so that normal Fick diffusion can be assumed and the pressure gradient due to reaction is negligible, (f) heat effects are assumed to be small so that temperature gradients can be neglected, and (g) the surface mobility of the adsorbed species is assumed to be negligible. Equation 1 can, therefore, be simplified,

$$\frac{\partial C_i}{\partial t} + D_{eff}(x, t) \frac{\partial^2 C_i}{\partial x^2} = \frac{2R_i}{r(x, t)} \quad (2)$$

where x is the axial position in the pore, $r(x, t)$ is the pore radius at position x and time t , and $D_{eff}(x, t)$ is the effective diffusion coefficient in the gas-phase at position x and time t in the pore.

The mass balance for the deposition of a solid on the pore wall reads,

$$\frac{dV_s}{dt} = \frac{M_w R_i S}{\rho} \quad (3)$$

and,

$$\frac{dr(x, t)}{dt} = \frac{M_{w,s} R_i}{\rho} \quad (4)$$

where V_s is the volume of deposited material, $M_{w,s}$ is the molecular weight of deposited material, and ρ is the density of the deposited material.

The gas-phase mass balance reaches, under typical operating conditions, equilibrium much faster than the evolution of the solid boundary, which justifies a semi-steady-state gas-phase mass balance at a given time:

$$\frac{d^2 C_i(x, t)}{dx^2} = \frac{2R_i}{r(x, t) D_{eff}(x, t)} \quad (5)$$

The boundary conditions for equations 4 and 5 are given by,

$$\frac{dC_i(0, t)}{dx} = 0 \quad (6)$$

Evaluation of ICVI with Langmuir-Hinshelwood type kinetics

$$C_i(\frac{1}{2}L, t) = C_{i, \text{bulk}} \quad (7)$$

$$r(x, 0) = r_{\text{init}} \quad (8)$$

where $C_{i, \text{bulk}}$ is the bulk concentration of species i , L is the pore length, and $r_{\text{init}}(x, 0)$ is the pore radius at $t=0$.

The diffusion coefficient is found by assuming it to be equal to the harmonic mean of the gas-phase diffusion coefficient and the Knudsen diffusion coefficient,

$$\frac{1}{D_{\text{eff}}(x, t)} = \tau \left[\frac{1}{D_{\text{gas}}} + \frac{1}{D_{\text{Knudsen}}(x, t)} \right] \quad (9)$$

where τ is the tortuosity factor of the substrate, D_{gas} is the diffusion coefficient in the gas phase, and $D_{\text{Knudsen}}(x, t)$ is the Knudsen diffusion coefficient at position x and time t in the pore. Diffusion coefficients for binary gas systems at a given temperature at pressures below 10 bar can be estimated by the Wilke and Lee relation [32]. Values of the diffusion coefficient estimated by this equation generally agree with experimental values to within 5 to 10 percent. A linear relationship exists between the gas-phase diffusion coefficient and the reciprocal pressure and reads,

$$D_{\text{gas}} = \frac{10^{-3} \cdot (3.03 - (0.98/\sqrt{2M_{AB}})T^{3/2}}{P\sqrt{2M_{AB}}\sigma_{AB}^2\Omega_D} \quad (10)$$

where T is the temperature, P is pressure, M_{AB} is the harmonic mean of the molecular weights of the gas-phase components A and B, σ_{AB} is the characteristic length of species A and B, ϵ_{AB} is the characteristic energy of species A and B, and Ω_D is the collision integral. The value of M_{AB} and the Lennard-Jones parameters σ_{AB} , ϵ_{AB} and the collision integral are tabulated or can be determined by equations given by Reid *et al.* [32]. The Knudsen diffusivity is calculated using the correlation resulting from the kinetic theory of gases and is valid for diffusion in a straight cylindrical pore of infinite length and reads,

$$D_{\text{Knudsen}}(x, t) = 97 \cdot r(x, t) \left[\frac{T}{M_{w,g}} \right]^{\frac{1}{2}} \quad (11)$$

where $M_{w,g}$ is the molecular weight of the diffusing species i .

3. PROCEDURES SOLVING THE MODEL

The analytical solution of equation 5 can be found in textbooks on heterogeneous catalysis when first-order kinetics and a constant pore geometry are assumed [33]. Incorporation of Langmuir-Hinshelwood kinetic behaviour in equation 5 complicates the analytical solving method to such an extent that the most direct method exists in the use of numerical techniques [34]. For CVI, it has to be taken into account that the pore radius varies in time and in the axial direction during densification of the pore. This implies that for an analytical solution of equation 5, an average radius has to be determined, which, in general, is not allowed. Therefore, numerical methods are chosen to solve the gas-phase second-order differential equation and the solid-phase first-order differential equation, without making the assumption of a distance independent pore radius.

In order to solve the above mentioned differential equations the following dimensionless variables are introduced.

$$C^* = \frac{C_i}{C_{i, \text{bulk}}} \quad x^* = \frac{x}{\frac{1}{2} \cdot L} \quad r^* = \frac{r}{r_{\text{init}}}$$

Substitution in differential equation 5 describing the gas phase results in equation 12.

$$\frac{d^2 C_i^*}{d(x^*)^2} = \frac{L^2}{r_{\text{init}} C_{i, \text{bulk}}} \cdot \frac{8 \cdot R_i}{r^*(x, t) \cdot D_{\text{eff}}(x, t)} \quad (12)$$

Using a first-order Euler approximation for the growth rate to solve the differential equation, the dimensionless form reads

$$r^*(x, t + \Delta t) = r^*(x, t) - \frac{M_{w,s} R_i \cdot \Delta t}{r_{\text{init}} \rho} \quad (13)$$

Due to the fact that only one of the two boundary conditions of equation 12 at one side of the pore is known, the other has to be determined by an iterative procedure. An iterative bisection-shoot method is coupled with two Runge-Kutta procedures [35] to solve the second order differential equation. The Runge-Kutta method divides the pore in a series of slabs in which ideal mixing is assumed; the value of the dependent variable is determined by a first-order Taylor expansion, using a weighed derivative. A guess of the concentration of component A is made halfway the pore (at $x^*=0$), subsequently the mass balance is solved; this procedure is repeated until the error in the dimensionless concentration at the pore outlet (at $x^*=0.5$) was smaller than 0.01%. With this $C^*(x, t)$ the new $r^*(x, t)$ is calculated with a

Evaluation of ICVI with Langmuir-Hinshelwood type kinetics

sufficiently small time step and the diffusion coefficient is determined along the pore. The resulting arrays of $r^*(x,t)$ and $D_{eff}(x,t)$ are used in the next iterative step of solving mass balance 12 until a critical outlet pore diameter of 0.3 nm is reached; at this critical diameter it is assumed that the mass flux inwards the pore equals zero. For each simulation the number of axial slabs and time steps is increased until the desired accuracy was achieved. The number of time steps and axial steps exceeded 200 in all simulations.

Evaluation of equation 5 is usually carried out by introducing the Thiele modulus as dimensionless quantity [36]. The generalized form derived from the semi-steady-state mass balance 5 reads [37],

$$\varphi \equiv \lambda \cdot R_i(C_{i,bulk}) \left[4 \int_0^{C_{i,bulk}} r \cdot D_{eff} \cdot R_i(\alpha) d\alpha \right]^{-1/2} \quad (14)$$

where φ is the Thiele modulus, λ is the ratio of volume and surface area perpendicular to the molecular flux, and α is a dummy variable for integration. This dimensionless number φ is very useful as a first approximation to determine the extent of limitation of the reaction rate by pore diffusion. For heterogeneous catalysis it has been shown that for first-order kinetic behaviour values of φ lower than 0.1 indicate that the reaction rate is determined by the intrinsic kinetic behaviour (no internal mass-transfer limitations). If φ is greater than 3 internal diffusion is the rate determining step in the reaction [38]. It should be noted that this Thiele modulus is independent in time. As mentioned before, in CVI the Thiele modulus changes in time due to the changing pore radius. Therefore, only a Thiele modulus at the initial stage of the densification can be used to evaluate the possible occurrence of mass transfer limitations. Equations 15 to 17 display the derived Thiele moduli for the three kinetic equations given in Table 1.

$$\varphi(wa) = \frac{L}{2} \left[\frac{kK_i}{2r_{init}D_{eff}} \right]^{\frac{1}{2}} \quad (15)$$

$$\varphi(sa) = \frac{L}{2} \left[\frac{kK_i}{4r_{init}D_{eff}} \right]^{\frac{1}{2}} \frac{K_i C_{i,bulk}}{1 + K_i C_{i,bulk}} \left[K_i C_{i,bulk} - \ln(1 + K_i C_{i,bulk}) \right]^{-\frac{1}{2}} \quad (16)$$

Chapter 2

$$\varphi(sd) = \frac{L}{2} \left[\frac{kK_i}{4r_{init}D_{eff}} \right]^{\frac{1}{2}} \frac{K_i C_{i,bulk}}{(1+K_i C_{i,bulk})^2} \left[\ln(1+K_i C_{i,bulk}) + \frac{1}{1+K_i C_{i,bulk}} - 1 \right]^{-\frac{1}{2}} \quad (17)$$

where $\varphi(wa)$, $\varphi(sa)$, and $\varphi(sd)$ are the Thiele moduli for weak associative, strong associative, and dissociative adsorption, respectively, and L is the length of the cylinder. Fig. 3 displays the Thiele moduli of strong associative adsorption and dissociative adsorption versus the concentration $C_{i,bulk}$. They are shown relative to the Thiele modulus of the weak associative adsorption, which is independent of the bulk concentration. At low values of $C_{i,bulk}$ the three Thiele moduli are identical ($\varphi(sa)/\varphi(wa) = \varphi(sd)/\varphi(wa) = 1$). This is a result of the identical behaviour at low concentrations of the rate equations as shown in Fig. 1.

4. MODEL PARAMETERS

In order to compare the different kinetic equations implemented in the mass balances, the situation at the beginning of the CVI process is used to define the constants that determine the starting point of solving equations 12 and 13.

The evaluation is performed for three different case studies. Case *a* is a model material for which the influences of pore geometry and reactor pressure on the residual porosity and final pore geometry are evaluated. The pore radii in case *a* are chosen in such a way that at the initial stage of the infiltration either gas-phase diffusion ($r_{init}=50\mu\text{m}$), or Knudsen diffusion ($r_{init}=0.5\mu\text{m}$) are the dominant mass-transfer mechanisms. The model parameters

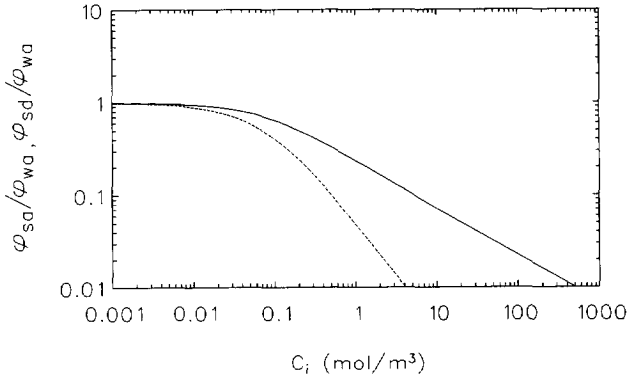


Fig. 3. The Thiele modulus as a function of the bulk concentration of the active species of the various kinetic models — $\varphi(sa)/\varphi(wa)$, — — $\varphi(sd)/\varphi(wa)$

Evaluation of ICVI with Langmuir-Hinshelwood type kinetics

used in case *b* are indicative for preforms used in densification processes. The influences of pore geometry, reactor pressure, and concentration on the final porosity are evaluated. The last case (*c*) stands for a catalyst carrier for which the influence of pore geometry on the final porosity is evaluated. The last two cases possess physical properties of preforms used in our laboratory. For each of these cases the influence of the kinetic behaviour on the final pore geometry will be discussed.

Evaluation of the different kinetic models is performed with identical reaction rates at the pore entrance; thus the same pore closure time is found for each of the three kinetic models. The intrinsic rate constant (k) is varied to satisfy this condition, while the other parameters remain constant. The physical constants of SiC and SiCl₄ are assumed to be indicative for a SiC-ICVI process based on the decomposition of methyltrichlorosilane. Experimental data of a mass spectroscopic study of the decomposition of methyltrichlorosilane in a hydrogen environment [39] indicate that SiCl₄ is the most abundant silicon-species in the gas-phase. Here it is assumed that SiCl₄ is the silicon precursor for the deposition of SiC.

Table 2. Model parameters

Symbol	Name	Value
r_{init}	initial pore radius	
	case a	50 to 0.5 μm
	case b	50 to 0.5 μm
	case c	500 to 5 nm
L/r_{init}	length over pore radius	20 to 20,000
T	temperature	1273 K
P	pressure	1 to 10^3 kPa
D_{eff}	effective diffusion coefficient	$33.07 \cdot 10^{-8}$ to $24.52 \cdot 10^{-4}$ $\text{m}^2 \text{s}^{-1}$
k_0	reaction rate constant	
	weak associative	$0.181 \text{ mol m}^{-2} \text{ s}^{-1}$
	strong associative	$1.996 \text{ mol m}^{-2} \text{ s}^{-1}$
	strong dissociative	$21.96 \text{ mol m}^{-2} \text{ s}^{-1}$
E_a	activation energy	120 kJ mol^{-1}
K_i	adsorption constant	$10 \text{ m}^3 \text{ mol}^{-1}$
$C_{i,\text{bulk}}$	concentration (1273 K, 100 kPa)	0.01 to 10 mol m^{-3}
M_i	molecular weight (SiCl ₄)	$169.898 \text{ g mol}^{-1}$
ρ	density deposit (SiC)	3120 kg m^{-3}
τ	tortuosity	
	case a	1
	case b	4
	case c	4

The adsorption constant is chosen in such a way that an almost zero-order kinetic behaviour is found at the outlet of the pore for strong associative adsorption and a negative order kinetic behaviour for the dissociative adsorption. For simplicity, co-adsorption of the gaseous byproduct hydrogen chloride is neglected. Table 2 displays the applied values of the model parameters.

5. RESULTS AND DISCUSSION

5.1 Evaluation of the residual porosity.

Table 3 will be used as a reference in which the conditions for all simulations are displayed. Furthermore, the residual porosity of each kinetic model calculation is shown. The numbers for the deposition profiles, given in the figures below, correspond to the numbers in Table 3.

In Figs. 4 to 6 the final pore geometries in a model pore (case *a*) are displayed for the three different kinetic models. Within each figure the final pore geometries are given which correspond to (a) an initial pore radius of $50\mu\text{m}$, and length over initial pore radius ratios of 200, 1000 and 2000, and (b) an initial pore radius of $0.5\mu\text{m}$, and length over initial pore radii ratios of 200, 1000 and 2000. The length of the pores is varied to satisfy these ratios. Fig. 4 reveals that lowering the length of the pore results in a more homogeneous deposition, resulting from a shorter diffusion path, and lowering the initial pore radius at a constant length over diameter ratio improves the infiltration of the pore, although the diffusion rate of the reactive species is lowered to the Knudsen diffusion regime. These effects have also been reported by Fedou *et al.* [38] for first-order kinetic behaviour. It originates from the assumption that comparison between equal geometrical ratios is valid. Thus, lowering the pore radius results in a decreased pore length (at constant length over diameter ratios). It is obvious that these simulations can be misleading, because it only involves a scaling factor, which is physically non-realistic. However, such a simulation of the ICVI process can be useful to study the influence of the different kinetic models on the deposition profiles. Therefore, evaluation of various initial pore radii can be performed at constant pore length or pore volume. Constant volume simulations will result in physically non-realistic pore lengths. The final deposition profiles given in Figs. 5 and 6 display a sigmoidal shape. This originates from a shift in deposition mechanism. This phenomenon will be evaluated in the next paragraph where the evolution of the pore geometry will be discussed. It should be noted, however, that these figures show that the residual porosity is not a quantity that can fully account for different deposition profiles originating from various deposition mechanisms.

Evaluation of ICVI with Langmuir-Hinshelwood type kinetics

Table 3. The residual porosity for the various kinetics

No.	case	Model parameters					Residual porosity		
		r_{init} (μm)	L (mm)	P (kPa)	C (mol/m^3)	τ	wa	sa	sd
1	a	0.5	0.1	100	1	1	0.0093	0.0041	0.007
2	a	0.5	0.5	100	1	1	0.167	0.115	0.288
3	a	0.5	1	100	1	1	0.466	0.414	0.641
4	a	50	10	100	1	1	0.123	0.0476	0.228
5	a	50	50	100	1	1	0.721	0.735	0.843
6	a	50	100	100	1	1	0.860	0.867	0.920
7	b	50	10	100	1	4	0.368	0.345	0.610
8	b	5	10	100	1	4	0.808	0.822	0.892
9	b	0.5	10	100	1	4	0.967	0.969	0.979
10	c	0.5	0.01	100	1	4	0.0004	0.0001	0.0001
11	c	0.05	0.01	100	1	4	0.032	0.016	0.030
12	c	0.005	0.01	100	1	4	0.636	0.669	0.795
13	a	0.5	1	1	1	1	0.359	0.764	0.925
14	a	0.5	1	10	1	1	0.364	0.690	0.876
15	a	0.5	1	500	1	1	0.534	0.171	0.157
16	b	50	10	1	1	4	0.035	0.229	0.671
17	b	50	10	10	1	4	0.074	0.272	0.670
18	b	50	10	10^3	1	4	0.775	0.412	0.221
19	b	50	10	100	0.01	4	0.368	0.778	0.929
20	b	50	10	100	0.1	4	0.368	0.698	0.876
21	b	50	10	100	10	4	0.368	0.010	0.003

Similar values of the residual porosity can be found for very different deposition profiles.

In Table 3 the values of the residual porosity are displayed for various length over radius ratios for case *a* (no. 1 to 6). These results indicate that there is an increase in residual porosity after pore closure with increasing pore length. For each of these simulations the initial pore radius is kept identical for each kinetic model.

Furthermore, there is an increase in residual porosity when the kinetic behaviour shifts from weak associative adsorption via strong associative adsorption to strong dissociative adsorption.

Simulation no. 7 to 12 in Table 3 show the residual porosity at a constant pore length for different pore radii for case *b* and *c*. These results can be used to study the influence of a specific porous material on the final porosity as discussed before. From these results it can be concluded that a decrease in initial pore radius will result in an increase in final porosity.

Chapter 2

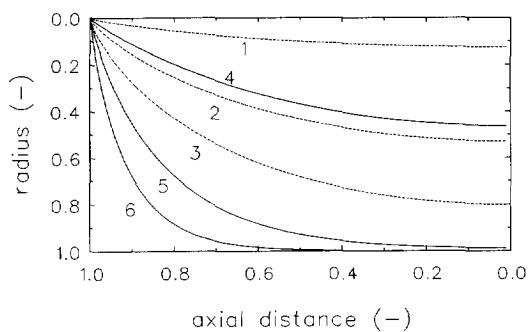


Fig. 4. Final pore geometry for weak associative adsorption, the numbers refer to Table 3

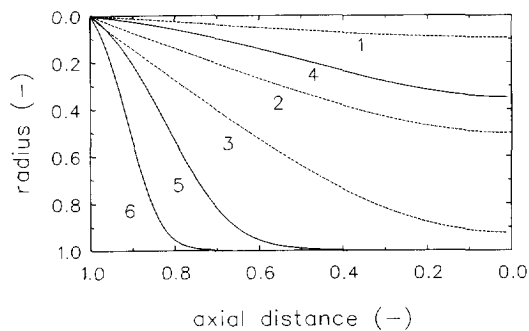


Fig. 5. Final pore geometry for strong associative adsorption, the numbers refer to Table 3

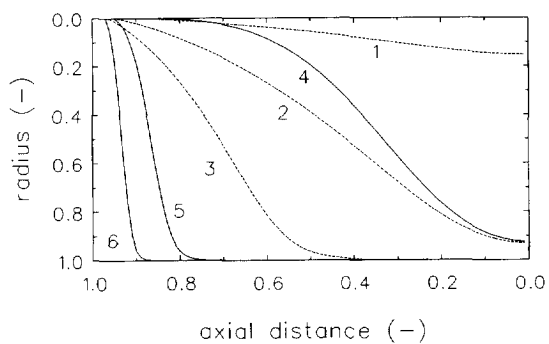


Fig. 6. Final pore geometry for strong dissociative adsorption, the numbers refer to Table 3

Evaluation of ICVI with Langmuir-Hinshelwood type kinetics

The results for case *b* (simulation no. 7, 8, and 9) indicate an increase in residual porosity when the kinetic behaviour shifts from weak associative adsorption via strong associative adsorption to strong dissociative adsorption. The influence of the different kinetic models on the residual porosity for case *c* (simulation no. 10, 11, and 12) is more difficult to comprehend. A similar behaviour as for case *b* is observed only for small initial pore radii. For preforms with larger initial pore radii it is necessary to determine the residual porosity by simulation in order to be able to obtain the influence of the different kinetic models on the final porosity.

5.2 Evaluation of the evolution of the pore geometry.

Not only the residual porosity changes as a function of process parameters but there is also a difference in the evolution of the deposition profiles and thus the shape of the final profiles. In Figs. 7 to 9 the pore geometry evolution of a model pore (case *a*) in time is shown as a function of axial distance for the three different kinetic mechanisms. The evolution of the pore geometry and concentration profiles is shown in time steps of 10 percent of the total deposition time.

First-order profiles display during deposition a gradual decrease in deposition rate moving to the middle of the pore as can be seen in Fig. 7. This effect enlarges in time due to a decrease in molecular flux of the active species.

The Langmuir-Hinshelwood simulations with strong associative and dissociative adsorption reveal a much more extreme axial dependence of the growth rate in the pore. From Figs. 7, 8, and 9 it is obvious that the pore filling mechanism shifts from a layered growth (weak associative adsorption, Fig. 7) to a moving front mechanism (strong associative and dissociative adsorption, Fig. 8 and 9). Due to the fact that the chosen parameters of the Langmuir-Hinshelwood kinetics lead to a zero (strong associative adsorption) and a negative (dissociative adsorption) reaction rate order at the pore entrance, the deposition rate inside the pore is **equal or larger** than the deposition rate on the edge. The place of maximal reaction rate depends on the pore geometry and moves in time to the outlet of the pore. A similar negative order effect has also been found by Smith and Carberry [40] in the catalytic oxidation of carbon monoxide (CO) over noble metals in a porous catalyst carrier. They solved similar conservation equations for heat and mass for a spherical pellet using a dissociative kinetic equation identical to the one used in this chapter. Their results show similar behaviour, *i.e.* that the usual adverse effect of diffusion in a porous system turns to advantage for negative order kinetics. This implies for ICVI systems that large differences in the final deposition profiles may exist between the various kinetic models.

The kinetic behaviour of weak associative adsorption gives rise to a final exponential-decay shaped deposition profile as shown in Fig. 4.

Chapter 2

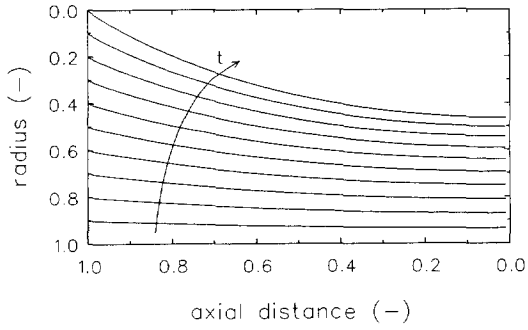


Fig. 7. Time evolution of the pore geometry for weak associative adsorption (no. 4 in Table 3)

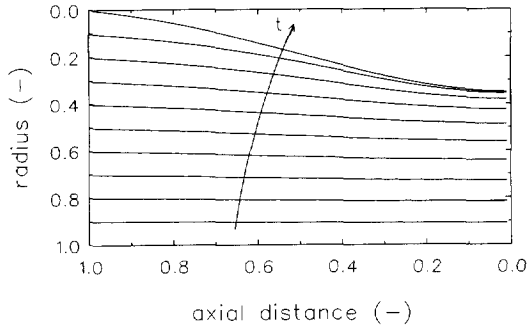


Fig. 8. Time evolution of the pore geometry for strong associative adsorption (no. 4 in Table 3)

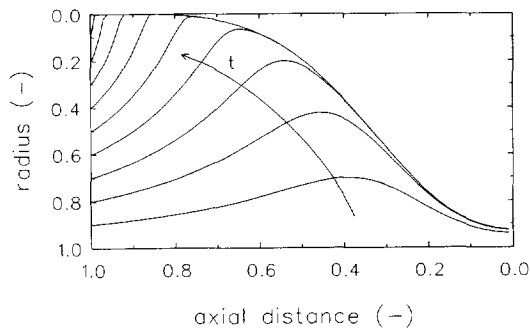


Fig. 9. Time evolution of the pore geometry for dissociative adsorption (no. 4 in Table 3)

Evaluation of ICVI with Langmuir-Hinshelwood type kinetics

However, from Figs. 5 and 6 it can be concluded that the strong associative and dissociative kinetic behaviour results in a final sigmoidal-shaped deposition profile. The dissociative adsorption kinetic behaviour shows this effect in the most pronounced form. As a consequence not only the residual porosity but also the final pore geometry has to be taken into account in order to be able to evaluate the densification of porous preforms.

5.3 Evaluation of the reactor pressure.

The influence of the reactor pressure on the residual porosity for the three different kinetic models is given in Table 3 (simulation no. 13, 14, and 15 for case *a*, and simulation no. 16, 17, and 18 for case *b*). For case *a*, the residual porosity increases at low pressures from weak associative adsorption via strong associative adsorption to dissociative adsorption, whereas at high pressures the reverse behaviour is found. For case *b* a similar behaviour is found as for case *a* but in a less pronounced form. Earlier reported ICVI simulations for first order kinetic behaviour [38] stated that lowering the reactor pressure increases the infiltration depth of the preform and thus decreases the residual porosity. This effect originates from the increase in diffusion rate and is found for weakly adsorbing species. However, strong associative and dissociative adsorption kinetic behaviour can result in a reverse trend. Hence, under the aforementioned ICVI conditions for associative and dissociative adsorption, it is shown to be possible to lower the residual porosity by **increasing** the pressure. This is a result from a combined effect of reactor pressure and concentration on an ICVI system. In general, by lowering the pressure, the first effect is that the diffusion coefficient of the gaseous component in the pore is enlarged until the Knudsen diffusion regime is reached. Secondly, the concentration of these gaseous components depends on the reactor pressure. This will influence the surface concentration of the reactive species and thus the reaction rate. Both effects contribute to the final porosity of the preform when Langmuir-Hinshelwood kinetic behaviour is assumed. Simulations comprising various concentrations of the active species at a constant reactor pressure have to be carried out in order to discriminate between the influence of concentration and reactor pressure on the final porosity of the preforms.

The last three simulations in Table 3 (no. 19 to 21) demonstrate the influence of the concentration of the active species at a pressure of 100 kPa on the residual porosity. The calculations show that no influence of the concentration on the residual porosity is found, when the reaction kinetics is described by weak associative adsorption kinetic behaviour, and that there is a decrease in final porosity with increasing concentration for the other kinetic models. At low concentrations of the active species the weak associative adsorption displays the lowest residual porosity, whereas at high concentration the lowest residual porosity is found for dissociative adsorption. The disappearance of the influence of the concentration on the residual porosity can be explained by substituting a first-order rate expression in equation

Chapter 2

12, resulting in equation 18.

$$\frac{d^2 C_i^*}{d(x^*)^2} = \frac{L^2}{r^0} \cdot \frac{8 \cdot k \cdot C_i^*}{r^*(x, t_i) \cdot D_{\text{eff}}(x, t_i)} \quad (18)$$

Equation 18 shows that the concentration profile in the pore does not depend on the bulk concentration of the active species. The physical rationale of this effect can be found in the change in concentration gradient over the pore. Lowering the bulk concentration of the active species results in a lower reaction rate in the pore (first-order kinetics). The diffusion rate displays an identical behaviour, *i.e.* it decreases with the same amount due to the lower concentration gradient. Hence, the ratio of the reaction rate over the rate of mass transport in the pore remains constant.

It is shown that large differences exist between the residual porosities for Langmuir-Hinshelwood kinetic behaviour, when the bulk concentration of the reactive species is increased. For optimum densification of the preform the concentration of the active species has to be taken as high as possible for Langmuir-Hinshelwood type kinetics at the given pore geometry. These trends can be predicted with the use of the generalized Thiele modulus. As shown by equation 15, the Thiele modulus remains constant with increasing concentration, when weak associative adsorption of the active species is assumed. For strong associative and dissociative adsorption a decrease of the Thiele modulus is found when the concentration is increased, as displayed in Fig. 3. Hence, the trends in Fig. 3 and simulations no. 19 to 21 are identical. These influences of the concentration and reactor pressure indicate that the change in residual porosity for the different kinetic models originate primarily from their concentration dependence. The trends for simulations 16 to 18 for the different kinetic models at various reactor pressures are not as strong as the ones at various concentrations due to the elimination of the adverse effect of the gas-phase diffusion coefficient.

The shape of the deposition profile has to be investigated in order to fully understand the influences of the reactor pressure and concentration on the residual porosity and final pore geometry. This leads to a similar discussion as in the preceding paragraph concerning the influences of initial pore geometries on the final densification. As illustrated in Fig. 1, the reaction rate is not necessarily linearly dependent on the concentration. As a result, the dependence of the reaction rate on the concentration can change as a function of axial place in the pore. The kinetics of the associative adsorption exhibits at high concentrations a nearly zero-order reaction rate dependence, which implies that the reaction rate is virtually independent on the axial place in the pore. Only when the reactant is depleted in such a way that the Langmuir-Hinshelwood associative kinetics behave like first-order kinetics, the rate of product formation will decrease moving inwards the pore. This phenomenon results in a

Evaluation of ICVI with Langmuir-Hinshelwood type kinetics

relatively homogeneous deposition in the pore as long as the kinetics behaves like a semi zero-order dependence. Furthermore, the decrease in reactant concentration in the zero-order region is constant, in contrast to first-order kinetics where the depletion is a linear function of the reactant concentration. Hence, the decrease will be more extreme compared to first-order kinetics. These combined effects result in a complex mechanism which determines the deposition profile and residual porosity. Lowering the pressure will result in a better diffusivity of the reactants in the pore but will also mean a shift to semi first-order kinetics and thus to a less homogeneous deposition. Increasing the pressure results in a more homogenous product formation along the pore, a faster reactant depletion, and slower diffusion.

It is obvious that these pressure influences affect the deposition profiles even more extremely, when the kinetic behaviour is described by a dissociative adsorption mechanism. In the negative-order region reactant depletion results in an increase in reaction rate until the first-order regime is reached via the zero-order region. This is shown as a maximum in the deposition profile. Owing to this increase in reaction rate, the reactant depletion is enhanced which is shown as a steep decline in the deposition profile in the pore. A decrease in pressure improves the gas-phase diffusivity, but shifts the reaction mechanism towards the first-order regime. A pressure increase pushes the position of maximum reaction rate inwards the pore causing a better infiltration, and a more homogeneous deposition in the pore. As discussed before, this effect can diminish due to the lowered gas-phase diffusivity of the reactant, provided that no Knudsen diffusion prevails.

5.4 Evaluation of the generalized Thiele modulus.

Fitzer *et al.* [11] used a Thiele modulus for a first-order reaction to calculate the maximum infiltration depth in a straight cylindrical pore. Evaluation with experimental data showed good agreement. They stated that the Thiele modulus should be lower than 0.4 for optimum densification of the pore. This condition originates from the effectiveness factor, which is commonly used in heterogeneous catalysis [37]. However, this condition is only valid when the influence of change in pore geometry is negligible in time. Hence, this condition cannot be used in ICVI processes, and implies the need for numerical solution. Their model can only predict the infiltration depth and not the final porosity. The 'Step Coverage Modulus' (*SCM*) is introduced by McConica and Churchill [41] as a dimensionless number. The square root of the *SCM* is proportional to the Thiele modulus in which zero order kinetic behaviour is incorporated. They evaluated the step coverage of tungsten CVD in contact holes and trenches of various dimensions. In principle, tungsten CVD in contact holes and trenches is similar to ICVI. However, it should be noted that in these systems much lower length over initial radius ratios are common, *i.e.* smaller than 20.

Chapter 2

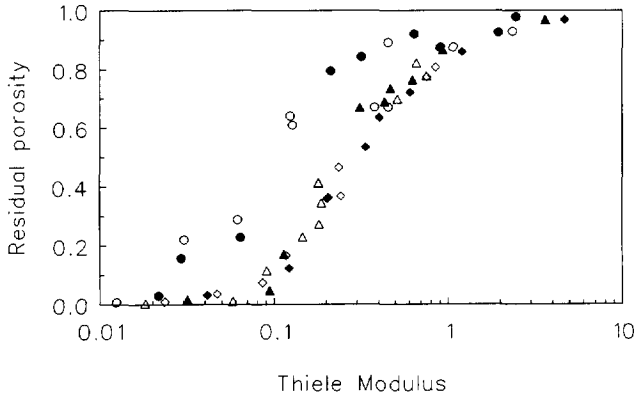


Fig. 10. Residual porosity vs. Thiele modulus, $r \leq 0.5 \mu\text{m}$: \diamond : wa, \triangle : sa, \circ : sd; $r = 50 \mu\text{m}$: \blacklozenge : wa, \blacktriangle : sa, \bullet : sd

Furthermore, this dimensionless number is not applicable in this situation, where the influence of the kinetic behaviour on the residual porosity has to be determined. By introducing a generalized Thiele modulus in which the various kinetic equations are implemented, the relationship between the residual porosity and the Thiele modulus can be plotted. This is shown in Fig. 10 in which the results of all presented simulations are implemented. Weak and strong associative adsorption display a nearly identical behaviour. The large change in deposition mechanism for dissociative adsorption results in a shift towards higher residual porosities for identical Thiele moduli. Furthermore, it can be concluded that at values of the Thiele modulus smaller than 0.02 the residual porosity is less than 0.01 and optimal densification is guaranteed.

6. CONCLUSIONS

With the model discussed above, it is possible to describe the ICVI process mathematically using kinetic equations based on adsorption isotherms. It is shown that the ICVI process has to be described by numerically solved mass balances in order to obtain insight into the complex influences of pressure, temperature, and concentration on the growth mechanism and final pore geometry. The mechanism of pore filling and the final pore geometry depend on the kinetic model used in the simulation. The growth mechanism changes from a layered growth to a moving front growth mechanism, when the deposition kinetics moves from first-order via associative Langmuir-Hinshelwood to dissociative Langmuir-Hinshelwood kinetics.

Evaluation of ICVI with Langmuir-Hinshelwood type kinetics

This results in a shift from an exponential decay-shaped deposition profile to a sigmoidal-shaped deposition profile, which indicates that in ICVI modelling, the use of correct kinetic equations is a prerequisite for an accurate process description of which the observed reaction rate is governed by reaction as well as diffusion.

The pressure parameter of the ICVI process affects the magnitudes of diffusion as well as concentration and thus the deposition profile. Weak associative adsorption of the reactive species implies that upon pressure decrease only the diffusion coefficient is enlarged, which exhibits a positive influence on the total densification of the preform. Langmuir-Hinshelwood behaviour of the reaction kinetics results in a positive (diffusion rate enhancement) and a negative (change in reaction order) effect on the total preform densification for the given experimental conditions. In general, optimum densification conditions are achieved at low pressures when weak adsorption of the active species is assumed. Strong associative or dissociative adsorption of the active species results in the optimum condition in which the concentration is as high as possible. It is also possible to reach this condition at high total pressures.

Application of a generalized Thiele modulus for various kinetic models gives a first impression of influences of process parameters on the **overall** densification process. For the kinetic models investigated in this chapter, it is shown that the Thiele modulus condition for nearly complete densification has to be taken more stringent than the condition for intrinsic reaction rate limited processes, used in heterogeneous catalyzed reactions (*i.e.* 0.02 instead of 0.1). The generalized Thiele modulus is a useful tool for optimizing the process conditions for nearly complete densification of preforms.

APPENDIX

The general rate law of a surface reaction is an extended product over all species and reads

$$R = k \prod_i (\theta_i)^{n_i} \quad (\text{A.1})$$

where R is the reaction rate per unit surface area, θ_i is the fractional coverage of species i , n_i is the exponent in the rate law, and k is the intrinsic rate constant. Assuming a proportional relationship between the reactant concentrations in the gas phase and the fractional coverage on the surface, a n^{th} order rate expression is found. A useful description of the fractional coverage of species i can be found by using the Langmuir adsorption isotherm [30]. A one-component non-dissociative adsorption is assumed to take place,

Chapter 2



where $A(g)$ is component A in the gas phase, s denotes a free adsorption site, $A(ads)$ is A adsorbed on the surface, and $A(s)$ is the solid deposit of A. Assuming thermodynamic equilibrium between adsorption and desorption the following expression for the fractional coverage can be derived,

$$\theta_i = \frac{K_i C_i}{1 + K_i C_i} \quad (A.3)$$

where K_i is the adsorption/desorption equilibrium constant of species i , and C_i is the reactant concentration of species i in the gas-phase. Langmuir [30] derived this equation, assuming that adsorption occurs in a mono-molecular layer in which attraction and repulsion between the adsorbed molecules are negligible. This will result in a constant free Gibbs energy of adsorption. The next condition is a homogeneous energy distribution on the adsorption surface. To derive kinetic expressions which describe the typical Langmuir behaviour, three types of adsorption behaviour of the reactive species are considered: weak associative adsorption, strong associative adsorption, and dissociative adsorption.

Assuming associative adsorption of an active species A, and a first-order reaction rate in the adsorbed active species, the rate law becomes upon combining equation A.3 with equation A.1:

$$R_A = k \frac{K_A C_A}{1 + K_A C_A} \quad (A.4)$$

This equation is the most simple of the Langmuir-Hinshelwood equations and shows a shifting order behaviour which is common to these equations. For weakly adsorbing components ($K_A C_A \ll 1$), this equation simplifies to a first-order rate expression.

$$R_A = k K_A C_A \quad (A.5)$$

The chemical equations of the one-component dissociative adsorption are described in A.6. The rate determining step is assumed to be the dissociation of an adsorbed species A-B, which results in rate expression A.7. Equation A.7 is a typical example of a dual-site mechanism which governs the rate determining step. The shifting order behaviour of equation A.7 is even more extreme; the reaction rate dependence shifts from a first order at very low partial pressure to an order of minus one at high partial pressure.

Evaluation of ICVI with Langmuir-Hinshelwood type kinetics



$$R_{\text{A-B}} = k \frac{K_{\text{A-B}} C_{\text{A-B}}}{(1 + K_{\text{A-B}} C_{\text{A-B}})^2} \quad (\text{A.7})$$

At high coverage of component A-B, no free surface sites are available for the dissociation of A-B to A and B, which results in a negative reaction rate order in the gas-phase concentration.

SYMBOLS

A(ads)	adsorbed species A
A(g)	component A in the gas-phase
A(s)	solid deposit of A
$C_i(x,t)$	concentration of component i at position x and time t (mol m^{-3})
$C_{i,\text{bulk}}$	bulk concentration of component i at $t=0$ (mol m^{-3})
C^*	dimensionless concentration
$D_{\text{eff}}(x,t)$	effective diffusion coefficient at position x and time t in the pore ($\text{m}^2 \text{s}^{-1}$)
D_{gas}	diffusion coefficient in the gas phase ($\text{m}^2 \text{s}^{-1}$)
$D_{\text{Knudsen}}(x,t)$	Knudsen diffusion coefficient in the pore at position x and time t ($\text{m}^2 \text{s}^{-1}$)
J_i	molar flux of component i
k	intrinsic rate constant ($\text{mol m}^{-2} \text{s}^{-1}$)
K_i	adsorption/desorption equilibrium constant ($\text{m}^3 \text{mol}^{-1}$)
L	length of a pore, which is open at both sides (m)
L/r_{init}	length over initial pore radius
M_w	molecular weight (g mol^{-1})
M_{ab}	harmonic mean of the molecular weights
n_i	reaction order
P	pressure (Pa)
$r(x,t)$	pore radius at position x and time t in the pore (m)
r_{init}	radius $t=0$
r^*	dimensionless radius
R	production rate per unit surface area ($\text{mol m}^{-2} \text{s}^{-1}$)
s	free adsorption site

Chapter 2

S	surface area (m^2)
SCM	Step Coverage Modulus
t	time (s)
T	temperature (K)
x	axial position in the pore (m)
x^*	dimensionless distance
V_s	amount of deposited material (m^3)
V	volume (m^3)

Greek letters

α	dummy variable for integration
ϵ_{ab}	characteristic Lennard-Jones energy (J)
φ	Thiele modulus
θ	fractional coverage of species i
λ	ratio of the total volume and surface area perpendicular to the molfflux (m)
Ω_D	collision integral
ρ	density of the deposited material (kg m^{-3})
σ_{ab}	characteristic Lennard-Jones length
τ	tortuosity factor of substrate (-)

Abbreviations

g	gas phase
s	solid phase
sa	strong associative adsorption
sd	strong dissociative adsorption
wa	weak associative adsorption

REFERENCES

1. R. Naislain, F. Langlais, and R. Fedou, in "Proceedings of the Seventh European Conference on CVD," M. Ducarroir, C. Bernard, L. Vandenbulke, Editors, editions de Physique, Les Ulis, C5-191 (1989).
2. T.M. Besmann, R.A. Lowden, B.W. Sheldon, and D.P. Stinton, in "Eleventh International Conference on Chemical Vapor Deposition," PV 90-12, K.E. Spear, Editor, p. 482, The Electrochemical Society, Pennington, NJ (1990).
3. H.O. Pierson and J.F. Smatana, In "Second International Conference on Chemical

Evaluation of ICVI with Langmuir-Hinshelwood type kinetics

- Vapor Deposition," J.M. Blocher and J.C. Withers, Editors, p. 487, The Electrochemical Society Softbound Proceeding Series, New York, (1970).
4. F. Christin, R. Naislain, and C. Bernard, in "Seventh International Conference on Chemical Vapor Deposition," PV 79-3, T.O. Sedgwick and H. Lydtin, Editors, p. 499, The Electrochemical Society Softbound Proceedings Series, Princeton, NJ (1979).
 5. R.E. Fisher, C.V. Buckland, and W.E. Bustamante, *Ceram. Eng. Sci. Proc.*, **6** (1985) 806.
 6. A.J. Caputo and W.J. Lackey, *Ceram. Eng. Sci. Proc.*, **5(7-8)** (1984) 654.
 7. J.D. Theis, in "Third International Conference on Chemical Vapor Deposition," F. A. Glaski, Editor, p. 561, American Nuclear Society, Hinsdale, IL (1972).
 8. Kohzo Sugiyama and Eiji Yamamoto, *J. Mater. Sci.*, **24** (1989) 3756.
 9. J.I. Morrell, D.J. Economou, and N.R. Amundson, *J. Electrochem. Soc.*, **139** (1992) 328.
 10. P. Wong and M. Robinson, *J. Am. Ceram. Soc.*, **53** (1970) 617.
 11. E. Fitzner and R. Gadow, *Am. Ceram. Soc. Bull.*, **65** (1986) 326.
 12. N.H. Tai and T.W. Chou, *J. Am. Ceram. Soc.*, **72** (1989) 414.
 13. S. Middleman, *J. Mater. Res.*, **4** (1989) 1515.
 14. B.W. Sheldon and T.M. Besmann, *J. Am. Ceram. Soc.*, **74** (1991) 3046.
 15. Y.S. Lin and A.J. Burggraaf, *Chem. Eng. Sci.*, **46** (1992) 3066.
 16. G.F. Froment and K.B. Bischoff, "Chemical Reactor Analysis and Design," 2nd ed., John Wiley & Sons, New York, (1990), chapter 2.
 17. H.C. Theuerer, *J. Electrochem. Soc.*, **108** (1961) 649.
 18. E.G. Bylander, *J. Electrochem. Soc.*, **109** (1962) 1171.
 19. E.G. Alexander, *J. Electrochem. Soc.*, **114** (1967) 65C.
 20. E. Kelder, in "Proceedings of the Seventh European Conference on CVD," M. Ducarroir, C. Bernard, L. Vandenbulke, Editors, editions de Physique, Les Ulis, C5-567 (1989)
 21. L. Vandenbulke and G. Vuillard, in "Eighth International Conference on CVD," PV 81-7, J.M. Blocher and G.E. Vuillard, Editors, p. 95, The Electrochemical Society (1981).
 22. Tsao Chin Jung, Chen Er Bao, and Miao Hue Fang, *Trans. Instn Min. Metall.*, **95** (1986) C63.
 23. Tsao Chin Jung, Du Yuan Sheng, and Miao Hue Fang, in "Tenth International Conference on Chemical Vapor Deposition," PV 87-7, G.W. Cullen and J.M. Blocher, Editors, p. 81, The Electrochemical Society Softbound Proceedings Series, Pennington, NJ (1987).
 24. C.Z. Rong, D.Y. Sheng, and M.H. Fang, *Surf. Eng.*, **5** (1989) 315.

Chapter 2

25. N. Nakanishi, S. Mori, and E. Kato, *J. Electrochem. Soc.*, **137** (1990) 322.
26. Kyoung-Soo Yi and John S. Chun, in reference 23, p. 570.
27. C.E. Morosanu and D. Iosif, *Thin Solid Films*, **92** (1982) 330.
28. F. Langlais and C. Prebende, in "Eleventh International Conference on Chemical Vapor Deposition," PV 90-12, K.E. Spear, Editor, p. 686, The Electrochemical Society, Pennington, NJ (1990).
29. K.H. Yang and O.A. Hougen, *Chem. Eng. Prog.*, **46** (1950) 146.
30. I. Langmuir, *J. Am. Chem. Soc.*, **40** (1918) 1361.
31. J.P. Dekker, R. Moene, H.J. Veringa, J.A. Moulijn, J. Schoonman, to be published.
32. R.C. Reid, J.M. Prausnitz and B.E. Poling, "The properties of gases and liquids," 4th ed., McGraw-Hill, New York, 587 (1989).
33. L.K. Doraiswamy and M.M. Sharma, *Heterogeneous reactions*, vol 1, John Wiley & Sons, New York, (1984).
34. Reference 33, p. 75.
35. P. Merluzzi, C. Brosilow, *Computing*, **20** (1978) 1.
36. E.W. Thiele, *Ind. Eng. Chem.*, **31** (1939) 916.
37. H.H. Lee, "Heterogeneous Reactor Design," Butterworth Publishers, Boston, p. 118 (1985).
38. R. Fedou, F. Langlais, and R. Naslain, in "Eleventh International Conference on Chemical Vapor Deposition," PV 90-12, K.E. Spear, G.W. Cullen, Editors, p. 513, The Electrochemical Society, Pennington, NJ (1990).
39. Y. Yeheskel, S. Agam, and M.S. Dariel, in "Eleventh International Conference on Chemical Vapor Deposition," PV 90-12, K.E. Spear, Editor, p. 696, The Electrochemical, Pennington, NJ (1990).
40. T.G. Smith and J.J. Carberry, *Can. J. Chem. Eng.*, **53** (1975) 347.
41. C.M. McConica and S. Churchill, in "Tungsten and Other Refractory Metals for VLSI Applications III," V.A. Wells, Editor, p. 257, MRS Publ., Pittsburgh (1988).

Chemical Vapour Deposition as a novel technique for catalyst preparation; modelling of active phase profiles*

ABSTRACT

Chemical Vapour Deposition has great potential in applying metals to catalyst supports and structured catalytic reactors *via* the gas phase. This technique increases the flexibility in process conditions and decreases the number of steps necessary for obtaining a loaded catalyst carrier. In this early stage of research, a model has been developed for the mathematical description of the deposition of catalytic material from the gas phase in porous structures. Thus, a catalyst pellet and a monolith are infiltrated with NiCl_2 which decomposes to Ni at elevated temperatures. Based on reported rate equations and kinetic data of the deposition of ceramic materials and semiconductors in literature, probable Langmuir-Hinshelwood type kinetic equations for metal deposition have been derived. The simulations indicate that preparation of catalysts with homogeneous and inhomogeneous active-site distributions is possible. Associative adsorption of the active species gives rise to catalysts with active-site distributions which vary between a degenerated egg-shell and a well formed egg-shell. Dissociative adsorption results in egg-shell, egg-white and (nearly) egg-yolk activity profiles. The same considerations are valid for the CVD of metals in monolithic reactors. Application of the concept of a generalized Thiele modulus shows a correlation between the Thiele modulus and the place of maximum deposition, when dissociative adsorption is assumed. This concept can be a convenient tool in catalyst design.

*R. Moene, M. Makkee, and J.A. Moulijn, *Chem. Eng. J.*, **53** (1993) 13-24.

1. INTRODUCTION

Supported catalysts, generally used in heterogeneous catalysis, consist of a support on which the active phase is finely dispersed. The support (usually high surface area Al_2O_3 , SiO_2 or activated carbon) acts as a stabilizer to prevent sintering of the active phase at reaction conditions and sometimes as a promoter in enhancing the activity and selectivity of the reaction. In most cases the active phase is applied by impregnation or precipitation. In general, three steps can be distinguished in these ways of preparation: (1) contacting the support with the solution of the precursor of the active phase; (2) drying or calcination of the support to remove the imbibed liquid, and (3) activation of the catalyst by reduction (or any other treatment like sulfiding) of the active-phase precursor. Dependent on the conditions of each of these steps, various activity profiles within the catalyst particle can be achieved. Much effort is devoted to the understanding and control of these stages of preparation and, as a result, catalysts can be manufactured which exhibit activity profiles like the ones depicted in Fig. 1. The black areas represent the place of the highest concentration of the active material. An excellent review in which relationships are given between preparation conditions and resulting profiles of the active material in the support is given by Lee and Aris [1]. Optimization of these activity profiles can result in an enhanced product yield or selectivity and improved resistance against deactivation of the catalyst [2]. An example, which shows the importance of optimal catalyst design in achieving a high selectivity, is the partial hydrogenation of a trace amount of ethyne in a stream of ethene [3]. Because ethyne adsorbs much stronger on the palladium catalyst than ethene, ethene is not hydrogenated until ethyne is fully consumed. It is clear that for optimum selectivity an egg-shell catalyst has to be used.

Another technique to equip a support with active material exists in the use of Chemical Vapour Deposition (CVD), by which the active phase is deposited on the catalyst support from gaseous metal precursors. CVD is usually carried out to deposit ceramic materials, *e.g.* titanium nitride (TiN) from titanium tetrachloride (TiCl_4) and nitrogen [4-6], silicon from silane (SiH_4) [7-9], and silicon carbide (SiC) from methyl trichlorosilane (CH_3SiCl_3) [10] on various substrates to improve their resistance against wear or oxidation.



Fig. 1. Activity profiles in catalyst pellets. The black areas represent the place of highest concentration of the active phase

CVD as a novel technique for catalyst preparation

Moreover, CVD can also be used to deposit pure metals, metal oxides and metal sulfides from the gas phase [11,12]. Thus, by applying CVD in catalyst preparation, the number of preparation steps necessary with impregnation can be reduced from three (or two) to one. This will simplify the practical operation to a large extent. Several additional advantages exist in the use of CVD over the conventional methods by which the catalyst is loaded with metal precursors from the liquid phase. First of all, the use of a gas-phase system will increase the flexibility compared to the liquid-phase system. Pore volume impregnation sets limits to the pH range that has to be used; this range depends on support properties (*e.g.* point of zero charge, solubility). Additionally, the maximum loading of the catalyst is restricted by the maximum solubility of the metal precursor in this pH range and the pore volume of the support. Gas-phase systems, however, can operate in wide ranges of concentration and time. The flexibility of the gas-phase system is further enhanced by the larger rates of diffusion in gaseous media and the absence of limitations in deposition temperature (boiling point of the solvent). Further, it may be possible to produce similar activity profiles (*e.g.* egg-shell, egg-yolk) as with impregnation by choosing the optimum deposition conditions. These conditions are determined by rate of diffusion and surface reaction of the gaseous precursor of the active species. Similar considerations apply to the densification of porous preforms of ceramic materials, which are usually so hard that it is impossible to structure them by conventional techniques like hot pressing or extrusion [13]. This special type of CVD is often referred to as Chemical Vapour Infiltration (CVI). An example is the infiltration of silicon carbide whiskers with SiC from CH_3SiCl_3 to produce high performance turbine wheels, which can operate at 1700 K in air. It should be noted that the dimensions of these preforms are very different from the ones found in heterogeneous catalysis. The total length can add up to several centimetres and the porosity of the preform can be regarded as micrometer pores. Catalyst supports are usually two orders of magnitude smaller. Another difference exists in the desired final structure of these two types of material. Infiltration of a ceramic matrix is carried out in such a way that the residual porosity of the material is as low as possible, whereas deposition of active material in porous catalyst supports has to result in a catalyst with open pores to expose the major part of the active material.

Several precursors are used in CVD to deposit metals from the gas phase [11,14]. Examples are halogenides (*e.g.* CrCl_2 , MoCl_5 , NiCl_2 , VCl_4 , and WCl_5), carbonyls (*e.g.* $\text{Mo}(\text{CO})_6$ [15], $\text{V}(\text{CO})_6$, $\text{Ni}(\text{CO})_4$, and $\text{Co}(\text{CO})_8$), carbonyl complexes (*e.g.* $\text{Pt}(\text{CO})_2\text{Cl}_2$ [16] and $\text{CoNO}(\text{CO})_3$), and organic compounds (*e.g.* $\text{Pd}(\text{C}_2\text{H}_5\text{O}_2)_2$ and $\text{Pt}(\text{C}_2\text{H}_5\text{O}_2)_2$). Characteristic properties of these compounds are their stability at room temperature, sufficient volatility at low temperatures, and ability to react cleanly in the reaction zone. The advantages of the metallo-organic compounds over the other groups can be found in their low decomposition temperature and higher volatility. These advantages can be used to overcome

the limitations of CVD for catalyst manufacture. The main restrictions are found in the high demands on the precursor (*i.e.* sufficiently high vapour pressure at low temperatures, sufficient stability in the carrier gas, and sufficiently low decomposition temperature). In general, by applying metallo-organic CVD (MOCVD) the deposition temperature can be lowered. The use of these materials expands the range of applicable catalyst supports that can be equipped with active material by CVD. The deposition of platinum from metallo-organic precursors is an example. Powell *et al.* [14] describe the use of platinum acetylacetonate, an air stable yellow powder. They recommend evaporation at 450 K *in vacuo*, followed by decomposition on a substrate at 650 K. However, they suggest the solid carbonyl chlorides as ideal for CVD applications. Evaporation is then to be carried out at 400 K, using carbon monoxide as carrier gas to prevent premature decomposition. Rand [16] evaluated these two platinum precursors in preparing a thin platinum layer on silicon, silicon dioxide, and alumina. The decomposition temperatures are 770-870 K and 460-870 K for the acetylacetonate and carbonyl chloride complex respectively. He showed that application of another precursor, platinum trifluorophosphine ($\text{Pt}(\text{PF}_3)_4$), results in a platinum layer that shows a much improved adherence to silicon dioxide and alumina. These reported experimental procedures give a first indication for the possibilities in the use of metallo-organic precursors for catalyst manufacture.

Finally, another demand on the precursor is the necessity of a high affinity for the substrate. This affinity will determine the precursor losses during catalyst manufacture resulting from deposition on the reactor wall.

The kinetic expressions of the thermal decomposition of the metal precursors are usually not known. The deposition of Ni from $\text{Ni}(\text{CO})_4$ is an exception [17,18], and this precursor is used for the preparation of nickel catalysts by CVD [19,20]. An example, which shows the flexibilities of CVD in catalyst manufacture, is the combination of impregnation and CVD. Pre-impregnation of a catalyst carrier can lead to a selective decomposition of the gaseous metal precursor on the metal clusters. Wielers *et al.* report a synthesis method by which nickel is selectively deposited on copper by CVD [21]. The metal precursor $\text{Ni}(\text{CO})_4$ decomposes on the Cu crystallites and forms a Ni/Cu alloy. This catalyst shows a suppressed amount of carbon deposition in the Fischer-Tropsch reaction as compared with monometallic nickel catalysts. Further, the use of CVD (or CVI) in the preparation of catalysts can open new areas for the formation of new materials, which exhibit interesting catalytic properties. Instances are the carbides and nitrides of transition metals [22]. These can be prepared by gas-phase decomposition of their volatile halogenides and carbonyls.

CVD has additionally a very high potential for the deposition of active material in structured catalytic reactors. Thus, monolithic reactors can be supplied with catalytic material *in situ*. This technique is useful for the *in situ* manufacture and regeneration of structured catalytic

CVD as a novel technique for catalyst preparation

reactors.

It may be clear that the use of CVD in the deposition of active material in catalyst supports or structured catalytic reactors possesses enormous potential. The CVD literature is quite extensive and much benefit can be obtained from this field of expertise. However, the number of possibilities is so huge, that modelling is indispensable in this early stage of research.

The objective of this chapter is to investigate the possibilities of applying the catalytically active phase by CVD on porous supports and structured catalytic reactors. A mathematical model is developed to describe the infiltration of the precursor, the deposition of the active phase, and evolution of the pore geometry in time. Simulations are carried out to explore the prospects of gas-phase depositions by assuming various Langmuir-Hinshelwood kinetic expressions which are commonly encountered in CVD.

As pointed out above, the major problem in modelling CVD systems is the absence of rate expressions which describe the kinetic behaviour of the gas-phase and surface reactions. Moreover, kinetic data are reported for only a few systems, *e.g.* the deposition of Si, TiN, and SiC. Much more attention is given to the macro and micro structure of the deposited material. This has led us to the following approach. We have chosen a system which is of interest in the field of catalysis. The deposition of Ni from NiCl₂ is taken as a possible CVD system. Derivations of various possible kinetic expressions have been made for the deposition of Ni from this precursor; all types of these derived rate equations are reported in literature for the deposition of ceramics and semiconductors from the gas phase. The physical properties of the nickel system are used for the calculation of transport properties.

2. DEPOSITION OF Ni FROM NiCl₂

As pointed out above, the deposition of Ni from NiCl₂ is taken as a possible CVD system, which can be of interest for catalyst manufacture. For practical convenience the decomposition of NiCl₂ in nitrogen is simulated. In practice, it is advisable to use additional hydrogen for the removal of the chlorine, which is formed during the reaction. Thus, the reaction rate will probably be enhanced and incorporation of chlorine in the deposited layer is decreased. The following reactions are assumed to be in thermodynamic equilibrium:



Chapter 3



where K_1 and K_2 are the equilibrium constants of reaction (1) and (2), respectively, and s denotes the free available sites on the surface.

The rate determining step is the surface decomposition of NiCl_2 :



where k is the reaction rate constant of this step.

Note that the decomposition of NiCl_2 results in a creation of a new site (*i.e.* the nickel atom). This "site generating process" is characteristic for CVD. This scheme results in the following rate expression:

$$(-R_{\text{NiCl}_2}) = k \frac{K_1[\text{NiCl}_2]}{\left(1 + K_1[\text{NiCl}_2] + \sqrt{K_2[\text{Cl}_2]}\right)^2} \quad (4)$$

where $(-R_{\text{NiCl}_2})$ is the consumption rate of NiCl_2 in the gas phase per unit surface area. It is obvious that co-adsorption of chlorine and high surface concentrations of NiCl_2 inhibit the formation of metallic Ni. Addition of hydrogen will result in a more complex denominator of equation (4). However, the quadratic characteristic will remain. An identical kinetic behaviour displayed by rate expression (4) is reported for the deposition of TiN from TiCl_4 and N_2 in a reducing atmosphere [6]. Assuming that the adsorption of Cl is less dominant over the adsorption of NiCl_2 and the adsorbed NiCl_2 dissociates in metallic Ni and gaseous chlorine the following rate expression for the formation of Ni can be derived:

$$(-R_{\text{NiCl}_2}) = k \frac{K_1[\text{NiCl}_2]}{1 + K_1[\text{NiCl}_2]} \quad (5)$$

An example of this kinetic behaviour can be found in the deposition of silicon from silane (SiH_4) [23]. At low coverage of the active species (weak adsorption or low gas-phase concentration of the metal precursor) rate equation (5) simplifies to first-order behaviour.

The above derived rate expressions corresponding to the three types of possible adsorption behaviour are summarized in Table 1.

CVD as a novel technique for catalyst preparation

Table 1. Adsorption mechanisms and corresponding kinetic equations

Adsorption mechanism	Kinetic equation
weak associative adsorption (wa)	$R_A = kK_A C_A$
strong associative adsorption (sa)	$R_A = k \frac{K_A C_A}{1 + K_A C_A}$
strong dissociative adsorption (sd)	$R_{A-B} = k \frac{K_{A-B} C_{A-B}}{(1 + K_{A-B} C_{A-B})^2}$

3. MODEL DEVELOPMENT

Mathematical modelling of the deposition of metals in porous structures has great similarity with the modelling of Isothermal Chemical Vapour Deposition. The deposition profile of the metal and the evolution of the pore geometry can thus be described mathematically by the methods developed in [30]. Thus the concentration profiles of the gas phase component and corresponding deposition profile of the solid phase is determined as a function of time by solving the general mass balance equation for one component.

$$\frac{\partial(V C_i)}{\partial t} + \nabla(V J_i) = R_i S \quad (6)$$

Procedures for solving eq. 6 have been reported in [30].

4. MODEL PARAMETERS

4.1 Deposition of Ni in a catalyst pellet.

In order to evaluate the influence of the process conditions on the deposition profiles in the catalyst support, the total deposition time is chosen to be one-tenth of the time necessary to close the pore of 20 nm diameter. This means that the maximum amount of deposited material adds up to a layer with a thickness of about 1 nm. The reaction rate is chosen to be 10 nm per hour. This corresponds to low deposition rates, lower than the ones reported in literature [16]. The temperature is selected at 1140 K to assure the decomposition of NiCl_2

[28]. In practice, this temperature will probably be too high, causing a substantial sintering of the support. However, as mentioned before, adding hydrogen to the gas mixture shall conveniently solve this problem by lowering the decomposition temperature. If necessary, a metallo-organic nickel compound can be used, which decomposes well below the temperature at which the support sinters. The adsorption constants are chosen in such a way that rate expressions (4) and (5) exhibit a shifting order behaviour. The adsorption constant of Cl is assumed to be twice as large as the one of NiCl_2 . Table 2 shows the numerical values of the model parameters used in the simulations.

4.2 Deposition of Ni in a monolith.

Due to the fact that in the model described above no forced flow of the precursor is incorporated, only diffusional mass transfer in the monolithic channels can be simulated. In practice, this means that the monolith is placed in an oven in which the metal precursor is evaporated, followed by diffusion into the monolithic channels from both sides and decomposition to the corresponding metal. Further, an extra parameter has to be added to account for the porous wall structure in the channels of the monolith. The model only accounts for a straight cylindrical pore, whereas the washcoat of the monolith consists of a porous structure. This problem can be overcome by introducing a parameter that embodies the ratio of the surface area of the washcoat and the surface area of the clean monolith. Thus, the diffusion and reactant depletion in the large monolithic channels are simulated, while the surface reaction is corrected by adjusting the surface area of the monolithic channel.

Table 2. Model parameters for the deposition of Ni from NiCl_2 in a catalyst pellet and a monolith

Symbol	Name	cat. pellet	monolith
$C_{\text{NiCl}_2, \text{ bulk}}$	bulk concentration (STP) (mol m^{-3})	0.5 to 20	0.5 to 20
k	reaction rate constant ($\mu\text{mol m}^{-2} \text{s}^{-1}$)	1.47	1.47
K_{Cl_2}	adsorption constant ($\text{m}^3 \text{mol}^{-1}$)	20	20
K_{NiCl_2}	adsorption constant ($\text{m}^3 \text{mol}^{-1}$)	10	10
L	pore length (m)	0.2	0.2
P	pressure (kPa)	100	100
r_{init}	initial pore radius (m)	10	10
S	surface area ($\text{m}^2_{\text{washcoat}} \text{m}^{-2}_{\text{monolith}}$)	-	100
t	deposition time (s)	300	300
T	temperature (K)	1140	1140

In these simulations the same kinetic expressions and values of the kinetic constants are used as in the simulations with the catalyst pellet. For the monolith, generally reported dimensions are used. Table 2 shows the numerical values of the model parameters used in the monolithic simulations.

5. RESULTS AND DISCUSSION

5.1 Total pore closure.

As a first example, the deposition of Ni in a catalyst pellet is continued until pore closure. This will show the evolution of the pore geometry and the corresponding concentration profile of NiCl_2 in time. The bulk concentration of NiCl_2 is selected to be 0.1 mol m^{-3} , so the kinetic behaviour can be assumed to obey first order. Due to the high diffusion coefficient of Cl_2 with respect to the diffusion coefficient of NiCl_2 the amount of Cl_2 in the pore can be neglected. In Figs. 2 and 3 the results of the simulations are presented. It can be concluded that the change in pore geometry during deposition gives rise to an axial and time dependent diffusion rate in the pore. This leads to a concentration profile which is time dependent. As a result of the severe mass transfer limitation, only the first 20% of the pore is coated with Ni. This type of profile is characteristic of a CVD system which displays intrinsic first-order kinetic behaviour combined with high mass-transfer limitations.

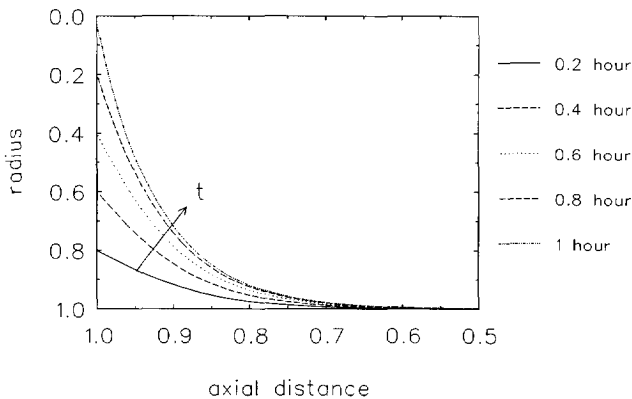


Fig. 2. Time evolution of the pore geometry during Ni deposition ($C_{\text{bulk}} = 0.1 \text{ mol m}^{-3}$)

Chapter 3

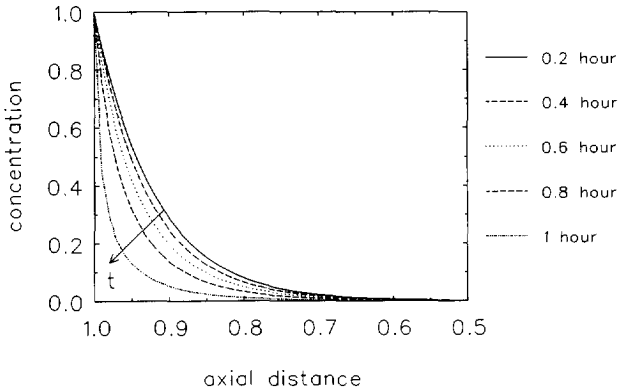


Fig. 3. Time evolution of the concentration profiles during Ni deposition for the same conditions as Fig. 3^A

5.2 Deposition in a catalyst pellet.

This section evaluates deposition profiles in a catalyst pellet according to adsorption behaviour. Fig. 4 displays the deposition profiles of the deposition of Ni from NiCl_2 assuming associative adsorption of the active species. It shows that the deposition profile changes from an exponential decay shaped form to a flat contour at increased concentrations. This is the result of the dependence of the reaction order of equation (5) with the concentration. At low concentrations it behaves like a first order reaction, whereas at higher concentrations it shifts to zero order. The outcome of this is a catalyst in which the site distribution shifts from a degenerated egg-shell to an well developed egg-shell.

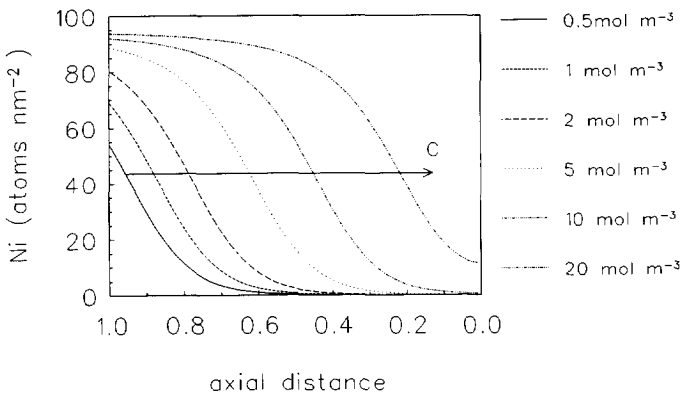


Fig. 4. Deposition profiles of Ni in a catalyst pellet as a function of the bulk concentration of the Ni precursor assuming associative adsorption. Deposition time: 300 s

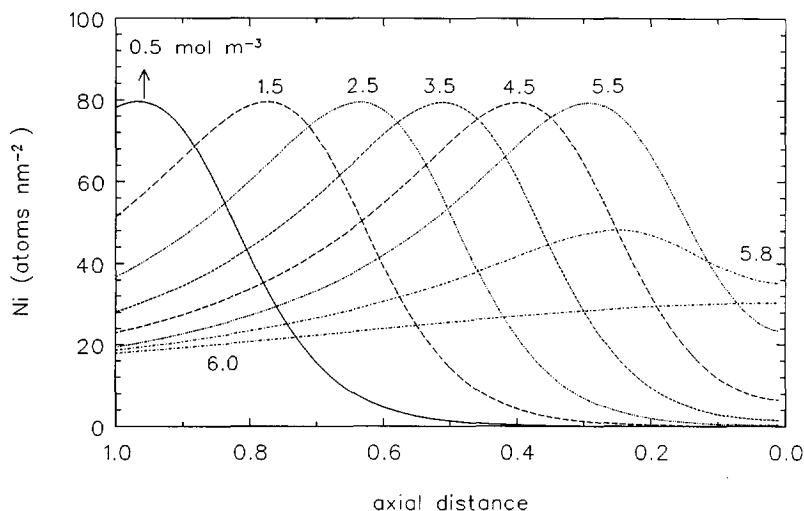


Fig. 5. Deposition profiles of Ni in a catalyst pellet as a function of the bulk concentration of the Ni precursor assuming dissociative associative adsorption. Deposition time: 300 s

Fig. 5 displays the deposition profiles in a catalyst pellet, assuming dissociative adsorption of the active species. All simulations are carried out with a deposition time of 300 seconds. It is shown that the deposition of Ni exhibits a strong non-uniformity in the pore. The maximum found in the deposition profile is shifted from the pore entrance at low bulk concentrations of NiCl_2 to the centre of the pore at increased bulk concentrations of NiCl_2 . This effect originates from the shifting order behaviour of rate equation (4). The bulk concentration of the Ni precursor is chosen in such a way that it exceeds the concentration at the maximum deposition rate. Thus, by reaction and decline in concentration the reaction rate is increased until the first-order region is reached resulting in a maximum in the deposition profile in the pore.

The maximum is shifted towards the centre of the pore by increasing the bulk concentration of the diffusing component. This is a consequence of the fact that the decrease in concentration needs a certain span of reaction, after which the maximum in deposition rate is reached. The shift of the maximum inwards the pore continues until the maximum in deposition rate cannot be reached by precursor depletion. This results in a nearly homogeneous distribution of active material in the catalyst support. At lower concentrations the active-site distribution changes from egg-shell ($C_{bulk} = 0.5 \text{ mol m}^{-3}$), egg-white ($C_{bulk} = 3.5 \text{ mol m}^{-3}$), to nearly egg-yolk ($C_{bulk} = 5.5 \text{ mol m}^{-3}$).

5.3 Deposition in a monolith.

In this section the deposition of Ni in a monolith is discussed. As addressed before, only diffusional mass transfer through the monolithic channels is considered.

Fig. 6 depicts the simulations in which the interior of a monolith is coated with Ni and associative adsorption of the active species is assumed. The nomenclature used for the description of activity profiles in a catalyst body is not applicable for the activity profiles along the axis of a monolithic channel. The egg-shell profile in a catalyst support corresponds to activity maxima at the entrances of a monolith (entrance mountain profile). The egg-white situation is shown in the monolith by two maxima in the activity profile, each on equal distance from the front and end of the channels (double mountain profile). The egg-yolk profile corresponds to one maximum in the middle of the monolithic channels (centre mountain profile). Of course, the diffusion into the channels can be limited to one side of the monolith, which will result in only one maximum in the activity profile. This will be situated at the front, the first half or the middle of the monolith.

It is shown in Fig. 6 that the deposition profile shifts from a degenerated entrance mountain profile to a normal entrance mountain structure, when moving to higher bulk concentrations of the diffusing species. However, compared to the dimensionless infiltration depth of Ni in the catalyst pellet, the penetration of the active sites is not as extensive. The discussion held for the deposition of Ni in a catalyst pellet is also valid here. The same shift in reaction order (from one to zero) is found, which accounts for the well defined mountain profile of the active-site distribution in the monolith. In Fig. 7 the results of the simulations are shown by incorporating dissociative adsorption of the active species in the model.

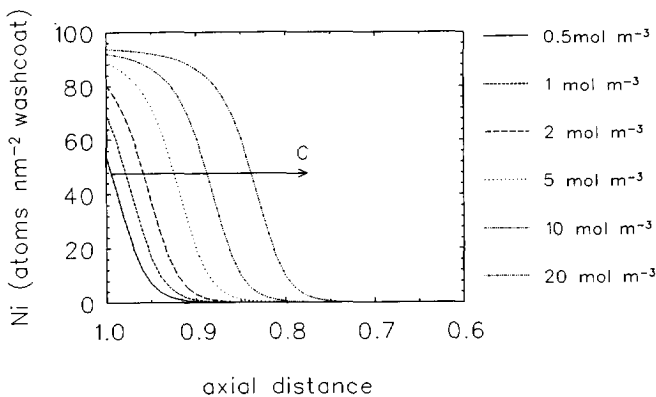


Fig. 6. Deposition profiles of Ni in the channel of a monolith as a function of the bulk concentration of the Ni precursor assuming associative adsorption. Deposition time: 100 s

CVD as a novel technique for catalyst preparation

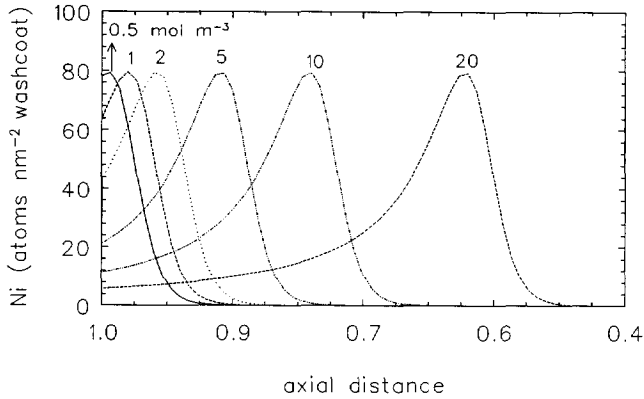


Fig. 7. Deposition profiles of Ni in the channel of a monolith as a function of the bulk concentration of the Ni precursor assuming dissociative adsorption. Deposition time: 100 s

At low concentrations the deposition is fixed at the channel entrance, whereas at increasing bulk concentrations a maximum in the deposition profile is shown, which shifts to the centre of the monolith. The results are similar to the simulations in which the catalyst pellet is applied with Ni, while dissociative adsorption is incorporated in the model. Here as well, the same discussion of the changing reaction order held for explaining the profiles in the catalyst pellet with dissociative adsorption is legitimate. These results are promising because monolithic reactors are very well suited to operate with inhomogeneous site distributions in the monolithic channels. CVD is indispensable in achieving these activity profiles. Application of a forced flow through the monolithic channels is a possibility. An advantage of this forced-flow system will be the larger infiltration depth in the monolith. However, the sharpness of the active-site distributions as shown in Fig. 7 will diminish.

5.4 Evaluation of the Thiele modulus.

By using the derived expression of the Thiele modulus for dissociative adsorption kinetics [27], an attempt has been made to find a correlation between the place of maximum deposition and the Thiele modulus. Both for the catalyst pellet and the monolith these calculations have been carried out. Fig. 8 shows identical trends between the curves of the two very different systems. As expected, at lower Thiele moduli the place of maximum deposition is shifted inwards the pore. As pointed out in [27], the lowering of the Thiele modulus is achieved by increasing the bulk concentration, which fits nicely in the trend shown in Fig. 8. The Thiele modulus is thus a useful tool for the first estimate of the places of the maxima in the active-site distributions and in catalyst design in general.

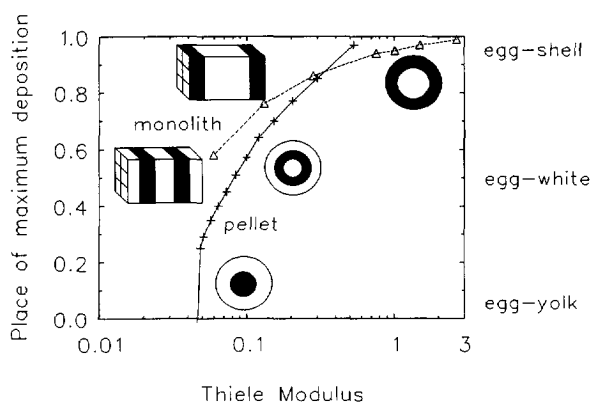


Fig. 8. The place of maximum deposition as a function of the Thiele modulus

5.5 Limitations of the simulations.

Of course, there are some restrictions that have to be mentioned regarding the discussion of the results. First of all, kinetic data or rate equations have to be gathered in order to fully evaluate the possibilities of the realization of inhomogeneous metal deposition in porous structures. The fact that the rate equations, which are used in this chapter for the deposition of Ni, are reported for the deposition of ceramics and semiconductors, is no guarantee that they are valid for the deposition of metals from the gas phase. The deposition of metals results, in general, in the formation of different types of bonding compared to ceramics or semiconductors. This can lead to other types of rate expressions. Secondly, it has to be mentioned that the deposition of metals from the gas phase can be catalyzed by the already formed metal clusters on the surface. It is clear that this catalytic effect will have drastic consequences for the applicability of the rate equations used in this chapter. Such an auto-catalytic effect can of course result in selective deposition at the pore entrance. However, it might be turned into advantage in the preparation of catalytically active alloys as reported by Wielers *et al.* [21]. Furthermore, such an auto-catalytic effect can be controlled by proper selection of deposition conditions and can result in a decreased deposition temperature. This increases the number of applicable catalyst carriers (*e.g.* polymers).

In conclusion, the absence of reported rate equations restricts the full evaluation in acquiring inhomogeneous site distribution in porous structures by CVD. This chapter shows the possibilities in obtaining these profiles under assumption of kinetic behaviour, which is reported for various CVD systems. Of course, the possibility of using various gaseous metal precursors gives opportunities in tuning the deposition mechanism, by which the deposition profiles can be controlled.

6. CONCLUSION

Chemical Vapour Deposition is a promising technique for application of active material on catalytic supports. It can lower the number of steps in catalyst manufacture. Moreover, the flexibility of a gas-phase deposition system is larger than that of the liquid-phase systems, used in current catalyst manufacture. Further, the activation and regeneration of structured catalytic reactors (*e.g.* monoliths) can be easily carried out *in situ*.

If the rate equations for the deposition of metals from the gas phase obey Langmuir-Hinshelwood behaviour, in which the decomposition of the adsorbed metal precursor can be regarded as the rate limiting step, it is possible to produce catalysts and structured catalytic reactors with an inhomogeneous active-site distribution. Depending on the precise mechanism of decomposition, various activity profiles can be achieved. Weak adsorption of the active species results in a non-uniform distribution in which the activity gradually decreases moving from the pore entrance to the centre. The resulting profiles vary between degenerated egg-shell and nearly uniform. Associative adsorption results in activity contours that diverge from a degenerated egg-shell to a well formed egg-shell. When the adsorption can be regarded as dissociative two other forms of activity distributions can be found. They alter from an egg-shell, *via* egg-white, to nearly egg-yolk. All these situations can be controlled by adapting the bulk concentration of the active species. So, CVD exhibits great potential in the design of catalysts and structured catalytic reactors with inhomogeneous active-site distributions. The Thiele modulus can be a useful instrument for a first understanding of the possible infiltration depths that can be achieved. It is shown that for decreasing Thiele moduli the place of maximum deposition shifts to the centre of the pore. This trend is valid for a catalyst pellet as well as for a monolith.

SYMBOLS

$C_{i,bulk}$	bulk concentration of component i at $t=0$ (mol m^{-3})
J_i	molar flux of component i
k	intrinsic rate constant ($\text{mol m}^{-2} \text{s}^{-1}$)
K_i	adsorption/desorption equilibrium constant ($\text{m}^3 \text{mol}^{-1}$)
L	length of a pore, which is open at both sides (m)
P	pressure (Pa)
$r(x,t)$	pore radius at position x and time t in the pore (m)
r_{init}	radius at $t=0$ (m)
R	reaction rate per unit surface area ($\text{mol m}^{-2} \text{s}^{-1}$)

Chapter 3

S	specific surface area of a monolith ($\text{m}^2_{\text{washcoat}} \text{m}^{-2}_{\text{monolith}}$)
t	time (s)
T	temperature (K)
x	axial position in the pore (m)
V	volume (m^3)

Greek letters

φ	Thiele modulus (-)
-----------	--------------------

Abbreviations

(g)	gas phase
s	site
sa	strong associative adsorption
sd	strong dissociative adsorption
wa	weak associative adsorption

REFERENCES

1. Sheng-Yi Lee and R. Aris, *Catal. Rev. -Sci. Eng.*, **27(2)** (1985) 207.
2. Masaharu Komiyama, *Catal. Rev. -Sci. Eng.*, **27(2)** (1985) 341.
3. P. Mars and M.J. Gorgels, in Proceedings of the 3rd European Symposium: Chemical Reaction Engineering, Pergamon Press, Oxford, *Chem. Eng. Sci. Suppl.* (1964) 55.
4. Tsao Chin Jung, Du Yuan Sheng and Miao Hue Fang, in G.W.Cullen and J.M. Blocher (eds.), Proceedings of the Tenth International Conference on Chemical Vapor Deposition, The Electrochemical Society Softbound Proceedings Series, Pennington, NJ, 1987, p. 81.
5. C.Z. Rong, D.Y. Sheng and M.H. Fang, *Surf. Eng.*, **5** (1989) 315.
6. N. Nakanishi, S. Mori and E. Kato, *J. Electrochem. Soc.*, **137** (1990) 322.
7. H.C. Theuerer, *J. Electrochem. Soc.*, **108** (1961) 649.
8. E.G. Bylander, *J. Electrochem. Soc.*, **109** (1962) 1171.
9. E.G. Alexander, *J. Electrochem. Soc.*, **114** (1967) 65C.
10. K. Minato and K. Fukuda, *J. Nucl. Mater.*, **149** (1987) 233.
11. H.O. Pierson, Handbook of Chemical Vapor Deposition (CVD), Noyes Publications, New Jersey, 1992.

CVD as a novel technique for catalyst preparation

12. M. Yano, N. Takashi, Y. Harano, and H. Ohi, in K.E. Spear (ed.), Proceedings of the Eleventh International Conference on CVD 1990, The Electrochemical Society, Pennington, NJ, 1990, p. 603.
13. T.M. Besmann, R.A. Lowden, B.W. Sheldon and D.P. Stinton, in K.E. Spear (ed.), Proceedings of the Eleventh International Conference on Chemical Vapor Deposition, The Electrochemical Society, Pennington, NJ, 1990, p. 482.
14. C.F. Powell, J.H. Oxley and J.M. Blocher, Vapor Deposition, John Wiley and Sons, New York, 1966.
15. A.A. Oosthoorn and J.A. Moulijn, *J. Mol. Catal.*, **8** (1980) 147.
16. M.J. Rand, *J. Electrochem. Soc.*, **120** (1973) 686.
17. A.P. Garratt and H.W. Thompson, *J. Chem. Soc.* (1934) 1822.
18. C.E.H. Bawn, *Trans. Faraday Soc.*, **31** (1935) 440.
19. J.C. Védrine, *J. Catal.*, **46** (1977) 434.
20. K. Omata, H. Mazaki, H. Yagita and K. Fujimoto, *Cat. Lett.*, **4** (1990) 123.
21. A.F.H. Wielers, C.M.A.M. Mesters, G.W. Koebrugge, C.J.G. van der Grift and J.W. Geus, in B. Delmon, P. Grange, P.A. Jacobs and G. Poncelet (eds.), Preparation of Catalysts IV, Elsevier Science Publishers B.V., Amsterdam, The Netherlands, 1987, p. 401.
22. S.T. Oyama, *Catal. Today*, **15** (1992) 179.
23. H. Kurokawa, *J. Electrochem. Soc.*, **129** (1982) 2620.
24. R.C. Reid, J.M. Prausnitz and B.E. Poling, Properties of gases and liquids, 4th ed., McGraw-Hill, New York, 1989, p. 587.
25. L.K. Doraiswamy and M.M. Sharma, Heterogeneous reactions, vol 1, John Wiley & Sons, New York, 1984.
26. L.K. Doraiswamy and M.M. Sharma, Heterogeneous reactions, vol 1, John Wiley & Sons, New York, 1984, p. 75.
27. R. Moene, J.P. Dekker, M. Makkee, J. Schoonman and J.A. Moulijn, *J. Electrochem. Soc.*, **141** (1994) 282;
Chapter 2 of this thesis.
28. R.C. Weast and D.R. Lide (eds.), CRC Handbook of Chemistry and Physics, 70th ed., CRC Press, Boca Raton, FL, 1989.

Chapter 4

Coating of activated carbon with silicon carbide by Chemical Vapour Deposition to improve the oxidation resistance and mechanical strength

ABSTRACT

Coating of activated carbon with silicon carbide by Chemical Vapour Deposition (CVD) has been investigated to improve the oxidation resistance and the mechanical strength of activated carbon extrudates. The oxidation resistance has been analyzed by thermal gravimetric analysis in air; the temperature at the maximum rate of oxidation (T_{max}) is used to compare the modified carbons. Selective deposition of SiC by reacting SiCl_4 with the carbon surface cannot be achieved below 1400 K. Silicon deposition has been encountered in all cases. Coating of activated carbon is achieved using a $\text{CH}_4/\text{SiCl}_4$ mixture which results in SiC deposition at 1376 K. The oxidation resistance of this modified activated carbon has been improved by 150 K ($T_{max}=1025$ K), while the side crushing strength improved additionally by a factor 1.7. The residual surface area was $176 \text{ m}^2/\text{g}$. SiC coatings have also been obtained by decomposing methyltrichlorosilane at temperatures above 1200 K. The side crushing strength of the extrudates improved by a factor of 1.4, while the resistance against oxidation remained similar to that of the original carbon. The residual surface areas and pore volumes averaged $530 \text{ m}^2/\text{g}$ and 0.33 ml/g , respectively. Both methods of SiC deposition result in surface areas which are high enough for catalyst support applications. Evaluation of the infiltration performance of this SiC-CVD process using methyltrichlorosilane shows that 20 to 95% of the SiC has been deposited inside the extrudates. The residual porosity of the extrudates is evaluated using an general mathematically developed Chemical Vapour Infiltration design chart, which correlates initial Thiele moduli with the porosity after deposition. Good agreement is obtained between the experimental data and the design chart.

1. INTRODUCTION

The use of activated carbon as catalyst support is mainly limited by its sensitivity towards reactions with oxygen and hydrogen [1]. The reactivity with oxygen can be lowered by modifying the carbon surface in such a way that the number of sites, which are active in the oxidation, is lowered. These active sites (often referred to as the Active Surface Area, ASA [2]) are responsible for the cyclic desorption of CO/CO₂ and adsorption of oxygen, which results in burning the carbon support. The reactivity towards molecular hydrogen of bare activated carbon is low. Transition or noble metals, applied on this support, however, catalyze the hydro-gasification of carbon into methane. Two different mechanisms can be distinguished. The first type of hydro-gasification is metal catalyzed dissociation of hydrogen, which subsequently 'spills over' to defects in the basal planes to form methane. Secondly, at elevated temperatures carbon can dissolve in the metal crystallite, diffuse to the gas-metal interface and react with hydrogen to methane. Research has primarily been focused on achieving an increased oxidation resistance by decreasing the ASA. A decrease in ASA can be achieved by heat treatment or impregnation with metal phosphates, chlorine compounds, and boron glasses [3,4], which all improve the oxidation resistance to a certain extent. Stegenga *et al.* [5] investigated the possibility of applying silicon carbide on the carbon surface. They impregnated activated carbon with tetraethoxysilane (Si(C₂H₅O)₄, TEOS), which was subsequently decomposed into SiO₂, followed by a heat treatment at 2273 K acquiring the SiC. This has resulted in an increase in oxidation resistance of 100 K, while a considerable amount of surface area was retained. Furthermore, the side crushing strength was improved by a factor two. An alternative method of modifying surfaces by SiC deposition to achieve an improvement in oxidation resistance is Chemical Vapour Deposition (CVD). Thus, carbon/carbon composites are coated with silicon carbide which acts as a diffusion barrier for carbon and oxygen [6]. Another mode of operation exists in the surface modification and densification of porous substrates. This technique, referred to as Chemical Vapour Infiltration (CVI), is one of the few in which ceramic composites can be manufactured consisting of undamaged fibres or whiskers embedded in a ceramic matrix. Thus, a very high toughness and strength can be combined, disclosing numerous applications of ceramic materials at demanding process conditions. Methyltrichlorosilane (CH₃SiCl₃, MTS) is frequently used to achieve either an oxygen resistant SiC coating or a ceramic composite consisting of toughening fibres and a SiC matrix. Table 1 shows examples of this and several other SiC precursors and their application. To achieve an optimal oxidation resistance, it is important that stoichiometric SiC is deposited. Although the C/Si molar ratio in methyltrichlorosilane is one, deposition of silicon is encountered at temperatures below 1200 K, whereas carbon is co-deposited with SiC above 1800 K.

Modification of activated carbon by CVD of silicon carbide

Table 1. SiC precursors and their application

SiC precursor	Conditions of synthesis		Application	Reference
	Temperature (K)	Pressure (kPa)		
CH ₃ SiCl ₃	1523 to 1873	n.r.	coating	24
	1400	1.7	coating	26
	1173 to 1273	10 to 35	} composite (CVI)	15
	1173 to 1373	10 to 100		16
	1252 to 1270	2 to 13.3		17
CH ₃ SiCl ₃ /CH ₄	1473 to 1723	4.6	coating	25
SiCl ₄ /CH ₄	1400 to 1600	100	coating	23
(CH ₃) ₂ SiCl ₂	1473 to 1600	n.r.	coating	21,22
SiCl ₄ /Carbon	1500 to 1700	100	coating	7,14,18
SiH ₄ /C _x H _y	1773 to 1923	100	electronic	10,11,27

n.r.: not reported

The mechanism of SiC deposition can be regarded as two independent sub-systems, *viz.* the deposition of carbon and the deposition of Si [8,9]. Equal rates will result in stoichiometric SiC. Detailed knowledge of the kinetics in the gas phase and on the surface is, however, limited, especially for chlorine containing SiC precursors like CH₃SiCl₃. The gas-phase kinetics for the SiH₄-hydrocarbon system is relatively well understood [10-12], here, more knowledge of the surface chemistry is needed. Thermodynamic calculations are widely used for a first insight in the condensed phases which are stable under process conditions [8,9,13]. Furthermore, the gas-phase composition can be determined at thermodynamic equilibrium. Considering a certain amount of gaseous components (varying from 6 to 45), it has been shown that SiCl₄ and CH₄ are the most abundant Si and C components in the Si-Cl-C-H system below 1000 K. SiCl₂ and C₂H₂ are formed at temperatures higher than 1800 K. Deposition of stoichiometric SiC is predicted at certain H₂/CH₃SiCl₃ ratios which depend on temperature and pressure. On a thermodynamic basis, silicon co-deposition is found at high H/Si ratios, whereas carbon is co-deposited at low H/Si ratios.

In this chapter Chemical Vapour Deposition of SiC is evaluated as a modification technique to achieve strong activated carbon particles with a high surface area and a high oxidation resistance. An obvious prerequisite, identifiable prior to this investigation, is the

formation of SiC layers with the capability of shielding the underlying carbon substrate while retaining a major part of the porous structure. Thermodynamic calculations are carried out to establish preliminary indications for optimal deposition conditions by determining equilibrium gas-phase compositions and stable solid phases at various conditions. Reactive CVD (using the activated carbon as carbon source) and conventional CVD (using $\text{SiCl}_4/\text{CH}_4$ or CH_3SiCl_3) are performed on activated carbon extrudates and the thermodynamic calculations are evaluated. Subsequently, the oxygen reactivity, residual surface area, and side crushing strength are evaluated according to their modification technique. Finally, the infiltration process will be compared with the results obtained by mathematical modelling of CVI.

2. THERMODYNAMICS

Table 2 shows the gaseous and solid components which are incorporated in the calculations. The thermodynamic data (*i.e.* $\Delta_f H^{298 K}$, $S^{298 K}$, and $C_p^{800-2000 K}$) are taken from JANAF Thermochemical Tables [28]. The calculations are carried out using atomic mass balances and minimization of the overall Gibbs energy using the program Solgasmix [29]. It should be noted that only the relative amounts of atoms determine final thermodynamic equilibrium compositions, hence, no distinction can be made between carbon originating from graphite or methane. Thermodynamic calculations are carried out for Si/(Si+C) ratios varying from 0 to 1 and for H/Si ratios of 40 and 400, at 10 kPa, and temperatures between 800 and 1800 K. Fig. 1 displays an example of the mixture of gaseous components with equilibrium pressures exceeding 10^{-10} bar for the system Si/C=1 and H/Si=40. SiCl_4 and CH_4 are the most abundant gaseous SiC precursors at low temperatures. The equilibrium pressure of methyltrichlorosilane does not exceed 10^{-8} bar, which originates from the low bonding energy of the Si-C bond (290 kJ/mol) in the MTS molecule relative to the Si-Cl (359 kJ/mol) and C-H bonds (338 kJ/mol).

Table 2. Components used in thermodynamic calculations

Ar	HCl	CH_4	CH_2Cl_2	CCl_3	SiHCl_3	SiCl_2
H	Si(s)	C_2H_2	CH_3Cl	CCl_4	SiH_2Cl_2	SiCl_3
H_2	SiC(s, β)	C_2H_4	C_2HCl	C_2Cl_2	SiH_3Cl	SiCl_4
Cl	C(s, graphite)	CHCl	CCl	C_2Cl_4	SiH_4	CH_3SiCl_3
Cl_2	CH_3	CHCl_3	CCl_2	C_2Cl_6	SiCl	

Modification of activated carbon by CVD of silicon carbide

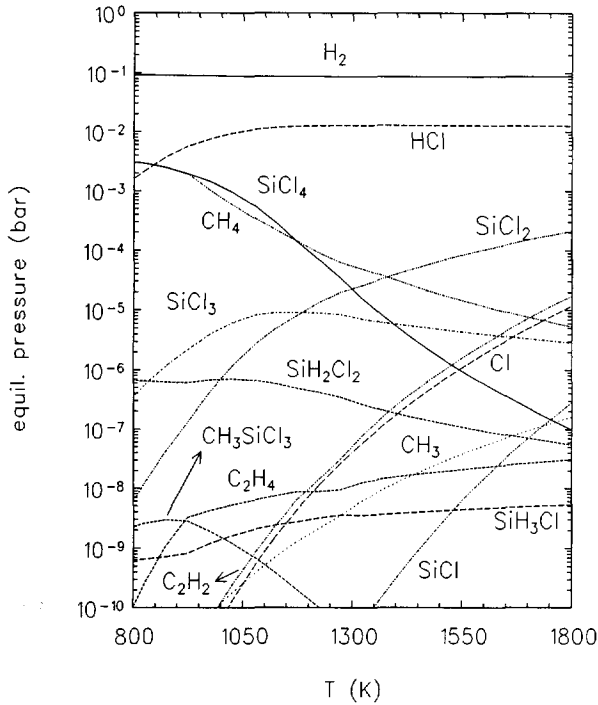


Fig. 1. Equilibrium gas phase composition (including SiC, Si or carbon formation) for $H_2/MTS=20$ and $P=10$ kPa

Above 1300 K the equilibrium pressure of $SiCl_2$ surpasses that of $SiCl_4$. The most abundant C-precursor shifts from methane to ethyne (C_2H_2) above 1700 K. The trends found in these calculations agree with those reported in literature for the Si-H-Cl-C system.

Figs. 2 and 3 show the condensed phases as a function of the input amount of silicon in the temperature range of 800 to 1800 K as a function of the ratio of silicon and carbon in the system. The effect of H/Si ratio has been investigated as well.

Three areas are encountered in Figs. 2 and 3, *viz.* regions of SiC+C, SiC, and SiC+Si deposition. Increasing the H/Si ratio from 40 (Fig. 2) to 400 (Fig. 3) results in a broader range of conditions in which Si is co-deposited, silicon is exclusively present at high Si/C ratios and low temperatures. This evolves from the equilibrium shift of reaction 1 to the right-hand side:



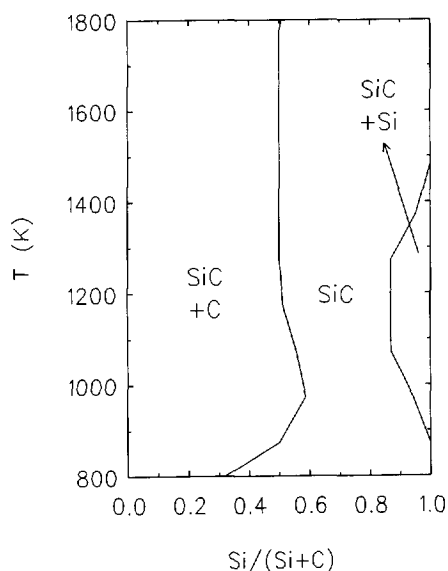


Fig. 2. CVD diagram for $H_2/SiCl_4=20$ and $P=10$ kPa. Condensed phases as a function of gas-phase composition and temperature

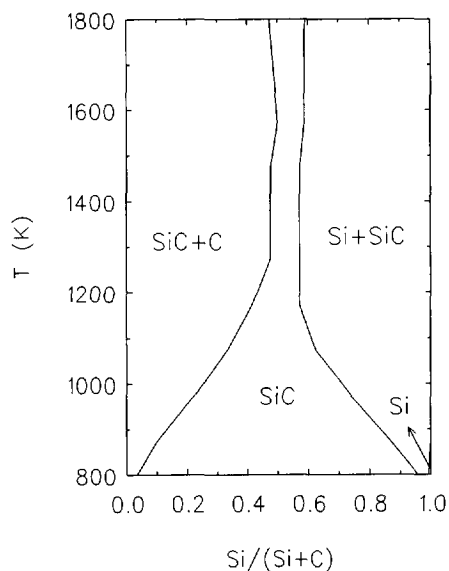
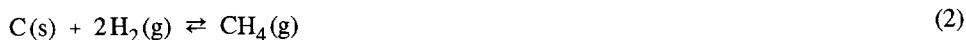


Fig. 3. CVD diagram for $H_2/SiCl_4=200$ and $P=10$ kPa. Condensed phases as a function of gas-phase composition and temperature

Furthermore, the region in which solid carbon is present decreases in size with increasing amounts of hydrogen at temperatures below 1200 K. This is the consequence of the equilibrium shift of reaction 2 to the right-hand side.



The CVD-diagrams have also been determined at 100 kPa (1 bar). Qualitatively, no differences are found compared to Fig. 2 and 3, except for the low temperature SiC area. This region is somewhat extended into the SiC+C region.

From these calculations it can be generally concluded that equimolar amounts of Si and C in the system are beneficial for stoichiometric SiC deposition. Furthermore, increasing the H/Si ratio from 40 to 400 decreases the amount of solid carbon, whereas the amount of co-deposited Si is enlarged. This might suggest optimal conditions for SiC deposition at $H_2/SiCl_4$ ratios below 40. The reverse of reaction $SiCl_4 + 2H_2 + C \rightleftharpoons 4HCl + SiC$, however, becomes significant at very low H_2/HCl ratios and thus a minimal excess of hydrogen is indispensable for SiC formation.

3. EXPERIMENTAL

3.1 Materials.

The modifications have been performed on steam activated, peat based, Norit activated carbon extrudates, type RW08. Prior to modification, the extrudates were separated according to degree of activation. The properties of the fraction used are shown in Table 3.

Table 3. The physical properties of the activated carbon extrudates

S_{BET} (m^2/g)	V_{pore} (ml/g)	S_t (m^2/g)	V_{micro} (ml/g)	$\rho(Hg)$ (kg/m^3)	$\rho(He)$ (kg/m^3)	ash (w%)	length (mm)	diameter (mm)
947	0.60	112	0.41	661	2167	5.2	3.0	0.81

The pore size distribution for the meso and macro pore region, determined by mercury porosimetry [37], is shown in Fig. 4. The typical poly-disperse porous structure [38] is evident. Two major contributions to the macro-pore structure are displayed, pores with radii of 250 nm and 1000 nm. The micro-pore region cannot be identified with Hg-porosimetry.

Hydrogen (99.99%), Ar (99.99%), and CH_4 (99.995%) were obtained from Hoek Loos. Purification of the gases was carried out by passing them through a bed of Pd/Al_2O_3 (hydrogen) or Cu/Al_2O_3 (Ar, CH_4) followed by a molecular sieve 5A for water removal. Silicon tetrachloride (99%) was obtained from Aldrich Chemical Company, methyl-trichlorosilane (98%) was obtained from Janssen Chimica, and were all used without further purification. Graphite plates ($10 \times 5 \times 1$ mm) were obtained from Johnson Matthey (batch 35142).

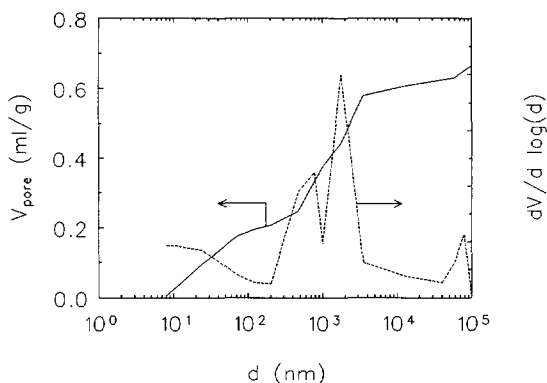


Fig. 4. Pore volume distribution of RW08

3.2 Chemical Vapour Deposition of silicon carbide.

A schematic picture of the CVD apparatus is shown in Fig. 5. A thin bed of extrudates (200 mg, 1 mm bed length) was positioned in a hot-wall tubular quartz reactor (ID 42 mm) to assure deposition under differential conditions. Prior to CVD, the substrates were heated in hydrogen with 0.167 K/s up to 1400 K (above the highest deposition temperature applied), followed by cooling to the deposition temperature, and adjusting to sub-atmospheric pressure. A graphite substrate, which was placed just upstream of the extrudates, was used to determine the rate of SiC deposition. The reactant gas was composed by bubbling argon through an evaporator filled with SiCl_4 or MTS (held at 410 or 400 K, respectively), which was subsequently mixed with hydrogen (and CH_4) before entering the reactor. The total gas flow equalled 5.6 ml/s (STP) and 27.8 ml/s (STP) for the SiCl_4 and CH_3SiCl_3 experiments, respectively.

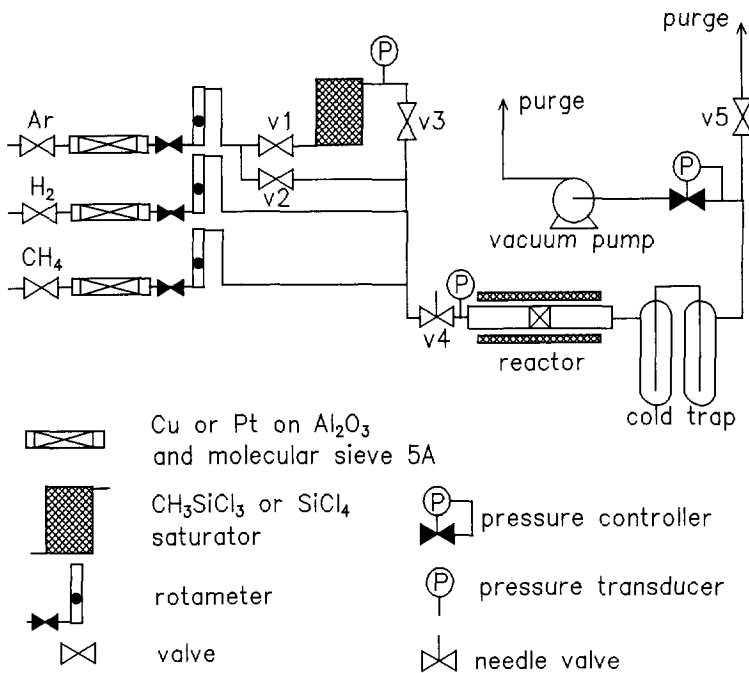


Fig. 5. Scheme of the CVD apparatus

3.3 Scanning electron microscopy.

The activated carbon extrudates and graphite substrate were analyzed by scanning electron microscopy (JEOL JSM-35, Au sputtering of 4 minutes) to investigate the morphology of the deposited material. Furthermore, the growth rate has been determined from the layer thickness on the graphite substrate. From a representative area, a micrograph was taken and a mean thickness was determined by measuring the SiC-layer on eleven places at equal distance from each other. The 95% confidence region has been acquired by assuming a t-distribution of averages, there this distribution is robust in the sense that even for small numbers of samples (5 to 10) the approximation of confidence region is usually relatively accurate [41].

3.4 Surface area measurements.

Nitrogen isotherms at 77 K were recorded on a Carlo Erba Sorptomatic 1800. Prior to measurement the samples were degassed at 423 K and 0.1 kPa. The BET surface area (S_{BET}), t surface area, (S_t) and micro-pore volume (V_{micro}) were determined according to literature [19,20].

3.5 Temperature Programmed Desorption.

Temperature Programmed Desorption (TPD) is carried out on home-made equipment by heating 200 mg activated carbon with 0.167 K/s to 1273 K in a helium-argon gas mixture (97v%/3v%). The gases evolved were recorded by a mass spectrometer (Varian Mat44 S) in multiple ion detection mode. Calibration was carried out by decomposing calcium oxalate monohydrate.

3.6 X-ray Diffraction.

Diffraction patterns were recorded on home-made equipment using a Cu-K α beam by measuring the Debye-Scherrer pattern.

3.7 Thermogravimetric Analysis.

A Setaram TAG 24 S thermobalance was used to determine the oxidation resistance. The samples (~30 mg) were heated with a heating rate of 0.167 K/s in air to 1273 K, while recording the weight change. The temperature at the point of maximum rate of weight loss (T_{max}) is generally assumed to be a suitable property for comparing the oxidation resistance of the activated carbon.

3.8 Side crushing strength.

The side crushing strength was determined with a Schleuniger-2E. The average value of

ten samples was used as a measure for the side crushing strength. The 95% confidence region has been acquired by assuming a t-distribution of averages.

4. RESULTS

4.1 Pretreatment.

Heating the activated carbon in hydrogen up to 1400 K (this first step of the modification procedure will be referred to as the pretreatment), resulted in a total weight decrease of 8.4%. The difference in oxidation behaviour compared to the original carbon is depicted in Fig. 6. The hydrogen pretreatment increases the resistance against oxidation by 80 K. This is shown by the identical increase in temperature at which the oxidation starts and the temperature at the maximum rate of oxidation (T_{max}). The improvement in oxidation resistance is the result of reducing the ASA by decomposing the oxygen containing surface groups into H_2O , CO_2 , and CO . Thus, the number of defects in the graphitic structure and, hence the oxygen reactivity, has been decreased. The decomposition of the oxygen containing surface groups of the fresh carbon during this initial step has been analyzed by Temperature Programmed Desorption in a helium-argon mixture. The results are shown in Fig. 7.

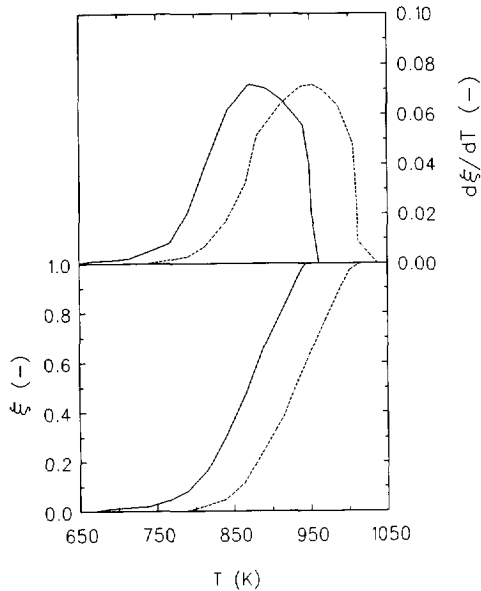


Fig. 6. Carbon conversion (ξ) and the first derivative ($d\xi/dT$) for the original (—) and H_2 -pretreated (---) carbon during TGA in air (heating rate 0.167 K/s)

Modification of activated carbon by CVD of silicon carbide

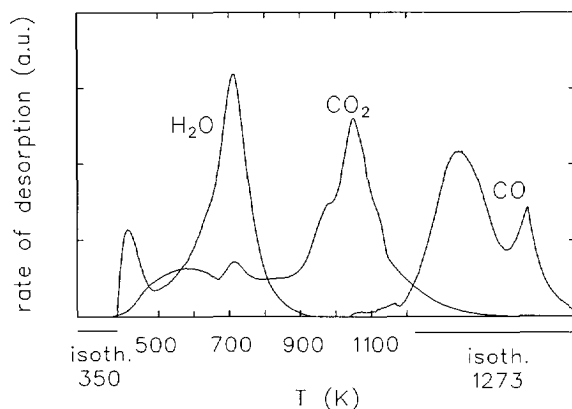
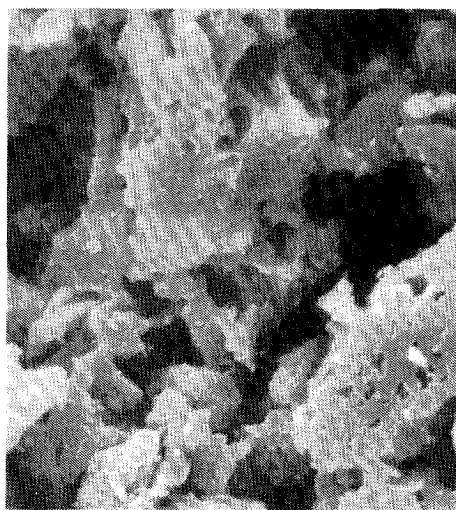


Fig. 7. Temperature programmed desorption of H₂O, CO₂, and CO from fresh RW08

Single oxygen functional groups generally produce CO onto decomposition of carbon-oxygen complexes, whereas CO₂ is formed from decomposing carboxylic acids. The weight losses of H₂O, CO₂, and CO were 2.4, 3.0, and 1.7 w%, respectively. The total weight loss is somewhat lower than that during the H₂-pretreatment.



5 μm
Fig. 8. Morphology of the external surface of RW08



5 μm
Fig. 9. Morphology of the internal surface of RW08

SEM analysis of the extrudates prior and after the pretreatment showed that the macro structure does not change. Figs. 8 and 9 are indicative for the structure of the carbon extrudates after the H_2 pretreatment. Conglomerated carbon particles of a grained structure can be distinguished, which are typical for a steam activated carbon. The outer surface appears to consist of granules of smaller diameter, as displayed in Fig. 9. The side crushing strength of the original and pretreated carbon was identical, viz. 20.9 ± 4.7 N.

In the following section, the three types of SiC formation will be discussed separately. The activated carbon which has been heated up to 1400 K in H_2 will be taken as reference material in all cases.

4.2 Reactive CVD of $SiCl_4$ on activated carbon ($C + SiCl_4 + 2 H_2 \rightarrow SiC + 4 HCl$).

A ratio of $H_2/SiCl_4$ equal to 20 has been used in all cases. The CVD-temperature ranged from 880 to 1380 K. After modification no differences in colour are encountered. Fig. 10 displays the amount of solid deposits, determined by TGA, and T_{max} as a function of deposition temperature. It is shown that the deposited amount decreases with increasing temperature and that the oxidation resistance has only slightly been improved compared to the H_2 pretreated carbon. XRD revealed only silicon as crystalline phase, no crystalline SiC has been detected.

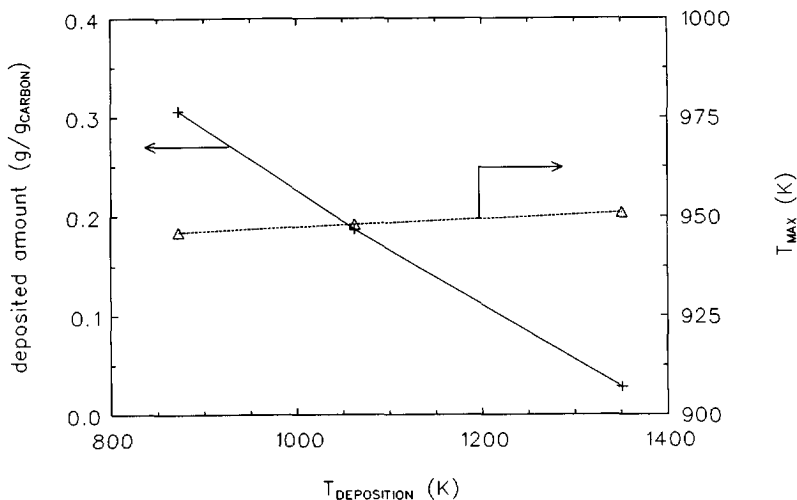


Fig. 10. Deposited amount (+) and T_{max} (Δ) as a function of deposition temperature

4.3 CVD of SiC using SiCl₄ and CH₄ on carbon (SiCl₄ + CH₄ → SiC + 4 HCl).

The results of this modification are displayed in Table 4.

Table 4. Modification of activated carbon by CVD using H₂/SiCl₄/CH₄. Reaction time 6 hours

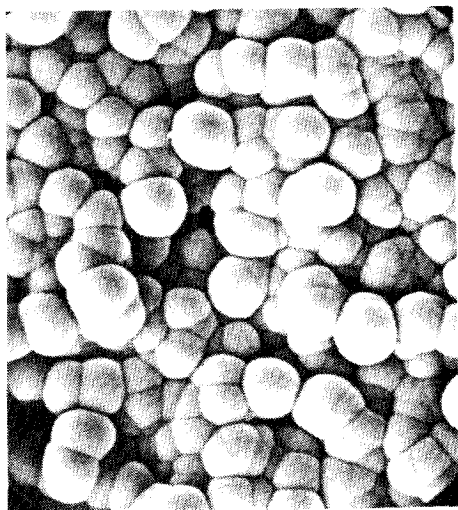
H ₂ /SiCl ₄ (mol/mol)	CH ₄ /SiCl ₄ (mol/mol)	T (K)	P (kPa)	deposited amount (g/g _{carbon})	T _{max} (K)	S _{BET} (m ² /g)	V _{pore} (ml/g)
170	1.8	1091	10	0.28 (Si)	945	431	0.23
170	1.8	1376	10	0.30 (SiC)	1025	176	0.12

The use of methane as an additional carbon source results in sole SiC deposition at a reaction temperature of 1375 K. Silicon deposition is encountered at lower temperatures. Activation of methane is probably the rate limiting step in the formation of SiC. An additional improvement (compared to the H₂-pretreated carbon) in oxidation resistance of 75 K has been achieved after reaction at 1375 K. The side crushing strength of this sample was 35.9±5.6 N, which is an improvement of a factor 1.7 compared to the original carbon.

4.4 CVD of SiC using CH₃SiCl₃ on activated carbon (CH₃SiCl₃ → SiC + 3 HCl).

After modification with methyltrichlorosilane above 1220 K, the extrudates and graphite substrate were covered with a shiny metallic grey film. X-ray diffraction showed deposition of stoichiometric β-SiC. SEM analysis revealed a cauliflower-like SiC morphology, as shown in Figs. 11 and 12, which is the typical SiC structure resulting from using this precursor under these conditions [30]. Deposition of SiC on graphite results in a more compact and dense layer than on activated carbon, which originates from the less rougher surface morphology. A crack in the SiC layer sometimes appears after prolonged deposition, which is caused by differences in expansion coefficients between graphite/activated carbon and SiC. Differences in nucleation can easily be identified from Fig. 12 and Fig. 14. The number of nucleation sites on activated carbon exceeds that of graphite as shown by the initially more grained structure of the first SiC deposited on activated carbon. The first phase of growth in a CVD process results in a thin microcrystalline layer of random orientation, imposed by the roughness of the substrate surface and barely limited growth of the first nuclei [42]. The influence of the substrate surface decreases at increasing layer thicknesses; a finely denticulated morphology is then formed, on top of which multi-star twin tips can be discerned. Owing to the extensive surface roughness of activated carbon, this grained SiC morphology remains visible even at substantial SiC layer thicknesses.

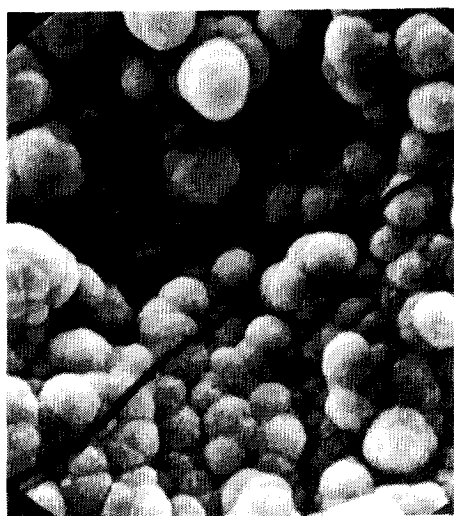
Chapter 4



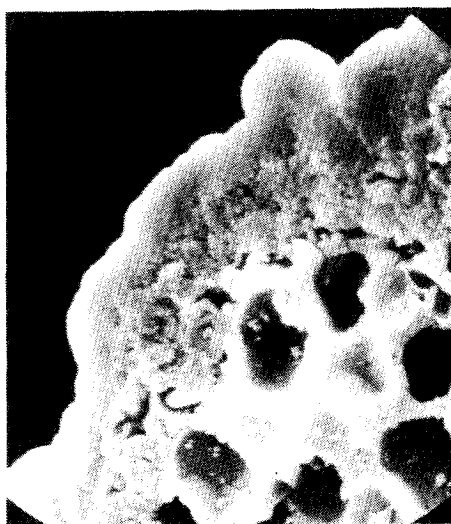
5 μm
Fig. 11. Surface of SiC deposited on a graphite plate



5 μm
Fig. 12. Side view of SiC deposited on a graphite plate



5 μm
Fig. 13. Surface of SiC deposited on activated carbon



5 μm
Fig. 14. Side view of SiC deposited on activated carbon

Modification of activated carbon by CVD of silicon carbide

4.4.1 Oxygen reactivity. The T_{max} of the modified extrudates varies between 985 and 1120 K, suggesting an additional increase in oxidation resistance of 35 to 170 K. The establishment of the exact position of the T_{max} is, however, difficult, owing to various maxima in the first derivative as displayed by Fig. 15. Four maxima in the range of about 950 to 1150 K can be distinguished for a heating rate of 0.167 K/s. The number of maxima decreases with decreasing heating rates (0.0167 and 0.00833 K/s), pointing to the limitation of oxygen diffusion into the extrudate during oxidation, rather than the existence of different SiC species causing an inhomogeneous carbon protection, which results in different onsets of oxidation.

4.4.2 Textural properties. Textural properties are of primary importance for utilizing these modified activated carbon extrudates as catalyst support. Table 5 displays the surface area and pore volume for several extrudates. For convenience, the data are also presented normalized to initial amount of carbon. This allows additionally the identification of the amount of surface area and pore volume lost solely by the weight increase due to SiC deposition.

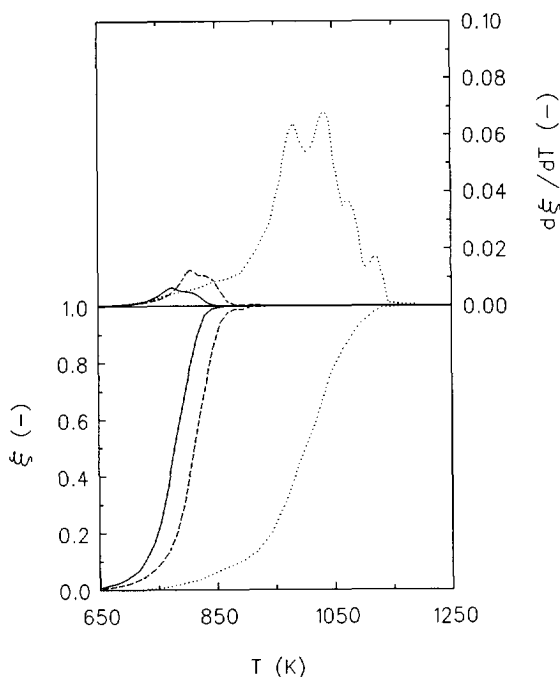


Fig. 15. Conversion and first derivative of a MTS modified carbon during TGA in air, heating rate: 0.00833 K/s (—), 0.0167 K/s (- -), and 0.167 K/s (···)

Chapter 4

Table 5. Textural properties of SiC-CVD modified activated carbon

conditions		textural properties							
T (K)	C_{MTS} (mmol/m ³)	S_{BET} (m ² /g, m ² /g _C)		V_{pore} (ml/g, ml/g _C)		S_t (m ² /g, m ² /g _C)		V_{micro} (ml/g, ml/g _C)	
1273 ⁽²⁾	100	532	729	0.33	0.46	49	67	0.23	0.32
1242 ⁽³⁾	102	533	712	0.33	0.44	53	71	0.23	0.31
1222 ⁽⁴⁾	104	512	672	0.31	0.41	44	58	0.23	0.30
1223 ⁽⁵⁾	42.6	576	712	0.37	0.45	60	74	0.25	0.31
1224 ⁽⁶⁾	140	510	712	0.31	0.43	45	63	0.23	0.32
1223 ⁽⁷⁾	69.8	571	714	0.35	0.43	47	59	0.26	0.33
1273 ⁽⁸⁾	134	471	670	0.28	0.40	38	54	0.21	0.30

The numbers in brackets refer to Fig. 16 and Table 7.

The surface areas (total and micro) and pore volumes (total and micro) after modification declined by around 50 percent of the initial value. Half of this decrease can be attributed to the weight increase due to SiC deposition. The remainder is probably caused by blocking parts of the porous structure.

4.4.3 Side crushing strength. Analysis of the strength of the modified activated carbon results in the 95% confidence regions of the side crushing strength (SCS) as displayed in Fig. 16. The extrudates are strengthened by an average factor of 1.4 after SiC-CVD modification. A direct relationship between the synthesis procedures and corresponding SCS is, however, difficult to obtain.

4.4.4 Kinetics of SiC deposition. The reaction rate of SiC formation has been determined by measuring the layer thickness of SiC deposited on the graphite substrates. The growth rate at 1222 K and 1273 K as a function of the MTS concentration is shown in Fig. 17. Fig. 18 displays the corresponding Arrhenius plot. The dependence of reaction rate on the concentration appears to be negligible in the parameter range investigated. A zero order dependence of the concentration on the reaction rate can be assumed based on Figs. 17 and 18.

Modification of activated carbon by CVD of silicon carbide

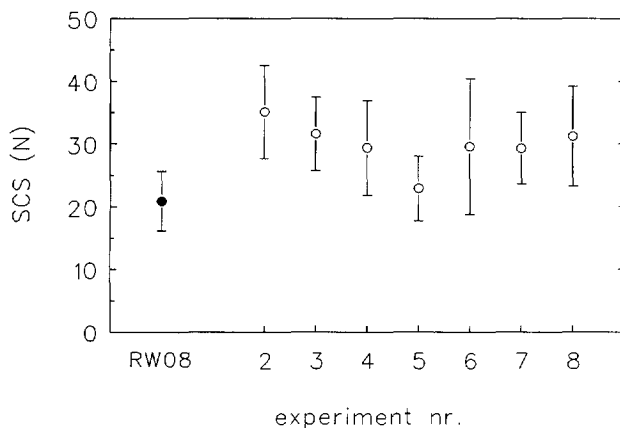


Fig. 16. Confidence regions (95%) of the side crushing strength (SCS) for various modified carbons. The experiment numbers refer to Table 5.

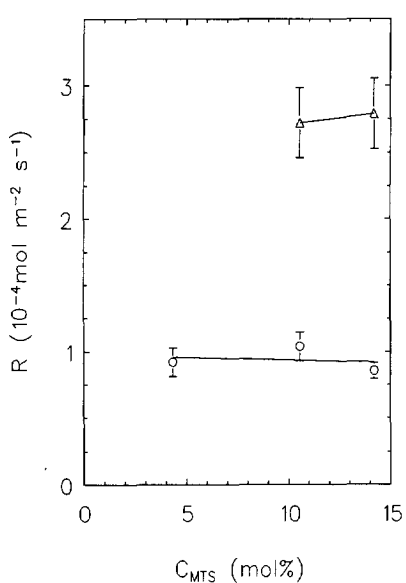


Fig. 17. Rate of SiC formation as a function of MTS concentration at 1223 K (○) and 1273 K (△). The lines are used to guide the eye.

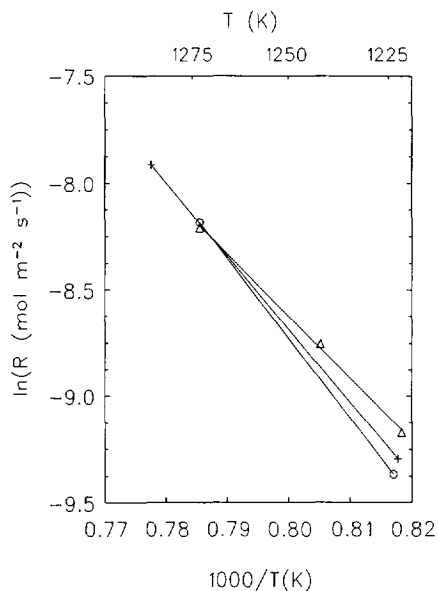


Fig. 18. Arrhenius plot for various MTS concentrations; 4.33 mol% (+), 10.5 mol% (△), and 14.2 mol% (○). The lines are used to guide the eye.

5. DISCUSSION

5.1 Evaluation of the catalyst support properties.

In the modification of activated carbon by SiC-CVD a compromise has to be met. First, the SiC layer has to be thick and dense, and uniformly deposited in the pores to ensure a considerable strength improvement, and to guarantee adequate protection against oxidation. Secondly, a sufficiently large surface area has to be available after modification for catalyst support applications. This means that the SiC layer has to be as thin as possible. This controversy should be born in mind when evaluating the various properties of the modified activated carbon. Reactive CVD is on first sight an elegant way to achieve both objectives. Here, the activated carbon acts as the carbon source for SiC formation. Hence, deposition of SiC is expected to be limited to the surface where carbon is exposed to SiCl_4 . Utilization of an additional gaseous carbon source (*e.g.* CH_4 , CH_3SiCl_3) can enhance the deposition rate. A selective deposition, however, cannot be obtained. In the section below, the influence of the pretreatment and modification technique on the oxidation resistance and mechanical strength will be discussed in detail. Heating activated carbon extrudates to the temperature for SiC deposition results in changes in the surface composition of the substrates. Comparison of the pretreatment in hydrogen and an argon-helium mixture results in comparable amounts of desorbed molecules, *viz.* 8.5 w% and 7.1 w%, respectively. The difference can be explained by the difference in final temperature, *i.e.* 1400 and 1273 K, respectively. The presence of hydrogen is expected to alleviate the decomposition of the oxygen containing surface groups (*e.g.* by termination of the dangling bonds which remain on the surface after decomposition). However, the total amount of desorbed molecules at temperatures above the synthesis temperature of the activated carbon (around 1300 K) is expected to be roughly similar in argon and hydrogen regarding the inertness of graphite in hydrogen environments. Two conclusions can be drawn from these observations. First, the amount of oxygen containing surface groups on activated carbon decreases significantly during heating to the temperature of deposition. This will substantially decrease the ASA and, hence, the oxygen reactivity. The T_{max} is elevated by 80 K compared with the untreated carbon. Additionally, since the formation of SiC is expected to start at surface defects (*i.e.* oxygen containing functional groups) in the graphite lattice, the number of nucleation sites for SiC growth will diminish as well. This might result in differences in the morphology of the SiC layer, and, thus the oxidation resistance. Secondly, desorption of CO starts at a temperature of 1050 K and just drops off after an isothermal period of one hour at 1273 K, which implies that the ASA is changing in the major part of the pretreatment trajectory. To achieve an identical starting material in all experiments, similar pretreatments are indispensable to assure the presence of identical amounts of oxygen containing functional

Modification of activated carbon by CVD of silicon carbide

groups and, hence, an identical oxygen reactivity and similar amounts of nucleation sites for SiC formation at the start of the experiment. These considerations have been the basis for utilizing the pretreatment procedure as described above.

Typical TGA profiles of all types of modification are displayed in Fig. 19. It is evident that, except for the MTS modification, the T_{max} represents a good parameter for the evaluation of the oxidation resistance. Oxidation of the MTS modified carbons results in an increased T_{max} , although the start of the oxidation is similar to that of the original carbon. This means that no real improvement in oxidation resistance has been achieved and that the increment in T_{max} originates from diffusion limitations of oxygen during oxidation.

5.1.1 Reactive CVD using SiCl_4 . RCVD at temperatures below 1400 K shows no significant increase in the T_{max} . In all cases considerable amounts of silicon are deposited which proves that RCVD is not a suitable technique for attaining improvements in the oxidation resistance.

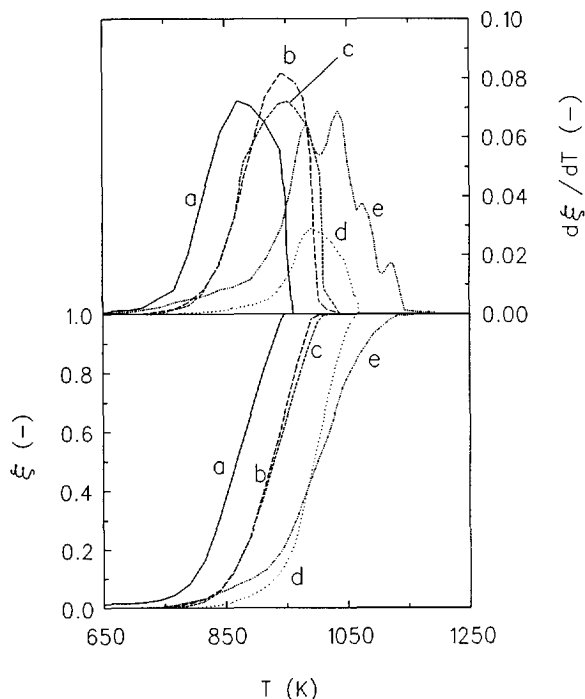


Fig. 19. Carbon conversion and first derivative of various modifications during TGA in air, heating rate 0.167 K/s, (a):RH08, (b): H_2 -pretreated, (c): SiCl_4 , (d): $\text{CH}_4/\text{SiCl}_4$, and (e): CH_3SiCl_3

Thermodynamically, silicon carbide deposition is found to be possible at temperatures above 800 K. Hence, it is concluded that SiC formation is kinetically controlled by the low reactivity of the activated carbon, resulting in silicon deposition.

5.1.2 CVD of SiC using a mixture of SiCl_4 and CH_4 . From the results presented above, it can be concluded that both objectives (improvement of oxidation resistance and mechanical strength) can simultaneously be achieved by SiC-CVD using a $\text{CH}_4/\text{SiCl}_4$ mixture at 1380 K. The oxidation resistance increases totally by 150 K (80 K for the pretreatment and 70 K by SiC deposition) with a concomitant side crushing strength improvement of a factor 1.7. The surface area of this material equals $176 \text{ m}^2/\text{g}$, which suffices for catalytic purposes. The decrease in S_{BET} originates mainly from blocking the micro-pore structure which implies that infiltration of SiC has been achieved. The results support the conclusion that this type of SiC deposition indeed lowers the oxygen reactivity and that the low reactivity of the activated carbon limits the SiC formation in the RCVD set-up.

5.1.3 CVD of SiC using CH_3SiCl_3 . Deposition of stoichiometric β -SiC has been achieved at 1200 K utilizing MTS as precursor. The oxidation resistance is, however, *reduced* compared to the H_2 -treated carbon. Curve d in Fig. 19 displays the early onset of oxidation, which might originate from the presence of hydrogen chloride (HCl) during deposition, which can restore a part of the ASA lost during the H_2 pretreatment. The side crushing strength improved by a factor 1.4. The deposition of SiC at the exterior of the particle has imposed diffusion problems for oxygen during oxidation, which resulted in multiple T_{max} values for one sample. The presence of this layer will undoubtedly aggravate the mass transfer inwards the particle, and thus limit the use as catalyst support at high temperatures.

5.2 Evaluation of the MTS-CVI technique.

MTS is a well known SiC precursor for the synthesis of SiC based composites, which allows evaluation of the modification in comparison with those reported in literature. No influence of MTS concentration on the reaction rate could be distinguished. It should, however, be noted that the number of these experiments is by far not sufficient to determine the crucial parameters of SiC deposition from MTS. However, qualitative trends can be determined. The reaction order with respect to MTS appears to be zero order, which is in accordance with the results obtained by Loumagne *et al.* [35]. The activation energy calculated from the Arrhenius plot amounts to $279 \pm 17 \text{ kJ/mol}$ with a pre-exponential factor of $7.26 \pm 0.64 \cdot 10^7 \text{ mol m}^{-2} \text{ s}^{-1}$. This activation energy is considerably higher than that reported by Loumagne *et al.*, *viz.* 160 kJ/mol . To explain this discrepancy, it is illustrative to display several kinetic expressions which have appeared in literature during the last decade (Table 6).

Modification of activated carbon by CVD of silicon carbide

Table 6. Reported kinetic models for SiC deposition from MTS

Experimental conditions			$k_0 \exp(-E_a/RT)C_{\text{MTS}}^n$		
T (K)	P (kPa)	H_2/MTS	n	E_a (kJ/mol)	Reference
1073 to 1373	100	0.5 to 1	1	120	Brennfleck <i>et al.</i> [33]
1250 to 1300	3.3	5 to 20	0	188	Besmann and Johnson [34]
1073 to 1373	20	0.7 to 4	1	255	Fitzer <i>et al.</i> [36]
1175 to 1225	5 to 10	1 to 5	0.1 to -1	160 ± 40	Loumagne <i>et al.</i> [35]
1075 to 1125	5 to 10	3 to 5	2.5	>300	Loumagne <i>et al.</i> [35]

The difficulty in kinetic modelling lies in the fact that SiC formation from MTS is governed by gas-phase decomposition reactions as well as by surface reactions. This means that the reactor geometry (*e.g.* the volume surface area ratio) and other experimental parameters like residence time of MTS in the hot zone of the reactor will influence the activation of MTS significantly. Gas-phase decomposition has been analyzed theoretically [32] and experimentally by Mass Spectrometry [31]. SiCl_4 , HCl , and CH_4 species are observed on decomposing MTS in hydrogen at 1428 K and 100 kPa. These results agree fairly well with the equilibrium pressures shown in Fig. 1. However, the way to extract information from these data establishing the active species in the SiC formation is ambiguous. It might be anticipated that MTS and a $\text{SiCl}_4/\text{CH}_4$ mixture show identical deposition characteristics. However, the SiC reaction rate and morphology from a $\text{SiCl}_4/\text{H}_2/\text{CH}_4$ and MTS/H_2 mixture differ significantly. Furthermore, compared to a $\text{SiCl}_4/\text{CH}_4$ mixture, the temperature necessary to deposit crystalline SiC is 200 K lower using MTS. This probably results from the gas phase formation of CH_3 radicals from MTS, which increases the reactivity of the carbon precursor.



Thus, stoichiometric SiC can be deposited at lower temperatures compared with the $\text{SiCl}_4/\text{H}_2/\text{CH}_4$ mixture. From this, it is evident that the rate of decomposition of MTS and reaction or recombination of radicals will have a major influence on the kinetics found for

Chapter 4

SiC deposition. This aspect of MTS as SiC precursor is one of the origins of disagreements between the kinetic models found by various authors, using different reactor set-ups.

The exact amount of SiC which is deposited inside the extrudates has to be estimated in order to assess the infiltration performance of the SiC-CVI procedure. The rate expression of SiC deposition based on the data given above is

$$R = 7.26 \cdot 10^7 \exp\left[\frac{-279000}{RT}\right] \quad (4)$$

Typical reaction rates are 1 to 4 nm/s at 1223 K and 1286 K, respectively. The polydisperse porous structure of activated carbon hampers the determination of a mean pore radius and, hence, (1) the pore closure time, (2) the amount of SiC deposited inside and outside the pores, and (3) the effective diffusion coefficient of methyltrichlorosilane. As a first rough estimate, the largest pores ($r=1000$ nm, $V_{pore}=0.6$ cm³/g) are assumed to determine the infiltration process. The smaller pores are supposed to be closed in the early stage of the infiltration process. The time necessary for pore closure of the 1000 nm pores is determined using eq. 4. SiC is deposited at the exterior of the extrudate in the remaining process period. The amount of SiC deposited after pore closure is subtracted from the total amount of deposited SiC. This yields the amount of SiC infiltrated in the porous structure. Subsequently, the residual porosity is calculated. The results are displayed in Table 7.

Table 7. Infiltration of SiC in activated carbon

experimental conditions				deposition characteristics		
exp. nr.	T (K)	C_{MTS} (mmol m ⁻³)	P (kPa)	$R \cdot 10^5$ # (mol m ⁻² s ⁻¹)	depos. amount (m _{SiC} /m _{carbon})	SiC infiltr. (%)
1	1286	40.5	10	36.5	0.224	21.3
2	1273	100	10	27.2	0.371	66.3
3	1242	102	10	15.8	0.336	81.3
4	1222	104	10	10.4	0.313	89.4
5	1223	42.6	10	9.2	0.236	88.7
6	1224	140	10	8.56	0.397	94.2
7	1223	69.8	5	7.33	0.250	93.4
8	1273	134	10	27.9	0.423	69.5

#: determined from SiC deposition on graphite

Modification of activated carbon by CVD of silicon carbide

The amount of deposited SiC varies between 0.22 to 0.42 $\text{g}_{\text{SiC}}/\text{g}_{\text{carbon}}$. No correlation is found between the reaction rate and total amount of SiC deposited on the carbon. The infiltration (SiC infiltr.) ranges from 21 to 94 % and improves for (a) decreasing temperatures and (b) increasing concentrations of MTS. The first effect is commonly encountered in CVI-processes; by reducing the reaction rate with respect to the diffusion rate, infiltration is enhanced, resulting in higher amounts of SiC in the pores. The second effect originates from the zero-order rate expression found for MTS. Increasing the MTS concentration does not affect the deposition rate of SiC. However, an increase in bulk concentration of MTS imposes a higher concentration gradient in the pore (and hence a higher diffusion rate). Moreover, depletion of MTS will occur at higher infiltration depths compared to lower bulk MTS concentrations.

To compare the influence of deposition conditions on the residual porosity, a plot of the residual porosity versus the Thiele modulus is applied. The Thiele modulus for a n^{th} order reaction is derived similar to the procedure described in [40]. The tortuosity is assumed to be 4 [39]. The gas-phase diffusion coefficient is taken from Sheldon and Besmann [17]. The total void fraction of the extrudates is derived from the He- and Hg densities given in Table 3, and equals 0.666. This results in a initial void fraction for pores with radii larger than 1000 nm ($V_{\text{pore}, r > 1000 \text{ nm}} = 0.6 \text{ ml/g}$, Fig. 4) of 0.40. The calculation of the surface area of this pore system is based on the pore volume of the region of the 1000 nm pores, *i.e.* 0.2 ml/g (Fig. 4), and equals 0.4 m^2/g . From these numbers the effective diffusion coefficients and the corresponding Thiele moduli are determined. For a full evaluation the Thiele moduli are to be related to the residual porosity of the extrudates. The residual porosity is defined in eq. 5.

$$\epsilon = \frac{(V_{\text{pore}, r > 1000 \text{ nm}})_{\text{final}}}{(V_{\text{pore}, r > 1000 \text{ nm}})_{\text{initial}}} \quad (5)$$

The results of the calculations are shown in Table 8.

Table 8. Thiele moduli and residual porosities for the MTS modified activated carbons

exp. nr.	1	2	3	4	5	6	7	8
φ	2.47	1.38	0.99	0.79	1.25	0.70	0.96	1.19
ϵ	0.97	0.87	0.85	0.85	0.89	0.80	0.88	0.84

A similar approach had previously been applied to the results of the mathematical modelling of Isothermal Chemical Vapour Infiltration [40]. The CVI process had been modelled as a transient process in which the pore geometry changes in time owing to the deposition of solids. The influence of various types of surface kinetics on the deposition profile and the porosity of the material after pore closure had been evaluated. A general correlation had thus been found between the residual porosity and the Thiele modulus, which was independent of the implemented kinetic model. This correlation or design chart is fitted by eq. 6 which is based on the equation that describes the relation between the effectiveness factor and Thiele modulus in heterogeneous catalysis.

$$\epsilon = 1 - \frac{3}{a \cdot \varphi} \left[\frac{1}{\tanh(a \cdot \varphi)} - \frac{1}{a \cdot \varphi} \right] \quad (6)$$

The constant a equals 20 ± 1 (95% confidence region) which shows that more stringent values of the Thiele modulus are needed to arrive at low residual porosities compared to reaching an effectiveness factor of one in the initial stage of the densification process. Fig. 20 displays the Thiele moduli and corresponding residual porosities of the experiments reported in Table 7 relative to the design chart. For comparison, data reported by Sheldon and Besmann [17] are included. Their results are obtained from the infiltration of a carbon fibre bundle with SiC. The average pore diameter of this preform ranges typically from 10 to 20 μm , which explains the considerably lower residual porosities achieved by these authors compared to those obtained for the modification of the activated carbon extrudates.

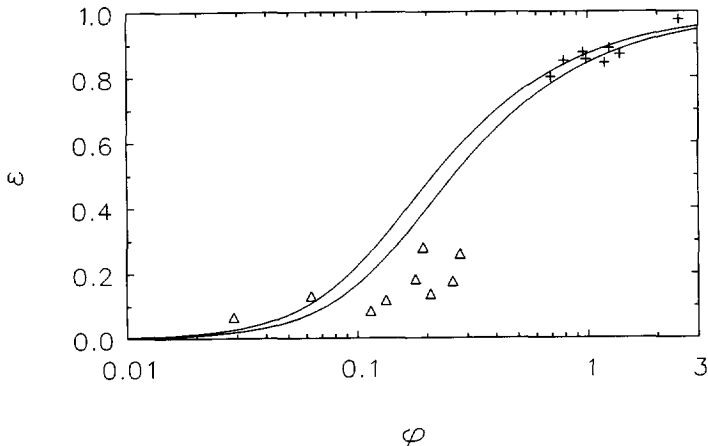


Fig. 20. The residual porosity (ϵ) vs. the Thiele modulus (φ) for data of Table 7 (+) and from [17] (Δ). The solid lines embody the 95% confidence region of the design chart [40]

Modification of activated carbon by CVD of silicon carbide

The theoretical design chart and experimentally obtained data display a good correlation for infiltrations in both low and high residual porosity regimes. This allows the use of Fig. 20 as a convenient pre-experimental design chart for optimization of CVI procedures. Numerical modelling and experimental validation are, of course, still indispensable for evaluating the process and the material produced.

6. CONCLUSION

Modification of activated carbon by SiC-CVD using $\text{SiCl}_4/\text{CH}_4$ results in improvements in oxidation resistance (up to 170 K) as well as in the side crushing strength (factor 1.7). The residual surface area is $176 \text{ m}^2/\text{g}$, which suffices for catalyst support applications. Additional advances require properties of the SiC layer to be deposited on the carbon surface which are conflicting to the characteristics necessary for catalyst support utilization, viz. a thin SiC coating to ensure the preservation of sufficient surface area. Selective deposition by reactive CVD cannot be achieved below 1400 K, silicon deposition has been encountered in all situations. Application of CH_3SiCl_3 (MTS) embodies the use of an additional gaseous carbon source. Here, SiC deposition and infiltration have been observed. The oxidation resistance did not improve; the side crushing strength enhanced by a factor 1.4. Utilization of these modified extrudates as catalyst support is feasible regarding their final specific surface area of $530 \text{ m}^2/\text{g}$. A zero-order relationship between the MTS concentration and the rate of SiC formation, the activation energy has been found to be 279 kJ/mol. The quantity of SiC deposited inside the extrudates ranges from 20 to 95% of the total amount deposited. Comparison of the residual porosity of the extrudates with an earlier mathematically developed Chemical Vapour Infiltration design chart shows good agreement.

SYMBOLS

a	fitting constant in eq. 6 (-)
ASA	active surface area
C_p	heat capacity ($\text{J mol}^{-1} \text{ K}^{-1}$)
D_{eff}	effective diffusion coefficient ($\text{m}^2 \text{ s}^{-1}$)
D_{gas}	diffusion coefficient in the gas phase ($\text{m}^2 \text{ s}^{-1}$)
D_{Knudsen}	Knudsen diffusion coefficient ($\text{m}^2 \text{ g}^{-1}$)
E_a	activation energy (kJ mol^{-1})
$\Delta_f H$	heat of formation (J mol^{-1})

Chapter 4

k	reaction rate constant ($\text{mol m}^{-3} \text{s}^{-1}$)
k_0	pre-exponential factor ($\text{mol m}^{-3} \text{s}^{-1}$)
L	characteristic diffusion length (m)
m	weight (kg)
m_0	initial weight (kg)
n	reaction order (-)
P	pressure (Pa)
R	reaction rate ($\text{mol m}^{-2} \text{s}^{-1}$)
S	absolute entropy ($\text{J mol}^{-1} \text{K}^{-1}$)
S_{BET}	surface area determined by the BET method ($\text{m}^2 \text{g}^{-1}$)
S_{ext}	external surface area of one extrudate (m^2)
S_v	specific surface area per unit volume ($\text{m}^2 \text{m}^{-3}$)
S_t	surface area determined by the t-method ($\text{m}^2 \text{g}^{-1}$)
SCS	side crushing strength (N)
T_{max}	temperature at maximum rate of oxidation during temperature programmed oxidation in air (0.167 K s^{-1})
V_{ext}	volume of one extrudate
V_{micro}	micro pore volume determined by the t-method ($\text{cm}^3 \text{g}^{-1}$)
V_{pore}	total pore volume ($\text{cm}^3 \text{g}^{-1}$)

Greek symbols

ϵ	residual porosity (-)
ξ	carbon conversion (-)
φ	Thiele modulus (-)
ρ	density (kg m^{-3})
τ	tortuosity (-)

REFERENCES

1. H. Jüntgen, *Fuel*, **65** (1986) 1436.
2. N.R. Laine, F.J. Vastola, and P.L. Walker, *J. Phys. Chem.*, **67** (1963) 2030.
3. N. Murdie, E.J. Hippo, and W. Kowbel, in *Proc. Carbon '88, Internat. Carbon Conf.*, (1988) p. 74.
4. P. Vast, G. Palavit, L. Montagne, J.L. Boulliez, and J. Cordier, in *Proc.*

Modification of activated carbon by CVD of silicon carbide

Carbon '88, Internat. Carbon Conf., (1988) p. 582.

5. S. Stegenga, M. van Waveren, F. Kapteijn, and J.A. Moulijn, *Carbon* **30** (1992) 577.
6. D.B. Stinton, T.M. Besmann, and R. Lowden, *Ceram. Bull.*, **67** (1988) 350.
7. H. Vincent, J.L. Ponthenier, L. Porte, C. Vincent, and J. Bouix, *J. Less Comm. Met.*, **157** (1990) 1.
8. J.E. Doherty, *J. of Metals*, **6** (1976) 6.
9. G.S. Fischman and W.T. Petuskey, *J. Am. Ceram. Soc.*, **68** (1985) 185.
10. C.D. Stinespring and J.C. Wormhoudt, *J. Cryst. Growth*, **87** (1988) 481.
11. Joon Ho Koh and Seong Ihl Woo, *J. Electrochem. Soc.*, **137** (1990) 2215
12. M.D. Allendorf and R.J. Kee, *J. Electrochem. Soc.* **138** (1991) 841.
13. A.I. Kingon, L.J. Lutz, P. Liaw, and R.F. Davis, *J. Am. Ceram. Soc.*, **66** (1983) 558.
14. H. Vincent, J.L. Ponthenier, C. Vincent, and J. Bouix, *Rev. Sci. Techn. Déf.*, **2** (1988) 89.
15. E. Fitzer, W. Remmele, and G. Schoch, in Proceedings of the 7th European Conference on CVD 1989, *Journal de Physique*, C5-209.
16. F. Christin, R. Naislain, and C. Bernard, In Proceedings of the 7th International Conference on CVD, T.O. Sedwick and H. Lydtin, eds., *The Electrochemical Society, Princeton 1979*, p. 499.
17. B.W. Sheldon and T.M. Besmann, *J. Am. Ceram. Soc.*, **74** (1991) 3046.
18. J. Bouix, M. Cromer, J. Dazord, H. Mouricoux, J.L. Ponthenier, J.P. Scharff, C. Vincent, and H. Vincent, *Rev. Int. Hautes Tempér. Refract., Fr.*, **24** (1987) 5.
19. S. Brunauer, P.H. Emmett, and E. Teller, *J. Amer. Chem. Soc.*, **60** (1938) 309.
20. J.H. de Boer, B.G. Linsen, and Th.J. Osinga, *J. Catal.*, **4** (1965) 643.
21. Tsutomu Kaneko, Takashi Okuno, and Hisami Yumoto, *J. Cryst. Growth*, **91** (1988) 599.
22. Tsutomu Kaneko, Takashi Okuno, and Isao Kabe, *J. Crystal Growth*, **108** (1991) 335.
23. A. Parretta, A. Camanzi, G. Giunta, and A. Mazzarano, *J. Mater. Sci.*, **26** (1991) 6057.
24. D.J. Cheng, W.J. Shyy, D.H. Kuo, and M.H. Hon, *J. Electrochem. Soc.*, **134** (1987) 3145
25. D.H. Kuo, D.J. Cheng, and W.J. Shyy, *J. Electrochem. Soc.*, **137** (1990) 3688.
26. F.J. Buchanan and J.A. Little, *Surf. Coat. Techn.* **46** (1991) 217.
27. J.M. Harris, H.C. Gatos, and A.F. Witt, *J. Electrochem. Soc.*, **118** (1971) 335.
28. M.W. Chase, Jr., C.A. Davies, J.R. Downey, Jr., D.J. Frurip, R.A. McDonald, and A.N. Syverud, JANAF, Thermochemical Tables, *J. Phys. Chem. Ref. Data*, **14** (1985).

Chapter 4

29. G. Erikson, *Chemica Scripta*, **8** (1975) 100.
30. F.J. Buchanan and J.A. Little, *Surf. Coat. Technol.*, **46** (1991) 217.
31. Y. Yehekel, S. Agam, and M.S. Dariel, in *Eleventh Intern. Conf. on CVD*, PV 90-12, K.E. Spear, Editor, The Electrochemical Society, Pennington, NJ (1990) p. 696.
32. M.D. Allendorf, C.F. Melius, and T.H. Osterheld, in *Twelfth Intern. Conf. on CVD*, PV 93-2, K.F. Jensen and G.W. Cullen, Editors, The Electrochemical Society, Pennington, NJ (1993) p. 20.
33. K. Brennfleck, E. Fitzer, G. Schoch, and M. Dietrich, *Nineth Intern. Conf. on CVD*, Mc D. Robinson et al., Editors, The Electrochemical Society, Pennington, NJ (1984) p. 649.
34. T.M. Besmann and M.L. Johnson, in *Proc. Int. Symp. on Ceramic Materials and Components for Engines*, V.J. Tennery, Editor, Amer. Ceram. Soc., Westerville, OH, 1989.
35. F. Loumagne, F. Langlais, and R. Naslain, Proc. of the 9th European Conf. on CVD, T. Mäntylä (ed.), 1993, p. 527.
36. E. Fitzer, W. Fritz, and G. Schoch, *High Temp. High Pres.*, **24** (1992) 343.
37. Internal report A8804, 1991, Norit Research Laboratory.
38. H. Jankowska, A. Swiatkowski, and J. Choma, Active Carbon, Ellis Horwood Series in Physical Chemistry, New York, 1991, p. 79.
39. C.N. Satterfield, *Heterogeneous Catalysis in Practice*, 2nd ed. McGraw Hill, New York, 1980.
40. R. Moene, J.P. Dekker, M. Makkee, J. Schoonman, and J.A. Moulijn, *J. Electrochem. Soc.*, **141** (1994) 282;
Chapter 2 of this thesis.
41. Perry's Chemical Engineers' Handbook, 6th ed., McGraw-Hill, New York, 1984, p. 2-85.
42. D.J. Cheng, W.J. Shyy, D.H. Kuo, and M.H. Hon, *J. Electrochem. Soc.*, **134** (1987) 3145.

Nickel-catalyzed conversion of activated carbon extrudates into high surface area silicon carbide by Reactive Chemical Vapour Deposition

ABSTRACT

A novel method for the synthesis of high surface area silicon carbide extrudates has been developed which consists of applying nickel onto activated carbon extrudates followed by reaction with silicon tetrachloride and hydrogen. Utilization of nickel is shown to be essential in order to obtain a considerable conversion. Selective SiC formation has been obtained at 1380 K and 10 kPa. Thus, methane is formed at the interior of the carbon *via* gasification: $C(s) + 2H_2(g) \rightleftharpoons CH_4(g)$, which subsequently reacts with silicon tetrachloride to silicon carbide: $SiCl_4(g) + CH_4(g) \rightleftharpoons SiC(s) + 4 HCl(g)$. The total carbon conversion ranges from 20 to 55 % for nickel contents of 2 and 8w%, respectively. Silicon co-deposition will occur when the gasification reaction diminishes in time due to deactivation of the nickel gasification sites. Extensive whisker formation of SiC is encountered owing to the operative Vapour Liquid Solid mechanism. Mass transport calculations show that methane is formed throughout the extrudate, whereas the front of SiC formation moves from the outside to the internal part due to diffusion limitations of $SiCl_4$ and nickel deactivation. The residual carbon can be removed after conversion by oxidation, resulting in high surface area SiC extrudates. The BET-surface areas after conversion vary from 359 to 154 m²/g; BET-surface areas after removal of the residual carbon are in the range of 57 to 32 m²/g. Pore-size distributions of the SiC supports show that the pore volume is evenly distributed over the meso- and macro-pore region (diameter: 2 to 100 nm) which allows the following areas of application (1) reactions at high temperatures and (2) liquid-phase reactions at demanding pH conditions.

1. INTRODUCTION

Catalysts based on activated carbon hold several advantages over silica and alumina based catalysts. Reaction between the support and the active material is limited to a large extent owing to the inertness of the graphitic surface. This can result in many cases in an optimal utilization of the metals applied. An example is the hydrodesulfurization of thiophene by supported cobalt molybdenum catalysts. Catalysts based on activated carbon display a higher activity per unit weight metal compared to Co-Mo/Al₂O₃ catalysts [1]. The same behaviour is found for Cu-Cr catalysts used in exhaust catalysis, *i.e.* high activities for the oxidation of CO and the reduction of NO have been reported for carbon based Cu-Cr catalysts [2]. The thermostability of activated carbon in inert environments at elevated temperatures is considerably higher than that of SiO₂ and Al₂O₃; up to 1700 K no significant sintering of the support is observed. Another benefit of activated carbon is its stability in caustic and acidic solutions. The use of activated carbon as catalyst support is limited despite these beneficial properties due to its reactivity in oxidizing environments and poor mechanical strength. Catalysts based on activated carbon are, therefore, predominantly applied in liquid-phase reactions at demanding pH conditions, in which the advantages (applicability at demanding pH conditions) prevail over the disadvantages (considerable attrition at high stirring rates). The mechanical strength of activated carbon can be improved by employing special types of manufacturing methods or by modifying activated carbon by deposition of silicon carbide (SiC) [3], a very hard and oxidation resistant material. Significant improvements in mechanical strength and the resistance against oxidation can be achieved by Chemical Vapour Deposition of SiC as well [4,5]. Synthesis of high surface area SiC, however, can render additional improvements that exceed those obtained by the surface modification of activated carbon. The last two decades much effort has been devoted to the development of high surface area non-oxidic ceramics [6-8]. It comprises mainly carbides, nitrides, and borides of transition metals, which possess interesting properties regarding their catalytic activity and stability. Research for the development of non-oxidic catalyst supports has mainly been focused on the preparation of high surface area (*i.e.* larger than 20 m²/g [9]) silicon carbide. The bulk properties of this material (an inert surface, high resistance against oxidation, and high mechanical strength) are claimed to provide a catalyst support with exceptional performance. Shaping of high surface SiC powder is expected to be laborious due to the low sinterability of the material. Utilization of a preformed precursor which exhibits good textural properties might resolve this obstacle. Conversion of activated carbon into SiC has potential in achieving high surface area SiC. Ledoux *et al.* [10] describe a method in which gaseous silicon monoxide (SiO) is reacted with activated carbon at 1400 K. Vannice *et al.* [11] describe the conversion of graphite powder into SiC by reacting it with SiCl₄ at temperatures

Nickel catalyzed conversion of activated carbon extrudates into high surface area silicon carbide

exceeding 1600 K. The combination of the advantageous aspects of both procedures might lead to a process, in which SiCl_4 is utilized at low temperatures. The stability of activated carbon in a hydrogen environment, however, limits its reactivity to SiC formation below 1600 K [4]. The application of catalysis for increasing the reactivity of the activated carbon may be the key for combining low temperature conversions with easily accessible reactants. In this chapter the influence of nickel on the conversion of activated carbon into high surface area SiC will be demonstrated. Both the chemical aspects regarding the carbon activation and SiC formation as well as the possible occurrence of mass-transfer limitations will be discussed.

2. EXPERIMENTAL

2.1 Materials.

Activated carbon extrudates RW08, a peat based, steam activated carbon has been supplied by Norit. To assure the application of well defined activated carbon, classification of the activated carbon extrudates of different degrees of activation has been carried out by fluidization of the extrudates in water for 2 hours. After settling the content of the column was separated in five layers of which the degree of activation increased from bottom to top. The middle fraction has been used and will be referred to as RW08. The properties of this fraction are shown in Table 1. $\text{Ni}(\text{NO}_3)_2 \cdot 6 \text{H}_2\text{O}$ (>99%) and silicon tetrachloride (>98%) were obtained from Janssen Chemica. The activated carbon extrudates (RW08) have been loaded with nickel by pore volume impregnation with a solution of $\text{Ni}(\text{NO}_3)_2$ in demineralized water to arrive at nickel contents of 2, 5, or 8 w%. Drying was performed at atmospheric pressure in air at 385 K. The gases were purified by passing them over a $\text{Cu}/\text{Al}_2\text{O}_3$ (argon) or $\text{Pd}/\text{Al}_2\text{O}_3$ (hydrogen) catalyst, followed by drying by molecular sieve 5A.

2.2 Conversion of activated carbon extrudates.

A schematic picture of the CVD apparatus is shown in Fig. 1.

Table 1. The physical properties of the activated carbon extrudates

S_{BET} (m^2/g)	V_{pore} (ml/g)	S_t (m^2/g)	V_{micro} (ml/g)	$\rho(\text{Hg})$ (kg/m^3)	$\rho(\text{He})$ (kg/m^3)	ash (w%)	length (mm)	diameter (mm)
947	1.05	112	0.41	661	2167	5.2	3.0	0.81

Chapter 5

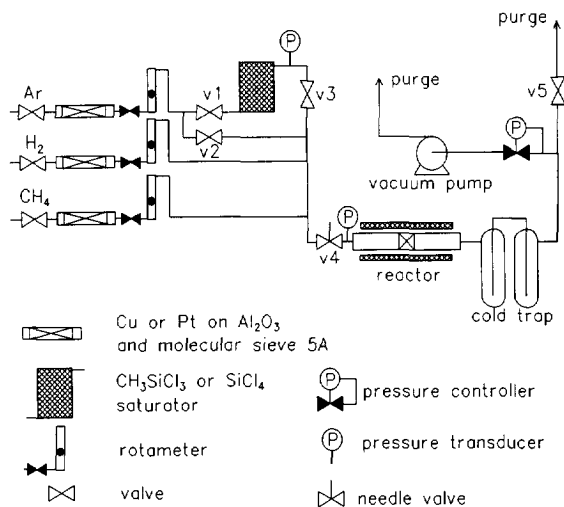


Fig. 1. Scheme of the CVD apparatus

A thin bed (length 1 mm) of dried extrudates (0.2 gram) is placed between two quartz wool pads in a tubular quartz reactor (ID 42 mm). The reactor is heated (0.167 K/s) under flowing hydrogen (0.18 mol/h) at 100 kPa to 1400 K and maintained at this temperature for 300 seconds. The reactor was subsequently cooled down to the desired reaction temperature. This procedure will be referred to as the pretreatment. The concomitant weight decrease for the 2w%, 5w%, and 8w% Ni/C systems was identical and amounted to 18 %. The hydrogen flow was then increased to 3.69 mol/h followed by pressure adjustment of the reactor to 8 kPa. Gaseous silicon tetrachloride (SiCl₄) or methyltrichlorosilane (MTS, CH₃SiCl₃) were introduced using argon as carrier gas, while the pressure of the saturator was kept constant at 100 kPa. The flow rates of SiCl₄ and CH₃SiCl₃ were determined using their Antoine equations [12,13] and amounted to 0.14 mol/h and 0.18 mol/h, respectively. After reaction the reactor was pressurized to 100 kPa and cooled down under flowing hydrogen to room temperature.

2.3 Removal of residual carbon.

The residual carbon, present after conversion, has been removed by oxidation in dry air at 1023 K in a tubular reactor.

2.4 X-Ray Diffraction (XRD).

X-Ray diffractograms of the extrudates were measured with a Philips powder

Nickel catalyzed conversion of activated carbon extrudates into high surface area silicon carbide

diffractometer (PW1840) using $\text{CuK}\alpha$ radiation (wavelength 0.154 nm).

2.5 Scanning Electron microscopy (SEM).

A JEOL (JSM-35) scanning electron microscope has been used to determine the morphology of the deposited phases. An acceleration current of 15 to 20 keV has been applied; the samples have been sputtered with gold or platinum to suppress charging during SEM analysis.

2.6 Thermal Gravimetric Analysis (TGA).

TGA has been carried out on a Stanton Redcraft (STA-1500) thermobalance. Samples (20 mg) were oxidized in air using a temperature increase of 0.167 K/s from room temperature to 1273 K. The weight change and concomitant heat flux were recorded simultaneously.

2.7 Surface area measurements.

Nitrogen isotherms at 77 K were recorded on a Carlo Erba Sorptomatic 1800 after degassing at 423 K and 0.1 kPa. The BET surface area, pore volume, t surface area, and micro-pore volume were determined according to literature [14,15].

3. RESULTS

3.1 Pretreatment.

The applied nickel nitrate decomposes during the pretreatment into NiO and NO_x . XRD profiles of the pretreated extrudates show that NiO is subsequently reduced to metallic Ni by hydrogen.

3.2 Nickel catalysis in the SiC formation utilizing SiCl_4 .

The influence of temperature on the nickel catalyzed SiC formation has been determined by XRD. Activated carbon extrudates loaded with 2w% Ni and reacted with H_2/SiCl_4 at 1075 K, 1250 K, and 1378 K have been analyzed. The results are visualized in Fig. 2. The XRD profile after reaction of SiCl_4 and H_2 with activated carbon in absence of nickel at 1380 K is incorporated as a reference (curve a). No bulk SiC deposition is observed in this case. It can be concluded from curves b, c, and d, that the presence of nickel at temperatures above 1250 K favours SiC formation. Silicon co-deposition, however, still appears in this system at all temperatures investigated.

Chapter 5

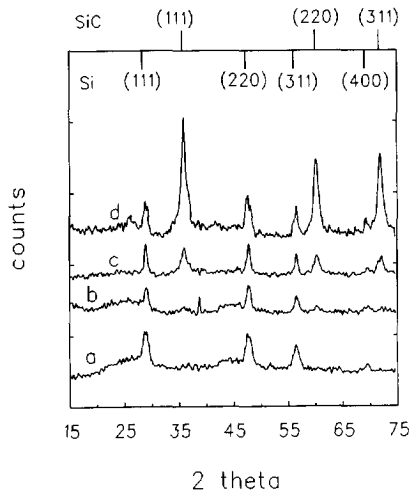
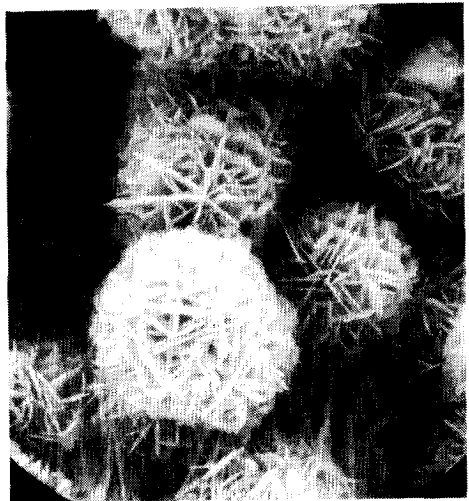


Fig. 2. XRD profiles of converted activated carbon, (a) without Ni-catalysis at 1380 K; (b), (c), and (d) 2w% Ni, 3600 s reaction, at 1075 K, 1250 K, and 1378 K, respectively



10 μm
Fig. 3. Secondary SiC growth on a SiC whisker
 $\text{H}_2/\text{SiCl}_4=26$, T: 1250 K, P: 8 kPa, t: 3600 s

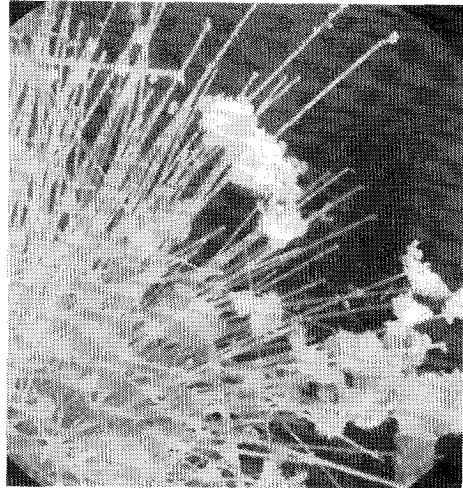


5 μm
Fig. 4. A cluster of SiC platelets, $\text{H}_2/\text{SiCl}_4=26$, T: 1250 K, P: 8 kPa, t: 3600 s

Nickel catalyzed conversion of activated carbon extrudates into high surface area silicon carbide



10 μm
Fig. 5. Bamboo-like SiC structures formed by densification of a cluster of platelets, $\text{H}_2/\text{SiCl}_4=26$, T: 1250 K, P: 8 kPa, t: 3600 s



15 μm
Fig. 6. Excessive whisker growth at the exterior of an extrudate, $\text{H}_2/\text{SiCl}_4=26$, T: 1380 K, P: 8 kPa, t: 3600 s

The SiC morphology has been analyzed by SEM as shown by Fig. 3 to 6. Fig. 3 displays the presence of SiC whiskers at the interior of the extrudate on which secondary nucleation developed. A SiC layer of 5 μm can be distinguished at the surface of the extrudate which consists of a cluster of SiC platelets as shown by Fig. 4. Bamboo-like SiC structures appear concomitantly (Fig. 5) of which the diameter equals that of the whiskers that are covered with platelets. Excessive whisker growth is encountered at the outside of the extrudate as well (Fig. 6). Insight in the origin of co-deposition of silicon after conversion at 1378 K can be achieved by XRD analysis of conversions at similar conditions with, however, a different time span of conversion and increased amounts of nickel applied. The results are displayed in Fig. 7. Selective SiC formation has been achieved after 600 seconds reaction for 2w% Ni and after 3600 seconds reaction, employing 5w% or 8w% Ni, respectively. SiC deposition is encountered as well on the quartz-wool pads downstream of the extrudates when 5 or 8w% Ni had been applied. A prolonged conversion time for the 5w% nickel loaded carbon results in Si co-deposition, similar to the situation in which a conversion time of one hour and 2w% Ni has been applied. A stage, which precedes SiC growth, is apparent after 600 seconds utilizing 8w% nickel as shown by two broad peaks around values of 2θ of 25 and 45, which originate from the activated carbon. The absence of detectable crystalline nickel is remarkable, because XRD detects in all cases nickel after the pretreatment of the nickel loaded carbon.

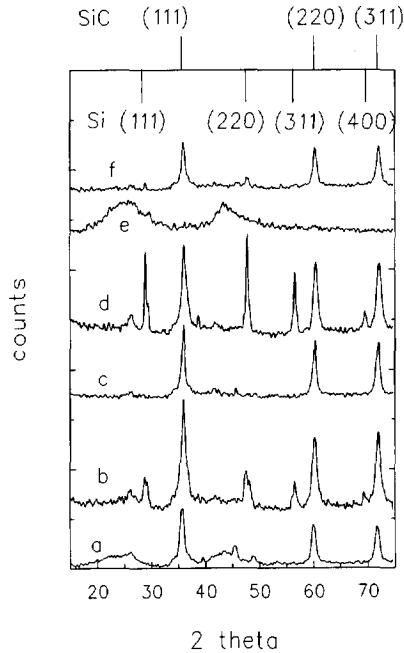


Fig. 7. XRD profiles of converted activated carbon 1378 K, (a) 2w% Ni, 600 s; (b) 2w% Ni 3600 s; (c) 5w% Ni, 3600 s; (d) 5w% Ni, 7200 s; (e) 8w% Ni, 600 s; (f) 8w% Ni, 3600 s

The following two processes, or a combination thereof, can account for this. Nickel either reacts with silicon tetrachloride in the initial stage to form an amorphous mixture Ni_xSi_y or re-disperses into very small nickel crystallites owing to the high temperature applied. This initial period shifts subsequently towards SiC formation (curve f). Micrographs of extrudates converted at 1380 K show the abundance of homogeneously distributed whisker growth throughout the extrudate (1 to 2 μm in length, 0.15 μm in thickness) after SiC formation. Small SiC granules (0.1 μm diameter) can be distinguished as well. The presence of these two SiC-morphologies points to the existence of two types of mechanisms operative in the SiC formation.

The influence of methane on the conversion is depicted in Fig. 8. Silicon carbide formation is achieved at 1380 K in the absence of nickel (curve 8^c). The use of methane in the absence and presence of nickel has resulted in a minor co-deposition of silicon as shown by diffractogram 8^b and 8^c, respectively. Peak broadening in curve 8^b implies the presence of a SiC structure with a higher stacking-fault density than that grown in the absence of additional CH_4 . Micrographs of the SiC structure formed from a $\text{SiCl}_4/\text{CH}_4$ mixture in the presence of nickel are shown in Fig. 9 and 10.

Nickel catalyzed conversion of activated carbon extrudates into high surface area silicon carbide

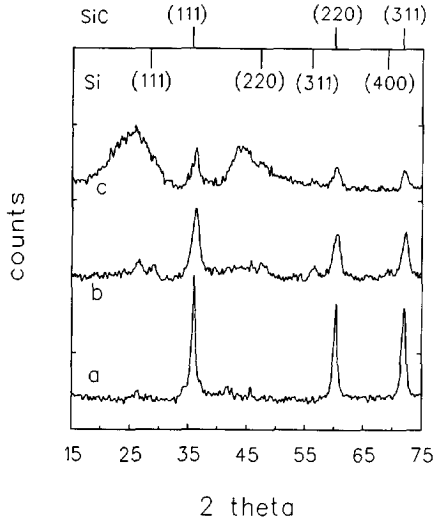
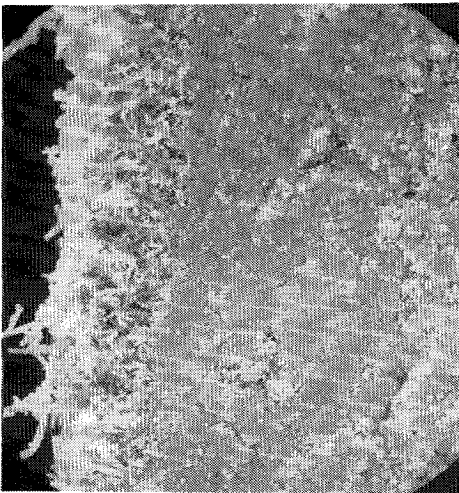
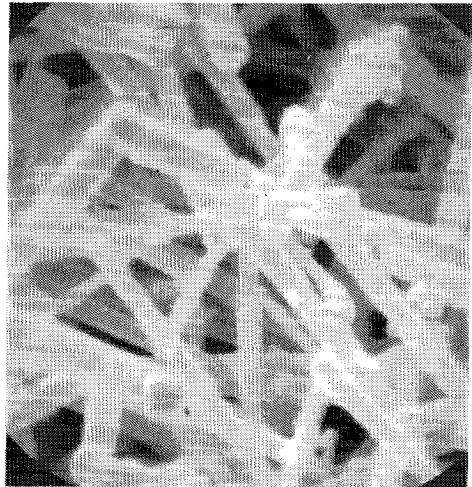


Fig. 8. XRD profiles, $H_2/SiCl_4=26$, reaction time 3600 s, 1380 K, (a) 5w% Ni; (b) 5w% Ni, $CH_4/SiCl_4=2$; (c) no nickel, $CH_4/SiCl_4=2$



10 μ m

Fig. 9. SiC whisker growth at the surface and substantial densification owing to methane addition



1 μ m

Fig. 10. Whiskers at the exterior of an extrudate as a result of added methane

Chapter 5

Extensive whisker growth is observed at the exterior of the extrudates. The whiskers are longer and thicker (0.2 to 0.5 μm) compared to those obtained in the absence of additional methane. The interior of the extrudate is densified to a large extent; SEM-analyses of several extrudates suggest the presence of a density gradient moving from the outside to the less denser inside.

Conversion of the carbon extrudates into SiC results in a weight increase owing to the deposition of silicon. Measuring this weight increase in combination with the amount free carbon present in the system permits the determination of a carbon and silicon mass balance. Table 2 displays the conversion conditions and corresponding weight increase. The second last column (Δw conv.) represents the weight increase after conversion of the carbon corrected for the weight loss during the pretreatment. The last column (w depos.) embodies the residual mass after oxidation of the non-converted carbon amended for the ash content of the carbon including the applied nickel. This represents thus the amount of deposited silicon carbide and silicon. It is shown that moving from reaction temperatures of 1075 K to 1378 K causes an increase in the quantity of deposition when 2w% Ni has been employed. An additional enlargement is achieved at higher nickel amounts and longer deposition periods. The weight increase after one hour conversion is largest at the investigated reaction conditions when 5w% nickel has been applied.

Table 2. Characteristics of conversion of activated carbon extrudates, $\text{H}_2/\text{SiCl}_4=26$, $P=8$ kPa

exp. nr.	Ni cont. (w %)	T (K)	t (s)	Δw conv. [#] (%)	w depos. [@] (%)
1	2	1075	3600	23.3	25.9
2	2	1250	3600	42.5	33.3
3	2	1378	3600	57.6	42.8
4	2	1376	600	31.7	29.0
5	5	1383	3600	67.8	54.4
6	5	1379	7200	75.2	55.9
7	8	1373	600	20.8	39.6
8	8	1379	3600	55.5	54.8
9 [§]	5	1379	3600	82.5	44.8

[#] Δw conv. = $(w_t / (w_0 - w_{\text{gasif.}})) * 100\%$

[@] w depos. = $(w_{\text{SiC}} + w_{\text{Si}} - w_{\text{ash}}) / (w_{\text{SiC}} + w_{\text{Si}} + w_{\text{ash}} + w_{\text{C}}) * 100\%$

[§] methane added ($\text{CH}_4/\text{SiCl}_4=2$)

*Nickel catalyzed conversion of activated carbon extrudates into
high surface area silicon carbide*

The residual mass after oxidation is, however, identical to that when 8w% Ni has been applied, after 3600 s deposition time.

3.3 Catalyst properties.

The extrudates converted at 1250 K and 1380 K remain intact after removal of the non-converted carbon by oxidation. The shape memory concept can thus be applied by using preshaped carbon bodies in order to synthesize shaped SiC.

The nitrogen isotherm at 77 K has been used to evaluate the texture and thus the potential of this support in catalysis. The BET method and the t-method then give the total surface area, the meso-/macro-pore surface area, and the micro-pore volume. The results are shown in Table 3. A distinction is made between the converted carbon prior to and after removal of the residual carbon. Pretreatment in hydrogen of a nickel loaded activated carbon results in a small increase in surface area (BET and t) and micro-pore volume owing to the gasification, which takes place during the pretreatment. The surface area after conversion has been reduced from 981 m²/g to values between 395 and 154 m²/g; the pore volume decreases from 0.67 ml/g to a value between 0.18 and 0.27 ml/g. These changes can predominately be ascribed to a decrease in micro-pore surface area and pore volume, showing that the micro-pore structure is blocked during conversion.

Table 3. Texture of SiC supports synthesized by carbon conversion at 1380 K and 8 kPa.

Material		S_{BET} (m ² /g)	V_{pore} (cm ³ /g)	S_t (m ² /g)	V_{micro} (cm ³ /g)
RW08		947	0.60	112	0.41
2w% Ni/RW08	pretreated	981	0.67	115	0.44
2w% Ni/RW08*	converted	395	0.22	215	0.10
	oxidized	57	0.37	57	0
5w% Ni/RW08*	converted	154	0.21	58	0.027
	oxidized	32	0.21	31	0
8w% Ni/RW08*	converted	189	0.18	88	0.041
	oxidized	36	0.15	33	0
5w% Ni/RW08**	converted	270	0.27	77	0.091
	oxidized	48	0.29	43	0

* H₂/SiCl₄=26, reaction 3600 s

** H₂/SiCl₄=16, reaction 3000 s

4. DISCUSSION

Several characteristics of the catalyzed carbon conversion emerge from the results described above. First of all, the optimal temperature when utilizing nickel as catalyzing species is established by XRD to be around 1380 K. Moreover, higher nickel contents seem to improve the conversion properties of the system. To gain full insight in the occurring mechanism, however, elaboration of these observations regarding the chemical aspects and mass-transfer considerations of the process are indispensable.

4.1 Chemical aspects.

SEM analysis of extrudates containing 2w% Ni which are converted at 1075 K displays the presence of small SiC granules of 0.3 μm diameter. The amount of deposited material and morphology of this system is comparable to that of modified activated carbon by methyl-trichlorosilane and nickel catalysis at 1073 K. The deposition of SiC on the quartz-wool pads at temperatures of 1380 K outside the extrudates suggests additionally that the carbon species which is active in the formation of SiC, utilizing SiCl_4 as silicon precursor, has been supplied *via* the gas phase. Formation of gaseous carbon species can be achieved according to the well known hydro-gasification of solid carbon as shown in Table 4. SiC deposition then ensues *via* the second reaction. Silicon formation will be encountered as a consequence of the reduction of SiCl_4 by hydrogen. The values of the enthalpy, entropy, and free Gibbs energy of reaction 1, 2, and 3, calculated from the Janaf thermochemical tables [16] are shown in Table 4 for the optimal SiC formation conditions, *i.e.* 1400 K and 10 kPa.

4.1.1 Hydro-gasification of carbon. Hydro-gasification at 1400 K and 10 kPa is thermodynamically not favoured as shown by the positive ΔG . The maximum equilibrium amount of methane formed under reaction conditions is 0.4 mol%. This explains that hydro-gasification at these conditions is feasible, though not favoured by thermodynamics. In general, two classes of hydro-gasification catalyzed by group VIII metals can be distinguished.

Table 4. ΔH , ΔS , and ΔG for the reactions during SiC synthesis at 1400 K and 10 kPa

	Reaction	ΔH (kJ/mol)	ΔS (J/(mol K))	ΔG (kJ/mol)
1	$\text{C} + 2 \text{H}_2 \rightleftharpoons \text{CH}_4$	-92.31	-136.8	99.18
2	$\text{SiCl}_4 + \text{CH}_4 \rightleftharpoons \text{SiC} + 4 \text{HCl}$	297.1	298.9	-121.4
3	$\text{SiCl}_4 + 2 \text{H}_2 \rightleftharpoons \text{Si} + 4 \text{HCl}$	277.6	169.6	40.08

*Nickel catalyzed conversion of activated carbon extrudates into
high surface area silicon carbide*

The first one, typically encountered at temperatures below 800 K, consists of dissociative adsorption of hydrogen on the metal surface and subsequent spill-over of H atoms to the graphite zones where methane production takes place [17]. The second class involves dissolution of carbon at the Ni-C interface, diffusion of carbon in Ni, and reaction of carbon with chemisorbed hydrogen at the Ni-gas interphase [18,19]. This mechanism develops at temperatures above 800 K and is probably operative in the described conversion of activated carbon.

4.1.2 Silicon carbide formation. XRD analysis has shown that conversion at 1250 K results in an considerable amount of SiC formed. The angle between the platelets present at the surface of the extrudate (70°) corresponds very well with values reported by Knippenberg for twinning in β - and α -SiC ($70^\circ 33'$) [20]. These dendritic crystals originate from secondary nucleation of SiC on long whiskers at the outer part of the extrudate as shown by Fig. 3. These branches form a skeleton which is filled up by continuous deposition between the platelets as displayed in Fig. 4. The thickness of these platelets ($0.1 \mu\text{m}$) corresponds well to that of the whiskers. Consecutive growth finally results in bamboo-like structures as shown by Fig. 5, which on their turn can be branched as well. The outlined mechanism is in agreement with the SiC growth phenomena described by Knippenberg [20]. At the interior of the extrudates SiC-granules ($0.3 \mu\text{m}$ diameter) are formed as well.

Carbon conversion at 1378 K results in the formation of large amounts of SiC as is shown by the X-ray diffractograms in Fig. 2. The substantial increase originates primarily from the catalyzed SiC whisker growth by the Vapour Liquid Solid (VLS) mechanism. Excessive whisker growth is visible throughout the entire extrudate. Fig. 6 is an example of a whisker explosion, which has probably been nucleated by a large nickel crystallite. The VLS mechanism has been introduced by Wagner and Ellis in 1964 [21] and has successfully been applied in whisker syntheses. Prior to their report the model proposed by Sears [22] assumed that whisker growth was initiated by a screw dislocation at the top of the growing crystal. Molecules that adsorbed at the whisker surface either diffused to the top of the whisker and would be incorporated in the crystal round the screw axis or desorb. This model left, however, much unclarified. Furthermore, only a few materials, like palladium, exhibited a screw dislocation at the top of the whisker [23]. The research of Wagner and Ellis was focused on the growth of silicon whiskers by the reduction of SiCl_4 by hydrogen at 1323 K and the influence of certain impurities thereof. They reported that (1) silicon whiskers do not contain an axial screw dislocation at the top of the Si-whisker, (2) the presence of certain impurities are indispensable for whisker growth, and (3) a liquid-like globule is present at the tip of the whisker during growth. The impurity (in their case gold) forms under reaction conditions a liquid droplet which acts as a preferred site for adsorption of the gaseous Si-

precursor. The surface of this droplet can be considered as atomically rough; this situation is similar to that of a (111) surface on which every surface site resembles an attractive growth site, which is attended by a high accommodation coefficient or sticking coefficient. Besides the adsorption process at the V-L surface (and concomitant chemical reactions), two other processes are of importance in the VLS mechanism, *i.e.* diffusion through the liquid droplet and incorporation of atoms in the crystal at the L-S interface. In principle, each of these processes can be the rate limiting step, but in most cases the incorporation of atoms in the crystal is considered to be rate limiting.

Growth of SiC whiskers can be catalyzed by several metals. Bootsma *et al.* [24] reported the use of iron in the system $\text{SiO}_2/\text{C}/\text{H}_2$ at 1473 to 1573 K. Heating to 1473 K resulted in the formation of Fe-Si-C droplets. The droplet diameters vary in the same range as the initially applied Fe particles (1 to 40 μm). These Fe-Si-C droplets are formed by taking a small amount of the substrate into solution, forming a shallow etch pit. After saturation with SiC, the etch pit is refilled by SiC growth and the alloy is lifted upwards. This process is typical for situations in which the substrate consists of one of the constituents of the whisker. Motojima and Hasegawa [25] grew β -SiC whiskers utilizing a gas mixture containing Si_2Cl_6 , CH_4 , H_2 , and Ar. Several metallic components (group VIIIa of the periodic system according to IUPAC) have been investigated for their catalytic effect on whisker growth. The following sequence was established in which the catalytic effect ranges from strongly positive to zero; $\text{Co} > \text{Ni} > \text{Cu} \approx \text{Cr} \approx \text{Au} > \text{Mn}$. Especially cobalt and nickel were shown to be very effective catalysts. The velocity of whisker formation is found to be in the order of several millimetres per hour, which is common for whisker growth, but high for conventional CVD processes. The minimal temperature for Co catalyzed whisker growth from Si_2Cl_6 is reported to be 1300 K. Nickel catalyzed growth with SiCl_4 as Si precursor is shown to be the best combination in the parameter area investigated. SiC whiskers were formed above 1363 K, whereas the use of cobalt necessitates temperature above 1443 K. The observations regarding the nickel catalyzed whisker growth are in agreement with the results attained in the conversion of activated carbon into SiC; substantial SiC formation is found at 1378 K.

4.1.3 Silicon co-deposition. The X-ray diffractograms sometimes display the presence of crystalline silicon. The point at which this co-deposition starts shifts to longer durations of conversion for higher nickel loadings (*e.g.* 3600 s for 2w% Ni and 7200 s for 5w% Ni). Silicon co-deposition can be attributed to deactivation of the nickel catalyst which takes part in the catalytic hydro-gasification of the carbon. Reaction with the ash of the carbon, contamination of nickel by dissolution of some silicon, or encapsulation by deposited SiC, are most likely the causes of deactivation. Thus, the concentration of gaseous carbon species in the extrudate diminishes, resulting in Si co-deposition. Chin *et al.* [26] decomposed CH_3SiCl_3 (MTS) to form SiC and report that the transitions between the zones of

Nickel catalyzed conversion of activated carbon extrudates into high surface area silicon carbide

stoichiometric SiC deposition and silicon co-deposition encountered on the substrate were not sharp but showed a gradual change in Si:C ratio in the deposits as the process parameters varied. X-ray diffraction displayed the presence of large amounts of Si, while electron probe micro analysis revealed an average composition of $\text{Si}_{1.18}\text{C}$. The excess silicon is incorporated in the SiC structure as small crystals as shown by Minatu *et al.* [27]. Free silicon is seen as small white spots in optical micrographs, which decrease in size and number at higher deposition temperatures. Silicon is reported to be invisible by SEM analysis. The addition of methane [28] or propane [29] to CH_3SiCl_3 generally results in less extensive Si formation. Stoichiometric SiC is then deposited at 1600 K (for CH_4) and 1473 K (for C_3H_8) using C/Si ratios of 2. A C/Si ratio of 3.4 is necessary at 1473 K to deposit SiC from a $\text{CH}_4/\text{CH}_3\text{SiCl}_3$ mixture. These reported observations are valid for H/Si ratio greater than 100. The use of lower H/Si ratios is expected to lower the necessary temperature or C/Si reactant ratio [4] in order to achieve stoichiometric SiC. The reason of silicon deposition during carbon conversion is thus to be conceived as methane deficiency during SiC deposition, imposed by the deactivation of gasifying nickel. The extent of deactivation increases with increasing conversion time, the C/Si ratio drops simultaneously, which causes at a certain moment the formation of free Si during SiC growth.

The addition of methane during carbon conversion results in minor Si-deposition as shown by XRD (Fig. 8), extensive densification, and the formation of a more extensive micro-grained SiC structure. The Si co-deposition can be rationalized by the fact that the relative extent of non-catalyzed SiC formation increases, which enlarges the number of stacking faults during SiC growth causing the co-deposition of Si in the SiC structure.

It can thus be concluded that silicon is co-deposited during SiC growth with a deficiency of gaseous carbon species, rather than an abrupt shift from SiC to Si deposition at the end of the conversion procedure.

The next section deals with the evaluation of the possible presence of mass-transfer limitations during the conversion of activated carbon into SiC.

4.2 Mass transport phenomena.

Kinetic measurements in catalytic studies are often disguised by mass-transport limitations of the reactants or products. Very fast surface reactions result thus in severe concentration gradients inside the catalyst pellet. These gradients in turn can impose the formation of external diffusion limitations. Both types of mass-transfer limitations are well known in the field of catalysis and Chemical Vapour Deposition. Obvious instances of internal mass-transport limitations can be found in the field of Chemical Vapour Infiltration [30]. Chemical Vapour Deposition on flat surfaces can suffer from mass-transport limitations as well.

Concentration gradients present in the diffusion layer around the surface can determine to a large extent the morphology of the deposits. Diffusion limited growth will result in deposits containing voids and a rough surface morphology owing to the enhancement of surface fluctuations during deposition. Kinetically controlled processes, however, will cause the formation of smooth surfaces. With the aid of thermal gravimetric analysis (TGA) the reaction rate of CH_4 and SiC formation has been determined. These figures are used to investigate the possible existence of diffusional limitations in this system of carbon conversion. Fig. 11 shows the overall rates of CH_4 and SiC formation for carbon conversions of 3600 s utilizing 2w%, 5w%, and 8w% Ni on carbon. The values given in Fig. 11 are average rates of the entire conversion period. Similar rates of formation of CH_4 and SiC are found for the carbon containing 2w% Ni. Both reaction rates increase with increasing amounts of nickel. The formation of methane is, however, enhanced to a larger extent. This process will cause higher carbon conversions but incomplete conversions of methane into silicon carbide as shown by Fig. 12. The observations described above seem to disagree with the thermodynamic calculations (Table 4). The subsequent reaction of methane with silicon tetrachloride to form silicon carbide is expected to consume the total amount of methane present in the pores of the extrudates. This effect can either have a kinetic or mass-transfer origin. The first is not likely to occur, because it would implicate that, when the total nickel content is increased, the amount of nickel responsible for the gasification increases to a larger extent than the amount of nickel which catalyzes the VLS growth of SiC. Mass-transport limitations, however, are to be expected in the experiments described above, owing to the high reaction rates encountered when the VLS mechanism is operative.

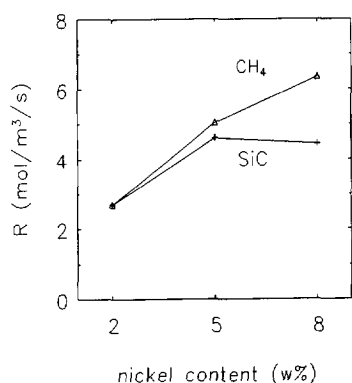


Fig. 11. Reaction rates for SiC and CH_4 formation as a function of nickel content, 3600 s reaction

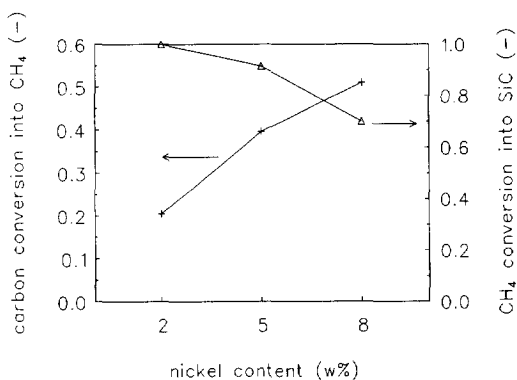


Fig. 12. CH_4 selectivity (+) and carbon conversion (Δ) as a function of the nickel content.

*Nickel catalyzed conversion of activated carbon extrudates into
high surface area silicon carbide*

Internal diffusion limitations are easily evaluated utilizing the Wheeler-Weisz number, which is the product of the effectiveness factor and the square of the Thiele modulus. This number can be calculated using observable quantities according to equation 1 [31].

$$\eta\varphi^2 = \frac{R_{obs}L^2}{D_{eff}C_b} \quad (1)$$

where η is the effectiveness factor, φ is the Thiele modulus, R_{obs} is the observed reaction rate in mol/s, L is a characteristic diffusion length (V_{pore}/A_{pore}), D_{eff} is the effective diffusion coefficient, and C_b represents the concentration of the diffusing species in the gas phase.

The effectiveness factor is close to one in the absence of internal mass-transfer limitations which results in the following criterion for those conditions:

$$\eta\varphi^2 < 0.15 \quad (2)$$

The effective diffusion coefficient is determined concordant the procedures given in chapter 2.

External concentration gradients can be observed in the presence of internal diffusion limitations. The Carberry number (Ca) is convenient for the evaluation of the magnitude of these gradients. It represents the relative concentration difference over the film around the particle and is calculated according to eq. 3.

$$Ca = \frac{R_{obs}}{k_g a' C_b} \quad (3)$$

where k_g is the mass transfer coefficient and a' is the specific area per unit volume (A_p/V_p). A relative concentration difference of 5% over the film (*i.e.* $Ca < 0.05$) is assumed to be the criterion from which external diffusion limitations are significant. For low Reynolds numbers ($5 < Re < 500$) the mass transfer coefficient can be determined from the following correlation in which the Stanton (St) and Schmidt (Sc) number are used [33].

$$St \cdot Sc^{2/3} = (0.81 \pm 0.05) Re^{-0.5} \quad (4)$$

with

Chapter 5

$$\text{St} = \frac{k_g \epsilon_b}{U_f} \quad \text{Re} = \frac{\rho_f U_f d_p}{\eta_f} \quad \text{Sc} = \frac{\eta_f}{\rho_f D_g} \quad (5,6,7)$$

where ρ_f denotes the density of the gas, ϵ_b is the porosity of the bed, U_f is the superficial gas velocity, d_p is the particle diameter, and η_f represents the viscosity of the gas.

The following conditions (Table 5) are used as an example in the determination of mass transfer limitations. The density and viscosity of hydrogen are assumed to be representative for the total gas mixture which consists of at least 80 mol% H₂. Silicon tetrachloride has been assumed to represent the major abundant gaseous Si species. The reaction rates of methane and silicon carbide formation in the conversion of 2w% Ni/C have been used to evaluate the possible presence of internal and external diffusion limitations.

Table 5. Numerical values applied in the calculations

Reactor				
temperature	T	1378	K	
pressure	P	10	kPa	
bed length	L _b	0.8·10 ⁻³	m	
bed porosity	ε _b	0.4	m ³ _{gas} m ⁻³ _{reactor}	
bed diameter	d _b	0.04	m	
support properties				
mean radius micro pore	r _{mi}	0.6	nm	
mean radius meso pore	r _{me}	10	nm	
mean radius macro pore	r _{ma}	400	nm	
tortuosity	τ	4	m ² _{gas} m ⁻² _{particle}	
porosity	ε _p	0.7	m ³ _{gas} m ⁻³ _{particle}	
input gas (at reactor conditions)				
flow	φ _f	2.21·10 ⁻⁶	kg s ⁻¹	
space velocity	U _f	1.04	m s ⁻¹	
density	ρ _f	1.7·10 ⁻³	kg m ⁻³	
viscosity	η _f	2.4·10 ⁻⁵	Pa s	
specific heat	C _p	15.93	J kg ⁻¹ K ⁻¹	

*Nickel catalyzed conversion of activated carbon extrudates into
high surface area silicon carbide*

Table 6. Mass transfer characteristics for H₂ and SiCl₄ in the conversion of extrudates containing 2w% Ni

	diffusion coefficients (10 ⁻⁶ m ² /s)			dimensionless numbers	
	SiCl ₄	H ₂		SiCl ₄	H ₂
D _{eff, mi}	0.03	0.27	Re	0.05	0.05
D _{eff, me}	0.48	4.4	Sc	2.6	0.97
D _{eff, ma}	19	170	St	1.9	3.7
	Wheeler Weizs			Carberry	
	SiCl ₄	H ₂		SiCl ₄	H ₂
$\eta\phi^2_{mi}$	1106	9.4	k _g	5	10
$\eta\phi^2_{me}$	66	0.60	Ca	<0.05	<0.05
$\eta\phi^2_{ma}$	1.7	0.01			

Internal mass-transfer limitations are evaluated depending on the pore dimensions of the carbon. In general, a tri-modal pore distribution is encountered in activated carbon which imposes the necessity of considering micro-, meso-, and macro-pores independently for the estimation of internal diffusion limitations. The results of applying the values of Table 5 for the calculation of the transport properties are displayed in Table 6. Calculation of the effective diffusion coefficients reveals that internal mass transport is in all cases primarily determined by the Knudsen regime, resulting in a ten fold higher overall diffusion coefficient for hydrogen compared to that of SiCl₄. Internal mass-transfer limitations are present for the SiCl₄ species invariably of the pores considered. It should be noted that thermodynamic calculations have shown that at these conditions the amount of SiCl₂ approaches the amount of SiCl₄ [4]. The diffusion coefficient of SiCl₂ is only 30 % larger (Knudsen regime) than that of SiCl₄, which will result in similar large internal mass-transfer limitations. Diffusion limitations for hydrogen are encountered in the micro pores as well as the meso pores. The Carberry numbers are in all cases smaller than 0.05, which means that external concentration gradients can be neglected for both the hydrogen as well for the silicon tetrachloride. The extent of internal mass-transfer limitations is calculated for the 5w% and 8w% Ni/C systems as well; silicon tetrachloride suffers in all these cases from severe transport limitations. The Wheeler-Weizs moduli of hydrogen are depicted in Fig. 13.

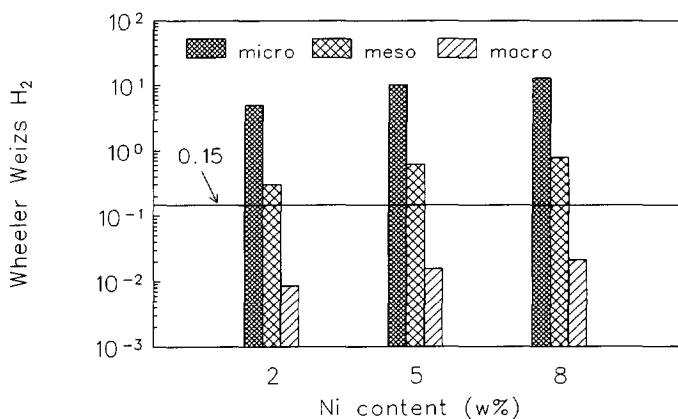


Fig. 13. Wheeler-Weisz number of H₂ in the micro-, meso-, and macro-pores for various nickel loadings (1 hour reaction).

Internal diffusion limitations of hydrogen increase using higher nickel loadings. These limitations, however, are absent in the macro pores of the carbon. The observed levelling off of the rate of formation of silicon carbide while the rate of methane formation enhances at increasing nickel loadings is thus shown to originate from mass-transfer limitations of silicon tetrachloride.

Fig. 14 presents the mechanism which envisages the mass-transfer considerations as well as the chemical aspects on atomic scale. Hydrogen is present throughout the carbon extrudate, its concentration decreasing to some extent moving to the middle of the extrudate. The presence of silicon tetrachloride, however, is in the initial stage of conversion mainly limited to the outer layer of the porous structure. Hydro-gasification as well as whisker growth occur simultaneously in the presence of SiCl₄ (region II). Region I is encountered inside the extrudate, where hydrogen is the only reactant present. In this initial period excess methane is formed at the interior of the extrudate which accounts for the incomplete CH₄ conversion into SiC as shown by Figs. 11 and 12 for the 5 and 8w% Ni/C extrudates. The amount of SiCl₄ diffusing into the porous structure does not suffice for the total methane conversion. The carbon conversion process after this period is to be conceived as a moving front of silicon carbide formation going from the outside to the inside, while methane is being formed throughout the particle. The extent of penetration of region II in the pore in the initial stage is determined by the rate of CH₄ formation and rate of SiCl₄ diffusion.

Nickel catalyzed conversion of activated carbon extrudates into high surface area silicon carbide

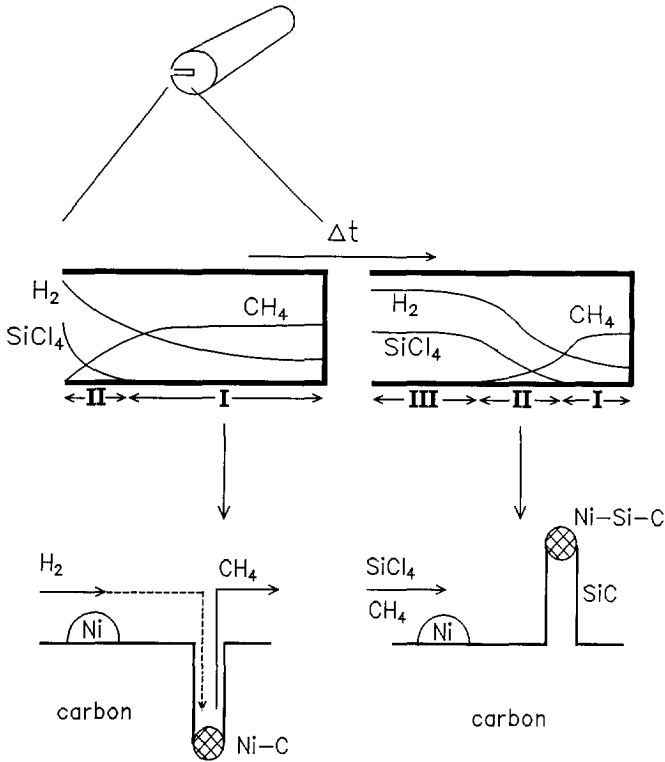


Fig. 14. The mechanism of nickel catalyzed conversion of activated carbon extrudates by reactive chemical vapour deposition, region I: hydro-gasification; II: hydro-gasification and whisker growth; III: possible Si deposition

The position of the front is stationary if these rates are identical. The inwards movement of the SiC formation front starts when the inward flow of SiCl₄ exceeds the outward flow of CH₄. This is induced by the deactivation of gasification sites resulting in a decrease in the rate of gasification. The deactivation is most probably caused by the reaction of nickel with the ash present in the carbon. Additionally, the silicon tetrachloride is to be expected to increase this rate of deactivation of the gasification sites by forming a Ni-Si alloy (probably Ni₃Si) when moving inwards. Hence, a third zone (region III) is induced where both SiCl₄ and H₂ are present in large amount, whereas CH₄ is nearly absent. Silicon co-deposition can then occur in region III via Si co-deposition during SiC growth.

4.3 Catalyst properties.

The textural properties of a catalyst support determine to a large extent the feasibility of application. Utilization of silicon carbide is, however, *a priori* limited to those fields in which substantial advantages are obtained over application of conventional catalyst supports (SiO_2 , Al_2O_3 , and activated carbon), due to the foreseen higher production costs. Areas in which silicon carbide may be employed are (1) high-temperature reactions, (2) liquid-phase reactions at demanding pH conditions, and (3) reactions in which the inertness of the silicon carbide surface is crucial. The exact manner of application depends on the achieved surface area and pore distribution. The surface areas of all synthesized SiC supports lay in the high surface area range (above $20 \text{ m}^2/\text{g}$) which is, compared to that of $\alpha\text{-Al}_2\text{O}_3$, sufficient for high-temperature applications. Catalytic operations at high temperatures, *e.g.* steam reforming of methane [34], suffer generally from severe diffusional limitations. Moreover, mass transport in catalyst pellets at high temperature (above 1000 K) mainly occurs in the Knudsen regime, which implies that the pore radius determines to a large extent the rate of diffusion. Hence, wide pore catalyst supports are most suitable, where moderate surface areas (*i.e.* $\approx 20 \text{ m}^2/\text{g}$) at normal pore volumina suffice.

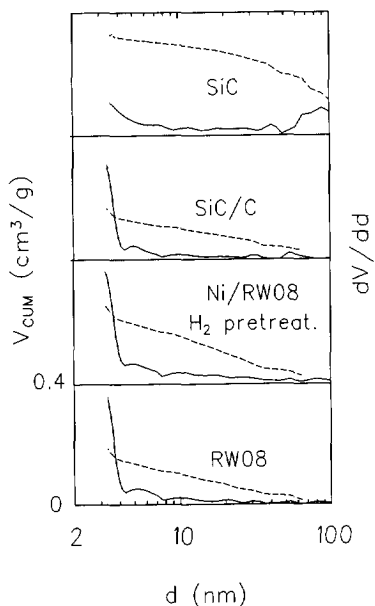
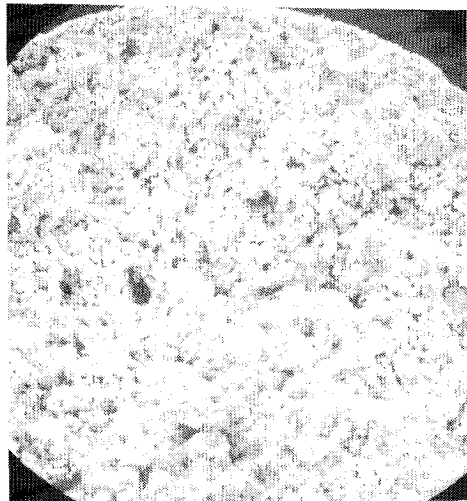


Fig. 15. Cumulative (---) and differential (—) pore volume distribution of the RW08, H_2 pretreated (Ni/RW08), converted (SiC/C), and the converted activated carbon after removal of carbon (SiC)

Nickel catalyzed conversion of activated carbon extrudates into high surface area silicon carbide

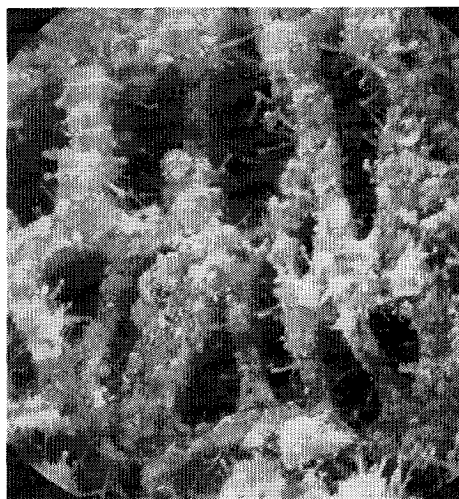
Elaboration of the nitrogen isotherms results in Fig. 15, which displays the cumulative and differential pore volume distributions, calculated using the corrected Kelvin equation, for all four stages in the synthesis. Note that only the meso/macro part of the pore-size distribution is given.

An increase at diameters below 4 nm is appearing indicating the onset of the micro-pore region for original, H₂ pretreated, and the converted carbon. The major part of the pore volume of the silicon carbide support, however, is positioned in the meso/macro-pore region which means that the entire surface area is available for catalysis. Additionally, the meso/macro-pore volume of the high surface area SiC is larger than the original carbon. The absence of micro-pore volume is shown as well by the equal values of S_{BET} and S_t (Table 3). Fig. 16 and 17 are micrographs of the SiC support which shows that this type of conversion enables the synthesis of wide pore SiC extrudates. The homogeneous conversion is confirmed in Fig. 16, while Fig. 17 displays the two types of SiC formation. Conventional SiC deposition results in the formation of granules, which act as support of the whiskers grown by the VLS mechanism.



100 μm

Fig. 16. Micrograph of the SiC support which shows the preservation of the extrudate shape



5 μm

Fig. 17. Magnification of Fig. 16, which shows the morphology of high surface area SiC

Chapter 5

5. CONCLUSIONS

A novel method has been developed for the synthesis of high surface area silicon carbide. It comprises the reaction of nickel loaded activated carbon extrudates with silicon tetrachloride and hydrogen at 1380 K and 10 kPa to form silicon carbide. Reaction at temperatures below 1380 K results in silicon co-deposition. A dual catalytic action of nickel has been observed, viz. hydro-gasification: $C(s) + 2H_2(g) \rightleftharpoons CH_4(g)$ and SiC formation $SiCl_4(g) + CH_4(g) \rightleftharpoons SiC(s) + 4 HCl(g)$. The total carbon conversion depends on the amount nickel used and ranges from 20 to 55% for 2 and 8w% Ni, respectively. The operative Vapour Liquid Solid mechanism causes the abundance of SiC whiskers throughout the converted extrudates. Calculation of mass-transport numbers shows that in the initial stage of conversion methane is formed in the entire extrudate, whereas SiC formation is limited to the outer part. This is the consequence of severe internal diffusion limitations of $SiCl_4$. Deactivation of gasification sites causes the inwards movement of SiC formation, until all gasification sites are deactivated and the conversion is ended. The surface areas of the SiC/C composites range from 154 to 395 m^2/g . Oxidation of the residual carbon at 1023 K results in high surface area SiC (57 m^2/g to 32 m^2/g). The meso/macro porous texture allows utilization of this catalyst support (1) at high temperature and (2) in liquid-phase reactions.

SYMBOLS

a'	specific area per unit volume ($m^2 m^{-3}$)
A_p	external surface area of particle (m^2)
A_{pore}	specific surface area ($m^2 g^{-1}$)
C_b	the concentration of the diffusing species in the gas phase ($mol m^{-3}$)
C_p	specific heat ($J kg^{-1} K^{-1}$)
d_p	particle diameter (m)
D_g	gas-phase diffusion coefficient ($m^2 s^{-1}$)
D_{eff}	effective diffusion coefficient ($m^2 s^{-1}$)
$D_{Knudsen}$	Knudsen diffusion coefficient ($m^2 s^{-1}$)
k_g	mass-transfer coefficient ($m s^{-1}$)
L	characteristic diffusion length (m)
L_b	length of bed (m)
M_w	mol weight ($g mol^{-1}$)
$r_{mi,me,ma}$	radius of micro, meso, or macro pore (m)
R	reaction rate ($mol m^{-3}_{carbon} s^{-1}$)

*Nickel catalyzed conversion of activated carbon extrudates into
high surface area silicon carbide*

R_{obs}	the observed reaction rate (mol s^{-1})
T	temperature (K)
U_f	superficial gas velocity ($\text{m}^3_{\text{gas}} \text{m}^{-2}_{\text{reactor}} \text{s}^{-1}$)
V_p	volume particle (m^3)
V_{pore}	pore volume ($\text{m}^3 \text{g}^{-1}$)
w_0	weight after pretreatment (kg)
w_{ash}	amount ash of pretreated carbon (kg)
$w_{\text{gasif.}}$	weight loss due to gasification (kg)
w_t	weight after conversion (kg)
$w_{\text{SiC/Si/C}}$	amount SiC/Si/C after conversion (kg)

Greek

ϵ_b	porosity of the bed ($\text{m}^3_{\text{gas}} \text{m}^{-3}_{\text{reactor}}$)
ϵ_p	porosity of the particle ($\text{m}^2_{\text{gas}} \text{m}^{-2}_{\text{particle}}$)
η	effectiveness factor (-)
η_f	viscosity of the gas (Pa s)
ϕ_f	mass flow (kg s^{-1})
φ	Thiele modulus (-)
ρ_f	density of the gas (kg m^{-3})
τ	tortuosity ($\text{m}^2_{\text{gas}} \text{m}^{-2}_{\text{particle}}$)

Dimensionless numbers

Ca	Carberry
Re	Reynolds
Sc	Schmidt
St	Stanton

REFERENCES

1. J.C. Duchet, E.M. van Oers, V.H.J. de Beer, and R. Prins, *J. Catal.*, **80** (1983) 386.
2. S. Stegenga, Automotive Exhaust Catalysis without Noble Metals, thesis, University of Amsterdam, The Netherlands, 1991 (English).

Chapter 5

3. S. Stegenga, M. van Waveren, F. Kapteijn, and J.A. Moulijn, *Carbon*, **30** (1992) 577.
4. Chapter 4 of this thesis.
5. R. Moene, M. Makkee, J. Schoonman, J.A. Moulijn, Carbon '92, Proceedings of the 5th Carbon Conference, Essen, German Carbon Group, 1992, p. 474.
6. R.B. Levy, in J.J. Burton and R.L. Garton (eds.), *Advanced Materials in Catalysis*, Academic Press, New York, 1977, p. 101.
7. L. Leclerq, in J.P. Bonnelle, B. Delmon, and E.G. Derouane (eds.), *Surface Properties and Catalysis by non-metals*, Reidel, Dordrecht, 1983, p. 433.
8. S.T. Oyama, *Catal. Today*, **15** (1992) 179.
9. R.W. Chorley and P.W. Lednor, *Adv. Mater.*, **3** (1991) 474.
10. M.J. Ledoux, S. Hantzer, C. Pham-Huu, J. Guille, and M.-P. Desaneaux, *J. Catal.*, **114** (1988) 176.
11. H. Vincent, J.L. Ponthenier, L. Porte, C. Vincent, and J. Bioux, *J. Less-Common Met.*, **157** (1990) 1.
12. R.C. Reid, J.M. Prausnitz, and B.E. Poling, *The properties of gases and liquids*, 4th ed., McGraw-Hill Book Company, New York, 1993, p. 632.
13. T. Boublik, V. Fried, and E. Hala, *The vapour pressures of pure substances*, Elsevier Scientific Publishing Company, Amsterdam, 1973, p. 32.
14. S. Brunauer, P.H. Emmett, and E. Teller, *J. Amer. Chem. Soc.*, **60** (1938) 309.
15. J.H. de Boer, B.G. Linsen, and Th. J. Osinga, *J. Catal.*, **4** (1965) 643.
16. *Janaf Thermochemical Tables*, 3rd ed., *J. Phys. Chem. Ref. Data*, **14**, 1985.
17. D.R. Orlander and M. Balooch, *J. Catal.*, **60** (1979) 41.
18. P.J. Goethel, R.T. Yang, *J. Catal.*, **108** (1987) 356
19. J.A. Tsamopoulos, H.W. Dandekar, and J.H. Scholtz, *J. Catal.*, **117** (1989) 549.
20. W.F. Knippenberg, *Growth phenomena in silicon carbide*, thesis, RU Leiden, The Netherlands, 1963, (English).
21. R.S. Wagner and W.C. Ellis, *Appl. Phys. Lett.*, **4** (1964) 89.
22. G.W. Sears, *Acta Met.*, **1** (1953) 457; **3** (1955) 361.
23. E.I. Givargizov, in "Current topics in materials science", E. Kaldis (ed.), vol. 1, North Holland Publ. Comp., 1978, p. 79.
24. G.A. Bootsma, W.F. Knippenberg, and G. Verspui, *J. Crystal Growth*, **11** (1971) 297
25. S. Motojima and Hasegawa, *J. Crystal Growth*, **87** (1988) 311.
26. J. Chin, P.K. Gantzel, and R.G. Hudson, *Thin solid Films*, **40** (1977) 57.
27. K. Minato and K. Fukuda, *J. Mater. Sci.*, **23** (1988) 699.
28. D.H. Kuo, D.J. Cheng, W.J. Shyy, and M.H. Hon, *J. Electrochem. Soc.*, **137**

*Nickel catalyzed conversion of activated carbon extrudates into
high surface area silicon carbide*

(1990) 3688.

29. B.J. Choi, S.H. Jeun, and D.R. Kim, *J. Europ. Ceram. Soc.*, **9** (1992) 357.
30. R. Moene, J.P. Dekker, M. Makkee, J. Schoonman, and J.A. Moulijn, *J. Electrochem. Soc.*, **141** (1994) 282;
Chapter 2 of this thesis.
31. J.A. Moulijn, A. Tarfaoui, and F. Kapteijn, *Catal. Today*, **11** (1991) 1.
32. R.C. Reid, J.M. Prausnitz, and B.E. Poling, *The properties of gases and liquids*, 4th ed., McGraw-Hill Book Company, New York, 1993, p. 587.
33. R.H. Perry, D.W. Green, *Perry's Chemical Engineer's Handbook*, 6th ed., McGraw-Hill Book Company, New York, 1984, p. 4-45.
34. J.R. Rostrup-Nielsen, *Steam Reforming Catalysts*, Danish Technical Press Inc., Copenhagen, 1973, p.34.

Synthesis of high surface area silicon carbide by Fluidized Bed Chemical Vapour Deposition

ABSTRACT

Activated carbon granulates loaded with small amounts of nickel have successfully been converted into high surface area silicon carbide granulates by reaction with hydrogen and silicon tetrachloride at 100 kPa and 1380 K ($C + SiCl_4 + 2 H_2 \rightarrow SiC + 4 HCl$). A cone shaped Fluidized Bed Chemical Vapour Deposition reactor is demonstrated to achieve reproducible and homogeneous conversions of considerable amounts of activated carbon. High surface area silicon carbide has thus been synthesized with surface areas ranging between 25 and 80 m²/g. The shape memory concept is applicable, because the shape of the activated carbon determines the morphology of the silicon carbide. The conversion process is shown to be limited by the gasification of carbon into methane. The formed methane is then totally converted into SiC *via* the Vapour Liquid Solid mechanism and conventional CVD. Carbon conversions range from 10 to 45%. The high surface area SiC obtained after conversion and removal of the residual carbon has high potential as catalyst support for liquid-phase application at demanding pH conditions and processes operating at high temperatures.

1. INTRODUCTION

High surface area silicon carbide can have great potential as catalyst support for processes operating at high temperatures and demanding pH conditions owing to its inert surface, high thermostability and high thermal conductivity. Vannice *et al.* [1] synthesized SiC of nearly 50 m²/g *via* gas-phase decomposition of Si(CH₃)₄ at temperatures of 1700 K. Shaping of the powder is, however, expected to be difficult and will probably result in a severe decrease in surface area. Ledoux *et al.* [2] synthesized SiC with a surface area of nearly 60 m²/g by reacting SiO with activated carbon. The macro structure of the activated carbon is thus retained, which overcomes additional shaping of the SiC. The maximal conversion of carbon into SiC is 50% due to stoichiometric formation of carbon monoxide. Difficulties in conversion are to be expected due to slow diffusion of reactants through the product layer which is inherent for gas-solid reactions. Other methods of synthesis are mainly based on solid-state reactions like organic gel pyrolysis [3]. A novel catalytic method for converting activated carbon into high surface area SiC has recently been developed and described in this thesis [4]. The carbon is hereby gasified by hydrogen into methane which subsequently reacts within the particle with silicon tetrachloride to form SiC. Both reactions are simultaneously catalyzed by nickel. The porous carbon acts thus as a reactant as well as template.



It has been shown that reaction 2 ensues partly via the Vapour Liquid Solid mechanism resulting in high rates of SiC whisker formation. Synthesis of shaped SiC extrudates with surface areas of 30 to 57 m²/g has shown to be feasible by conversion of activated carbon extrudates at 1380 K and 8 kPa in a fixed bed reactor. Typical carbon conversions range from 20 to 55%. The maximum amount of carbon to be converted in one batch was limited to about 0.2 gram in this fixed bed configuration in order to achieve a sufficiently homogeneous conversion throughout the bed. Fluidized bed reactors are well-suited for large scale operation of gas-solid reactions because of the good mixing of the solid phase. Fluidized bed CVD reactors have been used for this reason to coat particles with SiC [5,6], TiN, TiO₂ [7], and Al and Ti [8]. In this chapter the conversion of activated carbon granulates into high surface area SiC in a Fluidized Bed CVD (FBCVD) reactor is reported. Larger amounts of activated carbon can thus homogeneously be converted enabling the characterization and testing of the high surface area SiC as catalyst support.

2. EXPERIMENTAL

2.1 Materials.

The physical properties of the applied Norit activated carbons are given in Table 1.

Table 1. The physical properties of the activated carbon granulates

Carbon	S_{BET} (m ² /g)	V_{pore} (ml/g)	S_t (m ² /g)	V_{micro} (ml/g)	$\rho(Hg)$ (kg/m ³)	$\rho(He)$ (kg/m ³)	ash (%)
Azo	703	0.88	219	0.23	690	2100	6.9
Elorit	655	0.6	149	0.25	600	2100	8

The Azo carbon is sieved to obtain particles in the range of 63 to 180 μm and used without further pretreatment. The Elorit granulates are pre-fluidized for three hours to remove the fines and decrease the initial attrition of the carbon. A sieve fraction with a diameter of 300 to 425 μm has been selected for conversion. In some cases this fraction has previously been subjected to a washing procedure. This comprised subsequent washing with 5 litre of a 0.5 M NaOH solution (duration 8 hours), demineralized water until $\text{pH} < 8$, 5 litre of a 0.5 M HCl solution (duration 8 hours), and, finally, demineralized water until $\text{pH} > 6$. This washing procedure resulted in a decrease in ash content from 8w% to 5 w%. Nickel nitrate hexahydrate (>99%) and silicon tetrachloride (>98%), both from Janssen Chemica, were used. Activated carbon extrudates were loaded with nickel by pore volume impregnation of the carbon with a solution of $\text{Ni}(\text{NO}_3)_2 \cdot 6\text{H}_2\text{O}$ in demineralized water to arrive at nickel contents of 2, 5, or 8 w% nickel. Drying was performed at atmospheric pressure in air at 385 K. The gases used for carbon conversion, argon and hydrogen, were purified by passing them over a $\text{Cu}/\text{Al}_2\text{O}_3$ or $\text{Pd}/\text{Al}_2\text{O}_3$ catalyst, respectively, followed by drying by molecular sieve 5A.

2.2 Conversion of activated carbon granulates.

A schematic picture of the CVD apparatus is shown in Fig. 1. The carbon is fluidized in the cone-shaped quartz reactor (entrance diameter: 2.7 mm, cone angle 7°, cone length 140 mm) surrounded by an alumina tube. The gas velocity at the cone entrance exceeds the rate of entrainment of the carbon, whereas the velocity in the upper part of the bed surpasses the minimal fluidization velocity. The pressure is regulated by a pressure transducer at the cone entrance and a butterfly valve in combination with a vacuum pump downstream of the system, which allows CVD experiments to be carried out at sub-atmospheric pressures. The reactor is loaded with activated carbon (typically 3 to 5 gram) under flowing argon (16.7 ml/s).

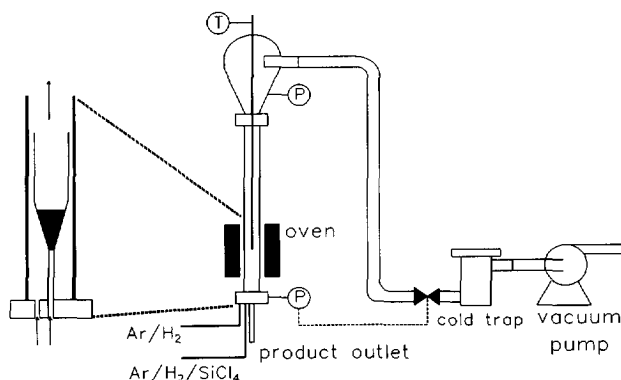


Fig. 1. Scheme of the fluidized bed CVD apparatus

Subsequently the reactor is evacuated twice to 10 kPa to remove oxygen while the flow rate is simultaneously decreased in steps to 2.5 ml/s to prevent entrainment of the particles out of the reactor. The reactor is heated under flowing argon to 1380 K at 100 kPa during which the nickel nitrate decomposes and the formed nickel oxide is carbo-thermally reduced to metallic nickel. The argon flow is subsequently lowered and hydrogen and silicon tetrachloride were admitted at the proper flow rates; the total flow rate equalled 16.7 ml/s (STP) and the pressure was kept at 100 kPa.

2.3 Determination of fluidization characteristics.

The minimum fluidization velocity of the sieved activated carbon granulates has been determined at ambient conditions in an all-glass fluidized bed reactor by measuring the pressure drop over the bed as a function of the gas (nitrogen) velocity and by visual confirmation of the bed behaviour. The fluidization regime under deposition conditions in the CVD reactor has been visually identified by replacing the alumina tube of the CVD reactor by a glass one. Pressure adjustment has been used to arrive at similar gas velocities as those existing at the high temperature CVD conditions.

2.4 Removal of residual carbon.

The residual carbon, present after conversion, has been removed by oxidation in dry air at 1023 K in a tubular reactor.

2.5 X-Ray Diffraction (XRD).

X-Ray diffractograms were measured with a Philips powder diffractometer (PW1840) using $\text{CuK}\alpha$ radiation (wavelength 0.154 nm).

2.6 Scanning Electron microscopy (SEM).

A JEOL (JSM-35) scanning electron microscope has been used to determine the morphology of the deposited phases. An acceleration voltage of 20 keV has been applied; the samples have been sputtered with gold or platinum to suppress charging during SEM analysis.

2.7 Thermal Gravimetric Analysis (TGA).

TGA has been carried out on a Stanton Redcraft (STA-1500) thermobalance. 20 mg samples were oxidized in air using a temperature increase of 0.167 K/s from room temperature to 1273 K. The weight change and concomitant heat flux were recorded simultaneously. Combination of the weight increase after conversion and the amount carbon present in the converted granulate allows a silicon and carbon mass balance to be made.

2.8 Surface area measurements.

Nitrogen isotherms at 77 K were recorded on a Carlo Erba Sorptomatic 1800. Prior to measurement the samples were degassed at 423 K and 0.1 kPa. The BET surface area (S_{BET}), t surface area (S_t), and micro pore volume (V_{micro}) were determined according to literature [9,10].

2.9 Particle size distribution.

Measurements of particle size distributions have been performed on a Malvern 2600 particle sizer, using the principle of Fraunhofer Diffraction.

3. RESULTS

3.1 Fluidization characteristics.

The particle size distributions after sieving of the Azo and Elorit activated carbon are characterized by d_{10} : 95 μm , d_{50} : 161 μm , and d_{90} : 261 μm and d_{10} : 324 μm , d_{50} : 456 μm , and d_{90} : 691 μm , respectively. These distributions appear to fall outside the range of diameters classified by sieving. This effect is, however, the consequence of a combination of non-sphericity of the carbon particles (the shape is a mixture of flake-like and cylinder-like) and the analysis method (the surface rather than the volume is analyzed). The minimum fluidization (u_{mf}) velocity of the Azo has been determined to be lower than 10 mm/s; the minimum bubbling velocity (u_{mb}) equalled 15 mm/s. Fluidization at reaction conditions in the CVD reactor demonstrated that the bed slugs severely, material loss occurs additionally through entrainment.

Chapter 6

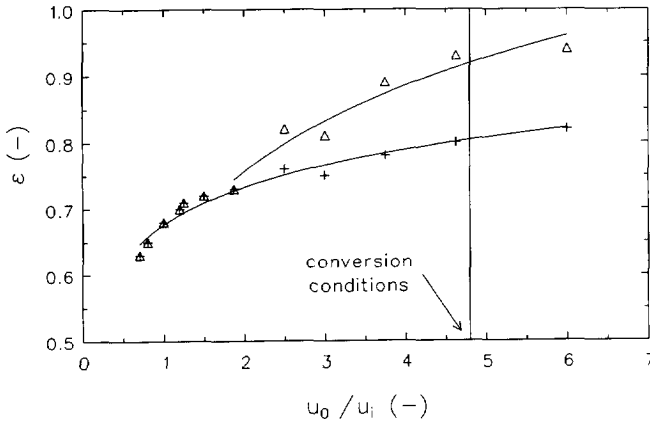


Fig. 2. Voidage (ϵ) vs. superficial gas velocity for the observed bed-height (+) and maximum slug height (Δ) (Elorit carbon). The lines are used to guide the eye. Conversion at $u_0/u_i=4.8$

A

B

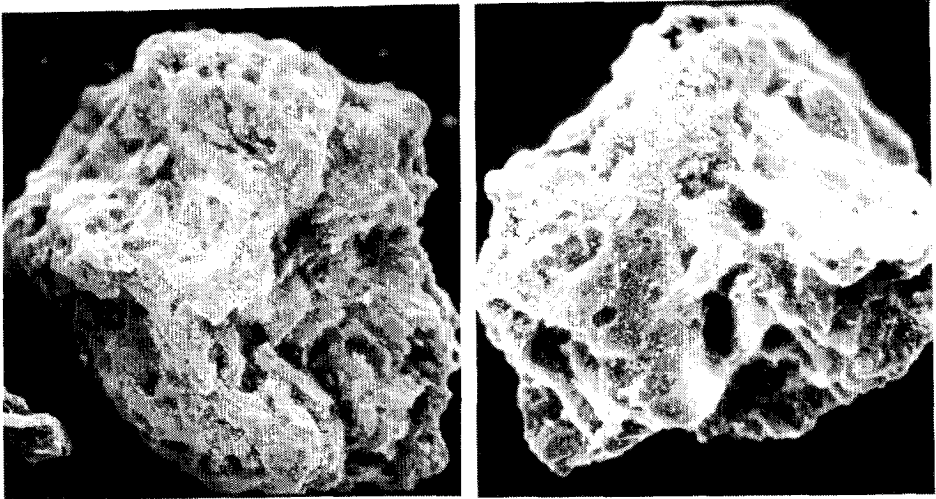


Fig. 3. ————— 100 μm .

The shape memory concept. 3^A is a micrograph of a granulate after conversion into SiC; whereas 3^B is a micrograph of another granulate after oxidation

Synthesis of high surface area silicon carbide by fluidized bed chemical vapour deposition

The u_{mf} and u_{mb} of the Elorit have been determined to be 21 mm/s and 42 mm/s, respectively. The voidage (ϵ) of the bed in the CVD reactor as a function of the superficial gas velocity is shown in Fig. 2. No characteristic superficial gas velocity (u_0) can be defined due to the use of the cone shaped reactor. Hence, u_0 has been normalized to the start-up superficial gas velocity (u_i), viz. 16.7 ml/s argon at ambient conditions. The voidage of the bed at minimum fluidization velocity ($u_0/u_i=0.7$) is slightly higher than that of the packed bed voidage, viz. 0.62. Above $u_0/u_i=1.8$ slugging starts, the bed expands considerably; the total void fraction approaches 0.95 at high gas velocities.

3.2 Morphology of the converted granulates.

Crystalline silicon carbide is detected by XRD after conversion of the Azo and Elorit at 1380 K in all cases. No crystalline silicon has been detected. Conversion of Elorit at lower temperatures (1330 K) resulted in silicon co-deposition. Removal of the residual carbon reveals that the shape memory concept is valid for this conversion process; no differences in particle diameter are encountered comparing the original and converted-oxidized carbon; Fig. 3 displays an example. SEM analysis of the SiC morphology discloses the presence of SiC whiskers grown via the Vapour Liquid Solid (VLS) mechanism [4].

3.3 Rates of methane and silicon carbide formation.

The rates of methane and silicon carbide formation can be determined independently by using a carbon and silicon mass balance. Both are obtained from TGA data which measure the amount of carbon and non-oxidizable material by combustion in air.

3.3.1. Azo activated carbon with 5w% nickel. Due to the rate of entrainment of the Azo carbon resulting in carbon loss during conversion, no reliable carbon and silicon mass balances could be obtained. Evaluation of the amount of silicon carbide present in the carbon after conversion can, however, be used as a first indication for the conversion characteristics in the FB-CVD reactor. The results are displayed in Fig. 4. A linear relationship between the H_2 content and amount SiC formed can be deduced, although the confidence region is quite large. The influence of $SiCl_4$ partial pressure on the amount of SiC formation is not significant.

3.3.2 Elorit activated carbon. The rate of gasification without SiC formation has been determined by reacting 5w% Ni/Elorit with a H_2/Ar mixture ($X_{H_2}=0.45$) at 1380 K for 40 minutes. The total carbon conversion equalled 5.5%. The carbon and silicon mass balance for the converted Elorit activated carbon can be determined, because significant entrainment does not occur and the pre-fluidization lessened the attrition during conversion substantially.

Chapter 6

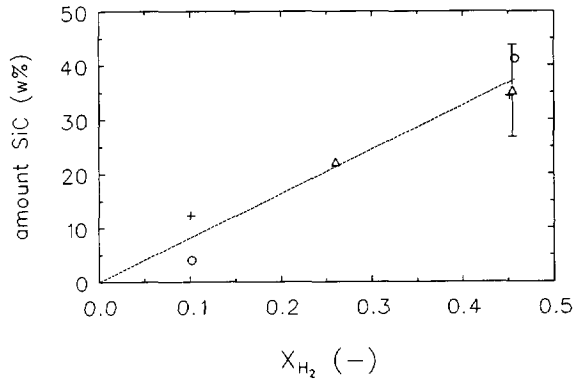


Fig. 4. SiC in Azo activated carbon after conversion vs. the molar fraction of H_2 in the feed for X_{SiCl_4} : (+) 0.045, (Δ) 0.090%, (\circ) 0.13. The 95% confidence region (two experiments) is included.

Some attrition and subsequent material loss through entrainment still transpires, however, which imposes a modest error in the calculation of the rate of gasification and the rate of SiC formation. The results of the conversion are given in Fig. 5, which displays the rate of CH_4 and SiC formation and related carbon conversions for Elorit carbon loaded with 5w% nickel.

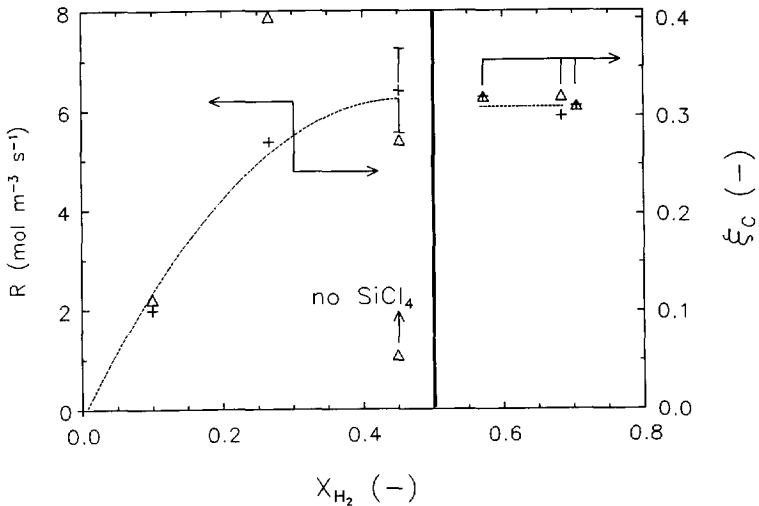


Fig. 5. Rate of CH_4 (Δ) and SiC (+) formation and corresponding carbon (Elorit) conversion at 1380 K vs. hydrogen content for 5w% Ni/Elorit, reaction time: 40 min.

Synthesis of high surface area silicon carbide by fluidized bed chemical vapour deposition

Carbon conversions vary between 0.1 and 0.3 for the conditions investigated. The conversion achieved in the absence of SiCl_4 (0.055) is considerably lower than that in the presence of SiC formation (0.3). The 95% confidence region has been determined from two experiments conducted at identical conditions. The amount of SiC present in these converted granulates is 50.6 and 48.6w%, respectively. This corresponds with carbon conversions of 0.32 and 0.305, demonstrating that the product composition is virtually identical, and that the large 95% confidence region is mainly imposed by the small number of experiments.

A linear correlation appears to exist between the reaction rate and H_2 content below 45 mol%. No increase in carbon conversion is found for H_2 concentration above 45 mol% indicating that the maximum conversion has been reached. The carbon conversions for various nickel loadings are shown as a function of reaction time in Fig. 6. It should be noted that the mol fraction hydrogen used in the experiments with 2w% Ni/Elorit is 0.27 instead of 0.45 as for the other experiments. The carbon conversion increases in the initial stage (up to 40 minutes) linearly with the reaction time, after which the conversion terminates. Higher nickel loadings result in higher final conversions and higher rates of conversion. Conversion of 5w% Ni/Elorit at a sub-atmospheric pressure of 50 kPa ($X_{\text{H}_2}=0.46$, $X_{\text{SiCl}_4}=0.045$, 40 minutes) resulted in a SiC content in the carbon of 39w% and a corresponding carbon conversion of 0.19.

Elorit subjected to a washing procedure displayed a carbon conversion which was slightly lower than that of the unwashed carbon. Fourteen batches of high surface area SiC have been prepared at the following conditions (1380 K, 100 kPa, X_{H_2} : 0.45, X_{SiCl_4} : 0.045, t : 40 minutes). The average carbon conversion was 0.2614 ± 0.0087 . The small 95% confidence region evidences the highly reproducible performance of the FBCVD set-up.

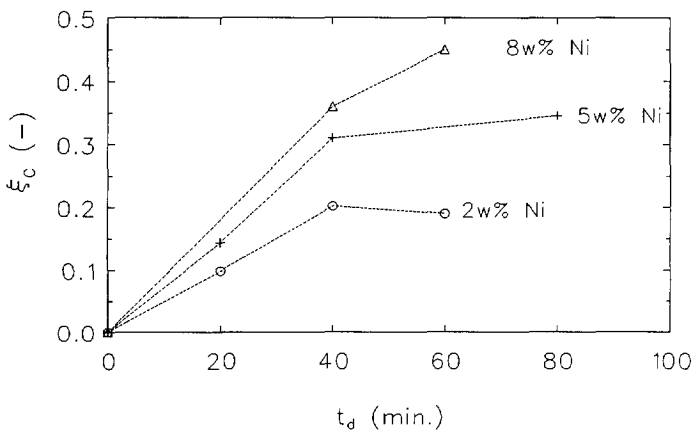


Fig. 6. Carbon (Elorit) conversion vs. reaction time at 1380 K. 2w% Ni: $X_{\text{H}_2}=0.27$, $X_{\text{SiCl}_4}=0.046$; 5 and 8w% Ni: $X_{\text{H}_2}=0.45$, $X_{\text{SiCl}_4}=0.046$

3.4 Texture of high surface area SiC.

The results of surface area analyses of the converted Elorit granulates are shown in Table 2. The BET surface area comprises the micro- and meso-pore area, whereas the t surface area contains only the surface area of the meso pores.

Table 2. Surface area (BET and t) of high surface area SiC, the conditions of conversion correspond to those of Fig. 6 at 40 min. conversion

	2w% Ni		5w% Ni		5w% Ni @		8w% Ni	
	S_{BET}	S_t	S_{BET}	S_t	S_{BET}	S_t	S_{BET}	S_t
after conversion	300	87	154	n.d.	206	66	137	49
after oxidation	80	66	25	n.d.	31	23	34	30

@ washed carbon

n.d. not determined

The surface areas after conversion range from 137 to 300 m^2/g and are composed of the original carbon and the SiC, shown by the substantial amount of micro pore surface. The SiC surface ranges from 31 to 80 m^2/g and contains primarily meso pores.

The influence of gas composition (H_2 and SiCl_4 content) on the texture after conversion and oxidation is displayed in Fig. 7. The surface areas extend between 25 and 68 m^2/g , while the pore volumes range from 0.24 and 0.37 ml/g . The results indicate that the highest surface areas are obtained at the highest SiCl_4/H_2 ratios. The influence of H_2 on the textural properties is not clear.

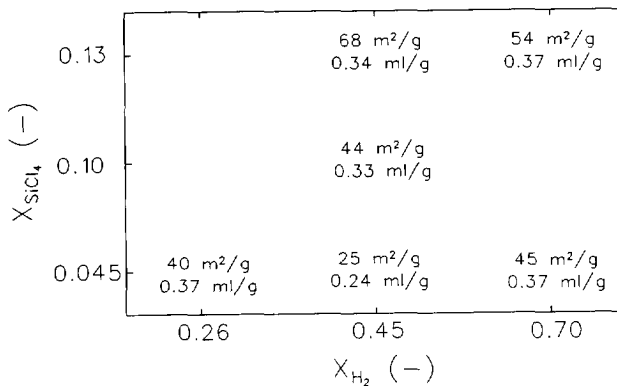


Fig. 7. BET surface areas and pore volume for converted and oxidized 5w% Ni/Elorit (not washed) as a function of gas composition

Synthesis of high surface area silicon carbide by fluidized bed chemical vapour deposition

Table 3. The texture of converted 5w% Ni/Elorit ($X_{H_2} = 0.45$, $X_{SiCl_4} = 0.045$) after oxidation as a function of conversion time

	conversion time		
	20 minutes	40 minutes	80 minutes
S_{BET} (m ² /g)	28	25	42
V_{pore} (ml/g)	0.22	0.24	0.29

The washing procedure significantly affects the texture by elevating the residual surface area from 25 m²/g (Fig. 7) to 31 m²/g (Table 2).

The influence of conversion time on the texture is envisaged in Table 3. The surface area and pore volume remain virtually constant up to 40 minutes of conversion, whereas a significant enlargement is achieved in the final stage.

4. DISCUSSION

4.1 Fluidization characteristics.

The FB-CVD reactor operates for both the Azo and Elorit carbon in the slugging mode during conversion. This causes considerable particle loss in the low diameter range, especially for the Azo. Major entrainment of the larger Elorit particles does not occur owing to the pretreatment procedure of the Elorit. The major contribution to particle loss, *i.e.* attrition, has been reduced sufficiently to obtain reasonable accurate mass balances.

According to the Geldart classification [11] for particles in fluidized bed technology, Elorit is located on the edge of the 'A' and 'B' regions. An important distinction between those two is that only Geldart A particles differ in minimal fluidization velocity (u_{mf}) and minimal bubbling velocity (u_{mb}), whereas in beds of Geldart B particles bubbles form as soon as the gas velocity exceeds u_{mf} . Elorit can be classified as a Geldart A particle because bubbling starts at $2 \cdot u_{mf}$. Other characteristics of Geldart A particles are that gas bubbles rise more rapidly than the rest of the gas, which percolates through the emulsion. These bubbles appear to split and coalesce frequently as they rise through the bed. Cross circulation of solids occurs even when only a few bubbles are present. This circulation is especially pronounced in large beds [11]. At the onset of fluidization the voidage of the bed should equal that of a packed bed, which in fact was experimentally found.

Another important parameter in fluidization technology is the sphericity factor (ϕ_s), which is used to correct for the non-sphericity of the particles and defined by eq. 3

$$\phi_s = \left[\frac{S_{\text{sphere}}}{S_{\text{particle}}} \right]_{\text{constant } V} \quad (3)$$

Reasonable values for Elorit should lie between 0.44 and 0.63 [11]. An estimation of ϕ_s can be acquired from eq. 4, which is generally used to predict the u_{mf} from known particle properties.

$$\frac{1.75}{\epsilon_{mf}^3 \phi_s} \left[\frac{d_p u_{mf} \rho_g}{\mu} \right]^2 + \frac{150(1 - \epsilon_{mf})}{\epsilon_{mf}^3 \phi_s^2} \left[\frac{d_p u_{mf} \rho_g}{\mu} \right] = \frac{d_p^3 \rho_g (\rho_s - \rho_g) g}{\mu^2} \quad (4)$$

which simplifies for small particles and $Re_{p,mf} < 20$ to

$$u_{mf} = \frac{d_p^2 (\rho_s - \rho_g) g \epsilon_{mf}^3 \phi_s^2}{150 \mu (1 - \epsilon_{mf})} \quad (5)$$

Calculation of ϕ_s using eq. 5, the experimentally determined u_{mf} and ϵ_{mf} , and a mean particle diameter of 456 μm results in a value of ϕ_s below 0.3, which is well outside the range expected. No ideal behaviour is, however, to be expected because the size distribution of particles is quite wide. The smaller particles are able to slip into the void spaces between the larger particles, and fluidize while the larger ones remain stationary. Using the d_{10} as characteristic particle size [12] the sphericity factor equals 0.38, which show that the granulate shape deviates considerably from spherical particles.

4.2 Conversion characteristics.

Conversion of activated carbon granulates into SiC in the FB-CVD reactor is shown to be feasible; carbon conversions up to 45% have been achieved. Moreover, the liberty of utilization of atmospheric pressure facilitates the operation to a large extent compared to fixed bed experiments [4].

4.2.1 Rate determining step. Both the Azo and Elorit display a linear dependence between the H_2 content and the carbon conversion as was observed in Fig. 4. No relationship between the SiCl_4 content and the carbon conversion has been encountered. From these observations it can be deduced that the first reaction (hydro-gasification, eq. 1) is rate determining in the conversion. This is evidenced by the nearly 100% utilization of the formed CH_4 for SiC deposition. Additional confirmation is found in the very low SiC deposition on the reactor wall indicating that the conversion transpires totally inside the granulates. Each particle can thus be envisaged as a small batch reactor, providing itself with the necessary methane.

Conversion of activated carbon extrudates displayed major internal diffusion limitations for SiCl_4 resulting in lower utilization of the formed CH_4 and SiC deposition downstream of the fixed bed [4]. Determination of the presence of internal diffusion limitations by calculation of the Wheeler-Weisz number [13] for Elorit, however, shows the absence of diffusion limitations for both SiCl_4 and H_2 in the meso and macro pores allowing the conversion to proceed homogeneously throughout the particles and to obtain a 100% CH_4 utilization. Moreover, in contrast to the extrudate conversions, no silicon is co-deposited during the synthesis of high surface area silicon carbide granulates. It is previously shown that Si co-deposits as a silicon rich SiC phase during SiC growth inflicted by a deficiency of methane in the region of the extrudate which had already partially been converted into SiC [4]. The homogeneous granulate conversion, however, provides a sufficiently high quantity of methane throughout the particle suppressing the local co-deposition of Si. The conversion halts abruptly and uniformly when the nickel which catalyzes the gasification is deactivated due to the formation of a silicide or due to reaction with the ash in the activated carbon, thus preventing silicon co-deposition.

The rate of gasification without SiC formation is substantially lower than that with SiC formation, which is quite remarkable because the presence of SiCl_4 is expected to deactivate a substantial amount of the gasification sites by forming whiskers or a nickel silicide granule during reaction. The formation of chlorine containing hydrocarbons as a gasification product cannot rationalize the higher rate of gasification, because thermodynamic calculations [14] have shown that the equilibrium concentrations of these products are several orders of magnitude lower than those of CH_4 and C_2H_4 . The presence of hydrogen chloride in the pores may account for this effect by increasing the nickel dispersion causing higher rates of gasification. It is, however, imaginable as well that the thermodynamic limitation of eq. 1 [4] determines the low amount of gasified carbon in the absence of SiC formation. The presence of SiCl_4 probably impedes the establishment of the thermodynamic equilibrium of eq. 1 by removing the formed CH_4 via deposition of SiC. The fact that the concentration of SiCl_4 does not influence the rate of conversion should then be imposed by the achievement of maximum attainable rate of gasification at these conditions.

4.2.2 Influence of pressure. Table 3 displays the result of sub-atmospheric conversion compared to atmospherically conducted experiments. Experiment 2 is carried out using a similar W_C/F_{H_2} ratio and hydrogen concentration as the one in experiment 1 and results in a higher carbon conversion. Although the mol fraction H_2 is not identical for both experiments, it can tentatively be concluded that performing the reaction at sub-atmospheric pressures lowers the rate of conversion. This can be ascribed to the pressure dependence of the thermodynamic equilibrium composition of eq. 1. Decreasing pressures impose a lower equilibrium concentration of methane, which is expected to lower the rate of conversion.

Chapter 6

Table 3. Influence of pressure on the conversion of carbon (5w% Ni Elorit, $X_{SiC14}=4.5$)

exp. nr.	P (kPa)	F^{STP} (ml/min.)	X_{H2} (-)	C_{H2} (mol/m ³)	t (min)	amount SiC (w%)	ξ_C (-)
1	50	500	0.46	2.0	40	35	0.19
2	100	1000	0.27	2.2	40	48	0.26

4.2.3 Influence of washing. The washing procedure decreases the ash content of the activated carbon from 8w% to 5w%, which improves the purity of the high surface area SiC. Washing decreases the carbon conversion and elevates the residual surface area of the SiC. The first effect might suggest that reaction of nickel with the ash during conversion is not the major cause of deactivation. The exact influence of the washing procedure on the conversion is, however, not completely clear.

4.3 Texture of high surface area SiC granulates.

The shape memory concept holds for this conversion process, similar to that of the conversion of activated carbon extrudates [4]. After conversion the BET surface areas decrease from 655 to 300, 206, and 137 m²/g, respectively for the 2, 5, and 8w% nickel loaded Elorit. Part of the decrease is caused by the weight increase by Si-deposition. The surface areas are corrected for deposition by normalization to the same volume as the original carbon (1 gram Elorit). The results are displayed in Table 4. It can be concluded that the absolute surface areas decrease to a similar degree during conversion. The micro-pore surface area decreases to the largest extent caused by pore-mouth plugging during SiC deposition. The surface areas after oxidation (Table 2 and Fig. 7) suffice for application as catalyst support. Processes operating at high temperatures in which diffusion limitations are encountered provide future areas of utilization owing to the absence of micro pores.

Table 4. Surface area (m²/g_{carbon}) of high surface area SiC

	2w% Ni		5w% Ni @		8w% Ni	
	S'_{BET}	S'_t	S'_{BET}	S'_t	S'_{BET}	S'_t
after conversion	395	115	351	112	235	91

@ washed carbon

5. CONCLUSION

A Fluidized Bed Chemical Vapour Deposition reactor is very well suited for the catalytic conversion of nickel loaded activated carbon into high surface area silicon carbide at 1380 K and pressures ranging from 50 to 100 kPa. The conversion process can be divided into a gasification step ($C + 2 H_2 \rightarrow CH_4$) and a CVD step ($SiCl_4 + CH_4 \rightarrow SiC + 4 HCl$). It is shown that the first one is rate limiting in the conversion. Carbon conversions up to 45% have been achieved. No internal diffusion limitations are encountered during conversion. The surface area after conversion ranged from 137 to 300 m²/g; removal of the residual carbon resulted in meso/macro porous SiC granulates with a surface area between 25 and 80 m²/g. The properties of this high surface area SiC allow the use as catalyst support in processes working at elevated temperatures and liquid-phase processes operating at demanding pH conditions.

SYMBOLS

d	diameter (m)
S	surface area (m ²)
S _{BET}	BET surface area (m ² g ⁻¹)
S _t	t surface area (m ² g ⁻¹)
t _d	conversion time
u ₀	superficial gas velocity at STP (m s ⁻¹)
u _i	superficial gas velocity (m s ⁻¹)
u _{mb}	minimal bubbling velocity (m s ⁻¹)
u _{mf}	minimal fluidization velocity (m s ⁻¹)
V	volume (m ³)
V _{micro}	micro-pore volume (ml g ⁻¹)
V _{pore}	pore volume (ml g ⁻¹)
X	mol fraction (-)

Greek

ε	porosity (m ³ free space m ⁻³)
φ _s	sphericity factor (-)
μ	viscosity (Pa s)
ρ	density (kg m ⁻³)

Chapter 6

REFERENCES

1. M.A. Vannice, Yu-Lin Chao, and R.M. Friedman, *Appl. Catal.*, **20** (1986) 91.
2. M.J. Ledoux, S. Hantzer, C. Pham Huu, J. Guille, and M-P. Desaneaux, *J. Catal.*, **114** (1988) 176.
3. J.R. Fox, D.A. White, S.M. Oleff, R.D. Boyer, P.A. Budinger, *Mater. Res. Soc. Symp. Proc.*, **73** (1986) 395.
4. Chapter 5 of this thesis.
5. J.I. Federer, *Thin Solid Films*, **40** (177) 89.
6. K. Minato and K. Fukuda, *J. Nucl. Mater.*, **149** (1987) 233.
7. S. Morooka, A. Kobata, and K. Kusakabe, *AIChE Sym. Ser.*, **87**(281), 32.
8. B.J. Wood, A. Sanjurjo, G.T. Tong, and S.E. Swider, *Surf. Coat. Technol.*, **49** (1991) 228.
9. S. Brunauer, P.H. Emmett, and E. Teller, *J. Amer. Chem. Soc.*, **60** (1938) 309.
10. J.H. de Boer, B.G. Linsen, and Th.J. Osinga, *J. Catal.*, **4** (1965) 643.
11. D. Kunii and O. Levenspiel, *Fluidization Engineering*, 2nd ed., Ellis Horwood (1991).
12. Personal communication with dr. J.C. Schouten.
13. J.A. Moulijn, A. Tarfaoui, and F. Kaptein, *Catal. Today*, **11** (1991) 1.
14. Chapter 4 of this thesis.

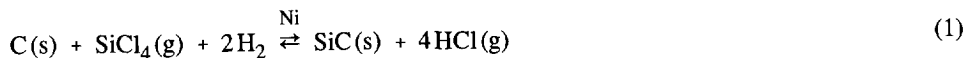
High surface area silicon carbide as catalyst support Characterization and stability

ABSTRACT

High surface area silicon carbide (SiC) of $30 \text{ m}^2/\text{g}$ has been synthesized by the catalytic conversion of activated carbon. The stability of this SiC in aqueous hydrogen fluoride and a boiling nitric acid solution is shown to be excellent. No corrosion is encountered by treatment with boiling HNO_3 , HF treatment causes the dissolution of the silica surface layer present on the SiC while the SiC remains intact. Oxidation in air at elevated temperatures has been analyzed by thermal gravimetric analysis, diffuse reflectance infrared spectroscopy, nitrogen adsorption, and X-ray diffraction. The thermal stability in non-oxidizing environments is shown to be excellent; no significant sintering has been observed after ageing in nitrogen for 4 hours at 1273 K. The presence of 2v% steam at 1273 K results in partial SiC oxidation into SiO_2 and considerable sintering. Air oxidation at 1273 K of pure SiC, SiC loaded with 5w% nickel, and HNO_3 treated SiC is shown to cause substantial SiC conversion, viz. 60 to 70 % after 10 hours. Air oxidation at 1080 K will result in complete conversion in about 100 days. This rate of oxidation agrees with reports on the oxidation of non-porous Acheson SiC and SiC coatings formed by Chemical Vapour Deposition. It is concluded that high surface area SiC can not be used as a catalyst support in processes operating in oxidizing environments and temperatures above 1080 K. SiC based catalysts are very well suited for (1) high-temperature gas-phase reactions operating in the absence of oxidizing constituents (O_2 or H_2O) and (2) strong acidic liquid-phase processes.

1. INTRODUCTION

Silicon carbide's physical bulk properties (high thermostability, high mechanical strength, and high heat conductivity) have been claimed to enable the use of this material as catalyst support at extreme process conditions, *viz.* processes operating at high temperatures and oxidizing environments [1]. The application of silicon carbide as catalyst support had mainly been limited by its low maximum attainable specific surface area. The last decade, various other methods for the synthesis of high surface area SiC have been reported. The method applied by Vannice *et al.* [1] comprises the gas-phase decomposition of tetramethylsilane resulting in SiC of nearly 50 m²/g. A new synthesis procedure for the preparation of high surface area SiC has been developed in which activated carbon is catalytically converted into SiC by the following overall reaction [2,3]



The mechanism of conversion comprises the gasification of carbon by hydrogen followed by the intra-particle deposition of SiC from SiCl₄ and CH₄ *via* the Vapour Liquid Solid (VLS) mechanism resulting in abundant whisker growth within the particle. Both reactions are catalyzed by nickel and the carbon acts as a source for CH₄ formation as well as a template for SiC deposition. The synthesis of SiC with surface areas ranging from 30 to 80 m²/g has been achieved. Application of a Fluidized Bed Chemical Vapour Deposition (FBCVD) reactor allows a very reproducible and homogeneous conversion of several grams of activated carbon [4] which alleviates to a large extent the investigations for possible applications of SiC supports. Research regarding the use of high surface area SiC at severe process conditions is limited. Vannice *et al.* [1] investigated silicon carbide based Ni and Pt catalysts for the hydrogenation of carbon monoxide at 473 and 773 K. The well-dispersed Pt/SiC catalyst displayed similar catalytic behaviour as SiO₂ and Al₂O₃ based catalysts. The Ni/SiC catalysts exhibited no H₂ chemisorption and unusual activity for the methanation of CO. Ledoux and co-workers [17] explored the use of SiC based cobalt molybdenum catalysts in hydrodesulfurization reactions. These tests are of fundamental importance. They are, however, not to be regarded as future applications of high surface area SiC, because the expected production costs of this material are higher than that of conventional supports and these will not be justified by the marginal benefits gained by using SiC in that field. An area in which the use of SiC might be beneficial are high-temperature processes in which sintering of high surface area SiC is probably less than that of alumina and silica, *e.g.* reforming of methane and dehydrogenation of paraffins. Another area comprises for instance hydrodemetallization of heavy oil fractions, because of SiC's resistance against corrosion in strong

High surface area SiC as catalyst support characterization and stability

acidic solutions during regeneration of the catalyst. Automotive exhaust catalysis based on SiC powder [5] and porous SiC [6] has been investigated as a possible application in the field of high-temperature processes. Here, the thermal stability of the silicon carbide itself and the limited reactions of the catalytically active components with the support are claimed to result in a superior operation compared to that of conventional alumina based catalysts. SiC has furthermore been suggested as a support for catalysts suitable for high-temperature combustion [7]. No extensive analysis and evaluation of high surface area SiC has been carried out to investigate the correctness of these assumptions. In this chapter the characterization and stability testing of high surface area SiC synthesized by the FB-CVD method are reported. The results are compared with those obtained for other porous forms of SiC and non-porous SiC and evaluated for support applications at extreme process conditions. The investigated properties comprise the thermal stability in N_2 , N_2/H_2O mixtures, and air. Furthermore, the resistance against corrosion in aqueous hydrogen fluoride and a boiling solution of nitric acid has been investigated.

2. EXPERIMENTAL

2.1 Materials.

Nitric acid (65%) HNO_3 (pro analysi) and $Ni(NO_3)_2 \cdot 6H_2O$ (pro analysi) were obtained from Merck. SiO_2 (Si-162-1, $S_{BET}=30 \text{ m}^2/\text{g}$, $V_{\text{pore}}=0.6 \text{ ml/g}$) has been obtained from Engelhard.

2.2 Synthesis of high surface area SiC.

High surface area SiC has been synthesized by FB-CVD using washed Norit Elorit carbon granulates (300 to 425 μm) loaded with 5w% nickel [4]. A gas composition of 45 mol% H_2 , 4.5 mol% $SiCl_4$, and 50.5 mol% argon is reacted with the carbon at 1380 K and 100 kPa for 40 minutes. The residual carbon present after conversion has been removed by oxidation at 1023 K in dry air. The resulting silicon carbide, with a surface area of 31 m^2/g and a pore volume of 0.2 ml/g will be referred to as SiC-5. Determination of the pore volume by adding water until external wetting of the granulates is perceived, revealed a total pore volume of 1.4 ml/g.

High surface area SiC-5 and SiO_2 have been loaded with 5w% nickel by incipient wetness of nickel nitrate in demineralized water and subsequent calcination in air at 773 K or 1273 K.

2.3 Thermal and hydrothermal stability.

The thermal stability of the high surface area SiC-5 has been determined in a tubular reactor under flowing nitrogen at 1273 K for 4 hours (1 gram SiC, 6 l/hour N₂ STP). The hydrothermal stability has been measured at 1023 K and 1273 K by adding steam in an amount of 2v% to the nitrogen.

2.4 Oxidation in air.

The rate of oxidation of the silicon carbide at 1080 K, 1180 K, and 1280 K has been determined by Thermal Gravimetric Analysis (TGA), measuring the weight increase during oxidation in dry air for 10 hours using a Stanton Redcraft 1500.

2.5 Treatment of high surface area SiC with aqueous hydrogen fluoride.

HF treatment of high surface area SiC-5 has been carried out in a polypropylene beaker by plunging 2 gram SiC in 100 ml demineralized water containing 2v% HF solution (demineralized water) for 24 hours. Subsequently the SiC has been washed to arrive at pH 7 and has been filtrated and dried at 423 K.

2.6 Corrosion of high surface area SiC by boiling nitric acid.

0.5 gram SiC-5 has been kept in a boiling solution (400 ml) of 5 M nitric acid (378 K) for 4 hours. After washing with demineralized water to arrive at pH 7, the SiC has been filtrated and dried at 423 K. The presence of corrosion has been evaluated using scanning electron microscopy, DRIFT, and measuring the rate of oxidation in air.

2.7 X-ray diffraction.

X-ray analysis has been carried out on a Philips powder diffractometer PW1840 using CuK α radiation. Diffractograms were taken from identical amounts of SiO₂, 5w% Ni/SiO₂ calcined at 773 K for 8 hours, 5w% Ni/SiC-5 calcined at 773 K for 8 hours, and 5w% Ni/SiC-5 calcined at 1273 K for 8 hours.

2.8 DRIFT.

Diffuse Reflectance Infrared Fourier Transform spectroscopy (DRIFT) has been carried out on a Nicolet Magna 550 using a data spacing of 1 cm⁻¹. A mixture of SiC in KBr (dilution ~ 100 times) has been used to identify the surface groups of the following materials: converted activated carbon, high surface area SiC-5, SiC-5 oxidized for one hour at 1273 K, SiC-5 oxidized for eight hours at 1273 K, and HF and HNO₃ treated SiC-5.

*High surface area SiC as catalyst support
characterization and stability*

2.9 Surface area.

Nitrogen isotherms at 77 K were recorded using a Carlo Erba Sorptomatic 1800. Prior to measurement the samples have been degassed at 423 K and 0.1 kPa. From the N₂ isotherm the BET surface area has been determined.

2.10 Scanning Electron Microscopy.

A JEOL JSM-35 has been used to investigate the surface of the SiC-5 (acceleration voltage 20 kV). Sputtering of the granulates with gold (4 minutes) is used to avoid charging.

3. RESULTS

3.1 Thermal and hydrothermal stability in nitrogen and steam.

The surface areas and pore volumes of SiC-5 after the thermal and hydrothermal stability tests are shown in Table 1.

The constant surface area after ageing in pure N₂ at 1273 K displays the excellent thermal stability of SiC-5. The stability in air and steam environments is less pronounced, which is evidenced by the decrease in surface area after ageing at 1273 K and partial oxidation of the silicon carbide into SiO₂.

3.2 Rate of oxidation.

The results of the rate of oxidation are displayed in Fig. 1, 2, and 3. The conversion of SiC-5 has been determined from the weight increase, assuming that equation 2 represents the stoichiometry of oxidation.

Table 1. Surface area (S_{BET}), pore volume (V_{pore}), and SiC-5 conversion into SiO₂ (ξ) of SiC-5 after ageing in N₂ and 2v% H₂O in N₂

properties	ageing process			
	N ₂	air	2v% H ₂ O in N ₂	
	4 hours	1 hour	4 hours	
	1273 K	1273 K	1023 K	1273 K
S_{BET} (m ² /g)	29	17	29	19
V_{pore} (ml/g)	0.22	0.16	0.25	0.14
ξ (-)	0	0.20	0	0.27

Chapter 7

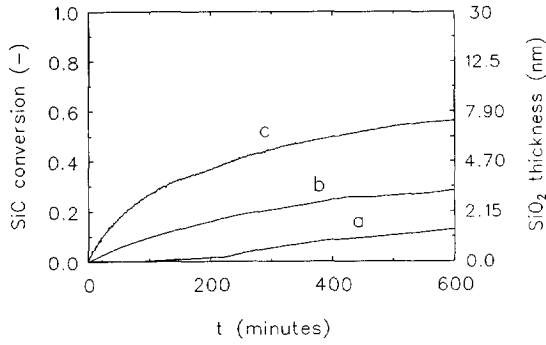


Fig. 1. Conversion of SiC-5 into SiO₂ by air oxidation at (a) 1080 K, (b) 1180 K, and (c) 1280 K

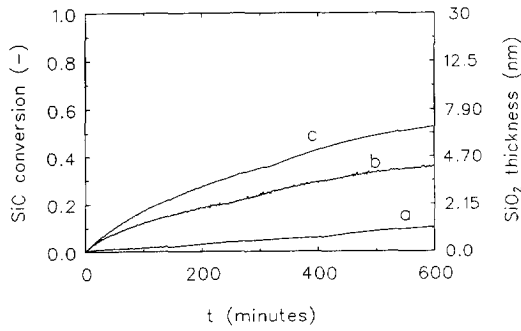


Fig. 2. Conversion of 5w% Ni/SiC-5 into SiO₂ by air oxidation at (a) 1080 K, (b) 1180 K, and (c) 1280 K

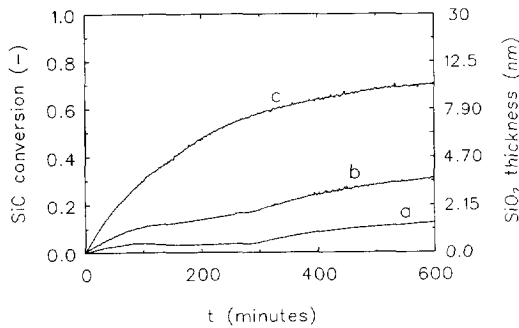


Fig. 3. Conversion of HNO₃ treated SiC-5 into SiO₂ by air oxidation at (a) 1080 K, (b) 1180 K, and (c) 1280 K

*High surface area SiC as catalyst support
characterization and stability*



The corresponding thickness of the formed SiO_2 layer has been calculated assuming that the oxidation ensues via the un-reacted shrinking core model and that the SiC-5 consists of agglomerated non-porous spheroids of 60 nm diameter. Further details are given in the section discussion. It is evidenced that both the rate and total amount of SiC-5 oxidation increase with increasing oxidation temperature. The rate of oxidation decreases in time. Oxidation at 1280 K for 10 hours causes abundant SiC conversion, viz. up to 70% for the HNO_3 treated SiC-5. Bare and Ni-impregnated SiC-5 exhibit comparable oxidation behaviour.

Fig. 4 shows XRD profiles for SiO_2 , 5w% Ni/ SiO_2 calcined at 773 K, 5w% Ni/SiC-5 calcined at 773 K, and 5w% Ni/SiC-5 calcined at 1273 K for 8 hours. The SiO_2 based catalysts are included for comparison.

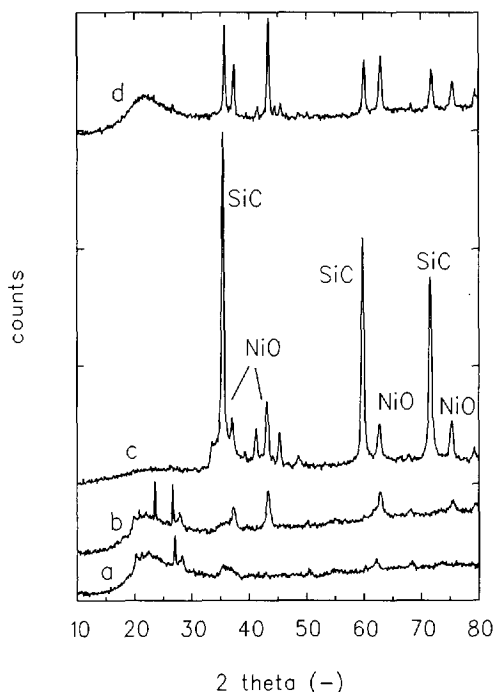


Fig. 4. X-ray diffractograms of (a) SiO_2 , (b) 5w% Ni/ SiO_2 calc. 773 K, (c) 5w% Ni/SiC-5 calc. 773 K, (d) 5w% Ni/SiC-5 calc. 1273 K

Diffraction lines of both crystalline SiC and nickel oxide are shown. The broad band displayed in diffractogram 4^a, 4^b, and 4^d between 2θ values of 20° and 30° originates from SiO₂ structures with a short-range periodicity. Calcination of 5w%/SiC-5 at 1273 K results in a conversion of SiC shown by the decrease in height of the SiC lines and the emerged band between 2θ values of 20° and 30° , compare curve 4^c and 4^d.

3.3 Surface groups on SiC-5 analyzed by DRIFT.

The results of the DRIFT analyses for the various samples are presented in Fig. 5. The adsorption bands at 900 and 790 cm⁻¹ originate from Si-C vibrations, whereas the broad band around 1100 cm⁻¹ is caused by the asymmetric stretching vibration of SiO₂ groups [15]. The results show that the presence of carbon lowers the infrared absorption of the Si-C bonds relative to the background as shown by spectrum 5^a. Removal of this carbon *via* oxidation at 1023 K discloses the Si-C absorption and concurrently an absorption of minor intensity arises at 1100 cm⁻¹ indicating the presence of some SiO₂. After HNO₃ treatment the spectrum remains identical implying that no additional surface oxidation occurs. The Si-O peak increases relative to the Si-C absorption with severity of oxidation in air as depicted by spectra 5^b, 5^c, and 5^d. The HF treatment causes dissolution of the SiO₂ layer as shown by the absence of Si-O absorbance in curve 5^e.

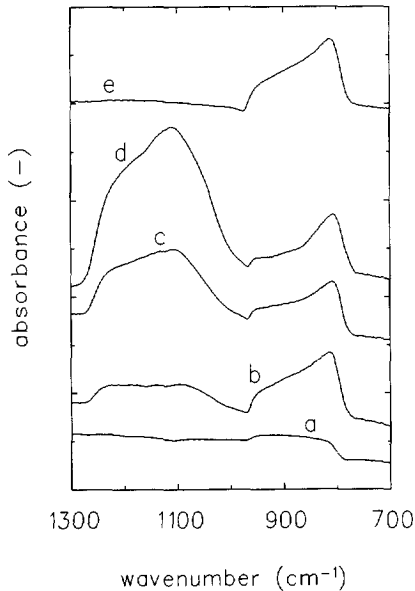
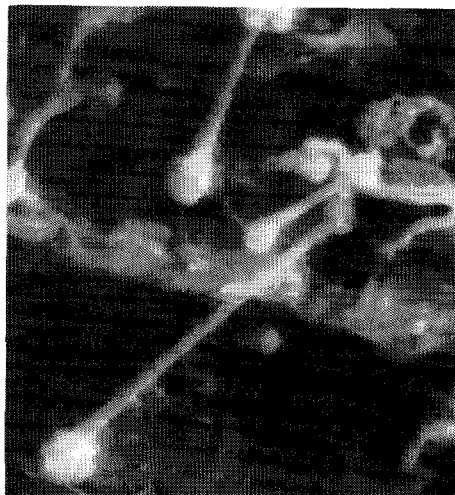


Fig. 5. DRIFT spectra of (a) SiC/C; (b) SiC-5; (c) SiC-5, 1 hour in air at 1273 K; (d) SiC-5, 8 hours in air at 1273 K; (e) HF treated SiC-5

*High surface area SiC as catalyst support
characterization and stability*



————— 2 μm
Fig. 6. Micrograph of HNO_3 treated SiC-5.

3.4 Oxidation of SiC-5 in boiling nitric acid.

SiC-5 treated with boiling HNO_3 displays in all cases similar oxidation behaviour as non-treated SiC-5 as shown by Figs. 1 and 3. DRIFT analyses give an identical spectrum as the non-treated SiC-5 (Fig. 5^b), indicating that no additional SiO_2 has been formed during the corrosion treatment. The surface topology of the SiC-5 after the HNO_3 treatment has been analyzed by scanning electron microscopy. A representative part is shown by Fig. 6. SiC whiskers are visible without any surface roughness and are similar to those without HNO_3 treatment.

4. DISCUSSION

4.1 Characterization of SiC.

4.1.1 SiC surface analysis. From the oxidation experiments (Fig. 1) it follows that the DRIFT spectra 5^c and 5^d correspond to silicon carbide converted for 20 and 55 % into SiO_2 , respectively. Boutonnet-Kizling and co-workers obtained similar effects for oxidized Pt/ α -SiC [5]. They correlated the intensity of Si-O vibrations with the degree of SiC oxidation [8]. A

HF treatment of SiC-5 completely removes the silica layer present on the SiC as shown by the disappearance of the 1100 cm^{-1} absorption band. The SiC structure remains, however, intact.

4.1.2 SiC bulk analysis. The conversion of SiC can be qualitatively determined by X-ray analysis. Calcination of 5w% Ni/SiC-5 at 1273 K for 8 hours causes 50% conversion of SiC into SiO_2 (Fig. 2). This appears as a decrease in SiC reflections and the occurrence of the broad SiO_2 band at low 2θ .

4.2 Corrosion of SiC in boiling nitric acid.

No differences between SiC-5 and HNO_3 treated SiC-5 in DRIFT spectra, rate of oxidation, and microstructure has been encountered, which indicates that corrosion of SiC-5 in boiling 5 M nitric acid is negligible. Rubio *et al.* [9] report on the corrosion of SiC fibres (Nicalon, Nippon carbon Co.) with 14 M HNO_3 and they found no differences in infrared spectra prior and after treatment, which agrees with our observations. They describe, however, a considerable increase in surface roughness after the HNO_3 treatment. This extent of oxidation might originate from the more acidic treatment applied by Rubio *et al.*

4.3 Stability of SiC at elevated temperatures.

The stability of SiC at elevated temperatures will be discussed below. The first paragraph will focus mainly on the sintering of SiC, while the second one will elaborate the conversion of SiC into SiO_2 .

4.3.1 Thermal and hydrothermal stability. The thermal stability of high surface area SiC-5 is excellent; no sintering at 1273 K in nitrogen is encountered. At elevated temperatures in air and steam containing atmospheres oxidation takes place accompanied by sintering. Exposure to steam containing nitrogen at 1273 K causes a decrease in specific surface from 31 to $26\text{ m}^2/\text{g}$, due to oxidation; the remaining loss in specific surface area (from 26 to $19\text{ m}^2/\text{g}$) is induced by sintering.

Thermal and hydrothermal stabilities of other high surface area silicon carbides are depicted in Table 2. The results obtained by Pugh [10] for α -SiC synthesized *via* the Acheson procedure has been included for comparison. The presentation by all authors of only one of the two crucial parameters of the ageing process limits the independent evaluation of sintering and ageing. Boutonnet Kizling *et al.* [8] investigated the oxidation of α -SiC (produced from SiO_2 and cokes) by infrared spectroscopy. Low temperature oxidation (973 K) for 16 hours is reported to cause SiC conversions up to 10 %. The rate of oxidation increased by adding steam to the oxygen or by using rhodium loaded SiC. During oxidation rhodium is embedded in the formed silica layer. Application of rhodium on a *prior* oxidized SiC sample does not result in an enhanced rate of SiO_2 formation.

*High surface area SiC as catalyst support
characterization and stability*

Table 2. Thermal and hydrothermal stability of high surface SiC

synthesis of SiC	$S_{\text{BET,initial}}$ (m^2/g)	Ageing process			$S_{\text{BET,final}}$ (m^2/g)	ξ_{SiC} (-)	reference
		environment	T (K)	duration (hour)			
C + SiCl ₄ + H ₂	31	N ₂	1273	4	29	0	Moene [Table 1]
		air	1273	1	17	0.20	
		2v% H ₂ O/N ₂	1023	4	29	0	
		2v% H ₂ O/N ₂	1273	4	19	0.27	
SiO ₂ + cokes	45	O ₂	973	4	n.r.	0.052	Boutonnet Kizling <i>et al.</i> [8]
		O ₂	973	10	n.r.	0.087	
		O ₂	973	16	n.r.	0.094	
SiO ₂ + cokes	13.4	air	1173	3	11.8	n.r.	Pugh [10]
		air	1273	3	10.7	n.r.	
		air	1373	3	9.6	n.r.	
pyrolyzed organosilicon polymer	172	N ₂	1273	4	145	n.r.	Lednor and de Ruiter [11]
		N ₂	1473	4	103	n.r.	
		H ₂ O	1023	4	111	n.r.	
		H ₂ O	1273	4	28	n.r.	
Pt impregn. SiC (SiO + activated carbon)	43	4v% H ₂ O/Ar	1073	16	25	n.r.	Pham- Huu <i>et al.</i> [6]
		4v% H ₂ O/air	1273	10	22	n.r.	

n.r.: not reported

The existing silica layer prevents the direct contact between the metal crystallites and the silicon carbide and hence the catalyzed oxidation of the silicon carbide. This agrees with the similar oxidation behaviour of SiC-5 and nickel loaded SiC-5, *cf.* Fig. 1 and 2. Removal of the residual carbon after conversion mildly oxidizes the SiC surface as shown by the DRIFT analyses.

Pugh [10] reports on the oxidation of low surface area α -SiC analyzed by XPS. The surface area is found to decrease with increasing temperature of oxidation. It can be concluded by combination of their reported oxidation data with surface analysis that the decrease in specific surface area at 1173 K can fully be accounted for by the weight increase owing to oxidation of the silicon carbide.

Lednor and de Ruiter [11] describe that heat treatment in N_2 for four hours at 1273 K of SiC prepared by pyrolysis of a organosilicon polymer at 1873 K [12] resulted in a decrease in specific surface area of 15.7 %. SiC, however, displays a higher thermal stability; heat treatment at 1273 K in N_2 for 4 hours causes a decrease in surface area of 6.5 %. Lednor and de Ruiter reported a surface area decrease for SiC after the hydrothermal treatment at 1023 K and 1273 K of 35 % and 84 %, respectively. Both are considerably higher than that of SiC-5. The synthesis procedure of their very high surface area SiC might suggest a higher thermal stability owing to the much higher synthesis temperature compared to that of SiC-5. This is, however, not the case. The physical rationale of these effects is probably the difference in initial surface area of the two silicon carbides. It is to be expected that their silicon carbide of $172 \text{ m}^2/\text{g}$ is prone to more extensive sintering than SiC-5 ($31 \text{ m}^2/\text{g}$).

The hydrothermal stability of SiC-5 is comparable with that of SiC synthesized by the reaction of SiO with activated carbon reported by Pham-Huu [6]. Similar reductions in surface area are encountered after ageing in steam and air.

4.3.2 Rate of oxidation. It is generally accepted that the passive oxidation of SiC (*i.e.* the formation of a protective silica layer *via* eq. 2) can be assumed to be kinetically controlled by diffusion of the oxidant species (and maybe the backward diffusion of CO) through the growing amorphous oxide surface film which coats the surface [13]. The assumption that the rate of oxidation is inversely proportional to the oxidic layer thickness results in a linear relationship between the layer thickness and the square-root of the time. This relationship has indeed been reported as a suitable manner to describe the oxidation of non-porous SiC granules [10], single crystals [14], and coatings [15]. The applicability is justified by assuming that the formed oxidic film is flat or much thinner than the total size of the particle and, hence, the conversion of SiC is low. From Fig. 1 to 3 a square-root like dependence might be qualitatively deduced between the time and SiC conversion. In the oxidation of high surface area SiC, however, the oxidic layer is certainly not flat while the conversion is extensive, which means that a shrinking un-reacted core model has to be applied for the

*High surface area SiC as catalyst support
characterization and stability*

mathematical description of the oxidation of the primary particles of the high surface area SiC. The conversion of SiC-5 proceeds of course homogeneously throughout the 300 to 425 μm particle. The rate equation [16] that describes the fluid-solid reaction 'aA(fluid) + bB(s) \rightarrow cC(s)' for fixed-size particles and diffusion through the ash as controlling step, is

$$\frac{t}{\tau} = 1 - 3(1-\xi)^{\frac{2}{3}} + 2(1-\xi) = 1 - 3 \left[\frac{r}{R} \right]^2 + 2 \left[\frac{r}{R} \right]^3 \quad (3)$$

in which

$$\tau = \frac{a\rho_s R^2}{6bD_{\text{eff}}C_g} \quad (4)$$

where τ represents the time necessary for complete oxidation, t is the duration of oxidation, ξ is the conversion, r denotes the radius of the non-converted part of the SiC, R is the initial radius, ρ_s is the density of SiO_2 , D_{eff} is the effective diffusion coefficient of O_2 , and C_g represents the concentration of O_2 .

Fitting of eq. 3 with the oxidation data of Figs. 1, 2, and 3 delivers τ and thus the time in which 100% conversion of the SiC is to be expected. The values with corresponding 95% confidence regions are shown in Table 3. The small 95% confidence regions of Table 3 suggest that eq. 3 is a suitable description of the oxidation of high surface area silicon carbide. Fig. 7 displays the experimental and fitted SiC-5 conversion. It is shown that the conversion at the start of the 1080 K oxidation is lower than that given by eq. 3. Oxidation at 1273 K is very well described by eq. 3. Finally, it can be concluded from Table 3 that high surface area SiC cannot be applied at high temperatures and oxidizing environments; total oxidation is to be expected within hundred days at temperatures exceeding 1080 K.

Table 3. Time (τ) necessary for 100 % conversion of SiC-5, 5w% Ni/SiC-5, and HNO_3 treated SiC-5 into SiO_2 by oxidation in air at various temperatures.

T (K)	τ (hours)		
	SiC-5	5w% Ni/SiC-5	HNO_3 treated SiC-5
1080	2232 \pm 68	3518 \pm 97	2169 \pm 63
1180	317 \pm 2	201 \pm 2	291 \pm 4
1280	62.9 \pm 0.2	84.9 \pm 0.8	34.6 \pm 0.2

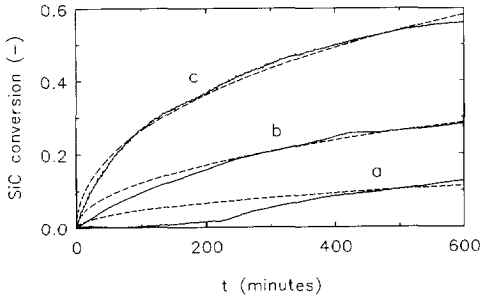


Fig. 7. Conversion of SiC-5 into SiO₂ by air oxidation at (a) 1080 K, (b) 1180 K, and (c) 1280 K. The dashed lines represent rate equation 3 (τ from Table 3)

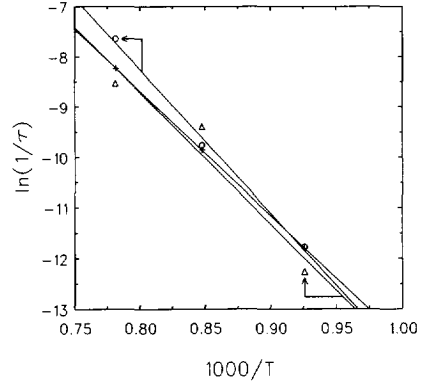


Fig. 8. Arrhenius plots for the oxidation of high surface area SiC assuming the shrinking unreacted core model, (+):SiC-5, (Δ):5w% Ni/SiC-5, (O):HNO₃ treated SiC-5

The activation energy of diffusion can be deduced from the data presented in Table 3. An Arrhenius type dependence is assumed for the diffusion coefficient

$$D = D_0 \cdot e^{\frac{-E_a}{RT}} \tag{5}$$

The activation energy is then obtained by plotting $\ln(1/\tau)$ vs. $1/T$ as depicted in Fig. 8. The activation energy of oxidation has been determined to be 205 ± 13 kJ/mol, 217 kJ/mol, and 205 ± 13 kJ/mol, respectively for the SiC-5, 5w% Ni/SiC-5, and HNO₃ treated SiC-5. Comparison of these numbers with reported data is troublesome, because of the wide range of activation energies reported for the oxidation of non-porous SiC, viz. 45 to 460 kJ/mol [10]. Differences can be ascribed to the use of different types of SiC (α , β , exposed surface face, etc.) and impurities present in the SiC. The results presented above show quite clearly the difficulties in applying SiC at elevated temperature in oxygen containing atmospheres. This can further be envisaged by evaluating the size of the primary SiC particles by assuming that the total surface area originates from non-porous non-agglomerated spheroids, viz.

$$S_{\text{BET}} = \frac{3}{\rho R} \tag{6}$$

*High surface area SiC as catalyst support
characterization and stability*

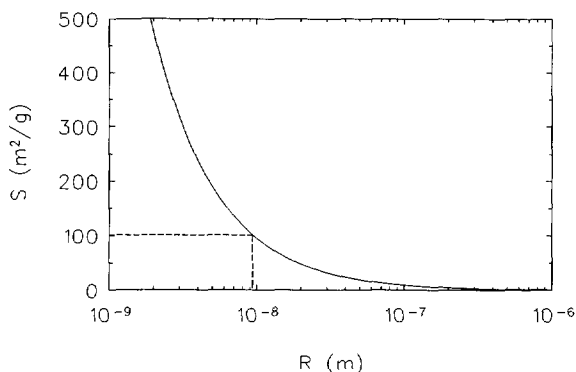


Fig. 9. Surface area as a function of the size of the primary particle, following eq. 6

Fig. 9 displays the correlation between the primary particle size and corresponding surface area. For instance, SiC with a surface area of $100 \text{ m}^2/\text{g}$ consists of primary particles of about 20 nm, $31 \text{ m}^2/\text{g}$ corresponds to about 60 nm particles. The last example represents SiC-5; the SiC crystallite size determined from the XRD line broadening is 13 nm, which is well below the size calculated from the BET surface area. This is probably caused by the presence of stacking faults in the SiC crystallites. While the rate of formation of a SiO_2 layer on SiC by oxidation around 1100 K typically equals a few nanometres per hour it is easily illustrated that the applicability of SiC is very limited at these conditions. This observation is valid irrespective of the type of SiC. Moreover, SiC of very high surface areas is converted to a larger extent than low surface area SiC at identical rates of oxidation (in nm/s).

Vannice *et al.* [1] decomposed tetramethylsilane ($(\text{CH}_3)_4\text{Si}$) into high surface area SiC ($42 \text{ m}^2/\text{g}$). Oxidation of this material in air caused a weight loss from removal of co-deposited carbon. Subsequent heating to 1173 K in air did not result in changes in surface area. The absence of sintering can be explained by the short span of time in which the silicon carbide has been exposed to air at 1173 K, as shown by curve b in Fig. 1. For instance, only 5% of the SiC is converted after 30 minutes at 1180 K.

Ledoux *et al.* [17,18] prepared porous SiC by reacting activated carbon with SiO at 1400 K and reported a high stability of this material at high temperatures in air. The surface area after removal of the residual carbon at 1373 K for 2 hours equalled 30 to $59 \text{ m}^2/\text{g}$. Pre-impregnation of the carbon with a uranium salt and subsequent reaction followed by oxidation at 1273 K results in a SiC- U_xO_y mixture with surface areas between 76 and $131 \text{ m}^2/\text{g}$. From their results the following can be deduced. The reported X-ray diffraction profile after oxidation of the pure SiC shows a considerable decrease in peak heights of SiC which suggest

abundant SiC conversion during oxidation. Calcination of the SiC-U_xO_y mixture causes even complete disappearance of a crystalline SiC signal, only crystalline U₃O₇ and U₃O₈ are visible. Their assumption that the replacement of uranium for carbon in the SiC lattice results in the formation of an amorphous SiC is not convincing. Complete conversion of SiC into SiO₂ is more likely to occur. Finally, the variation in surface area for the SiC and SiC-uranium samples after oxidation lies probably in the difference of oxidation temperature and not necessarily in the use of uranium doped SiC. These new interpretations agree with the results of the thermal stability tests conducted by Pham-Huu *et al.* [6] on the same high surface area SiC and cerium doped SiC (prepared by impregnation of activated carbon with cerium nitrate and subsequent conversion with SiO). Their XRD profiles of Pt/Rh loaded SiC and SiC/Ce used in exhaust catalysis, display a similar broad band at low 2θ as does profile a, b, and d shown in Fig. 4, which was not visible before reaction. This points to the formation of a limitedly ordered silica phase onto both catalyst systems. Utilization of cerium doped SiC is shown to be beneficial for the catalytic performance. Their hypothesis that the presence of cerium would in this case prevent the formation of silica by replacing it with cerium oxide is, however, probably not correct. The conversion of SiC is in our opinion not suppressed but enhanced by the presence of cerium, which can be concluded from the virtually vanished SiC reflections in the XRD profiles of the Pt-Rh/SiC-Ce sample compared to the Pt-Rh/SiC sample. Moreover, the broad band around low 2θ is for the cerium doped SiC significantly larger, which indicates extensive SiO₂ formation. This higher conversion might (following Boutonnet-Kizling [8]) originate from a catalytic action of Ce in the oxidation of SiC (*e.g.* by the destruction of the SiC structure *via* the formation of silicides) or from the larger specific surface area of the Ce doped SiC (95 *vs.* 43 m²/g) which inherently results in higher SiC conversions.

Concluding, the passive oxidation of silicon carbide is extensively investigated in literature. All authors report on the conversion of SiC into silica in oxidizing environments above 1000 K. The formed silica layer reduces the rate of oxidation but does not prevent further oxidation. The mechanism of oxidation repression is diffusion limitation of the oxidizing compound through the silica layer, and hence, this mechanism will only be effective for thick ($> 0.1 \mu\text{m}$) silica layers. This prerequisite for oxidation protection makes the concept of oxidation inhibition *via* an oxidic protective coating inapplicable for SiC based catalyst supports, in which the primary particles are one to two order of magnitude smaller than the required protective silica layer. This means that high surface area silicon carbide is only applicable at high temperatures in the absence of oxygen or steam. Additionally, the thermal stability of silicon carbide in various environments can not be evaluated by the variations in surface area alone. The degree of oxidation in the presence of steam and oxygen has to be determined simultaneously. Most reports on the SiC stability highlight only one of

*High surface area SiC as catalyst support
characterization and stability*

these two aspects which imposes difficulties in the determination of the stability. Moreover, it may lead to incorrect interpretations and unjustified propositions to use SiC at high temperatures in oxidizing environments.

5. CONCLUSION

The potential of high surface area SiC prepared by the catalytic conversion of activated carbon as catalyst support has been studied. The thermal stability in non-oxidizing environments is shown to be excellent. No sintering has been observed in nitrogen atmospheres at temperatures of 1273 K. Utilization of air or the presence of steam at 1273 K results in partial SiC oxidation into SiO₂ and considerable sintering. Oxidation in air at elevated temperatures has been analyzed by thermal gravimetric analysis and DRIFT and is shown to cause substantial SiC conversion (60 to 70 % after 10 hours at 1273 K). Air oxidation of SiC with a surface area of 30 m²/g at 1080 K will result in complete conversion in about 100 days. Additionally the rate of conversion increases with increasing surface area. This implies that high surface area SiC can not be used as a catalyst support in processes operating in oxidizing environments and temperatures above 1080 K, *e.g.* exhaust catalysis and high-temperature combustion. SiC based catalysts are exclusively applicable in high-temperature gas-phase reactions operating in the absence of oxygen or steam. The stability of high surface area SiC in aqueous HF and 5 M HNO₃ solutions is shown to be excellent, which opens up another area of application for SiC, *viz.* strong acidic liquid-phase processes.

SYMBOLS

a, b	stoichiometric coefficients of the gas-solid reaction (mol mol ⁻¹)
C _g	concentration of O ₂ (mol m ⁻³)
D _{eff}	effective diffusion coefficient of O ₂ (m ² s ⁻¹)
E _a	activation energy (kJ mol ⁻¹)
r	radius of the non-converted part of the SiC (m)
R	initial radius (m)
S _{BET}	BET surface area (m ² g ⁻¹)
t	time (hour)
T	temperature (K)
V _{pore}	pore volume (ml g ⁻¹)

Chapter 7

Greek

ξ	conversion (-)
ρ, ρ_s	density of SiC and SiO ₂ , respectively (kg m ⁻³)
τ	time necessary for complete oxidation (hour)

REFERENCES

1. M.A. Vannice, Y-L Chao, and R.M. Friedman, *Appl. Catal.*, **20** (1986) 91.
2. Chapter 5 of this thesis.
3. R. Moene, L.F. Kramer, J. Schoonman, M. Makkee, and J.A. Moulijn, Catalyst Preparation VI, Preprints of Scientific bases for the preparation of heterogeneous catalysts, Louvain-la-Neuve, 1994, p. 379.
4. Chapter 6 of this thesis.
5. M. Boutonnet-Kizling, P. Stenius, S. Andersson, and A. Frestad, *Appl. Catal. B*, **1** (1992) 149.
6. Pham-Huu Cuong, S. Marin, M.J. Ledoux, M. Weibel, G. Ehret, M. Benaissa, E. Peschiera, and J. Guille, *Appl. Catal. B*, **4** (1994) 45.
7. M.F.M. Zwinkels, S.G. Järås, P.G. Govind, and T.A. Griffin, *Catal. Rev. —Sci. Eng.*, **35** (1993) 319.
8. M. Boutonnet-Kizling, J.P. Gallas, C. Binet, and J.C. Lavalley, *Mat. Chem. Phys.*, **30** (1992) 273.
9. J. Rubio, F. Rubio, and J.L. Oteo, *J. Mater. Sci.*, **26** (1991) 2841.
10. R.J. Pugh, *J. Coll. Interface. Sci*, **138** (1990) 16.
11. P.W. Lednor and R. de Ruiter, in "Inorganic and Metal-Containing Polymeric Materials", J.E. Sheets, C.E. Carraher, C.U. Pittman, M. Zeldin, and B. Currel (eds.), Plenum, New York, 1990, p. 187.
12. D.A. White, S.M. Oleff, and J.R. Fox, *Adv. Ceram. Mater.*, **2** (1987) 53.
13. E. Fitzer and R. Ebi, in "Silicon Carbide 1973", R.C. Marshall, J.W. Faust, Jr., and C.E. Ryan (Eds.), University of South Carolina Press, Columbia, 1973, p. 320.
14. Z. Zheng, R.E. Tressler, and K.E. Spear, *J. Electrochem. Soc.*, **137** (1990) 854.
15. L. Philipuzzi, R. Naslain, and C. Jaussaud, *J. Mater. Sci.*, **27** (1992) 3330.
16. Perry's Chemical Engineer's Handbook, R.H. Perry and D. Green eds., 6th ed., 1984, McGraw-Hill, New York, p. 4-9.
17. M.J. Ledoux, S. Hantzer, C. Pham-Huu, J. Guille, and M.P. Desaneaux, *J. Catal.*, **114** (1988) 176.
18. M.J. Ledoux and C. Pham-Huu, *Catal. Today.*, **15** (1992) 263.

Synthesis and thermal stability of Ni, Cu, Co, and Mo catalysts based on high surface area silicon carbide

ABSTRACT

The potential of high surface area silicon carbide as catalyst support has been evaluated regarding the Metal-Support Interaction (MSI), Metal-Support Stability (MSS), and affinity for ion-adsorption. Nickel, cobalt, copper, and molybdenum catalysts have been prepared by incipient wetness impregnation. These SiC based catalysts all show after calcination at 773 K a MSI lower than that of their silica and alumina based counterparts. Reaction of the metal with SiC at elevated temperatures may cause the formation of metal silicides and limits the maximum temperature of application. The MSS of the incipient wetness Ni/SiC catalyst is high. An easily reducible NiO species is retained on the SiC surface after calcination at 1273 K, whereas substantial deactivation of the Ni/Al₂O₃ and Ni/SiO₂ catalysts occurs. These results suggest a high potential of Ni/SiC catalysts in high-temperature processes. Highly dispersed Ni/SiC catalysts (the diameter of the nickel particles equals 4 nm) have been prepared by adsorption of Ni(NH₃)₄(H₂O)₂²⁺ on SiC. The nickel is thus grafted on SiC and SiO₂ as nickel silicate (antigorite). The formed amount of antigorite per unit surface area is on SiC three times higher than that on silica, which points to the presence of a very reactive oxidic layer on the SiC. Calcination at 1273 K causes substantial SiC conversion and nickel sintering, which points to a low MSS, in contrast to the Ni/SiC catalyst prepared by incipient wetness. This probably originates from the intimate contact of the nickel phase with the SiC surface and the resulting catalyzed oxidation of the SiC.

1. INTRODUCTION

Silicon carbide (SiC) supported catalysts are claimed to possess several advantageous properties compared to conventional catalyst supports like alumina and silica [1]. These benefits are based on the unique bulk properties of silicon carbide and comprise the high stability of the support at high temperatures, the high hardness, high thermal conductivity, and the inertness of the surface. It has recently been shown that the thermal stability of high surface area SiC is very high [2,3]. The presence of steam or oxygen in the gas phase at temperatures above 1100 K results, however, in substantial conversion into silica [2]. The inertness of the SiC surface suggests the prevention of reaction of the catalytically active phase with the support which ensures an optimal utilization of the applied metal and allows quick recovery of the metals from spent catalysts by acid washing [4]. This low reactivity of the SiC surface might, however, impose difficulties in catalyst preparation. The scarcity of sites which can act as anchor places for metal-ion adsorption during incipient wetness impregnation or ion-exchange may obstruct the formation of highly dispersed SiC based catalysts. Moreover, significant sintering of the active phase can be foreseen in the absence of an interaction of the active phase and the support. Specialized techniques for applying metals are reported to overcome these problems, an example is impregnation with a solution containing nano-size metal particles synthesized by a micro-emulsion technique [5]. Some interaction between the applied metals and high surface area silicon carbide might, however, exist as can be deduced from the high dispersion (0.7) of Pt (1.9 w%) on oxidized (air, 973 K, 3 hours) SiC (46 m²/g) catalysts achieved by incipient wetness impregnation [1]. The rationale is probably that the partially oxidized surface (< one monolayer) provides Si-O exchange sites, which function as anchoring places for metal deposition. Additionally, Boutonnet-Kizling *et al.* [5] report that the presence of rhodium on the SiC surface catalyzes the oxidation of SiC. This indicates also that a certain interaction is present between the applied active phase and the SiC surface.

To our knowledge reports dealing with both the Metal-Support Interaction (MSI) and the thermal stability of SiC based catalysts are very scarce. We report on the synthesis of Ni, Cu, Co, and Mo catalysts based on silicon carbide prepared *via* incipient wetness impregnation. The applied high surface area SiC has been obtained by the catalytic conversion of activated carbon granulates [6]. The extent of interaction of the metals with the SiC surface has been determined by Temperature Programmed Reduction after calcination of the catalysts at 773 K. The reducibility of the catalysts after calcination at 1273 K is used to evaluate the extent of reaction of the active phase with the support, and thus the Metal-Support Stability (MSS) in air. Additionally, the ion-exchange capacity of the silicon carbide surface has been investigated in order to determine the necessity for utilizing specialized

*Synthesis and stability of Ni, Cu, Co, and Mo catalysts
based on high surface area SiC*

techniques for the application of metals on SiC. For this purpose ion-exchange experiments have been conducted with silicon carbide.

2. EXPERIMENTAL

2.1 *Materials.*

Nitric acid (65%) (>99%) and $\text{Ni}(\text{NO}_3)_2 \cdot 6\text{H}_2\text{O}$ (>99%) were obtained from Merck. Ammonium nitrate (>98%), cobalt nitrate (>99%), ammonium heptamolybdate (>99%), copper nitrate (>99%), and ammonia (>98%) were supplied by J.T. Baker. Pyridine (99%) is obtained from Janssen Chimica. SiO_2 (Si-162-1, $S_{\text{BET}}=30 \text{ m}^2/\text{g}$, $V_{\text{pore}}=0.6 \text{ ml/g}$) and $\alpha\text{-Al}_2\text{O}_3$ (Al-4196, $S_{\text{BET}}=12 \text{ m}^2/\text{g}$, $V_{\text{pore}}=0.6 \text{ ml/g}$) were a gift from Engelhard.

2.2 *Synthesis of high surface area SiC.*

High surface area SiC has been synthesized by Fluidized Bed Chemical Vapour Deposition [6]. Acid and alkaline washed Norit Elorit carbon granulates (300 to 425 μm) loaded with 5w% nickel are converted into SiC by reaction with 45 mol% H_2 , 4.5 mol% SiCl_4 , and 50.5 mol% argon at 1380 K and 100 kPa for 40 minutes. The overall reaction proceeds according to $\text{C} + \text{SiCl}_4 + 2 \text{H}_2 \rightarrow \text{SiC} + 4 \text{HCl}$. The residual carbon present after conversion has been removed by oxidation at 1023 K (4 hours) in dry air. The resulting silicon carbide exhibits a surface area of 31 m^2/g and a nitrogen pore volume of 0.2 ml/g. Determination of the pore volume by adding water until external wetting is perceived, revealed a total pore volume of 1.4 ml/g.

The oxidic layer formed on the SiC during the removal of the residual carbon has been removed from one batch by immersing 1 gram SiC in 100 ml demineralized water containing 2v% hydrogen fluoride for 15 hours. The particles have subsequently been washed to arrive at a pH of 7.

2.3 *Catalyst synthesis.*

2.3.1 *Incipient wetness.* SiC, SiO_2 , and Al_2O_3 have been loaded with 5w% nickel, copper, cobalt and molybdenum by incipient wetness of nickel nitrate, copper nitrate, cobalt nitrate, and ammonium heptamolybdate, respectively, in demineralized water and subsequent calcination in air at 773 K or 1273 K both for 8 hours.

2.3.2 *Ion-exchange.* Prior to ion-exchange, sulfur contaminants present in the silica have been removed by a two hour hydrogenation at 1073 K, causing the surface area to decrease to 20 m^2/g . A jacketed and stirred glass flask is filled with a 150 ml 1 M ammonium nitrate

Chapter 8

solution, nickel nitrate is subsequently added to arrive at nickel contents of 0.1, 0.2, and 0.5 M. The pH was set to 8.3 by bubbling gaseous NH_3 through the liquid, and subsequently 2 gram SiC or desulfurized SiO_2 was added. Stirring commenced at 298 K for 24 hours, in which period the pH of the solution decreased to about 8.1. The particles were removed from the solution by filtering and washed with 300 ml of a 1 M ammonium nitrate solution. The particles were finally dried at 353 K and calcined in air at either 773 K or 1273 K for 8 hours.

2.4 Temperature Programmed Reduction (TPR).

Temperature Programmed Reduction has been performed in a home-made TPR apparatus. Catalyst samples (100 to 200 mg) diluted with non-porous SiC were heated with 0.167 K/s in a hydrogen/argon mixture. Gas composition used were 66v% H_2 in Ar for catalysts prepared by incipient wetness and 5v% H_2 in Ar for the catalysts prepared by ion-exchange, respectively. The hydrogen consumption is determined by a calibrated Thermal Conductivity Detector, comparing the thermal conductivity of the reactor gas feed and the dried reactor effluent. In some cases a FID detector is applied to determine the amount of combustible components (*e.g.* methane) present in the effluent.

2.5 Pyridine adsorption.

Pyridine adsorption is carried out using a STA-1500 thermobalance (Stanton Redcraft) measuring the weight increase and decrease during adsorption and desorption. A helium gas stream saturated with pyridine at 273 K was led over approximately 12 mg desulfurized SiO_2 or SiC. The following temperature programme was applied: (1) heating to 340 K, (2) cooling to 298 K, (3) heating to 773 K all with a rate of 0.0167 K/s, (4) isothermal at 773 K for 3600 s, and (5) cooling to 293 K with 0.0333 K/s.

2.4 X-ray diffraction.

X-ray analysis has been carried out on a Philips powder diffractometer PW1840 using $\text{CuK}\alpha$ radiation.

2.5 High Resolution Electron Microscopy.

Specimens for electron microscopy were made from a suspension of crushed sample in ethanol by putting a few droplets on a holey carbon film supported on a copper-grid. For HREM analysis a Philips CM30 ST FEG electron microscope, equipped with a Field Emission Gun, was operated at 300 kV with a point resolution of 0.20 nm and a line resolution of 0.13 nm.

3. RESULTS

3.1 Metal-Support Interaction (MSI) and Metal-Support Stability (MSS) of SiC based catalysts prepared by incipient wetness.

The MSI and MSS of the Ni, Cu, Co, and Mo catalysts have been determined by TPR. It is assumed that the ease of reduction of the metal oxide is representative for the MSI; close similarity of the temperature at maximum rate of reduction (T_{max}) between the supported and unsupported metal oxide represents a low MSI. The MSS is evaluated using a high temperature calcination step (1273 K, 8 hours in air) and subsequent reduction in a TPR apparatus. A large difference in T_{max} then originates from a low MSS.

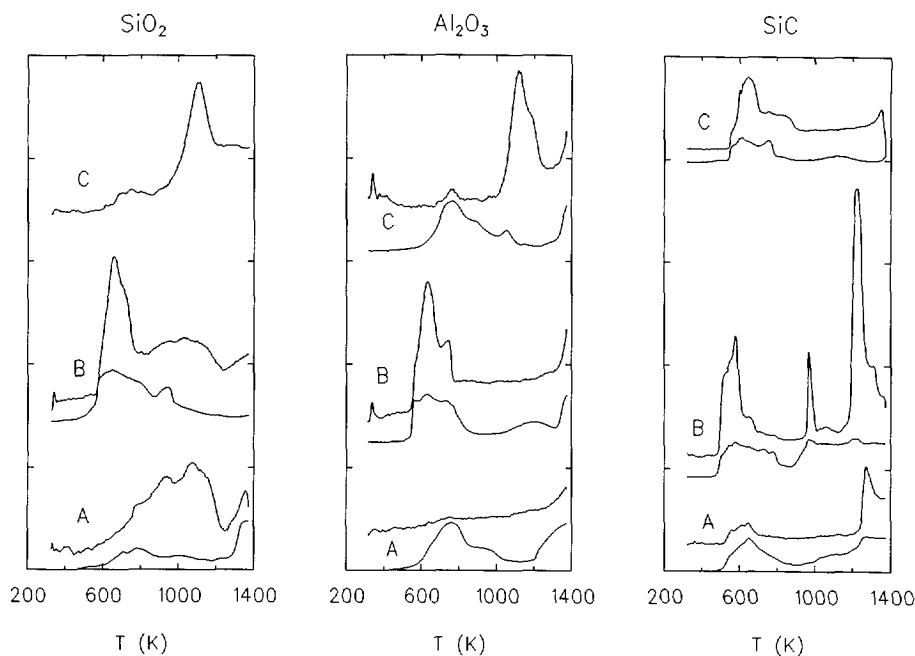


Fig. 1. TPR profiles of nickel catalysts based on silica, alumina, and SiC. Curve A represents the support, B is the 5w% nickel catalyst calcined at 773 K, and C depicts the nickel catalyst calcined at 1273 K. Both the TCD and FID signal are shown (upper and lower curve, respectively)

3.1.1 Nickel. The TPR profiles for the nickel catalysts are shown in Fig. 1. The silica contains sulfate which produces a broad peak from 600 to 1200 K (profile A). The TPR profile of a 5w% Ni/SiO₂ catalyst calcined at 773 K for 8 hours shows a reduction peak between 600 and 700 K, which is in agreement with literature [7,8]. Calcination at 1273 K leads to a considerable increase of the temperature at the maximum reduction rate (T_{max}), viz. from 655 K to 1110 K. A similar trend is observed for the alumina catalysts; an increase in calcination temperature from 773 K to 1273 K corresponds to a shift in the T_{max} from 630 K to 1120 K. Both observations can be explained by solid-state reactions of NiO with the support resulting in nickel silicates and nickel aluminates, respectively [9,10]. The TPR profiles of the NiO/SiC-5 catalysts differ considerably compared to those of the conventionally supported NiO catalysts. It is shown in profile SiC^A that part of the nickel oxide, applied in the carbon conversion process, reduces around 600 K. TPR of the 5 w% Ni/SiC catalyst calcined at 773 K discloses the presence of an easily reducible nickel oxide species as is shown by the low T_{max} (575 K). After the formation of metallic nickel a second, sharp, peak arises at elevated temperatures (955 K) and the FID signal increases concomitantly. Finally, a third large peak appears at 1220 K. Reduction of the same catalyst calcined at 1273 K (SiC^C) displays the presence of nickel oxide which is reduced at a very low temperature, viz. 600 K, pointing to a very stable bulk-like nickel oxide species. Reduction profile SiC^C is also obtained for a Ni/SiC catalyst, which is calcined at 773 K, reduced at 1373 K, and subsequently calcined at 1273 K for 8 hours. Fig. 2 displays the XRD profile of the 5w% Ni/SiC catalyst after calcination at 1273 K and subsequent reduction at 773 K (1 hour). It is shown that no crystalline NiO is present. The diameter of the nickel crystallites determined from XRD line-broadening equals 22 nm.

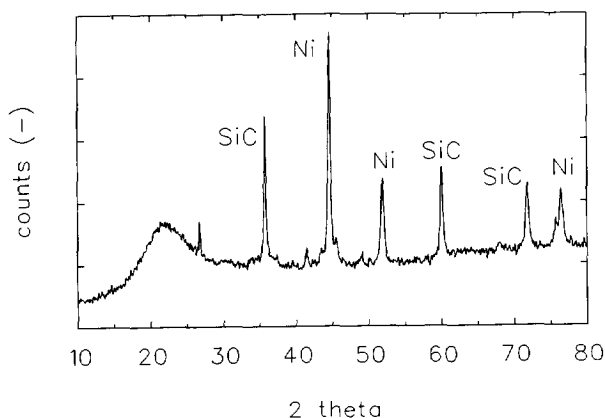


Fig. 2. XRD profile of 5w% Ni/SiC-5 after calcination at 1273 K (8 hours) and subsequent reduction at 773 K.

*Synthesis and stability of Ni, Cu, Co, and Mo catalysts
based on high surface area SiC*

3.1.2 Copper. The TPR profiles of the copper catalysts are displayed in Fig. 3. Calcination at 773 K results in a easily reducible copper oxide (T_{max} : 470 K, 480 K, and 435 K, respectively for the silica, alumina and silicon carbide based catalysts), whereas the copper oxide is reduced at higher temperatures in all cases after calcination at 1273 K (T_{max} : 550 K, 670 K, and 530 K, respectively for the silica, alumina and silicon carbide). The increase in T_{max} is highest for the alumina catalyst. The copper oxide on SiC is in all cases most easily reduced. An additional peak arises in profile SiC^A of the CuO/SiC catalyst at approximately 1200 K; the FID signal increases concomitantly.

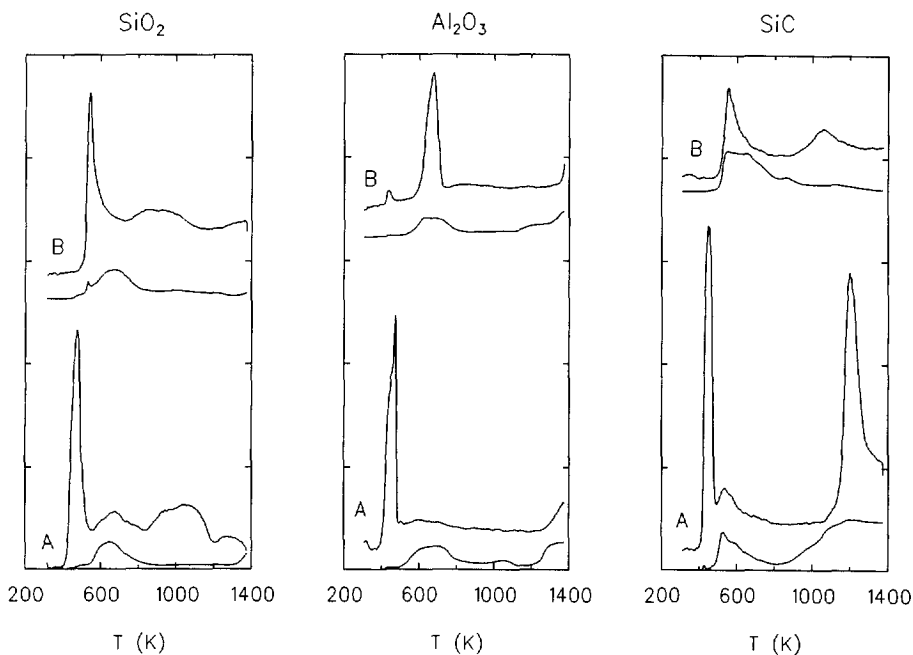


Fig. 3. TPR profiles of copper catalysts based on silica, alumina, and SiC. Curve A represents the 5w% copper catalyst calcined at 773 K, and B depicts the copper catalyst calcined at 1273 K. Both the TCD and FID signal is shown (upper and lower curve, respectively).

3.1.3 Cobalt. The TPR profiles of the cobalt based catalysts are displayed in Fig. 4 and 5. Silica supported cobalt oxide calcined at 773 K exhibits the maximum rate of reduction at 685 K. Calcination at 1273 K causes a T_{max} shift to 1100 K. The silicon carbide based catalyst displays after calcination at 773 K a similar behaviour as the nickel catalyst; three peaks appear during a TPR experiment *viz.* at 605 K, 950 K, and 1210 K. High temperature calcination (1273 K) results in a single reduction peak at 1175 K.

3.1.4 Molybdenum. The TPR profiles of the molybdenum catalysts are displayed in Fig. 6. Two peaks can be distinguished in the reduction of supported MoO_3 . The peak maxima in the range silica, alumina, SiC are situated at 815 K, 820 K, and 770 K for the low temperature peak, whereas the high temperature peak is located at 1085 K, 995 K, and 960 K, respectively. The reduction maxima for the SiC supported MoO_3 are in both cases the lowest.

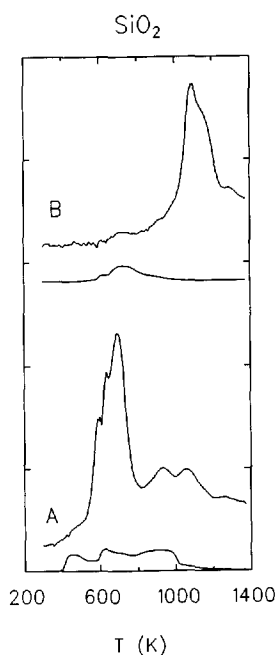


Fig. 4. TPR profiles of 5w% Co/SiO₂ calcined at 773 K (A) and 1273 K (B). Both the TCD and FID signal is displayed (upper and lower curve, respectively)

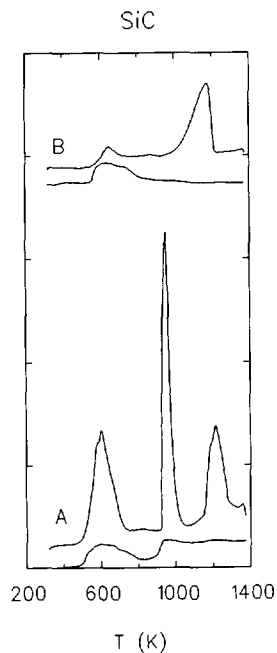


Fig. 5. TPR profiles of 5w% Co/SiC calcined at 773 K (A) and 1273 K (B). Both the TCD and FID signal is displayed (upper and lower curve, respectively)

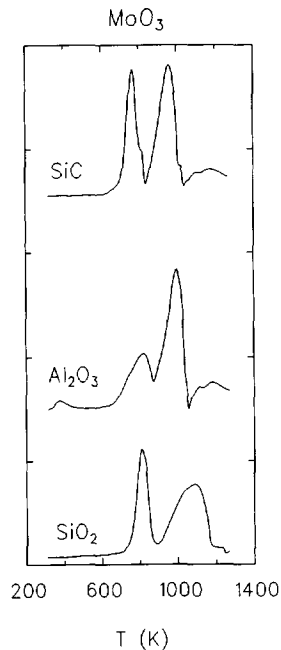


Fig. 6. TPR profiles of molybdenum catalysts, 5w% Mo on SiO₂, Al₂O₃, and SiC, calcined at 773 K

*Synthesis and stability of Ni, Cu, Co, and Mo catalysts
based on high surface area SiC*

3.2 Metal-Support Interaction and Metal-Support Stability of Ni/SiC and Ni/SiO₂ catalysts prepared by ion-exchange.

In this section the ion-exchange capability of high surface area SiC will be compared to that of the desulfurized silica. The amount of adsorbed nickel has been analyzed by Atomic Absorption Spectrometry (AAS). The interaction between the adsorbed nickel and the support is determined by TPR, using a 5v% hydrogen in argon gas stream. Table 1 will serve as a reference in which the data obtained from AAS and TPR are outlined. Nickel contents after ion-exchange measured by AAS vary between 0.57 w% and 3.77 w% in the case of SiO₂, whereas significantly higher nickel contents, viz. between 3.04 and 11.2 w%, are found for SiC using an identical nickel concentration. These results are remarkable considering the assumed scarcity of exchange sites on SiC.

Table 1. Amount nickel (in weight percent and atoms/nm²) present on SiO₂ and SiC after ion-exchange analyzed by AAS and the contributions of moderately and strongly interacting NiO determined by TPR (expressed as NiO^{700 K} and NiO^{800 K} or NiO^{900 K}, respectively), as a function of nickel concentration of the exchange solution (Ni²⁺ (aq))

Ni ²⁺ (aq) mol/l	SiO ₂		
	Ni ^{AAS} w% , at./nm ²	NiO ^{700 K} %	NiO ^{800 K} %
0.1	0.57 , 2.92	4	96
0.2	1.33 , 6.82	22	78
0.5	3.77 , 19.3	33	67
Ni ²⁺ (aq) mol/l	SiC		
	Ni ^{AAS} w% , at./nm ²	NiO ^{700 K} %	NiO ^{900 K} %
0	0.27 , 0.92	100	0
0.1	3.04 , 10.4	56	44
0.2	9.70 , 33.2	47	53
0.5	11.2 , 38.3	45	55
0.2 *HF	4.90 , 16.8	43	57

*HF: HF washed SiC and subsequent ion-exchange

Moreover, the number of exchange sites on SiC appears to exceed those on SiO₂ as indicated by the higher nickel surface concentrations (2.92 at./nm² for silica vs. 10.4 at./nm² for SiC at Ni²⁺(aq)=0.1 M). Removal of the oxidic layer from the SiC causes a reduction of 50 % of the quantity of nickel adsorbed on the support. The adsorbed amount per unit surface area, however, still exceeds by far that of silica.

The results of the TPR analyses of the ion-exchanged silica samples after calcination at 773 K are displayed in Fig. 7. A broad NiO reduction band appears with a T_{max} of 800 K, which is accompanied by a second peak around 700 K for higher Ni²⁺ concentrations. It should be noted that bulk NiO exhibits a reduction peak at 600 K. The low temperature region peak corresponds with the reduction of moderately interacting NiO, whereas the high temperature peak agrees with the reduction of nickel oxide in strong interaction with silica. This indicates that the quantity of both moderately and strongly interacting NiO increases with increasing amounts of nickel in the ion-exchange solution. The relative contributions can be quantitatively determined by peak deconvolution of the TPR profiles and the results have been presented in Table 1. The relative amount of strongly interacting NiO decreases with increasing NiO loadings. Calcination of the Ni/SiO₂ system causes a shift in T_{max} to 1175 K, which is comparable to that of the incipient wetness system.

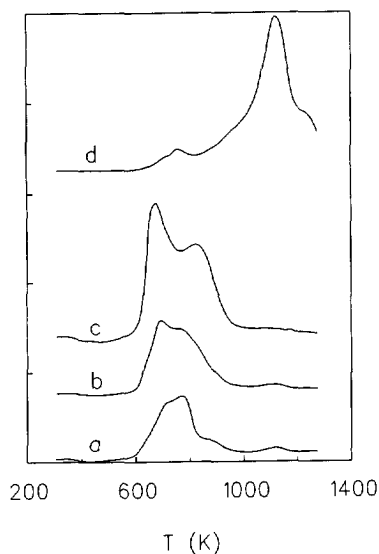


Fig. 7. TPR profiles of calcined (773 K) Ni/SiO₂ catalysts synthesized by ion-exchange at pH: 8.3 with Ni²⁺ (aq); (a): 0.1 M, (b): 0.2 M, (c) 0.5 M, (d) 0.5 M calcined at 1273 K

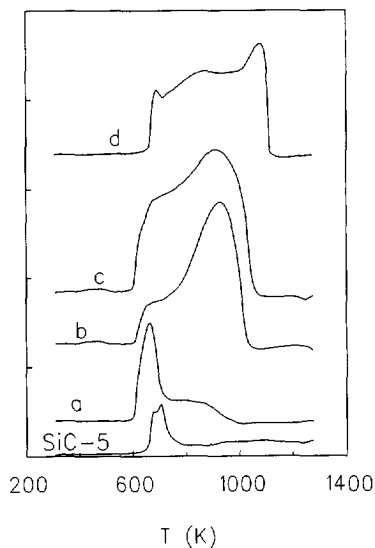


Fig. 8. TPR profiles of calcined (773 K) Ni/SiC catalysts synthesized by ion-exchange at pH: 8.3 with Ni²⁺ (aq); (a): 0.1 M, (b): 0.2 M, (c) 0.5 M, (d) 0.5 M calcined at 1273 K

*Synthesis and stability of Ni, Cu, Co, and Mo catalysts
based on high surface area SiC*

The corresponding TPR profiles of the ion-exchanged Ni/SiC catalysts are shown in Fig. 8. Profile SiC-5 corresponds to pure SiC, in which the NiO originating from the conversion is reduced around 700 K. Ion-exchange results in a Ni-adsorption which is higher than that on silica; NiO is formed after calcination which exhibits behaviour corresponding to a mixture of moderately and strongly interacting NiO, both in roughly equal amounts. Both the moderately and strongly interacting nickel increase with increasing Ni^{2+} concentration. Calcination at 1273 K results in a broad reduction peak initiated just before 700 K and ending at 1100 K. This reduction profile is similar to that of the sample calcined at 773 K, which might suggest that the reaction between the nickel and SiC during calcination is limited.

XRD analyses of the ion-exchanged SiC samples and Ni/SiC catalyst prepared by incipient wetness with identical Ni loadings are displayed in Fig. 9 and 10, respectively. The ion-exchanged silica samples were totally X-ray amorphous. The presence of crystalline fcc NiO is clearly visible in the incipient wetness samples, whereas the ion-exchanged samples exhibit almost no crystalline NiO diffraction patterns; profound NiO diffraction lines appear only after calcination at 1273 K. The SiC reflections diminish concomitantly.

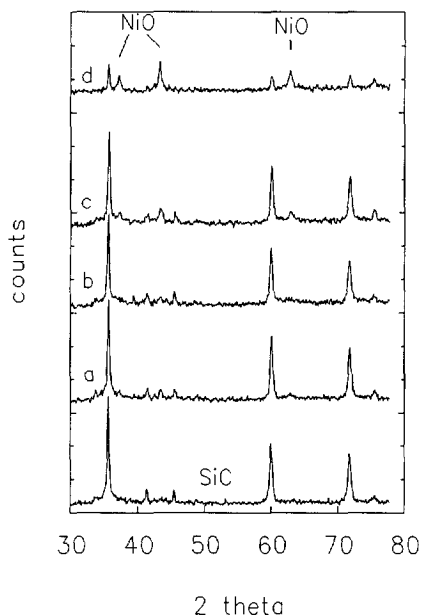


Fig. 9. XRD profiles of calcined (773 K) Ni/SiC catalysts prepared by ion-exchange at pH:8.3 with Ni-loading; (a): 3w%, (b): 9.7w%, (c): 11.2w%, (d) 11.2w% calcined at 1273 K

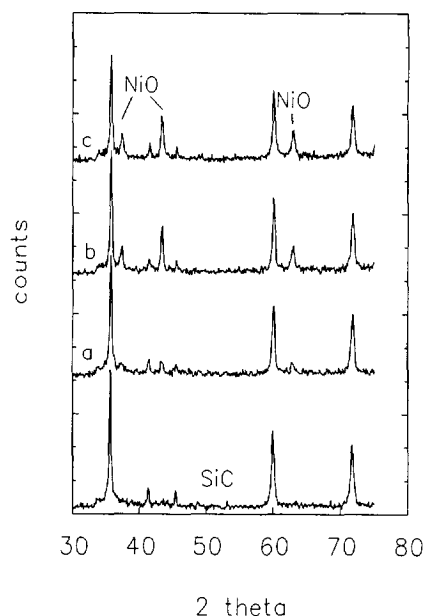


Fig. 10. XRD profiles of calcined (773 K) Ni/SiC catalysts prepared by incipient wetness, Ni loading; (a): 3 w%, (b): 9.7 w%, (c) 11.2 w%

The influence of HF treatment of the silicon carbide prior to ion-exchange on the adsorption properties is shown in Fig. 11. A significant decrease in Ni-adsorption (around 50%) is caused by the HF-treatment (Table 1). This reduction is evenly distributed between the bulk-like NiO and NiO interacting with the SiC surface. Calcination at 1273 K discloses, however, the presence of larger amounts of bulk-like NiO compared to the untreated ion-exchanged SiC. Additionally, the presence of strongly interacted nickel appears as shown by the peak at 1100 K.

3.2.1 High Resolution Electron Microscopy. Micrographs of the ion-exchanged SiC (0.2 M Ni^{2+}) after calcination at 773 K and reduction (973 K) are envisaged in Figs. 12 and 13. The nickel oxide morphology on the SiC is easily identified as nickel silicate as shown by the abundance of lamellar structures. On the basis of the morphology and the diffraction patterns it can be concluded that the nickel silicate is of the antigorite type. Subsequent reduction at 973 K results in nickel particles with a mean diameter of 4.2 nm as shown by Fig. 13.

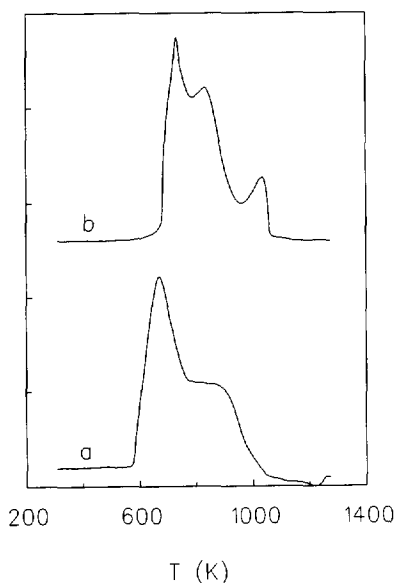


Fig. 11. TPR profiles of ion-exchanged HF-treated SiC-5 (0.2 M Ni^{2+}) after calcination at (a) 773 K and (b) 1273 K

*Synthesis and stability of Ni, Cu, Co, and Mo catalysts
based on high surface area SiC*



50 nm
Fig. 12. Micrograph of ion-exchanged SiC after calcination at 773 K



50 nm
Fig. 13. Micrograph of ion-exchanged SiC after calcination at 773 K and subsequent reduction at 973 K

3.2.2 Pyridine adsorption

The results of pyridine adsorption are displayed in Table 2. It is assumed that one molecule pyridine adsorbs on one hydroxyl group. Silica possesses, as expected, the highest silanol density, compared to SiC. The HF treatment of SiC causes a 50% decrease in silanol density indicating that a portion of the initial ion-exchange capacity has still been retained after removal of major part of the oxidic layer as shown in Table 1.

Table 2. The hydroxyl density of the applied supports determined by pyridine adsorption

	SiO ₂	SiC	SiC HF treated
Si-OH density (groups/nm ²)	7.94	5.65	2.58

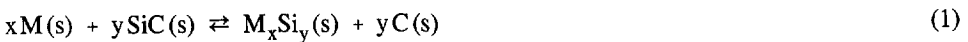
4. DISCUSSION

Comparison of the interaction of the active phase with the support is very important in evaluating the characteristics of SiC based catalysts compared to alumina and silica based catalysts. Literature reports mainly discern a Weak or a Strong Metal-Support Interaction (WMSI and SMSI, respectively). The SMSI effect described in literature [21-23] is mainly

concerned with changes of the active phase imposed by a high temperature reduction. This results in partial coverage of the active phase by the support (Pt/TiO₂) or reaction of the support with the active phase (Ni/SiO₂). The greater the change in catalyst properties (*e.g.* hydrogen chemisorption, rate of benzene hydrogenation) the stronger is the Metal-Support Interaction. It can be argued that the property 'Metal-Support Interaction' has to be replaced by the property 'Metal-Support Stability'. The Metal-Support Stability is a measure of stability of the entire catalytic system, *i.e.* active phase and support. Differences in catalytic behaviour and chemisorption which are attributed to the SMSI-*state* are mainly the resultant of a "reaction" of the metal with the support. Hence, every supported catalyst possesses a SMSI-*state* if calcined or reduced at a temperature at which an extensive reaction takes place between the metal and the support (*e.g.* formation of a solid solution). It would be more suitable to refer to a stability rather than an interaction because thus a distinction is made between catalytic systems which exhibit a SMSI effect after reduction/calcination at low and high temperature. Besides, stability is an intrinsic property, whereas an interaction refers to a property that depends on the catalyst treatment. Hence, evaluation of the Metal-Support Interaction in this section is performed for catalyst systems after identical calcination treatments (*i.e.* 773 K in air). The Metal-Support Stability is then evaluated by determination of the Metal-Support Interaction after calcination at 1273 K in air). A correlation between the reduction behaviour in TPR and the MSI is assumed in both cases.

4.1 Catalysts prepared by incipient wetness.

Both the cobalt and nickel catalyst supported by SiC and calcined at 773 K display an unusual reduction pattern. Three TCD peaks appear; the first one arises from the reduction of nickel oxide or cobalt oxide. The second TCD peak is accompanied by a sharp increase in the FID signal, which leads to the conclusion that it probably originates from the formation of metal silicides, *viz.* Ni_xSi_y or Co_xSi_y and a carbon phase according to reaction 1, which is gasified under TPR conditions according to reaction 2.



Similar solid-state reactions are described by Chou *et al.* [11], who reported extensive reaction of SiC with Pt in a helium atmosphere at temperatures exceeding 1270 K. They observed the formation of periodic structures consisting of alternating layers of platinum silicides and carbon. Reaction of SiC with Ni and Fe is reported to occur within the temperature range of 923 to 1373 K [20]. The products of the reaction of nickel with SiC are

*Synthesis and stability of Ni, Cu, Co, and Mo catalysts
based on high surface area SiC*

Ni₂Si, Ni₅Si₂, and solid carbon. The temperature at which this reaction initiates had not been determined. The peak at 950 K (Co) and 955 K (Ni) in the TPR profile originates from the intimate contact between the metal and support causing the first SiC layer to react with nickel or cobalt. The solid carbon gasifies simultaneously causing hydrogen consumption and methane formation, detected by both the TCD and FID, respectively. Support for this suggested mechanism is that cobalt and nickel impose this second peak, whereas copper does not. Gasification of solid carbon at these temperatures necessitates atomic hydrogen and thus a metal with a high capacity for splitting hydrogen, *i.e.* Co and Ni. The fact that the temperature of the second peak is similar in both cases indicates that the reactivity of the formed carbon determines the starting point of gasification. Finally, at 1220 K reaction 1 accelerates and starts to consume the SiC considerably. The above described mechanism is outlined in Fig. 14. The most remarkable feature of this incipient wetness prepared 5w% Ni/SiC-5 system is, however, its behaviour after calcination at 1273 K for 8 hours. Nickel oxide reduction occurs in a broad region of which the T_{max} (640 K) is similar to that of Ni/SiO₂ and Ni/Al₂O₃ catalysts calcined at 773 K. This points to a high Metal-Support stability causing a moderate MSI-state. It has been reported that 45% of the SiC is converted into SiO₂ during calcination of the 5w% Ni/SiC catalyst at 1273 K [2]. The formed Si-O layer, however, does not correspond to bulk SiO₂ as is shown by the differences in reduction temperatures of NiO in SiC and SiO₂ after calcination at 1273 K.

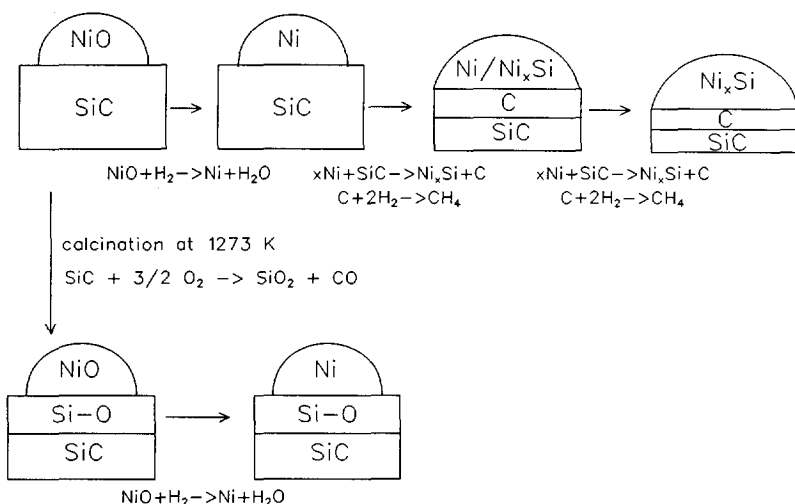


Fig. 14. Mechanism of the formation of nickel silicides on SiC during TPR and the inhibition thereof by high temperature oxidation

The appearance of a broad shoulder in the reduction profile of this Ni/SiC sample in the temperature range of 700 to 900 K suggests the presence of nickel in interaction with the support [7]. The oxidic layer probably prevents reaction of metallic nickel with the underlying silicon carbide up to temperatures of 1373 K as is shown by the absence of the second and third peak in the TPR profile. XRD analysis of this sample after reduction at 773 K shows only the presence of crystalline Ni with a diameter of 22 nm, which is common for low temperature calcined Ni/SiO₂ catalysts prepared by impregnation [7]. The high temperature treatment caused neither a substantial sintering of the nickel oxide nor extensive reaction between nickel and SiC. Fig. 15 shows that a complete reduction of NiO is achieved below 1000 K for all catalysts after calcination at 773 K. The amount of nickel oxide reduced in the high temperature region (above 1000 K) relative to the total reduced amount NiO, increases to over 90 % for the silica and alumina based catalysts calcined at 1273 K. Complete reduction of NiO is achieved in the low temperature region for the SiC based catalyst calcined at 1273 K. The presence of Ni₂O₃ can rationalize the more than stoichiometric hydrogen consumption of the Ni/SiC catalyst. High temperature calcination decreases the maximum reducible NiO amount for the SiO₂ catalyst to 70%. Although some difficulties are encountered in integrating the reduction peak owing to the presence of sulfur in the SiO₂, this may point once more to a significant difference between the interaction of NiO on partially oxidized SiC and on SiO₂.

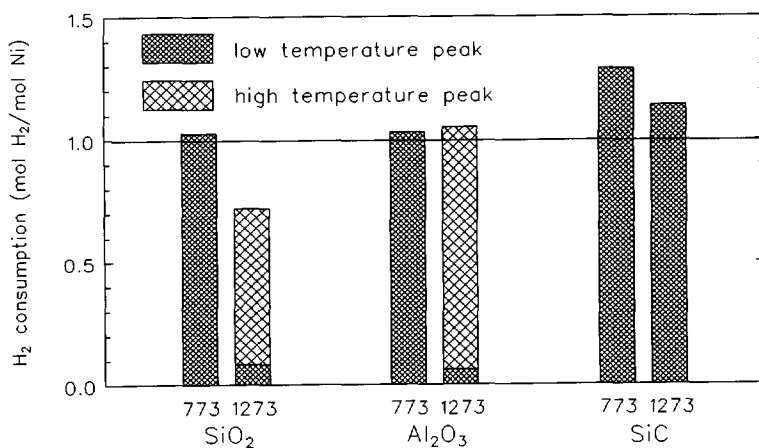


Fig. 15. Conversion of NiO on SiO₂, Al₂O₃, and SiC-5 calcined at 773 and 1273 K, calculated from the total hydrogen consumption, 1000 K is used to distinguish a low and high temperature region

*Synthesis and stability of Ni, Cu, Co, and Mo catalysts
based on high surface area SiC*

The Metal-Support Interaction of Co/SiO₂ (T_{max} =690 K) is higher than that of Co/SiC (T_{max} =600 K) catalysts. The T_{max} of bulk CoO lays around 600 K [12], indicating that the MSI on SiC is very low.

The reduction of unsupported CuO is reported to occur in the range 610 K to 640 K and application of copper on silica reduces the T_{max} by about 70 K compared to bulk CuO [13]. It is suggested [13] that the support acts merely as a dispersing agent, enhancing the reactivity of the oxide toward reduction. Cu/SiC displays the lowest T_{max} compared to silica and alumina supported Cu. This might either be induced by a higher dispersion obtained for the Cu/SiC catalyst, or a weaker MSI of the Cu/SiC catalyst at dispersions similar to that on silica and alumina. The CuO conversions achieved in TPR are displayed in Fig. 16. The ratio H₂/Cu is in all cases lower than 1 indicating either the presence of Cu₂O or the presence of non-reducible copper oxide. Calcination at 1273 K decreases this ratio, which is most pronounced for the Cu/SiC catalyst.

The Metal-Support Stabilities of the SiC based copper and cobalt catalysts is similar to that of the corresponding silica based catalysts. Calcination at 1273 K causes a significant shift in reduction temperature, due to reaction of the metal with the support, resulting in higher Metal-Support Interactions. It should be noted that reactions of the metal with SiC (according to reaction 1) might limit the range of application in reducing environments. The maximum temperature of operation for Co/SiC catalysts lies just in front of the second peak maximum, *i.e.* 950 K. Cu/SiC catalysts possess a wider application range, *i.e.* up to 1015 K.

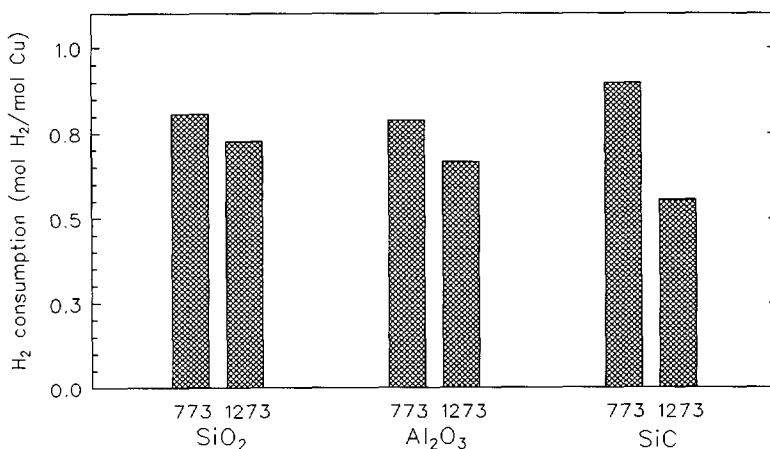


Fig. 16. Conversion of CuO_x during TPR for silica, alumina and silicon carbide based catalysts after calcination at 773 K and 1273 K

The molybdenum catalysts display in all cases a double reduction peak. Arnoldy *et al.* [14] attributed both peaks to the presence of two oxidic Mo phases. They reported for silica that the low temperature peak corresponds to the complete reduction of Mo^{6+} surface species and reduction of bulk MoO_3 to MoO_2 . The formed MoO_2 is subsequently converted into metallic Mo in the high temperature peak. The formation of water during reduction decreases the reduction rate due to kinetic (blocking of reduction nuclei) and thermodynamic limitations ($\text{MoO}_3 + \text{H}_2 \rightleftharpoons \text{MoO}_2 + \text{H}_2\text{O}$). During the reduction of the surface species formed water is easily removed, which, combined with a low Metal-Support Interaction, causes the reduction in the low temperature region. Finally, reduction of bulk-like MoO_3 on silica is then thermodynamically limited by the formation of water. The interaction of Mo species with alumina is much larger. This results in the reduction of Mo^{6+} surface species in the high temperature peak, while Mo^{6+} bi-layer and multi-layer species are reduced to Mo in the low temperature region. The presence of water is in both cases not limiting, owing to the high dispersion of Mo on Al_2O_3 [14]. Assuming that the interaction of MoO_3 with the SiC surface is comparable to that on silica the following observations might hold. The interaction between Mo^{6+} surface species and SiC is lower compared to that on silica (T_{max} : 770 K and 815 K, respectively). Additionally, bulk MoO_3 is more easily reduced on the SiC surface. The contribution of surface species and bulk MoO_3 is determined from the TPR peak areas. The amount of Mo^{6+} surface species relative to the total amount of Mo^{6+} species is determined to be 4.4 and 5.2 %, for the SiO_2 and SiC, respectively, which corresponds with a concentration of the surface species of 0.46 and 0.55 at./nm^2 , respectively. This agrees quite well with results of Arnoldy *et al.* [14] who report that 50% of the molybdenum of a 1.5 at.Mo/nm^2 - SiO_2 catalyst is present as a Mo^{6+} surface species. These relatively low amounts of Mo surface species cause difficulties in determining the MSI of Mo^{6+} with the SiC surface. The amount of Mo^{6+} -surface species is so low that no reliable conclusions can be drawn. The observation, however, that reduction of bulk MoO_3 is evidently lower on SiC than that on silica remains.

The Metal-Support Stability of the Mo based catalysts has not been analyzed by calcination at 1273 K, because of the high volatility of MoO_3 at that temperature, which limits the application of Mo catalysts at high temperatures.

4.2 Catalysts prepared by ion-exchange.

The ion-exchange experiments had been carried out to investigate the necessity for application of special techniques in order to equip the assumed inert surface of SiC with catalytically active material. The OH-groups on the surface of silica are responsible for the ion-exchange capacity. Pyridine adsorption shows that the OH-density on silica equals 7.9 groups/ nm^2 , which is typical for silica which is dehydrated at low temperature (around

*Synthesis and stability of Ni, Cu, Co, and Mo catalysts
based on high surface area SiC*

400 K) [15]. The hydroxyl density on SiC is 70% of that on silica, while a further decrease (to 32%) is found after the HF treatment of SiC. These OH-densities and additional surface information (*viz.* the existence of a Si-O-C surface phase) previously obtained [2] indicate that the surface of SiC resembles to some extent that of silica. This suggests that the synthesis procedures applicable for silica based catalysts can be of use in the preparation of SiC based catalysts. Several procedures for ion-exchange of nickel on silica have been reported in literature *e.g.* [9,16,17]. The influence of pH ($6 < \text{pH} < 11$) and type of nickel complex (ammonium, ethylenediamine) have been studied in detail. Clause *et al.* [16] report that ammoniacal solutions of nickel nitrate at pH 8.3 consist of 45% $\text{Ni}(\text{NH}_3)_4(\text{H}_2\text{O})_2^{2+}$, 20% $\text{Ni}(\text{NH}_3)_5\text{H}_2\text{O}^{2+}$, and 35% $\text{Ni}(\text{NH}_3)_6^{2+}$. The tetramine complex is suggested to play an important role in grafting nickel on silica. Thus nickel silicate structures are formed, which are not easily reduced. In order to obtain highly dispersed nickel without the concomitant formation of silicate, the use of ethylenediamine as ligand has been suggested. Assuming that the ion-exchange capacity of silica is directly proportional to the OH-density [16], one square nanometre can accommodate a maximum of 8 nickel ions. This means that a large part of the total (19.3 at./nm^2) amount of Ni^{2+} adsorbed on silica from a 0.5 M Ni^{2+} solution cannot be deposited by a ion-exchange mechanism. The same considerations are valid for *all* SiC ion-exchange experiments because in all cases more nickel is adsorbed than can be accounted for by an ion-exchange mechanism alone. The XRD analyses show that during ion-exchange of Ni on silica and SiC no significant formation of bulk fcc-NiO has occurred in contrast to the Ni/SiC samples prepared by incipient wetness [2]. This absence of bulk NiO agrees with results obtained by several authors [9,17-19] who report the formation of a nearly X-ray amorphous interaction compound, nickel antigorite type, after ion-exchange of nickel on silica at pH values above 8. The presence of these silicate structures on SiC is confirmed by HREM analysis. This means that the SiC surface does not only exhibit a strong affinity for metal ions in solution, but that these adsorbed ions are strongly bound to the SiC surface. Reduction at 900 K results in highly dispersed Ni/SiC catalysts ($d_{\text{Ni}} = 4.2 \text{ nm}$). For convenience, the results of the pyridine adsorption and TPR analyses have been combined in Fig. 17. The reduction peak at 800 K in TPR profile 7^a confirms the presence of nickel silicates at nickel loadings of 2.9 at./nm^2 . The amount nickel silicate increases proportionally with increasing amounts of deposited nickel, while a second nickel compound emerges as well which reduces around 700 K. The relative amount of this Ni-compound increases moving to higher nickel loadings. This nickel species probably consists of very well dispersed NiO, considering the fact that it is X-ray amorphous and easily reduced.

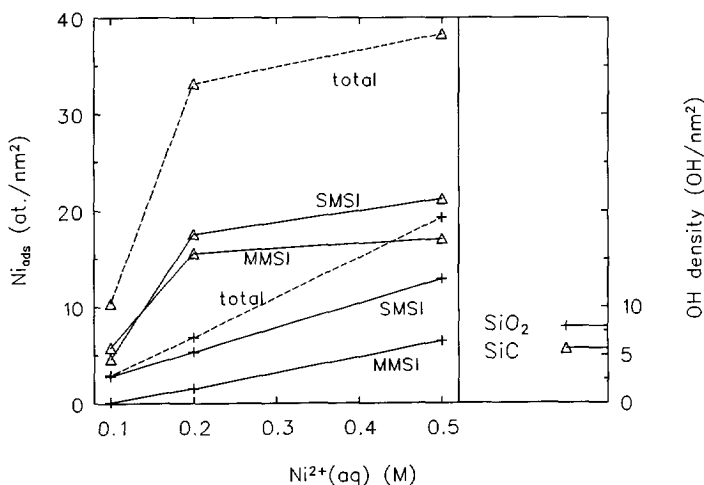


Fig. 17. Adsorbed Ni vs. $Ni^{2+}(aq)$ for silica (+) and SiC (Δ) separated in Moderate and Strong Metal-Support Interaction (MMSI and SMSI)

The ion-exchanged silicon carbide displays another trend. Both very well dispersed NiO and nickel silicates are present in equal amounts for the entire range of nickel loadings. Compared to silica the total amount of deposited NiO (19.3 at./nm² vs. 38.3 at./nm²) is larger, and the temperature of Ni-silicate reduction ($T_{max}(Ni\text{-silicate}/SiO_2) = 800$ K, $T_{max}(Ni\text{-silicate}/SiC) = 975$ K) is higher on SiC. The high amounts of deposited nickel probably originate from the dissolution of minor amounts of silica during the ion-exchange process, causing alternative adsorption of nickel ions and re-adsorption of silica and thus the formation of multi-layer silicate structures [18].

It is striking that the silica-like layer existing on the silicon carbide is in this respect much more reactive than its SiO_2 counterpart, resulting in higher amounts and more strongly interacted adsorbed nickel oxide. The HF treated SiC adsorbs half of the amount of Ni-ions compared to the untreated silicon carbide. This correlates very well with the decrease in pyridine adsorption of 50% and thus the hydroxyl concentration. It appears as if the hydroxyl concentration on the SiC determines to a certain extent the adsorption of Ni^{2+} although the ion-exchange mechanism is not operative. The amount of OH surface species correlates perhaps with the reactivity of the silica layer.

The Metal-Support Stability of the ion-exchanged Ni/SiC catalyst is low compared to the Ni/SiC catalyst prepared by incipient wetness. Although the TPR profile does not change extensively after calcination at 1273 K, cf. curve 8^c and 8^d, X-ray analysis discloses a significant increase in NiO crystallinity (higher and thinner NiO-peaks in curve 9^d).

*Synthesis and stability of Ni, Cu, Co, and Mo catalysts
based on high surface area SiC*

Additionally, conversion of SiC into SiO₂ occurs concomitantly during the calcination as can be derived from the significant decrease in SiC reflections, *cf.* curve 9^c and 9^d. The difference in Metal-Support Stability of the Ni/SiC catalysts prepared by incipient wetness and ion-exchange is probably caused by the intimate contact between the nickel silicate and the underlying silicon carbide. After decomposition of the silicates into well-dispersed NiO during calcination, the silicon carbide is catalytically oxidized into SiO₂, comparable to the enhanced rate of oxidation when rhodium is present on SiC [24]. The silicon carbide and the NiO sinter significantly during oxidation.

5. CONCLUSION

Silicon carbide based catalysts differ from silica and alumina based catalysts with respect to their Metal-Support Interaction and Metal-Support Stability. The Metal-Support Interaction of Ni, Cu, Co, and Mo catalysts after calcination at 773 K is in all cases lower than that of silica and alumina based catalysts as shown by the decreased temperature of reduction. Reaction of Ni, Co, and Cu with SiC at elevated temperatures, however, can limit the application of these catalysts, due to the destruction of the support material and deactivation of the catalytically active material. In this case the onset of formation of metal silicides is the limiting factor as found for the Ni, Cu, and Co catalysts. The Metal-Support Stability of Ni/SiC catalysts is very high; after calcination at 1273 K an easily reducible nickel species is retained, while no significant sintering occurs ($d_{\text{Ni}} = 22$ nm), whereas the alumina and silica based catalysts show extensive reaction between Ni and the support resulting in high reduction temperatures.

The surface of SiC is mildly oxidized which enables the use of well-known catalyst preparation techniques similar to those used for the application of metal on silica. Highly dispersed Ni/SiC catalysts ($d_{\text{Ni}} = 4.2$ nm) with high Ni-loadings have been prepared *via* an ion-exchange technique. The existing surface silica layer on SiC exhibits an activity for adsorption of metal-ions which is higher than that of silica and causes the formation of nickel silicate structures. The Metal-Support Stability of these Ni/SiC catalysts is lower than their incipient wetness counterparts, owing to the intimate contact between the nickel silicates and the underlying SiC. Calcination at 1273 K causes thus severe SiC oxidation and nickel sintering.

Chapter 8

REFERENCES

1. M.A. Vannice, Y-L Chao, and R. Friedman, *Appl. Catal.*, **20** (1986) 91.
2. Chapter 7 of this thesis.
3. P.W. Lednor and R. de Ruiter, in "Inorganic and Metal-containing Polymeric Materials", J.E. Sheets, C.E. Carraher, C.U. Pittman, M. Zeldin, and B. Currel (eds.), Plenum, New York (1990) p. 187;
P.W. Lednor, *Catal. Today*, **15** (1992) 243.
4. Pham-Huu Cuong, S. Marin, M.J. Ledoux, M. Weibel, G. Ehret, M. Benaissa, E. Peschiera, and J. Guille, *Appl. Catal. B*, **4** (1994) 45.
5. M. Boutonnet-Kizling, P. Stenius, S. Andersson, and A. Frestad, *Appl. Catal. B*, **1** (1992) 149.
6. Chapter 6 of this thesis.
7. E.E. Unmuth, L.H. Schwartz, and J.B. Butt, *J. Catal.*, **61** (1980) 242.
8. B. Mile, D. Stirling, M.A. Zammitt, A. Lovell, and M. Webb, *J. Catal.*, **114** (1988) 217.
9. O. Clause, L. Bonneviot, and M. Che, *J. Catal.*, **138** (1992) 195.
10. B. Scheffer, P. Molhoek, and J.A. Moulijn, *Appl. Catal.*, **46** (1989) 11.
11. T.C. Chou, A. Joshi, and J. Wadsworth, *J. Mater. Res.*, **6** (1991) 796.
12. P. Arnoldy and J.A. Moulijn, *J. Catal.*, **93** (1985) 38.
13. N.W. Hurst, S.J. Gentry, and A. Jones, *Catal. Rev. Sci. Eng.*, **24** (1982) 233.
14. P. Arnoldy, J.C.M. de Jonge, and J.A. Moulijn, *J. Phys. Chem.*, **89** (1985) 4517.
15. R.K. Iler, *The Chemistry of Silica*, John Wiley & Sons, New York, 1979, p. 631.
16. O. Clause, M. Kermarec, L. Bonneviot, F. Villian, and M. Che, *J. Am. Chem. Soc.*, **114** (1992) 4709.
17. A. Gil, a. Diaz, L.M. Gandia, and M. Montes, *Appl. Catal. A*, **109** (1994) 167.
18. J.P. Espinos, A.R. Gonzales-Elipse, A. Caballero, J. Garcia, and G. Munuera, *J. Catal.*, **136** (1992) 415.
19. M. Houalla, F. Delannay, I. Matsuura, and B. Delmon, *J.C.S. Faraday I*, **76** (1980) 2128.
20. R.C.J. Schiepers, PhD thesis, Eindhoven, 1991, chapter 5, (English).
21. S.J. Tauster, S.C. Fung, and R.L. Garten, *J. Amer. Chem. Soc.*, **100** (1978) 170.
22. G. Haller and D.E. Resasco, *Adv. Catal.*, **36** (1989) 173.
23. R. Fréty, L. Tournayan, M. Primet, G. Bergeret, M. Guenin, J.B. Baumgartner, and A. Borgna, *J. Chem. Soc. Faraday Trans.*, **89** (1993) 3313.
24. M. Boutonnet-Kizling, J.P. Gallas, C. Binet, and J.C. Lavalley, *Mat. Chem. Phys.*, **30** (1992) 273.

Chapter 9

The stability of high surface area silicon carbide in a high-temperature gas-phase reaction; carbon dioxide reforming of methane

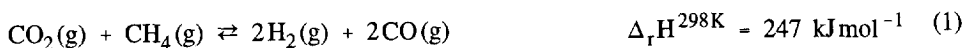
ABSTRACT

The stability of high surface area SiC has been evaluated in the carbon dioxide reforming of methane at temperatures of 1170 K. It is shown that high surface area SiC, which is synthesized by the nickel catalyzed conversion of activated carbon, is stable at 1170 K and CO_2/CH_4 ratios of 1. No sintering, oxidation, or change in SiC crystallinity occurs after operation for 80 hours at 1170 K. The metal dispersions on both the alumina and SiC catalysts have decreased after 80 hours at 1170 K by a factor of ten or more. The reforming activities are primarily determined by the metal-type (Rh or Ru) and dispersion. Optimization of the dispersion of Rh and Ru on SiC might lead to CO_2 reforming catalysts which possess beneficial properties over the alumina based ones, *viz.* high heat conductivity and thermal shock resistance.

1. INTRODUCTION

Previous research has shown that the thermal stability of high surface area SiC is very high. The presence of oxidizing constituents at temperatures exceeding 1100 K, however, causes extensive oxidation and sintering of the support. Hence, testing and possible application of high surface area SiC in a high-temperature reaction is limited to reactions at non-oxidizing environments. Carbon dioxide reforming of methane has been chosen as a test-reaction suitable to evaluate the Metal-Support Stability of SiC based catalysts, *viz.* sintering of the support, sintering of the active phase, and reaction of the active phase with the support. CO₂ reforming (eq.1) is often referred to as 'dry' reforming because of the absence of large amounts of steam during reaction. This reaction is suitable for high temperature performance testing of SiC based catalysts considering the susceptibility towards oxidation.

Carbon dioxide reforming of methane has potential as important alternative for steam reforming of methane in the production of synthesis gas with low H₂/CO ratios [1-7].



Reaction of CO₂ with hydrocarbons has been commercialized in the Calcor process [8]. CO₂ reforming of methane is also suggested as a suitable candidate for application in Chemical Energy Transmission Systems [9-11]. Here, fossil or solar energy is applied to drive a reversible highly endothermic reaction to its equilibrium at high temperature. The products of this reaction store the incident energy, which is subsequently released at another location with the reverse of reaction 1. The main problem in the CO₂ reforming of methane compared to steam reforming is the higher driving force for carbon formation *via* the decomposition of methane (eq. 2) and the Boudouard reaction (eq. 3):



Carbon free CO₂ reforming can be achieved using partially sulfur poisoned Ni catalysts [12] or noble-metal catalysts which display an intrinsic low rate of carbon formation. Rhodium [2,4-7,9,11,13], ruthenium [2,4,5,10], iridium [2,4,5,10], platinum [2,4,5], nickel [2,5], and palladium [2,4,5,7] have been investigated as suitable catalytic material. Rhodium and ruthenium are considered to be the best candidates for carbon-free CO₂ reforming [2,11]. Rostrup-Nielsen and Bak Hansen concluded that ruthenium is preferred in view of its higher activity and lower price compared to rhodium [2]. The influence of the support on the activity has been investigated as well [6,7,13]. The role of the support in the CO₂ reforming

Carbon dioxide reforming of methane

over Rh catalysts based on TiO_2 , SiO_2 , and Al_2O_3 has been evaluated by Nakamura *et al.* [6]. Erdöhelyi and co-workers included MgO in that series as support in determining the activity of palladium [7] and rhodium [13] catalysts. The influence of the support on catalytic activity is reported to comprise dispersion effects, Metal-Support Interactions, and CO_2 activation. High surface area silicon carbide can have high potential as catalyst support in the CO_2 reforming of methane. Beneficial properties are the high thermal stability, high thermal conductivity, and high thermal shock resistance. The advantages of the first two properties are obvious, regarding the high operating temperature and the heat duty of reaction 1, respectively. The thermal shock resistance might overcome the problems expected in the solar energy driven CO_2 reforming reaction regarding the variable solar energy input during operation. The susceptibility of SiC towards oxidation can, however, limit its application due to the production of steam during CO_2 reforming. Previous research has shown that high surface area SiC is stable in air and steam up to temperatures of 1080 and 1025 K, respectively, while higher temperatures cause considerable conversion of SiC into SiO_2 [14,15]. The stability of the catalytically active phase is of importance as well because sintering and reaction with the support have to be minimized. We report on the stability of high surface area SiC as support for noble-metal catalysts in the CO_2 reforming of methane. High surface area SiC is obtained by a method developed earlier [17], *viz.* the catalytic conversion of activated carbon into SiC with a surface area of $30 \text{ m}^2/\text{g}$. The objective is to determine the stability of the SiC based catalysts regarding the support surface area, metal dispersion, catalytic activity, and reaction of the active phase with the support.

2. EXPERIMENTAL

2.1 Materials.

Rhodium trichloride (>99% purity) was supplied by Aldrich, ruthenium trichloride and platinum dichloride (>99% purity) were obtained from Johnson Matthey. Methane (99.995% purity) and carbon dioxide (99% purity) have been obtained from Air Products. α -Alumina ($30 \text{ m}^2/\text{g}$) was a gift from Norton (SA 3232).

2.2 Synthesis of high surface area SiC.

High surface area SiC has been synthesized by Fluidized Bed Chemical Vapour Deposition [17] using washed Norit Elorit carbon granulates (300 to $425 \mu\text{m}$) loaded with 5w% nickel and a gas composition of 45 mol% H_2 , 4.5 mol% SiCl_4 , and 50.5 mol% argon at 1380 K and 100 kPa. The duration of conversion was 40 minutes. The residual carbon present after conversion has been removed by oxidation at 1023 K in dry air. The resulting silicon carbide

possesses a surface area of $30 \text{ m}^2/\text{g}$ and a pore volume of 0.2 ml/g . Determination of the pore volume by adding water until external wetting is perceived, revealed a total pore volume of 1.4 ml/g .

Additional purification of the SiC has in one case been carried out by immersing 1 gram SiC in 100 ml demineralized water containing 2v% hydrogen fluoride overnight. The particles have subsequently been washed to arrive at pH 7.

2.3 Catalyst preparation.

The catalysts have been prepared by incipient wetness impregnation using a solution of the corresponding metal chloride to arrive at a 1w% metal loading. After drying overnight at 353 K the catalysts have been calcined in air at 773 K for 8 hours.

2.4 Catalyst testing.

Catalyst testing is carried out in a set-up comprising six parallel quartz reactors (ID=6 mm). The catalyst temperature is determined by a thermocouple in the catalyst bed. The reaction products of each reactor are sequentially monitored by a Hewlett-Packard HP5710A gas chromatograph equipped with a Porapak Q and molecular sieve 5A column to determine CO_2 and H_2 , CH_4 , and CO , respectively (carrier gas: helium).

Initial ageing (2 hours) has been carried out by imposing a temperature programme under reforming conditions (10 ml/min CH_4 , 20 ml/min CO_2 and 120 ml/min Ar) to 100 mg catalyst diluted in 0.5 g Acheson SiC which comprised heating (0.05 K/s) to 1173 K, hold-time 1 hour, cooling to 873 K (0.033 K/s), and heating to 1173 K (0.05 K/s) with a hold-time of 1 hour. These catalysts have subsequently been analyzed by Temperature Programmed Reduction.

Activity testing after prolonged ageing for 80 hours at 1170 K has been carried out with a CO_2/CH_4 ratio of 1, using 10 mg catalyst diluted in 0.5 gram Acheson SiC. Gas flows used (STP) were 10 ml/min CH_4 , 10 ml/min CO_2 and 130 ml/min Ar . These conditions correspond to a GHSV of $700,000 \text{ m}^3_{\text{gas}} \text{ m}^{-3}_{\text{cat}} \text{ h}^{-1}$ and a W/F of $0.407 \text{ g}_{\text{cat}} \cdot \text{h/mol}_{\text{CH}_4}$. After this ageing procedure the influence of space time on the conversion is investigated. The activities of the bare SiC and HF treated SiC are investigated as well.

2.5 Catalyst characterization.

Catalyst characterization has been carried out after synthesis and ageing at reforming conditions. BET surface areas have been determined by N_2 -adsorption at 77 K using a Quantachrome Autosorb 6. Dispersion measurements have been carried out using CO chemisorption at 293 K after reduction of the catalysts (1 hour at 725 K, $25 \text{ ml H}_2/\text{min}$). X-ray diffraction is done with a Philips powder diffractometer PW 1840 using $\text{CuK}\alpha$

Carbon dioxide reforming of methane

radiation. Temperature Programmed Reduction is carried out using the apparatus described elsewhere [16]. A 5v% H₂ in Ar gas mixture and a heating rate of 0.167 K/s are applied. The catalysts were calcined at 773 K prior to TPR analysis.

3. RESULTS

3.1 BET surface area.

The BET surface areas of the SiC and Al₂O₃ based catalysts are shown in Table 1. A limited amount of sintering is encountered after 80 hours at 1170 K under reforming conditions for both the SiC and alumina (10 to 20% decrease in S_{BET}) catalysts.

Table 1. BET surface areas. After synthesis and spent catalysts (at 1170 K for 80 hours under reforming conditions, CO₂/CH₄=1)

	Al ₂ O ₃				SiC			
	after synthesis		spent catal.		after synthesis		spent catal.	
	Ru	Rh	Ru	Rh	Ru	Rh	Ru	Rh
S _{BET} (m ² /g)	29	34	27	26	31	36	26	28

3.2 Metal dispersion.

The metal dispersions after synthesis and after ageing under reforming conditions are displayed in Table 2.

Table 2. Metal dispersion of reforming catalysts. After synthesis and spent catalysts (80 hours at 1170 K under reforming conditions)

	Ru			Rh	
	Al ₂ O ₃	SiC	SiO ₂	Al ₂ O ₃	SiC
D _{initial} (%)	4.4	5	0.4	46	20
D _{spent} (%)	0.4	0.1	n.d.	2	0.8

D = (surface metal atoms)/(total metal atoms)

n.d. : not determined

Similar dispersions of Ru are obtained after synthesis on SiC and Al₂O₃.

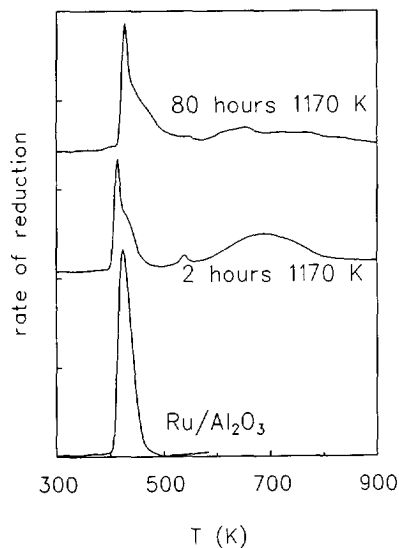


Fig. 1. TPR profiles of Ru/Al₂O₃ after synthesis, ageing, and reforming for 80 hours

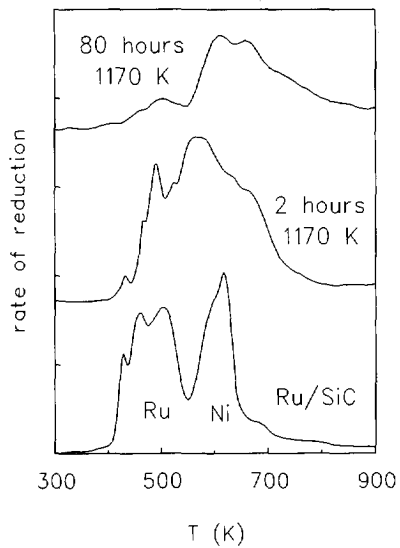


Fig. 2. TPR profiles of Ru/SiC after synthesis, ageing, and reforming for 80 hours

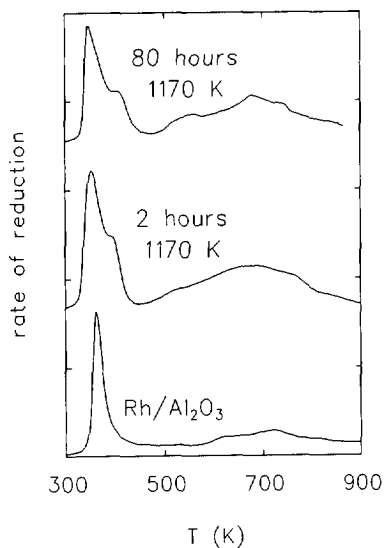


Fig. 3. TPR profiles of Rh/Al₂O₃ after synthesis, ageing, and reforming for 80 hours

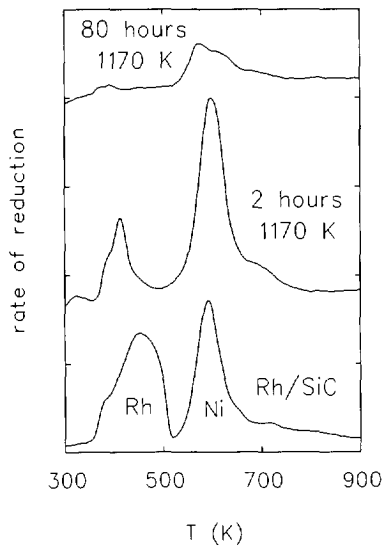


Fig. 4. TPR profiles of Rh/SiC after synthesis, ageing, and reforming for 80 hours

Carbon dioxide reforming of methane

The dispersion on silica, included for comparison, is one order of magnitude lower. The alumina based Rh catalyst displays a higher initial dispersion compared to its SiC based counterpart. Ageing at reforming conditions causes in both cases severe sintering of the active phase. Sintering of ruthenium on SiC is somewhat more than on alumina. The highest residual dispersion is displayed by the Rh/Al₂O₃ catalyst, viz. 2%.

3.3 X-ray diffraction.

XRD-profiles of the fresh and spent SiC based catalysts (80 hours, 1170 K) are identical and reveal only the presence of crystalline SiC. No diffraction lines of the applied metals nor those of the residual nickel (originating from the SiC synthesis procedure) or silica (possibly formed *via* SiC oxidation) are found. The peak shapes (intensity and width) of the SiC diffraction lines are identical of the fresh and spent catalysts.

3.4 Temperature Programmed Reduction.

The TPR profiles of the calcined ruthenium and rhodium catalysts are displayed in Figs. 1 to 4. The TPR profiles in one figure have been normalized to a standard amount of catalyst. The reduction of ruthenium supported by alumina is observed for the fresh and aged catalysts between 410 and 425 K. The aged catalyst displays an additional broad peak at 700 K. The reduction profile of ruthenium oxide on SiC is accompanied by the reduction of nickel oxide (T_{\max} : 615 K) originating from the SiC synthesis procedure. The ruthenium oxide reduction appears to consist of a three-step process (peak maxima at 430 K, 455 K, and 500 K, respectively). Ageing causes the ruthenium oxide reduction to move to higher temperatures, which results in an overlap of the peaks of ruthenium oxide and nickel oxide. Both peaks diminish almost completely after prolonged reforming. The fresh Rh/Al₂O₃ catalyst shows a single reduction peak at 365 K, while the aged catalysts and those used in reforming develop a shoulder at 405 K. Reduction of the Rh/SiC catalyst occurs in a broad peak (T_{\max} : 455 K, shoulder: 380 K). Ageing at 1170 K for 2 hours causes the Rh peak to decrease and the Ni peak to increase. Both peaks diminish after prolonged reforming.

3.5 Reforming activity of spent Ru/SiC, Rh/SiC, Ru/Al₂O₃, and Rh/Al₂O₃ catalysts.

Fig. 5 displays the activity of a 1w% Pt/SiC catalyst at 1170 K and a CO₂/CH₄ ratio of one. The activity of the catalyst increases in the first 30 hours of reforming and remains fairly constant after that period. Fig. 6 displays the CH₄ conversion at 1170 K as a function of space time for catalysts which have been exposed to reforming at 1170 K for 80 hours. The SiC based catalysts display in all cases substantial reforming activity. The highest activity is achieved by the Rh/Al₂O₃ catalyst which approaches thermodynamic equilibrium at W/F values above 0.5.

Chapter 9

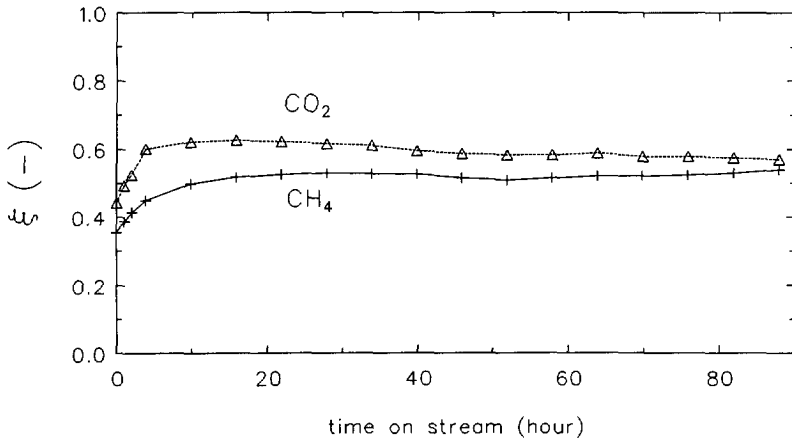


Fig. 5. Activity of 1 w% Pt/SiC vs. time on stream at 1170 K, $CO_2/CH_4=1$, $W/F = 2.5 \text{ g}_{\text{cat}} \text{ h/mol}_{CH_4}$

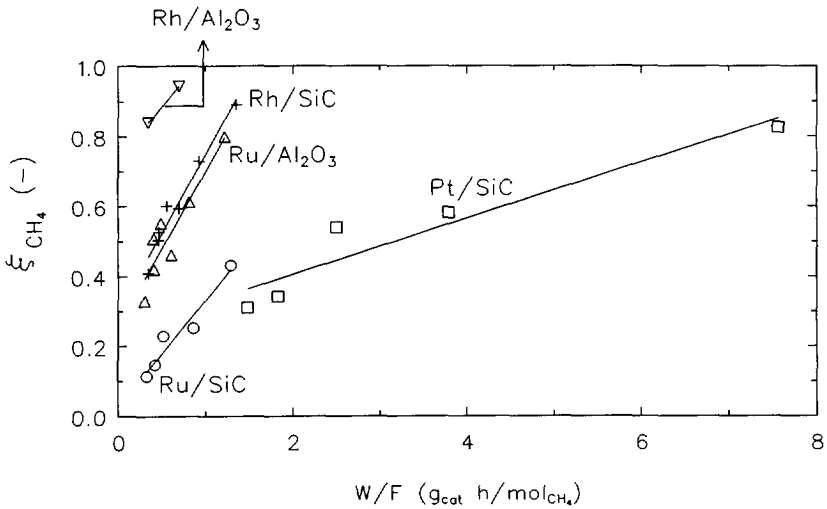


Fig. 6. CH_4 conversion vs. space velocity at 1170 K and $CO_2/CH_4=1$ for spent Rh/Al₂O₃ (▽), Rh/SiC (+), Ru/Al₂O₃ (Δ), Ru/SiC (○), and Pt/SiC (□), the lines are used to guide the eye

Carbon dioxide reforming of methane

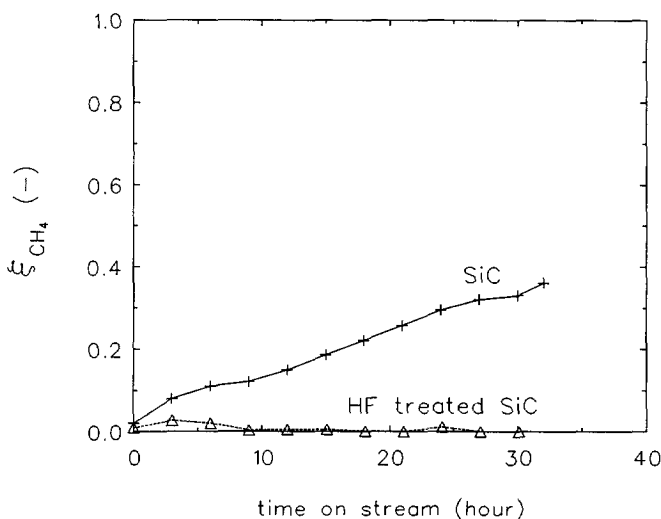


Fig. 7. Activity of SiC and HF treated SiC vs. time on stream at 1170 K, $CO_2/CH_4=1$, $W/F=4.2 \text{ g}_{cat} \text{ h/mol}_{CH_4}$

The activity of the Rh/SiC and Ru/ Al_2O_3 catalysts is somewhat lower, while the lowest activity is displayed by the Pt/SiC catalyst. The activity of the bare SiC support is shown in Fig. 7; for comparison HF treated SiC is included as well. These results show that the activity of bare high surface area SiC increases approximately linearly as a function of time on stream. The CH_4 conversion after 30 hours at 1170 K amounts to 0.4. The HF treated SiC displays negligible activity.

4. DISCUSSION

The objective of this research is to determine the stability of SiC based catalysts in a high temperature gas-phase reaction. The total stability of this catalyst system is categorized in four parts: (1) sintering of the SiC, (2) sintering of the active phase, (3) reaction of the active phase with the support, and (4) catalytic activity.

4.1 Sintering of high surface area SiC.

It is shown that the high surface area SiC retains major part (>80%) of its surface area, which means that SiC does not sinter under the applied reforming conditions. Although CO_2 reforming is referred to as "dry" reforming, some steam (~2%) is present under reaction

conditions, due to the water-gas shift reaction. Previous reports showed that the presence of steam at elevated temperatures causes extensive oxidation and sintering of SiC [14,15] leading to low surface area SiO₂. The presence of this SiO₂ can easily be identified by X-ray diffraction, *viz.* a decrease in SiC reflections and a concomitant appearance of short-range SiO₂ periodicity at 2θ values between 20 and 30 [14]. It can be concluded that the SiC structure is stable, because the XRD profiles do not alter after exposure to reforming conditions for 80 hours. The BET and XRD results also show that the entire SiC structure is not significantly affected by CO₂ reforming at elevated temperatures during the investigated period of time.

4.2 Sintering of the active phase.

It is shown in Table 2 that dispersed SiC based catalysts can be produced by incipient wetness impregnation. The dispersion of ruthenium achieved on SiC is ten times higher than that on SiO₂, which points to a specific interaction of the partially oxidized SiC surface with the active species during catalyst synthesis. This difference between the partially oxidized SiC surface and SiO₂ has been previously reported for the Metal-Support Stability of Ni catalysts, and the synthesis of highly dispersed Ni catalysts by ion-exchange [16].

The active phase on both the alumina and the SiC based catalysts sinters extensively during reforming. Similar reductions in dispersion are observed for the Rh/SiC and Rh/Al₂O₃ catalysts; after reforming for 80 hours at 1170 K the dispersion decreased by a factor 25; the final dispersion on Al₂O₃ is twice that on SiC. Sintering of ruthenium on SiC (factor 50) is more extensive than on Al₂O₃ (factor 10).

4.3 Reaction of the active phase with the support.

Differences in Metal-Support Interactions can usually be elucidated by application of TPR analyses analogously to [16]. It is shown in Figs. 1 and 3 that variations in MSI for the alumina based Ru and Rh catalysts occur mainly in the two hour ageing process. This agrees with observations of Richardson *et al.* [11], who describe that sintering of rhodium supported on Al₂O₃ is most extensive in the first 2 to 3 hours. The origin of the broad peak at 700 K of the Ru/Al₂O₃ and Rh/Al₂O₃ catalyst is not clear. It might be attributed to Ru and Rh in strong interaction with the support which are consequently more difficult to reduce.

The rhodium and ruthenium SiC based catalysts display after synthesis a separate reduction for the applied metal and the nickel which is present in the SiC. After utilization in reforming the reduction of the Rh and Ru oxide shifts to the temperature of Ni reduction. The ruthenium oxide reduction overlaps the NiO reduction peak, whereas part of the reduction of rhodium oxide appears to shift entirely into the NiO peak.

Carbon dioxide reforming of methane

Table 3. Turnover numbers for the aged ruthenium and rhodium catalysts

	ruthenium		rhodium	
	SiC	Al ₂ O ₃	SiC	Al ₂ O ₃
TON (molec _{CH₄} site ⁻¹ s ⁻¹)	920	735	360	370

The cause of these peak changes (position and intensity) is not known, but might be attributed to either reaction with the SiC (formation of silicides), either alloying with nickel.

4.4 Reforming activity.

The activation of both Pt/SiC and bare SiC during reforming as shown in Figs. 5 and 7 is probably caused by the catalytic activity of the synthesis nickel. Major part of this nickel is initially present as nickel silicide (Ni_xSi_y). During reforming this phase might decompose in a silicon phase and metallic nickel, which accounts for the activity enhancement. Treatment of SiC with HF removes this synthesis nickel and the activity is negligible.

The activity of the spent SiC based catalysts in CO₂ reforming (after 80 hours at 1170 K) shows that active catalysts can be synthesized suitable to operate at high temperatures. It should be mentioned that the activity of the SiC support containing synthesis nickel does not influence these catalytic data to a large extent, because the activity of the noble metal catalysts is much higher than that of the support alone. The turnover numbers (TON) for each catalyst are displayed in Table 3 which shows that similar TON are obtained for rhodium supported by alumina and SiC, while the activity of Ru on SiC appears to be slightly higher than that on the alumina counterpart. The fact that ruthenium is more active than rhodium (based on TON) agrees with reports of Rostrup-Nielsen and Bak Hansen [2] and Solymosi *et al.* [4].

It can be concluded that application of SiC based catalysts in the CO₂ reforming of methane is feasible. The fact that alumina and silicon carbide based Rh and Ru catalysts display similar turnover numbers proves that when similar metal dispersions can be achieved on both supports, full benefit can be obtained from the advantageous SiC support properties, *viz.* high heat conductivity and thermal shock resistance.

5. CONCLUSION

High surface area silicon carbide is stable at reforming conditions at a CO₂/CH₄ ratio of 1. No sintering, oxidation, or change in SiC crystallinity occurs after 80 hours reforming at 1170 K. The dispersions of rhodium and ruthenium decrease after 80 hours on stream by a

Chapter 9

factor of ten or more. Comparison of alumina and SiC based catalysts shows that the extent of sintering of rhodium is similar on SiC and on Al_2O_3 . The decrease in dispersion of ruthenium is fractionally larger on SiC than on alumina. The synthesis nickel in the SiC activates at reforming conditions. The influence on the activity of the investigated noble metal catalysts is, however, negligible. Removal of the nickel phase can be achieved by washing with a HF solution. No significant influence of the support on activity is found for the alumina and silicon carbide based catalysts (based on turnover numbers). This means that optimization of the dispersion of Rh and Ru on SiC might lead to CO_2 reforming catalysts which possess beneficial properties over the alumina based ones, viz. high heat conductivity and thermal shock resistance.

REFERENCES

1. J.R. Rostrup-Nielsen, *Stud. Surf. Sci. Catal.*, **36** (1988) 73.
2. J.R. Rostrup-Nielsen and J-H. Bak Hansen, *J. Catal.*, **144** (1993) 38.
3. A.M. Gadella and B. Bower, *Chem. Eng. Sci.*, **43** (1988) 3049.
4. F. Solymosi, Gy. Kutsán, and A. Erdöhelyi, *Catal. Lett.*, **11** (1991) 149.
5. P.D.F. Vernon, M.L.H. Green, A.K. Cheetham, and A.T. Ashcroft, *Catal. Today*, **13** (1992) 417.
6. J. Nakamura, K. Aikawa, K. Sato, and T. Uchijima, *Catal. Lett.*, **25** (1994) 265.
7. A. Erdöhelyi, J. Cserényi, E. Papp, and F. Solymosi, *Appl. Catal. A*, **108** (1994) 205.
8. S. Teuner, *Hydroc. Proc.*, **64** (1985) 106.
9. R.E. Hogan, JR., R.D. Skocypec, R.B. Diver, J.D. Fish, M. Garrait, and J.T. Richardson, *Chem. Eng. Sci.*, **45** (1990) 2751.
10. J.S.H.Q. Perera, J.W. Couves, G. Sanker, and J.M. Thomas, *Catal. Lett.*, **11** (1991) 219.
11. J.T. Richardson and S.A. Paripatyadar, *Appl. Catal.*, **61** (1990) 293.
12. H.C. Dibbern, P. Olesen, J.R. Rostrup-Nielsen, P.B. Tøtrup, and N.R. Udengaard, *Hydroc. Proc.*, **65** (1986) 71.
13. A. Erdöhelyi, J. Cserényi, and F. Solymosi, *J. Catal.*, **141** (1993) 287.
14. Chapter 7 of this thesis.
15. P.W. Lednor and R. de Ruiter, in "Inorganic and Metal-Containing Polymeric Materials", J.E. Sheets, C.E. Carraher, C.U. Pittman, M. Zeldin, and B. Currel (eds.), Plenum, New York, 1990, p. 187.
16. Chapter 8 of this thesis.
17. Chapter 6 of this thesis.

General conclusions and summary

Introduction

The research described in this thesis was initiated for improving the physical properties of activated carbon in order to enlarge its field of application as catalyst support. The special target was the reduction of the susceptibility of activated carbon towards oxidation and attrition. A thermally and mechanically very stable catalyst support would thus be available, which is proficient for operation in gas-phase systems at elevated temperatures (no sintering) and liquid-phase systems (slurry reactors, no attrition). The aim was to shield the activated carbon surface with a thin layer of silicon carbide, well known for its hardness and resistance against oxidation. Chemical Vapour Deposition (CVD), a powerful tool for deposition of thin, high purity ceramic films, had been defined as the most promising modification technique. Chapter 1 deals with the physical properties of activated carbon and SiC and provides an overview of the possibilities for CVD applications in the modification of catalyst supports. In this case, a thin but rigid SiC film is targeted for, which protects the underlying activated carbon without reducing the surface area significantly. Homogeneous coating of the carbon surface with SiC necessitates operation in the kinetically controlled regime to overcome diffusion limitations. Similar prerequisites are encountered in deposition of ceramic materials in porous structures (Chemical Vapour Infiltration, CVI), which is frequently applied in the manufacture of ceramic composites. Significant problems are encountered due to diffusion limitations present in the porous structure which cause premature pore closure during deposition of the solid phase. This induces a density gradient, which weakens the composite considerably. Moreover, the appearance of diffusion limitations during densification might be considered as an autocatalytic phenomenon, which of course is most pronounced when operating in the Knudsen diffusion regime. Physical methods are applied to ensure low final density gradients like imposing a temperature and pressure gradient over the preform during deposition. It is shown in Chapter 2 that improved densification techniques can also be obtained by applying chemical methods. The developed mathematical model demonstrates that exploitation of the Langmuir-Hinshelwood type kinetics by proper selection of deposition conditions may lead to lower residual porosities of the densified

preforms. The generally accepted CVI guidelines to realize low residual porosities, however, are no longer valid, and have to be adapted for every individual case. Crucial parameters are type of deposition kinetics, substrate geometry, temperature, and pressure. Chapter 2 describes these general concepts and delivers a design chart for swift evaluation and optimization of the CVI conditions.

CVD modelling as a tool for designing catalysts and structured catalytic reactors

A trend in catalyst design is the strategy to develop catalytic converters in which the boundary between catalyst body and reactor has disappeared. Examples are the application of structured catalytic packings, monolithic based reactors, fixed bed reactors based on sintered metals, and reactive distillation, see Fig. 1. Loading of large structured packings with the active phase is expected to be either extremely laborious or impossible when conventional catalysts preparation techniques like impregnation are applied. Part of these problems might be overcome by structured packings, e.g. by using a helical twisted belt of bags which contains the catalyst particles. Conventionally loaded catalyst pellets can thus be structured to ensure counter-current gas-liquid flow, while retaining good catalyst wetting.

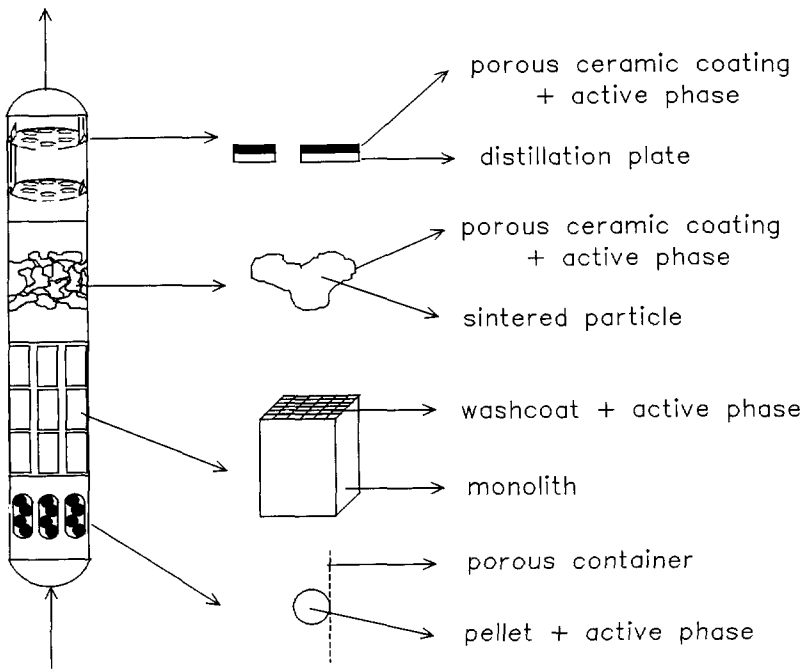


Fig. 1. Catalyst-reactor integration leading to structured catalytic reactors

General conclusions

This procedure has been applied in catalytic distillation processes [1]. Reactors with complex internal structures cannot be equipped with the active material by impregnation. Here, CVD is indispensable for achieving a catalytically active convertor. Additionally, optimal tuning of the mass transfer in combination with the chemical reaction rates necessitates in some cases the utilization of more sophisticated internal reactor configurations. The model studies carried out in Chapter 3 suggest that application of CVD has potential in these situations for obtaining active catalytic reactors in a reproducible way. We feel that the use of this technique will expand in the near future owing to the inherent higher process flexibility, ease of scale-up, and facility of tailoring the active-site distribution in the catalyst support by proper selection of deposition conditions.

Conventional CVD can alleviate the difficulties concerning regeneration of structured catalytic reactors, such as monoliths, because rejuvenation is then allowed to be carried out *in situ*. Some requirements, however, have to be met. To reestablish the active phase, two types of regeneration can be distinguished. First, the active phase can be redispersed by exposing the sintered material to a gas atmosphere which enhances the mobility of the active phase. Prerequisites are in this case a strong interaction between the active phase and the support, and the capability of the reactor to withstand the conditions of rejuvenation. Secondly, the deactivation can be irreversible (*e.g.* due to reaction of the active phase with the support) which implies that a fresh active phase has to be supplied to the reactor. This means that a suitable volatile precursor has to be used which decomposes to the desired active phase at conditions applicable in the reactor. The critical parameters are temperature, pressure, and gas composition. The engineering requirements are depicted in Fig. 2.

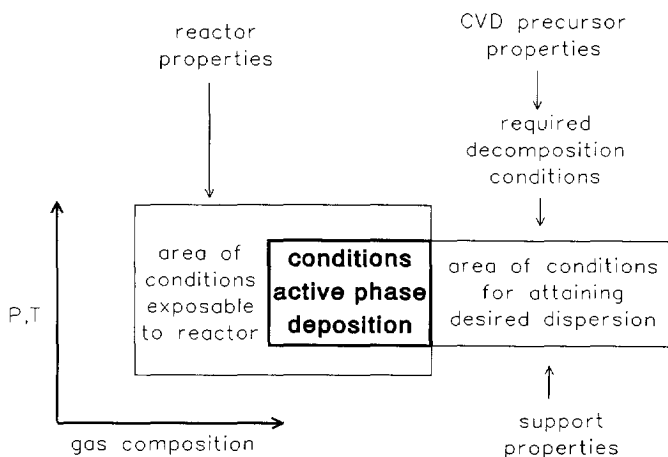


Fig. 2. Engineering requirements for the application of CVD in catalytic reactor design

Application of Chemical Vapour Deposition in catalyst modification

The concepts acquired from CVI modelling in Chapter 2 have been incorporated in the CVD modification of activated carbon. In the coating of activated carbon similar diffusion problems are encountered due to its meso and micro porous structure. The deposition starts with the difficult penetration of reactants from the very beginning, comparable with the final most difficult densification stage in the manufacture of ceramic composites. The required operation in the kinetically controlled regime has to be obtained by using SiC precursors with very low reactivities. From the results described in Chapter 4 it is concluded that application of a $\text{SiCl}_4/\text{CH}_4$ mixture is suitable for attaining a good SiC infiltration in the porous structure. Activated carbon extrudates which exhibit both an improved mechanical strength as well as an improved oxidation resistance have thus been obtained. The use of more reactive SiC precursors like CH_3SiCl_3 causes SiC deposition on the exterior of the particle (20 to 80 % of the total amount deposited), resulting exclusively in an improved mechanical strength. The design chart developed in Chapter 2 correlates the residual porosity and initial Thiele modulus, and is shown to agree with experimental data of Chapter 4 and data reported in literature.

Conversion of activated carbon into high surface area SiC

The modification of activated carbon by a SiC coating improves the physical properties to a significant extent. However, further advances in the development of a high temperature catalyst support can only be achieved by constructing a support which consists entirely of SiC. This view directed the research to *conversion* of activated carbon into SiC, which had mainly been limited by the low reactivity of the carbon as shown in Chapter 4. The development of a catalytic conversion method is then a logical step. Nickel is a well known catalyst for carbon activation in hydrogen environments (*viz.* hydro-gasification), and has thus been applied in this system. Activated carbon extrudates and granulates can be converted (up to 50%) into porous SiC with surface areas ranging from 20 to 80 m^2/g *via* eq. 1 and 2.



The procedure and mechanism have been described in Chapter 5 and embody the concept of catalyzed conversion of a porous solid acting both as reactant and template. The starting point is this porous solid which has been loaded with a suitable catalyst. A mixture of reacting gases is subsequently admitted which (1) gasifies the solid and (2) reacts with the gasification products to form the desired material.

General conclusions

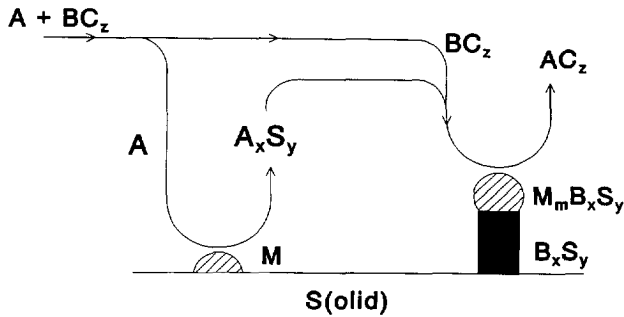


Fig. 3. The mechanism of catalyzed solid conversion for the synthesis of catalysts. The reactions occur simultaneously in the porous particle which acts both as reactant and template

Fig. 3 displays the mechanism. Both reactions ensue catalytically as illustrated by the processes occurring on the shaded spherical halves. The external solid morphology determines the final structure of the product (shape memory), while the final textural properties are governed by the pore structure of the original solid. The conversion on a macroscopic scale resembles that of a gas-solid reaction with its inherent experimental simplicity, whereas on a microscopic level adsorbed gaseous molecules react to form the desired product. Obvious difficulties in gas-solid reactions, regarding reactant diffusion through the developed product layer, are hereby elegantly overcome. This concept of a dual catalytic action and dual utilization of the solid is completely new. Fig. 4 displays the parameters which control the final textural properties of the high surface area silicon carbide.

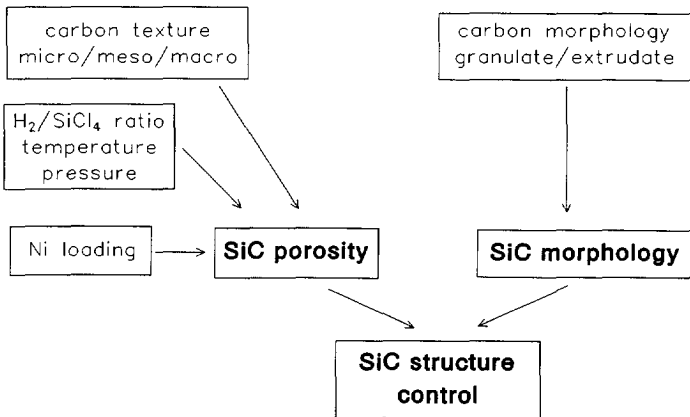


Fig. 4. Design parameters for the synthesis of high surface area silicon carbide by the catalytic conversion of activated carbon

It is shown in Chapter 5 that the conversion temperature should exceed 1363 K to enable the formation of a liquid Ni-Si-C phase for selective SiC formation. The first step in the conversion (carbon hydrogasification) is at these temperatures, however, thermodynamically not favoured. This means that the temperature has to be chosen just above 1363 K. Extrudate conversion has been carried out in a fixed bed configuration. Homogeneous conversion of large amounts of activated carbon necessitates application of a Fluidized Bed CVD reactor. Development and use of FBCVD is described Chapter 6. It is shown that activated carbon can thus be converted in a homogeneous and reproducible way, which allows testing of SiC based catalysts. Sub-atmospheric FBCVD operations are possible as well.

High surface area SiC as catalyst support

Bulk silicon carbide is well known for its thermal stability and resistance against oxidation. It is shown in Chapter 7 that no sintering of high surface area SiC ($31 \text{ m}^2/\text{g}$) is observed in a nitrogen environment up to 1280 K. Tests in air and steam have shown that high surface area SiC is stable at temperatures below 1080 K. More severe oxidizing environments cause sintering and oxidation of SiC, which limit to some extent the area of application.

The stability of SiC in strong acidic environments allows application in liquid-phase slurry reactors, where the high mechanical strength is of major advantage over the normally applied activated carbon.

Synthesis of SiC based catalysts, Metal-Support Interaction and Metal-Support Stability

In order to be a suitable catalyst carrier, SiC has to meet several requirements. The first one is a high dispersive ability to allow the preparation of catalysts with a high active phase utilization. Additionally, the sintering of the active phase has to be minimal. This means that the interaction between the active phase and the support has to be moderate during catalyst synthesis. Strong enough to realize a high dispersion and weak enough to enable easy activation of the active phase. Additionally, the entire catalyst system (active phase and support) has to be stable to ensure that an active catalyst is obtained after exposition to reaction conditions. This property will be referred to as the Metal-Support Stability (MSS) of the system, analogous to the expression Metal-Support Interaction [2]. It should be noted that the MSS embodies the whole catalyst system. Secondly, the Metal-Support Stability includes, of course, other active phases as well, *e.g.* metal oxides, metal sulfides, *etc.* A catalyst that possesses a High Metal-Support Stability retains its activity after severe ageing procedures. Catalysts with a Low Metal-Support Stability lose part of their activity and deactivate, *e.g.* by evaporation or sintering of the active phase, reaction of the active phase with the support, or coating of the active phase by the support. Another possibility is an

General conclusions

increase in their activity owing to an increased dispersion of the active phase. Hence, the Metal-Support Stability is controlled by the active phase, support, and environment. This means that the Metal-Support Stability determines the state of Metal-Support Interaction (MSI). The MSS of a catalyst is thus an intrinsic property, whereas the MSI refers to a state of the catalyst after a certain treatment. Fig. 5 depicts several possibilities for final MSI states and the corresponding driving forces, which comprises amongst others of surface tension and energy of reaction. A well-known phenomenon is **coating** of Pt by partially reduced TiO_2 after a high temperature reduction [2]. **Diffusion S→M** is encountered when reducing Ni/SiO_2 catalysts at high temperature [3], where probably a $\text{Ni}_x\text{Si}_y\text{O}_z$ phase is formed. **Diffusion M→S** is significant for spinel forming Al_2O_3 based catalysts (e.g. $\text{Ni/Al}_2\text{O}_3$ and $\text{Co/Al}_2\text{O}_3$). These three final stages (displayed at the bottom of Fig. 5) are well-known SMSI-states, and represent special cases of deactivated catalysts.

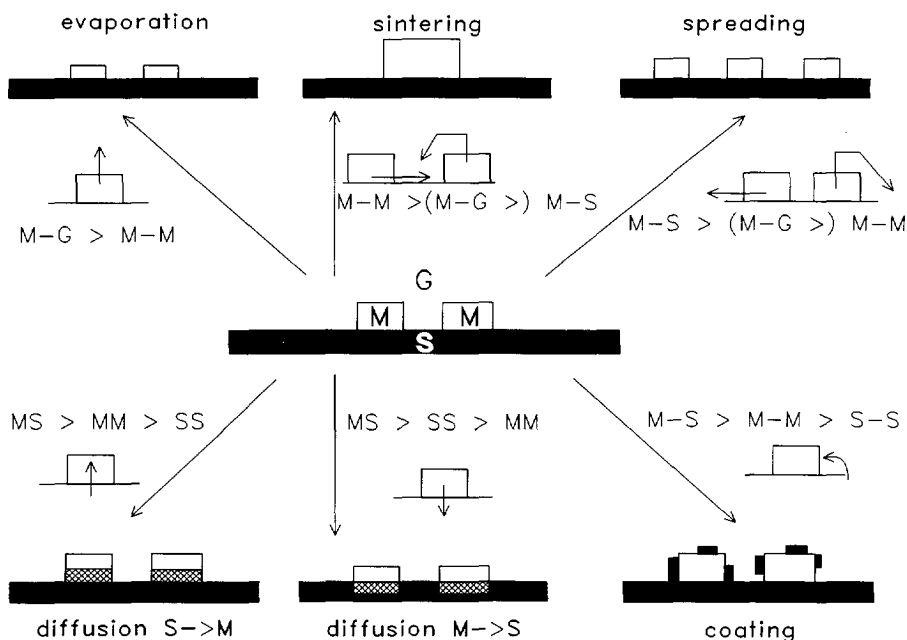


Fig. 5. Stability chart for heterogeneous catalysts.

G:gas-phase, M:active phase, S:support. M-S represents the active phase - support affinity. MS represents the free energy of formation of a reaction product of the active phase and the support.

Evaporation occurs when the partial pressure of the active phase is important, or when the active phase is gasified due to reaction with a gas-phase constituent. Examples are the Pt/Rh gauze catalyzed oxidation of ammonia, and Pt-based exhaust catalysts. **Sintering** and **spreading** of the active phase is caused by the presence of surface mobility of the active phase. High mutual affinity of the active-phase molecules causes sintering whereas spreading is the result of either a high affinity between the support and active phase or between the gas phase and the active phase. **Sintering** and **spreading** might even be induced by the gas phase by enhancing the mobility (or even evaporation) of the active phase. An example of this last case is the *in situ* rejuvenation (coke removal and redispersion) of platforming catalysts by a Cl_2/O_2 treatment. The Metal-Support Interaction is in these last three cases not altered.

Chapter 8 highlights the interactions between the active phase and the SiC during and after synthesis. It is shown that the MSI of SiC and aqueous nickel nitrate during synthesis is comparable to that of SiO_2 supports, owing to the partially oxidized SiC surface. Incipient wetness impregnation on SiO_2 and SiC leads to comparable Ni-dispersions after calcination. The Metal-Support Stability of these Ni/SiC catalysts is remarkably high after oxidation at 1273 K for 8 hours, shown by the presence of an easily reducible nickel species. Sintering of Ni is virtually absent, which suggests that this catalyst system might possess advantages over conventional Ni/ Al_2O_3 systems in high temperature reactions. It should be mentioned, however, that although the MSS in air is high for 8 hours, prolonged application of SiC in oxidizing environments is limited at temperatures above 1100 K as shown in Chapter 7. The Ni-SiC contact of Ni/SiC catalysts calcined at 773 K is intense which results in reaction of Ni with SiC into Ni_xSi_y and carbon at temperatures exceeding 900 K and subsequent support decomposition. This is another example of a low MSS as displayed by Fig. 5: **Diffusion M→S**. Calcination at 1273 K improves the MSS by generating a SiO_x spacing layer between the Ni and SiC.

The MSI of other SiC based catalysts (Cu, Co, and Mo) is generally lower than that of the silica and alumina based counterpart, as shown by Temperature Programmed Reduction.

Owing to the partially oxidized surface of the SiC, the manufacture of highly dispersed Ni/SiC catalysts is realized using an ion-exchange technique. Adsorption of a nickel tetramine complex causes extensive formation of nickel silicates on SiC. Nickel particles (diameter 4 nm) are subsequently formed after reduction at 900 K. Considering the specific surface area ($30 \text{ m}^2/\text{g}$) and nickel content (10w%) it is clear that this catalyst system possesses a very high nickel density.

Catalyst performance testing

Initial screening experiments have been carried out in applications where SiC has potential, *i.e.* a high temperature gas-phase reaction and a liquid-phase slurry reaction.

General conclusions

Application of SiC as catalyst support in the carbon dioxide reforming of methane at 1170 K has shown that initial activities are obtained for Ni/SiC catalysts which are higher than the ones obtained with a commercial steam-reforming catalyst (normalized to amount nickel). The origin of this is not clear yet, additional research is necessary to rationalize this.

Notwithstanding the presence of some steam during CO₂ reforming (due to the operative water-gas shift reaction), SiC is shown in Chapter 9 to be stable at reforming conditions after 80 hours on stream. No significant sintering, oxidation or changes in the crystallinity of the SiC has been encountered after operation at 1170 K for over 80 hours. These results are promising for the application of SiC in high temperature reactions and non-oxidizing environments. It should be mentioned, however, that sintering of the active phase is extensive for both the alumina and silicon carbide based catalysts. After prolonged ageing of the catalysts (80 hours at 1170 K) both the SiC and Al₂O₃ based catalysts still show very high reforming activity. No significant influence of the support on the catalyst activity is found (based on turnover numbers). This means that optimization of the metal dispersion on SiC allows the application of SiC based catalysts in the CO₂ reforming of CH₄. Thus, much profit can be obtained from the advantageous properties of SiC over alumina, *viz.* high heat conductivity and high thermal shock resistance.

Additional screening experiments have been carried out in the batch-wise liquid-phase partial hydrogenation of benzene. A four-phase system has been applied [4], *viz.* hydrogen, water and zinc sulfate, benzene, and catalyst. This set-up increases the cyclohexene yield from 0.1 % to 20 % when ruthenium-black is applied as catalyst. It is shown that Ru/SiC catalysts display benzene conversions and cyclohexene selectivities comparable to other supported catalyst systems. This shows that application of SiC in liquid-phase reactions is feasible and allows utilization in liquid-phase operations at demanding pH conditions.

Final remarks

This research had been initiated in order to improve crucial physical properties of activated carbon by SiC-CVD. It has led to the development of a novel method for the reproducible manufacture of high surface area SiC.

The results presented in this thesis prove that this SiC is a promising catalyst support material. The thermal stability is very good and the dispersive capability is comparable to conventional catalyst supports. However, material improvements can be made. First of all, the strength of the high surface area SiC can be enhanced. Due to the removal of the residual carbon after the conversion, a fluffy material is retained. Optimization of the carbon conversion to higher quantities is the key to arrive at a very hard and durable support material. Directions of this future research should additionally incorporate the application of carbon sources which possess the appropriate porous structure, *viz.* macro and meso porosity.

Chapter 10

The presence of impurities in the activated carbon and the necessary presence of nickel in the conversion might impose difficulties in catalytic applications. The first problem can be tackled by utilization of activated carbon with very low ash contents or other porous forms of carbon, like carbon black or petroleum pitch. Nickel, however, is indispensable for achieving high carbon conversions. Hence, a method for nickel removal after synthesis must be aimed for. The results presented in Chapter 9 suggest that a hydrogen fluoride washing treatment is efficient to achieve this objective. Finally, the conversion of other carbon morphologies has to be evaluated, following the shape memory concept reported in Chapter 5 and 6. Conversion of carbonaceous monoliths and foams provides the opportunity of synthesizing high surface area SiC based structured catalytic packings.

REFERENCES

1. L.A. Smith, E.M. Jones, and D. Hearn, AIChE Spring National Meeting, Houston, 1991.
2. S.J. Tauster, S.C. Fung, and R.L. Garten, *J. Amer. Chem. Soc.*, **100** (1978) 170.
G. Haller and D.E. Resasco, *Adv. Catal.*, **36** (1989) 173.
3. H. Praliaud and G.A. Martin, *J. Catal.*, **72** (1981) 394.
4. M. Soede, E.J.A.X. van de Sandt, M. Makkee, and J.J.F. Scholten, *Stud. Surf. Sci. Catal.*, **78** (1993) 345.

Samenvatting

Toepassing van Chemical Vapour Deposition in het ontwerpen van katalysatoren

Ontwikkeling van siliciumcarbide met een hoog specifiek oppervlak

Het onderzoek beschreven in dit proefschrift is geïnitieerd om de fysische eigenschappen van actieve kool te verbeteren en diens toepassingsgebied als katalysatordrager te vergroten. Verhoging van de resistentie tegen oxydatie en attritie waren de specifieke doelen. De modificatie is uitgevoerd met behulp van Chemical Vapour Deposition (CVD) technieken. Het idee bestond uit het beschermen van het kooloppervlak met een dunne deklaag van siliciumcarbide (SiC), een zeer hard en oxydatieresistent keramisch materiaal, waarmee, door combinatie van de textuur van de kool en de fysische eigenschappen van het siliciumcarbide, een veelbelovende katalysatordrager verkregen zou worden. Hoofdstuk 1 behandelt de fysische eigenschappen van actieve kool en siliciumcarbide en beschrijft de mogelijkheden voor het gebruik van CVD in het modificeren van katalysatordragers. Het is noodzakelijk voor bereiken van een homogene deklaag in het poreuze substraat om de gasfase depositie van SiC in het kinetisch gecontroleerde regime uit te voeren. Hoofdstuk 2 beschrijft de ontwikkeling van een mathematisch model waarmee de poriegeometrie tijdens SiC-depositie als functie van de tijd beschreven kan worden. De heterogene CVD reacties zijn, gefundeerd op literatuurgegevens, beschreven met Langmuir-Hinshelwood vergelijkingen. Het toepassen van dit type reacties in het mathematisch modelleren heeft geleid tot nieuwe inzichten in het optimaliseren van CVD in poreuze structuren. Tevens is een ontwerpdiagram ontwikkeld, waarmee de residuale porositeit gecorreleerd wordt aan de Thiele modulus bij het starten van infiltratie. Hiermee is het mogelijk om op een eenvoudige manier de residuale porositeit te voorspellen op basis van de depositiekinetiek en substraatgeometrie.

De modelstudies die zijn uitgevoerd in hoofdstuk 3 laten zien dat CVD bovendien potentieel heeft in het beladen van poreuze structuren met katalytisch actief materiaal. Voorbeelden zijn katalysatordeeltjes, monolieten en gestructureerde reaktoren. Tevens is het mogelijk inhomogene distributies van het actieve materiaal te verkrijgen in katalysatordeeltjes en monolieten; voorbeelden zijn zogenaamde egg-shell en egg-yolk profielen.

De concepten verkregen uit de CVD-modelleringen in hoofdstuk 2 zijn in de CVD modificering van actieve kool gebruikt. Bij het bedekken van actieve kool met een laag siliciumcarbide veroorzaakt de aanwezigheid van de meso- en micro-poreuze structuur namelijk identieke diffusieproblemen. Om de CVD operatie in het kinetisch bepaalde regime uit te voeren is het noodzakelijk SiC precursors toe te passen die een lage reactiviteit bezitten. Uit de resultaten van hoofdstuk 4 is geconcludeerd dat toepassing van een gasmengsel bestaande uit waterstof, siliciumtetrachloride en methaan geschikt is voor het verkrijgen van een goede SiC infiltratie in de kool. Op deze manier wordt zowel de mechanische sterkte als de oxydatieresistentie verbeterd. Het gebruik van reaktievere SiC precursors, zoals methyltrichloorsilaan (CH_3SiCl_3), leidt tot significante SiC depositie aan de buitenkant van de kooldeeltjes, en resulteert daardoor slechts in een verbeterde mechanische sterkte. Het ontwerpdiagram dat in hoofdstuk 2 ontwikkeld is komt goed overeen met de experimentele data van hoofdstuk 4.

Het modifieren van actieve kool met behulp van conventionele CVD verbetert de fysische eigenschappen beduidend. Verdere verbeteringen en de ontwikkeling van een hoge temperatuur drager kunnen alleen bereikt worden door het gebruik van de actieve kool als koolsubstraat en dus door kool-conversie naar poreus SiC. Deze conversie wordt echter door de geringe reactiviteit van de actieve kool met waterstof en siliciumtetrachloride, zoals beschreven is in hoofdstuk 4, gelimiteerd. De ontwikkeling van een katalytische conversiemethode is dan een logische stap. De reactiviteit van koolstof in een waterstofmilieu wordt door nikkel, een bekende vergassingskatalysator sterk verhoogd. Het aanbrengen van nikkel op de kool gevolgd door reactie met waterstof en siliciumtetrachloride in een vast-bed reaktor, volgens vergelijking 1 en 2, leidt tot koolconversies variërend van 20 tot 50%. Verwijdering van de residuale kool door oxydatie resulteert in hooggoppervlakkig SiC (20 tot $80 \text{ m}^2/\text{g}$).



De exacte procedure en het mechanisme worden beschreven in hoofdstuk 5; de basis is het concept van gekatalyseerde conversie van een poreus materiaal dat zowel als reaktant als template optreedt. De uiteindelijke textuur van het hooggoppervlakkig SiC wordt bepaald door (1) de kooltextuur, (2) de nikkelbelading en (3) de H_2/SiCl_4 ratio. De SiC morfologie (granulaat, extrudaat) is volledig identiek aan de koolmorfologie, hetgeen betekent dat de problematische vormgeving van SiC overbodig is, en door de eenvoudige vormgeving van actieve kool kan worden vervangen. De conversie van kleine hoeveelheden actieve kool extrudaten is in een vast-bed reaktor uitgevoerd.

Voor het bereiken van homogene conversies van grotere hoeveelheden actieve kool granulaten is een fluïde-bed CVD (FBCVD) reaktor echter het meest geschikt. De

ontwikkeling en toepassing hiervan is in hoofdstuk 6 beschreven. Aktieve kool kan op deze manier homogeen en reproduceerbaar worden omgezet, waardoor het mogelijk is grote hoeveelheden hoogoppervlakkig SiC te synthetiseren en te testen als katalysatordrager. Het is tevens mogelijk gebleken in de FBCVD reaktor bij subatmosferische drukken kool om te zetten, hetgeen eventueel bij de synthese van andere keramische materialen van nut kan zijn.

Bulk SiC staat bekend om zijn hoge thermische stabiliteit en oxydatieresistentie. Hoofdstuk 7 laat zien dat hoogoppervlakkig SiC ($31 \text{ m}^2/\text{g}$) inderdaad niet sintert bij 1280 K in een stikstofmilieu. Dit SiC is tevens stabiel in lucht- en stoom-milieus tot temperaturen van 1080 K. Sterker oxyderende omgevingen (bijvoorbeeld hogere temperaturen) geven aanleiding tot aanzienlijke oxydatie van SiC naar SiO_2 en sintering. De stabiliteit van SiC in sterk zure oplossingen maakt toepassing mogelijk als katalysatordrager in vloeistoffase reacties bij extreme pH condities.

Katalysator karakterisering staat centraal in hoofdstuk 8. Behalve de interactie na katalysatorsynthese als ook de stabiliteit van de katalysatoren komen aan de orde. De metaal-drager-interactie (Metal-Support Interaction) tussen de nikkel-precursor en de drager is voor silica en siliciumcarbide vergelijkbaar. De metaal-drager-stabiliteit van Ni/SiC katalysatoren is daarentegen substantieel hoger dan die van silica katalysatoren. Een gemakkelijk reduceerbaar NiO/SiC systeem blijft na 8 uur calcineren bij 1273 K behouden. Langere oxydatieperiodes zullen resulteren in de volledige conversie van SiC in SiO_2 , zoals beschreven is in hoofdstuk 7. Uit de resultaten van hoofdstuk 8 kan geconcludeerd worden dat de metaal-drager-interactie van SiC gebaseerde katalysatoren over het algemeen lager is dan die van silica en alumina. De stabiliteit van SiC katalysatoren is afhankelijk van zowel het aangebrachte metaal als het milieu waaraan het wordt blootgesteld.

Het gedeeltelijk geoxydeerde SiC oppervlak maakt tevens de synthese van hoog disperse nikkel-katalysatoren mogelijk met behulp van een ionenwisselings techniek. Hierbij wordt van de hoge reaktiviteit van de SiO_x oppervlaktelaag in basische milieus gebruik gemaakt.

Hoofdstuk 9 is op het testen van de thermische stabiliteit van hoogoppervlakkig SiC als dragermateriaal gericht. Er is gekozen voor de hoge temperatuur CO_2 reforming van methaan omdat het milieu van deze reactie niet sterk oxyderend is. Onderzoek aan verschillende katalysatorsystemen laat allereerst zien dat de dispergerende kwaliteiten van SiC goed zijn. Met behulp van droge impregnatie worden op eenvoudige manier rhodiumdispersies bereikt van 20%. De SiC-stabiliteit is tevens zeer goed met betrekking tot behoud van kristalliniteit en textuur tijdens reformen bij 1170 K. Uit deze resultaten kan geconcludeerd worden dat SiC inderdaad geschikt is voor gebruik als katalysatordrager onder extreme procescondities, mits deze niet oxyderend zijn. Is aan deze voorwaarde voldaan, dan kunnen de goede eigenschappen van SiC (hoge thermische geleidbaarheid, hardheid) ten volle benut worden.

Er kan geconcludeerd worden dat de de doelstellingen, die aan het begin van dit projekt gedefinieerd waren, grotendeels behaald zijn. Methoden, waarmee de de oxydatieresistentie en de attritie van actieve kool verbeterd kunnen worden, zijn ontwikkeld. Voor een volledige

evaluatie van het SiC met een hoog specifiek oppervlak is het echter bovendien noodzakelijk om een vloeistoffase testreactie mee te nemen. Bovendien zouden de hoge temperatuur gasfase testreacties uitgebreid kunnen worden naar lange duur experimenten (langer dan 100 uur). Op basis van deze resultaten zal dan een afgewogen oordeel over het gebruik van dit type katalysatordragers gegeven kunnen worden.

Nawoord

Verscheidene personen hebben ieder hun eigen bijdrage geleverd aan het tot stand komen van dit proefschrift. De volgende mensen wil ik daarvoor speciaal bedanken.

De samenwerking met de tandem Jacob Moulijn - Michiel Makkee heb ik als erg plezierig ervaren. Jacob, bedankt voor het vertrouwen om in grote vrijheid dit onderzoek uit te voeren. Je motiveerde en inspireerde met gepointeerde opmerkingen en discussies. Michiel, jij stond altijd klaar voor het voeren van discussies en het doorlezen en becommentariëren van manuscripten en regelde allerlei dagelijkse zaken. Bovendien heb je ook met niet-wetenschappelijke gesprekken (bijvoorbeeld onderweg naar de IOP-bijeenkomsten) invloed gehad op de vorm van dit proefschrift.

De gastvrijheid in de groep Toegepaste Anorganische Chemie geschonken door Prof. Schoonman leidde tot een synergetische samenwerking: katalytische CVD bestaat!

Jan Pieter Dekker heeft een grote bijdrage geleverd in het opzetten van hoofdstuk twee en zorgde voor de inwijding in wereld van de praktische CVD.

De technische hulp en deskundigheid van Ben Meester bij het ontwerp van de fluïde-bed CVD reaktor en het oplossen van allerlei experimentele problemen is onmisbaar geweest.

Een gedeelte van het beschreven werk is uitgevoerd door afstudeerders.

Henk Boon (conventionele CVD, "Hier is het schijfje monoliet"), Frank Tazelaar (kool-conversie, "Hier heb je het SEM-fotoboek"), Loeki Kramer (FBCVD en katalysator testen, "Ik wil/moet hard, veel en breed werken"), Edwin Tijssen (katalysator-synthese, -karakterisering en -testen, "Wow, bekijk die hoeveelheid cyclohexeen eens") en Theo Vergunst (CO₂-reformen, "Ik heb maar het vijftiende doosje floppen gehaald") zullen ieder hun bijdrage terugvinden.

Het totale team "Industriële Katalyse", Anja, Mark, Jean-Paul, Matthijs, John, Guido, Jan-Remmert, Gerard, Bastiaan, Freek, Dick, Andrzej C., Robert, Ahmed, Wridzer, Xander, André, Emile, Sytse, Annelies, Joop, Jaap, Paul, Adriëtte, Jolinde, Hank, Marco, José, Grégorio, Rafael, Dolf, Xiao Ding en Jan-Baptist zorgde voor de nodige ontspanningsmogelijkheden tijdens onvergetelijke zeil- en Ardennen weekeinden.

Bart Boshuizen heeft alles geautomatiseerd wat te automatiseren viel. Van de ondersteunende diensten zou ik Jaap Teunisse, Thom van Velzen en Fred Hammers voor respectievelijk ontelbare textuur-analyses, het verzorgen van de gassen en het uitvoeren van allerlei fotografische zaken willen bedanken.

De begeleidingscommissie van het IOP (Dr. ir. M. Makkee, Prof. dr. J.A. Moulijn, Prof. dr. ir. H. van Bekkum (allen TU Delft), Prof. Ir. J.W. Geus (Universiteit Utrecht),

Dr. W.M.T.M. Reimerink (Norit), Dr. E.G.M. Kuijpers (Engelhard), Dr. P.W. Lednor (Shell), Dr. F.T.B.J. van den Brink (DSM) en Dr. N.G. Minnaard (Solvay Duphar)) zorgde op de halfjaarlijkse bijeenkomsten voor toepassingsanalyses. Van deze groep wil ik met name Margriet Reimerink bedanken voor het beschikbaarstellen van actieve kool en de gastvrijheid op het Norit Research Laboratorium.

Tenslotte wil ik nog vier mensen uit de grond van mijn hart bedanken. Mijn ouders en Karin hebben mij tijdens en na mijn keuze om te gaan promoveren onvoorwaardelijk gesteund en gemotiveerd. Dit is voor mij zeer belangrijk geweest. Monique, vooral het laatste jaar was een redelijke heksenketel. Jij was en bent echter het vaste baken in roerige tijden en zorgde er zo mede voor dat dit boekje zijn huidige staat heeft bereikt.

Curriculum Vitae

Robert Moene werd geboren op 1 november 1966 te Leidschendam. In 1979 is gestart met het Voorbereidend Wetenschappelijk Onderwijs aan het Stedelijk Gymnasium te Leiden. Na het behalen van het diploma in 1985 is in hetzelfde jaar gestart met de opleiding Scheikundige Technologie aan de Technische Universiteit Delft. Het afstudeeronderzoek is verricht onder leiding van Prof. dr. J.J.F. Scholten en betrof het ontwikkelen van gedragen katalysatoren voor de partiële hydrogenering van benzeen naar cyclohexeen. Het ingenieursdiploma is behaald in februari 1991. Maart 1991 is het promotie-onderzoek gestart aan de Technische Universiteit Delft in de groep Industriële Katalyse onder leiding van Prof. dr. J.A. Moulijn. De resultaten daarvan zijn in dit proefschrift weergegeven. Maart 1995 treedt Robert Moene in dienst van het Koninklijke/Shell-Laboratorium, Amsterdam.

List of publications

ARTICLES

- R. Moene, J.P. Dekker, M. Makkee, J. Schoonman, and J.A. Moulijn, Evaluation of Isothermal Chemical Vapour Infiltration with Langmuir-Hinshelwood Type Kinetics, *J. Electrochem. Soc.*, **141** (1994) 282.
- R. Moene, M. Makkee, J.A. Moulijn, Chemical Vapour Deposition as a Novel Technique for Catalyst Preparation, Modelling of Active Phase Profiles, *Chem. Eng. J.*, **53** (1993) 13.
- R. Moene, L.F. Kramer, J. Schoonman, M. Makkee, and J.A. Moulijn, Conversion of Activated Carbon into Porous Silicon Carbide by Fluidized Bed Chemical Vapour Deposition, Scientific Bases for the Preparation of Heterogeneous Catalysts, Proceedings of the 6th Intern. Symp., 1994, Preprints, vol. 1, p. 379.
- R. Moene, J. Schoonman, M. Makkee, and J.A. Moulijn, Nickel catalyzed conversion of activated carbon into porous silicon carbide, synthesis and properties, to appear in "Advanced Catalytic Materials", Proceedings of the Materials Research Society, MRS Fall '94.
- R. Moene, F.W. Tazelaar, M. Makkee en J.A. Moulijn, Werkwijze voor de Bereiding van een Poreus Silicium Carbide, Nederlandse octrooi-aanvraag nr. 93.00816.
- J.P. Dekker, R. Moene, H.J. Veringa, J. Schoonman, The Influence of Surface Kinetics in Modelling Chemical Vapour Deposition Processes in Porous Preforms, submitted for publication.
- J. Struik, R. Moene, T. van der Kamp, and J.J.F. Scholten, Partial Liquid-Phase Hydrogenation of Benzene to Cyclohexene over Ruthenium Catalysts in the Presence of an Aqueous Salt Solution, *Appl. Catal. A*, **89** (1992) 77.

ABSTRACTS

- R. Moene, M. Makkee, J. Schoonman, and J.A. Moulijn, Development of High-Temperature Catalytic Supports Based on Active Carbon, Carbon '92, Proceedings of the 5th Carbon Conference, Essen, German Carbon Group, 1992, p. 474.
- R. Moene, M. Makkee, J.A. Moulijn, Evaluation of Isothermal Chemical Vapour Infiltration with Langmuir-Hinshelwood Type Kinetics, Carbon '93, Proceedings of the 21st Biennial Conference on Carbon, Buffalo, American Carbon Society, 1993, p. 110.
- R. Moene, F.W. Tazelaar, M. Makkee, J.A. Moulijn, Conversion of Activated Carbon into Porous Silicon Carbide by Reactive Chemical Vapour Deposition, Carbon '94, Proceedings of the 6th Carbon Conference, Granada, Spain, 1994, p. 532.

Chapters 5 to 9 will be submitted for publication in Journal of Catalysis, Applied Catalysis, or Catalysis Letters.